A Computational Study of *E. coli* Chemotaxis

This thesis was reviewed by:

prof. dr. D. Bray
prof. dr. F. C. MacKintosh
prof. dr. B. Mulder
dr.ir. E. W. Peterman
dr. A. Vaknin
dr.ir. G. J. Wuite

ISBN-13: 978-90-77209-26-4
ISBN-10: 90-77209-26-3

A digital version of this thesis can be downloaded from http://www.amolf.nl

Cover: Simon Tindemans, "Push-pull network"

The work described in this thesis was performed at the FOM-Institute for Atomic- and Molecular Physics, Kruislaan 407, 1098 SJ, Amsterdam, The Netherlands. The work was supported by the Nederlandse Organisatie voor Wetenschappelijk Onderzoek (NWO). The work of the FOM-institute is part of the research program of the Stichting Fundamenteel Onderzoek der Materie (FOM) and is supported by NWO.

VRIJE UNIVERSITEIT

A Computational Study of *E. coli* Chemotaxis

ACADEMISCH PROEFSCHRIFT

ter verkrijging van de graad Doctor aan
de Vrije Universiteit Amsterdam,
op gezag van de rector magnificus
prof.dr. L.M. Bouter,
in het openbaar te verdedigen
ten overstaan van de promotiecommissie
van de faculteit der Exacte Wetenschappen
op maandag 8 september 2008 om 13.45 uur
in het auditorium van de universiteit,
De Boelelaan 1105

door

Siebe Bruno van Albada

geboren te Charlottesville, VA, Verenigde Staten

promotor: prof.dr. P.R. ten Wolde

Contents

Chapter 1 Introduction 7
1.1 Introduction 7
1.2 The receptor cluster 11
1.3 The intracellular chemotaxis network 15
1.4 The flagellar motors 16
1.5 Outline 17

Chapter 2 Enzyme colocalization can drastically affect signal amplification 21
2.1 Introduction 21
2.2 Results 23
2.3 Discussion 33
2.4 Methods: The push-pull network 35

Chapter 3 The canonical model of E. coli chemotaxis 39
3.1 Introduction 39
3.2 Decomposing the response 41
3.3 Original model: the canonical push-pull network 45
3.4 Changing parameters in the canonical model 49
3.5 Summary 58
3.6 Methods 58
Appendix: Mapping between canonical push-pull network and chemotaxis network 59

Chapter 4 Differential affinity and catalytic activity of CheZ 61
4.1 Introduction 61
4.2 Differential affinity and catalytic activity of CheZ 62
4.3 The effect of cooperativity 68
4.4 Discussion 70
4.5 Methods 72
Appendix A Cooperativity in the phosphatase reaction 72
Appendix B The full model 76

Chapter 5 Particle-based simulations on the effects of colocalization of antagonistic enzymes 79
5.1 Introduction 79
5.2 The system 81
5.3 Results 83
5.4 Discussion and conclusions 93
5.5 Methods 94
Appendix: Mean-field model Colocalization 98

Chapter 6 Switching dynamics of the bacterial flagellar motor 101
6.1 Introduction 101

6.2 The stator-rotor interaction 104
6.3 The rotor switching dynamics 109
6.4 Flagellum dynamics 112
6.5 Discussion 115
Appendix: Power Spectra of an equilibrium system 116

Bibliography 119

Samenvatting 123
Denken zonder brein 123
Chemotaxis 123
Push-pull-netwerken 124
Verdeling van de eiwitten over de cel 125
Resultaten in dit proefschrift 125

Dankwoord 129

1 Introduction

1.1 Introduction

Sensing and responding to external signals are essential for any living organism. In order to survive, organisms have to measure signals from the environment, and react to them. Let us first briefly consider how we take care of these tasks ourselves, before we move to a much simpler organism, the unicellular *Escherichia coli*. It turns out that, besides the obvious differences, there are also large resemblances.
For measuring signals we use our senses, such as vision, hearing, taste, smell and touch. Subsequently, the response takes place in our neural system. Our brain is a very complex computer that has evolved to be extremely good at certain tasks, such as pattern recognition and detection of changes in the environment. In general, it is trained by evolution to react in the best possible way to the environment. The brain as a whole is immensely complex. However, it helps to think of it as a collection of very many - about 100 billion - subunits, called neurons, each of which is connected to, on average, 700 other neurons to form a large interconnected circuit.
The working of a single neuron is easier to understand. A single neuron is able to perform a number of simple, but important tasks. Its first task is to *measure input signals*. The input of the signal usually takes place at the dendrites, branched extensions that conduct impulses from adjacent cells inward toward the soma (cell body). Since the input signal may be very complex, it should first be processed in the soma. Importantly, if multiple, possibly contradicting input signals are received, the different signals first have to be *integrated*.
Next, the signal has to be transmitted to a possibly distant part of the cell. *Signal transduction* takes place through the axon(s). Nerve cells can receive and transmit signals without significant loss of signal strength. To this end, they can *amplify* signals. Furthermore, a nerve cell can respond on different time scales. That means that the cell has both short and long term *memory*. Finally, an *output* signal is given by the release of neurotransmitters at the synapses at the axon terminal. These neurotransmitters bind to chemo-receptors at the cell surface of, for instance, the dendrite of another neuron. The output of a neuron is an all-or-none signal.
Let us now have a look at the bacterium *Escherichia coli*, which is arguably the most studied bacterium and the best-understood organism. It lives in the gut of warm-blooded animals, such as human beings. *E. coli* has a spherocylindrical shape; it is about one micrometer in diameter and two-and-half long, and it is propelled forward by a number of flagellar rotary motors, which are randomly distributed over its cell surface. How

does a simple bacterium like *E. coli* sense external signals, and how does it respond to them? *E. coli* does not have the senses that we have, nor does it have a brain in the form of a neural network. In fact, the bacterium consists of one single cell, like a single neuron. Still, *E. coli* is able to take decisions, for instance concerning how to respond to changing nutrient signals.
The most obvious requirement for any form of life to be able to survive is that it should be able to collect enough nutrients. At the end of the nineteenth century, bacteria were shown to move in the direction of attractants, as well as away from repellents. This mechanism was termed *chemotaxis*. A swimming *E. coli* bacterium continually decides whether to keep swimming forward, or to look for a better swimming direction. As the bacterium is too small to measure concentration gradients, it makes a *temporal* comparison: If the nutrient concentration increases over time, it keeps swimming in the same direction, and if it decreases, it picks a new swimming direction *at random*. Thus, the bacterium switches between only two different modes: It either swims in a forward direction (a so-called *run*, or it stops swimming and reorients into another direction (a so-called *tumble*).
Julius Adler, a pioneer in the field of chemotaxis, found that *E. coli* contains a signal transduction mechanism similar to the synaptic response in higher eukaryotes: Certain chemicals that act as an input signal bind to chemo-receptors at the cell surface, which in turn regulate the activity of enzymes within the cytoplasm, catalyzing the activation of a secondary messenger.
Many of the above-mentioned aspects of the working of a nerve cell are also present in the chemotaxis system of *E. coli*. The first task of the chemotaxis pathway is to *measure the input signal*, namely concentrations of nutrients and other chemicals. The detection of chemicals occurs via binding of the molecules to a cluster of chemo-receptors that is typically located at one or both poles of the cell (see Fig. 1.1). At the receptor cluster, different signals are *integrated*, leading to one single response output. Furthermore, the input signals are also *amplified* at the receptor cluster, since the input signal may be extremely weak. Since *E. coli* makes temporal comparisons of the ligand concentrations, it also needs a *memory* for the concentration at earlier times. This memory, as we will describe below, is provided by chemical reactions taking place at the receptor cluster. The receptor cluster can thus perform a large number of computational tasks. Indeed, it may be considered the central processing unit of the chemotaxis system.
After the input signal has been processed by the receptor cluster, it is transmitted from the cluster to the flagellar motors (see Fig. 1.1). The signal is transmitted by a messenger protein, called CheY, which diffuses from the receptor cluster to the flagellar motors. Upon binding of activated CheY molecules, the flagellar motors are biased to change their direction of rotation from counterclockwise (CCW) to clockwise (CW), resulting in a tumble. Also in this last step of the chemotaxis pathway, the signal is strongly amplified. Like the output of a neuron, the output of the chemotaxis pathway is an all-or-none signal: each motor rotates either in the CW or in the CCW direction.

The chemotaxis network of *E. coli* thus has an information processing capacity that rivals that of modern electronic circuits. Yet, its design principles are markedly different. In a biochemical network such as the chemotaxis pathway of *E. coli* the signals are processed via molecules that chemically and physically interact with one another.

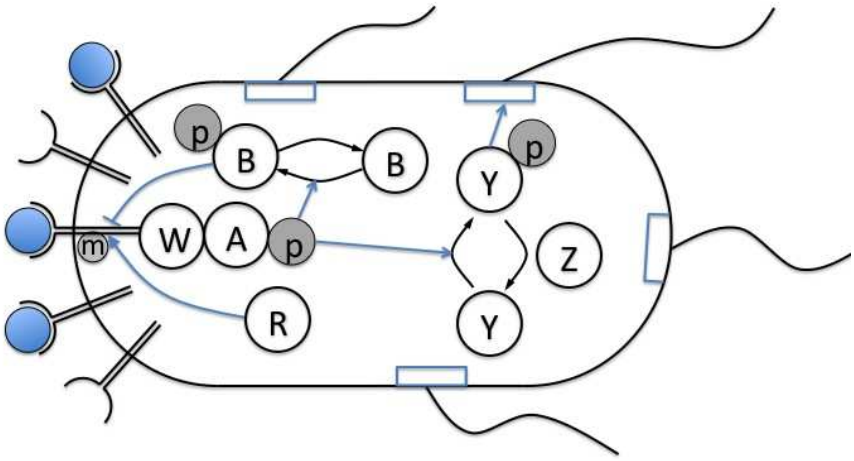

FIGURE 1.1 The chemotaxis pathway of *E. coli*. W stands for CheW, A for CheA, Y for CheY, Z for CheZ, R for CheR, B for CheB, p for a phosphoryl group and m for a methyl group. Upon binding of repellent to the trans-membrane receptors, or upon release of food, the activity of the receptors increases. As a consequence, the autokinase activity of CheA, that is linked to the receptors via the adaptor CheW, increases. CheA donates its phosphoryl group either to the messenger protein CheY, or to the methylesterase CheB. Phosphorylated CheY binds to the flagellar motors to increase their clockwise bias and, therefore, the tumble frequency. Thus, addition of repellent in the end leads to a higher tumbling frequency, as expected. The phosphatase CheZ increases the rate of dephosphorylation of CheYp by an order of magnitude. At a timescale slow as compared to ligand binding and signalling, the phosphorylated adaptation protein CheB demethylates the trans-membrane receptors, making them less active and thereby restoring the average phosphorylation level. Receptor methylation happens by the methyltransferase CheR. Receptor methylation counteracts the binding of attractant and leads to a higher kinase activity.

These molecules behave stochastically. They often move in an erratic fashion, namely by diffusion, and also the chemical and physical interactions are probabilistic in nature. Since chemical networks of living organisms need to be highly dynamic, the interactions are often relatively weak, i.e., on the order of 1 to 10 k_BT. This means that cooperative interactions are needed to amplify signals. A paradigm example is the receptor cluster of *E. coli*, which has been successfully modeled as an Ising system [1]. Clearly, to understand the performance of a biochemical network, we have to use concepts from statistical physics, such as diffusion, biochemical noise, and cooperative interactions.

This makes biochemical networks not only of interest to biologists, but, increasingly, also to physicists.
The *E. coli* chemotaxis pathway is an ideal model system, precisely because such a large body of biological data is available. Decades of biological experiments have provided a wealth of information on the topology and the rate constants of the network, and new technological developments have made it possible to study the network in unprecedented detail. For example, the distribution of individual molecules within a single cell can be traced via fluorescent labeling of the molecules, and even the interactions between two protein species can be made visible via fluorescence resonance energy transfer (FRET). In combination with more conventional biochemical assays, these techniques allow the study of the effect of, for instance, the spatial distribution of the molecules on the response of the network. As another example, new techniques allow the precise measurement of power spectra of the switching dynamics of the flagellar motors, that contain much information on the design principles of the motors. The more quantitative the experiments become, the more quantitative the system can be modeled.

More generally, understanding biochemical networks is not only of fundamental interest, but also has implications in the food industry, health and energy. It is increasingly recognized that many diseases are caused not by the malfunctioning of single proteins, but rather by malfunctioning of the network as a whole. Moreover, much effort is devoted to manipulating signalling and metabolic networks of algae, to increase energy production for biofuels. While the *E. coli* chemotaxis system is relatively simple and may seem to bear no relevance for these developments, it should be recognized that this system exploits network motifs, which are omnipresent in both prokaryotes and eukaryotes. For example, the intracellular chemotaxis pathway consists of a so-called push-pull network, in which two enzymes (CheA and CheZ, respectively, see Fig. 1.1) covalently modify a substrate (CheY). Such push-pull networks constitute the building blocks of many signal transduction pathways in prokaryotes and eukaryotes. Homologues of the two central proteins CheA and CheY are widely conserved among different species. Furthermore, virtually all motile prokaryotes use essentially the same mechanism to regulate their motility. Since *E. coli* plays a role in the flora of the gut, and since also toxic strains exist, it is of importance to the food industry as well as to drug design. In addition, maybe the ultimate example of nanotechnology is given by the rotary flagellar motor of *E. coli*, which has the design of an electromotor, but is no larger than 50 nm in diameter.

In the remainder of this chapter, we first give an overview of the three modules of the chemotaxis system. We discuss the receptor cluster in considerable detail, since that has been studied extensively in the past years, both theoretically and experimentally. We then discuss the second and third module of the chemotaxis system: the intracellular signal transduction pathway and the flagellar motors. We end this chapter with a brief summary of the contents of this thesis.

1.2 The receptor cluster

1.2.1 Structure

At the beginning of the chemotaxis pathway are a large number of trans-membrane receptors that bind to chemo-attractants and -repellents. These receptors form homo-dimers [2], which act as the functional units for ligand binding. In addition, the receptors form a stable complex with the kinase CheA and the adaptor protein CheW [3, 4]. The structure of the cytoplasmic portion of the trans-membrane receptors has been determined to be a long α-helical coiled coil. The tails of three receptor dimers are thought to come together, such that the receptors form *trimers of dimers* [5]. Genetic analysis also supports the idea of interactions between three dimers [6]. As trimers of receptor dimers are stable against the presence of CheW, CheA, ligand, and the methylation state, Studdert and Parkinson argued that trimers of dimers form the basic building blocks for the signaling complexes [7]. The trimers of dimers, however, are still not the largest aggregates: the receptors form a cluster at the cell pole [8]. The nature of the interactions between the trimers of dimers has yet to be unraveled.
Within the receptor cluster, there are five different types of receptors, and each of them can respond to multiple stimuli. Two of these, the serine receptor Tsr and the aspartate receptor Tar are present in high abundance, whereas the other three receptor types Trg, Tap and Aer are present at very low concentrations. It is commonly assumed that the chemo-receptor dimers can be in either of two conformational states: an active conformation stimulating auto-phosphorylation of the kinase CheA, and an inactive one, inhibiting CheA auto-phosphorylation. Upon binding of chemo-attractant to the receptor cluster, or upon release of a repellent, the receptor activity decreases. Binding of a repellent and unbinding of an attractant have the opposite effect and lead to an increased receptor activity.

1.2.2 Adaptation

On its search for food, *E. coli* senses concentration gradients rather than absolute concentrations [9]. Namely, if the bacterium starts out at a certain fixed concentration, and later arrives at some other concentration, it will return to its old swimming behavior after some time. This is due to adaptation [10].
Importantly, the adaptation reactions are much slower than the reactions that constitute the response: ligand binding and the phosphorylation reactions. This separation of time scales makes it possible to respond to changes in the ligand concentration at short time scales, and adapt to these changes on longer time scales.
Adaptation could in principle take place at various stages of the adaptation pathway. However, it happens near the beginning of the chemotaxis pathway, by resetting of the receptor activities via methylation by CheR and demethylation by CheB. As a consequence, the concentration of CheYp always remains near the sensitive range of the flagellar motors. This would not have been the case if, for example, the motors had been responsible for adaptation. An interesting question is, why adaptation does not take place at an even earlier stage of the chemotaxis pathway, namely, by modifying the affinity of the receptor cluster, such that always about half of the receptors would be occupied by ligand molecules. The advantage would be, that the sensitivity of the

receptor cluster is largest if fifty percent of the receptors is occupied by ligand molecules. However, *E. coli* would in that case not be able to respond to concentrations that are so low that not enough ligand molecules are present to cover half of the receptors. Wild type *E.coli* is in fact able to respond to the binding of a few ligand molecules.
The ability of *E. coli* to adapt to different background concentrations is remarkable: the concentration range over which *E. coli* is able to adapt is very wide. *E. coli* responds to successive increases in its concentration over a range spanning over five orders of magnitude, from 0.3 μM to 0.1 M of the artificial attractant α-methylaspartate [11]. The adaptation mechanism must work nearly perfectly, since the behavior of *E. coli* is almost independent of the background concentration.
A possible explanation for the near-exact adaptation was given by Barkai and Leibler [12]. They proposed a scheme in which CheB only methylates active receptors, whereas CheR demethylates both active and inactive receptors. In this case, adaptation is not only exact; it is also robust. That means that the concentrations of the different network components, as well as the rate constants and diffusion coefficients, need not have specific values in order for the adaptation mechanism to work; a bacterium adapts to its steady state irrespective of its system parameters. This does not, however, mean that the steady state of the chemotaxis system is independent of the system parameters. On the contrary, variations in the system parameters lead to behavioral variability between the individual bacteria of a colony: every bacterium adapts to its own steady state. This is indeed known to be the case experimentally. Interestingly, the model predicts that the steady-state tumbling frequency and the adaptation time of an individual bacterium are strongly correlated, something that had been found in experiments before [13].
The mechanism for robust adaptation as proposed by Barkai and Leibler [12] is consistent with a large body of experimental observations. It is widely believed that CheR indeed methylates active as well as inactive receptors [14, 15], whereas CheB demethylates only active receptors [16, 17]. Furthermore, Alon et al. verified that *E. coli*'s adaptation mechanism is not only exact, but also robust [18].

Barkai and Leibler stated that mechanisms will in general adapt robustly if the modification and demodification rates only depend on the activity of the receptors. For example, if the methylation rate r by CheR is constant, and the demethylation rate bA by CheB is proportional to the activity A of the cluster, then the change in the methylation level z is given by $dz/dt=r-bA$. In steady state, the activity is then constant: $A=r/b$. Thus, as the activity is independent of the methylation level, adaptation is robust. Yi et al. [19] ascribe the property of robust adaptation to *integral feedback* and they prove that perfect adaptation is always equivalent to integral feedback control. In fact, the adaptation needs not be exact, but must be accurate enough to keep the cells near the middle of the flagellar motor response curve [20]. This keeps the sensory pathways from saturating, and allows cells to remain sensitive to concentration changes over a wide range of chemical environments.

1.2.3 Receptor interactions and amplification

Impressively, *E. coli* responds to very small changes: smaller than one percent in the receptor occupancy with aspartate over concentrations spanning three orders of magnitude

[21]. A net change in Tar occupancy by aspartate of 0.4% can result in a 22% increase in the CCW motor rotation bias [22]. This means that input signals are amplified very strongly to produce a response.

Bray et al. proposed that interactions between the receptors in a regular lattice could lead to a strong amplification of the signal if neighboring receptors would be sensitive to each other's activity [23]. The binding of a single attractant molecule could then lead to a large cluster of inactive receptors. Particularly, if neighboring receptors interact in an Ising-type fashion, enormous signal amplification can be obtained if the system is close to the critical point [1, 24]. In the latter model, receptors are assumed to flip between an active and an inactive state with probabilities dependending upon three energy inputs: ligand binding, methylation level due to adaptation, and the activity of neighbouring receptors.

Since no method exists to directly measure the activity of the receptor cluster, Sourjik and Berg came up with a nice way to measure the activity indirectly [25]. In steady state, the rate of phosphorylation of CheY by CheA – which is proportional to the receptor activity – equals the rate of dephosphorylation by CheZ. Sourjik and Berg therefore used FRET to measure the interaction between CheY and CheZ as a measure for the activity of the receptor cluster. They found that a small increase in the concentration of α-methyl aspartate produced a large decrease in CheA activity. By comparing the change in receptor occupancy expected from measured binding curves to different methylated forms of the receptor, they concluded that the decrease in CheA activity is about 35 times greater than the relative change in receptor occupancy.

Mello and Tu [26] were able to fit the response curves as measured by Sourjik and Berg in [25] quite accurately, using a mean-field Ising-type model. They considered Tar and Tsr receptors, for which the energy difference between the active and the inactive state depends on ligand binding, on the methylation state, and the activity of the other receptor species. Interactions between the Tar and Tsr receptors turned out to be necessary to fit the data.

The key observation they made, was that different strains, for which the Tar receptors were known to be in the same, fully unmethylated state, responded totally differently to methylaspartate. In particular, the part of the response curves corresponding to the response through the Tar receptor differed markedly between the two strains. Since the methylation levels of the Tsr receptors were known to be different for the two strains, Mello and Tu postulated that there is a strong coupling between the Tar and Tsr receptors, and that the interaction depends on the methylation state of the receptors.

Ames et al. found that the receptors have a preference for the formation of mixed clusters, which also speaks for heterogeneous interactions [6].

Experiments by Gestwicki and Kiessling added to the proof of the importance of heterogeneous interactions between the different receptor species [27]. By artificially increasing the clustering between the receptors through the addition of multivalent attractants that bind to the low-abundant Trg receptor, the response to serine was increased over 100-fold. Interestingly, the response decreased if the Tar or Tap receptors were not

expressed, clearly suggesting that the Tar and Tap receptors, which do not bind serine, assist in responding to serine.

The experimental observations mentioned above suggest that the response strongly depends on the composition of the receptor cluster. This is indeed what Sourjik and Berg found [28]. CheA and CheW turn out to play an important role in the connectivity between the receptors. Also, the expression levels of the different receptor types play a major role. For example, increasing the level of expression of either Tar or Tsr in a *tsr tar tap* strain gave responses to MeAsp or serine with Hill coefficients increasing from 2 to 10, respectively. Such a large Hill coefficient cannot be obtained by assuming only interactions within trimers of dimers. The dependence of the cooperativity on the receptor connectivity can be explained via clusters of increasing size in terms of an MWC model [29]. In the MWC model, a cluster of N binding sites can be either in an active or in an inactive form. The binding of each attractant molecule multiplies the relative probability for the inactive state by a constant factor. This factor is also equal to the ratio of the dissociation constants of attractant for inactive and active states of the receptors. The MWC model of size N is equivalent to an Ising model of size N with infinite coupling strength in an external magnetic field. Mello and Tu were indeed able to fit the data from Sourjik and Berg by using a generalized MWC model [30]. As in their Ising model, heterogeneous interactions between the receptor types turned out to be of crucial importance.
Keymer et al. [31] also used the MWC model to fit the results of Sourjik and Berg [25]. They made the observation that there exist two regimes of the MWC model, depending on the energetics of a single receptor. In the first case, the receptor is active most of the time if no attractant molecule is bound. Upon addition of attractant, the receptor will turn to the inactive state. This transition will become sharper and sharper if more receptors are added to the cluster, since the energy difference between the active and the inactive states increases more rapidly. The affinity for ligand, however, will stay the same. In the other case, the receptor is already in its inactive state most of the time, even if no attractant has been added. Upon addition of attractant, the receptor will stay in the active state. The Hill coefficient will always be one, no matter how large the receptor cluster is. However, the sensitivity will increase for larger cluster sizes. Thus, in the former case, receptor coupling leads to a higher Hill coefficient, while in the latter case, receptor coupling leads to higher sensitivity to ligand. Both regimes are present in the measurements of Sourjik and Berg.

Shimizu et al. proposed an elegant model for the structure and functioning of the receptor cluster [32]. According to the model, the receptor dimers form a regular two-dimensional lattice, based on the trimer-of-dimers configuration. Herein, the ends of the receptor dimers are inserted into a hexagonal array of CheA and CheW molecules. Downstream signalling can then take place at the outer CheA plane of the cluster. Locked between the CheA plane and the membrane, there is a separate compartment for adaptation of the receptors via (de-)methylation by the adaptation enzymes CheR and CheB. The adaptation enzymes CheR and CheB could move via a mechanism termed molecular brachiation [33]. This mechanism is based on the fact that the adaptation

molecules have a dumbbell shape: The active domain and the binding domain are separated by a flexible linker. If both domains have an intermediate binding affinity for the receptors, the molecule as a whole can bind firmly, while it can, at the same time, rapidly diffuse through the receptor cluster. Compartmentalized or not, the adaptation molecules remain bound to the receptor cluster, and are very efficient in methylating and demethylating the receptors.

1.3 The intracellular chemotaxis network

The topology of the chemotaxis network is similar to that of a push-pull network [34]. In a push-pull network, two antagonistic enzymes, E_a and E_d, reversibly modify a substrate molecule X. The enzyme E_a activates X to form X^*, whereas the enzyme E_d deactivates X^* to form X. Both reactions obey Michaelis-Menten kinetics, which means that the enzymes bind tightly to their substrate before they can modify them:

$$E_a + X \underset{k_b^a}{\overset{k_f^a}{\rightleftharpoons}} E_aX \overset{k_{cat}^a}{\rightarrow} E_a + X^* \tag{1.1}$$

$$E_d + X^* \underset{k_b^d}{\overset{k_f^d}{\rightleftharpoons}} E_dX^* \overset{k_{cat}^d}{\rightarrow} E_d + X \tag{1.2}$$

We will now make two assumptions: i) the total substrate concentration is much larger than the enzyme concentrations, and ii) the enzymes are saturated with their substrates which means that nearly all enzyme is present in the bound forms E_aX or E_dX^*. Under these conditions, both enzymes work at their maximum rates, so that the production rates of the two Michaelis-Menten reactions are simply constant; they do not depend on the substrate concentrations:

$$\frac{d[X^*]}{dt} \approx k_{cat}^a [E_a]_T \tag{1.3}$$

and

$$\frac{d[X]}{dt} \approx k_{cat}^d [E_d]_T \tag{1.4}$$

Therefore, since the conversion of X to X^* and the conversion in the other direction, of X^* to X happen at constant rates, the fastest of the two reactions will in the end simply convert all of its substrate into product. If the maximum rates for the two reactions lie very close together, a small change in either rate can cause a dramatic change in the concentration of modified substrate. This mechanism is termed zero-order ultrasensitivity.

Vaknin and Berg showed that the spatial distribution of the components of a push-pull network can have a drastic influence on the response [35]. They used single cell FRET experiments to measure the interations between $CheY_p$ and CheZ. It was known that CheZ can bind to $CheA_s$, a short, non-phosphorylating version of CheA, and that $CheA_s$ enhances the activity of CheZ [36]. It turned out that, although CheZ is a diffusive protein, binding to CheYp preferentially takes place at the receptor cluster. Thus, both phosphorylation (by CheA) and dephoshorylation of CheY (by CheZ) take place

at the receptor cluster. In steady state, the concentration profile of CheYp is then homogeneous. This could be advantageous, as all the flagellar motors experience the same concentration of CheYp. It is an interesting question what other consequences there are of the colocalization of the antagonistic enzymes (see chapters 2 and 5). In [35], also a non-localizing CheZ mutant was studied. In this case, the steady state profile of CheYp is to a good approximation exponentially decaying:

$$[\mathrm{Y_p}](x) = [Y_p](0)\exp(-x/\lambda). \tag{1.5}$$

where x is the distance from the cell pole, $\lambda = \sqrt{D/\mu}$, D is the diffusion coefficient and μ is the phosphatase rate of Y_p per second, which is assumed to be constant over the cell length.

1.4 The flagellar motors

The flagellar motors of *E. coli* pretty much resemble an electromotor, the most obvious difference being that it is only 50 nm in diameter. *E. coli*'s motor consists of a stator and a rotor. The power source is an electrochemical gradient across the inner membrane of the cell. Driven by the electrochemical gradient, protons move through the stators, which as a consequence undergo a conformational change, and exert a force on the rotor, causing it to turn one step further. As it turns out, the rotation of the motor is tightly coupled to proton translocation [37, 38].

The force that the motor can apply, depends on how fast the motor rotates [39, 40, 41]. The force is nearly constant if the motor rotates at low and intermediate speeds, until it reaches a knee value, and then declines rapidly at high rotation speeds.
Based on these experiments, Xing et al. proposed a model that is consistent with the above observations [42]. Importantly, according to their model, protons can only move through the rotors at specific angular positions of the rotor, as the ion channels open up. With this condition, the knee in the torque-speed relation can be reproduced.

Thus far, we have only considered rotation of the motor in one direction. However, the motor can rotate in two directions: counterclockwise (CCW), corresponding to the swim state, and clockwise (CW), giving rise to a tumble. The rotor contains 26 FliM units, which can each bind a CheYp molecule. Binding of CheYp leads to a sharp increase of the CW bias. Scharf et al. found quite a scharp response curve, with an apparent Hill coefficient of 4, via population-averaged measurements [43]. They were able to fit their switching data and motor bias of the motor by an MWC model, the same model that is used to explain the sharp response of the receptor cluster.

Cluzel et al. repeated the same experiments, but with a fluorescently labelled mutant of CheY [44]. They found that the CW bias depends sigmoidally on the concentration of CheYp with an apparent Hill coefficient around 10 (see Fig. 1.2). Cluzel et al. proposed that the steep input-output characteristic of the motors is related to a cooperative binding process of the CheY-P molecules to the FliM subunits. However, this turned out not to be the case. In [45], the binding of CheYp to FliM was measured with FRET. Here, the binding of CheYp to FliM does not seem to be strongly cooperative. This was

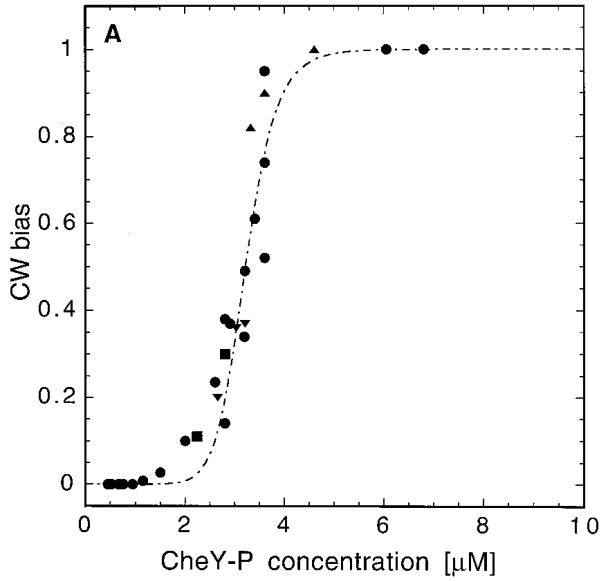

FIGURE 1.2 The sharp response curve of the rotation direction of the motors as a function of the CheY-P concentration. The curve has an apparent Hill coefficient of 10. The figure was taken from Ref. [44]

confirmed in [46]. This means that the chemotactic signal is amplified within the motor, subsequent to the CheYp binding.
A one-dimensional Ising model [47] or an MWC model could account for the ultrasensitive dependence of the CW bias on the CheYp concentration.

Korobkova et al. discovered that motor switching is a non-exponential process [48] and that there are long-time correlations up to 15 minutes. They attribute these correlations to the slow methylation dynamics of the receptor by CheR and CheB. They also found that each individual bacterium has its own, personal, switching dynamics. In a new experiment, Korobkova et al. took power spectra from binary time series of motor switching, and found that these exhibited a peak around 1 Hz [49]. In chapter 6 we will develop a model for the switching of the bacterial flagellar motor.

1.5 Outline

In this thesis, we focus on the second and third module of the chemotaxis pathway: the transduction of the signal from the cluster to the flagellar motors and the switching of the motors. As mentioned, the intracellular chemotaxis pathway consists of a push-pull network, which can strongly amplify signals via the mechanism of zero-order ultrasensitivity. In the modelling of these networks, it is commonly assumed that the system is well-stirred, meaning that the components are uniformly distributed in the system at all times. However, the chemotaxis system is not a well-stirred system. The messenger CheY diffuses in the cytoplasm. In contrast, CheA, the enzyme that activates the messenger, is located at the receptor cluster. The spatial distribution of CheZ, the

enzyme that deactivates the messenger, is less clear. It had long been believed that CheZ is distributed in the cytoplasm, but recent experiments [25] show that CheZ is also located at the receptor cluster. In particular, a recent study by Vaknin and Berg [35] showed that the spatial distribution of CheZ can markedly affect the response of the network: the spatial distribution affects both the sensitivity and the gain of the network.

In chapter 2 of this thesis, we perform a detailed mean-field analysis of the effect of the spatial distribution of the antagonistic enzymes on the steady-state response of a generic push-pull network. The principal finding is that the spatial distribution can dramatically affect the gain. The gain is maximized when the enzymes are either colocalized in one region of the cell or uniformly distributed in the system. Depending on the diffusion constants, however, the gain is strongly reduced when the antagonistic enzymes are spatially separated.

In the next chapter, we specifically address the question whether the commonly accepted model of the chemotaxis system of *E. coli* can explain the experiments by Vaknin and Berg [35]. We argue that this is probably not the case and that this model needs to be augmented. In the subsequent chapter we present such a model. In this model, a small, yet highly active fraction of CheZ is located at the receptor cluster, while the remainder freely diffuses in the cytoplasm. This model can describe the experimental results of Vaknin and Berg and is consistent with a large body of other experimental data.

The analyses presented in chapters 3 and 4 are mean-field analyses using chemical rate equations. In such mean-field analyses, it is assumed that the concentrations are large and that fluctuations can be neglected. In chapter 5 we perform particle-based simulations of push-pull networks. These particle-based simulations take into account the discrete nature of the components, the stochastic character of their interactions, as well as their spatial distribution. We compare the response of a network in which all components freely diffuse in the cytoplasm with the response of a network in which the antagonistic enzymes are located at the receptor cluster. We find that the spatial distribution of the enzymes can strongly affect the response dynamics. However, the steady-state input-output relation is quite insensitive to the spatial distribution of the enzymes; indeed, our results support the use of chemical rate equations, if one is interested in the steady-state response.

In chapter 6 we study the switching dynamics of the flagellar motors. Recently, Cluzel et al. measured power spectra of the motor switching dynamics of both wild-type and mutant cells [49]. The power spectra of mutant cells, that are believed to reflect the intrinsic switching dynamics of the motor, exhibit a pronounced peak around 1 Hz [49]. This peak means that the switching is non-Poissonian, and that there is a characteristic time scale on which the motors switch. We point out that the peak in the spectrum implies that the switching dynamics is coupled to a non-equilibrium process. We argue that this non-equilibrium process is the relaxation behaviour of the flagellum. In particular, we predict that the peak is caused by the interplay between the exponential dependence of the intrinsic motor switching rate on the load, and the relaxation behaviour of the flagellum, which determines the load on the motor. In essence, the switching process can

be described by a two-state model, with a switching propensity function that increases with time.

2 Enzyme colocalization can drastically affect signal amplification

Push-pull networks are ubiquitous in signal transduction pathways in both prokaryotic and eukaryotic cells. They allow cells to strongly amplify signals via the mechanism of zero-order ultrasensitivity. In a push-pull network, two antagonistic enzymes control the activity of a protein by covalent modification. These enzymes are often uniformly distributed in the cytoplasm. They can, however, also be colocalized in space, for instance, near the pole of the cell. Moreover, it is increasingly recognized that these enzymes can also be spatially separated, leading to gradients of the active form of the messenger protein. In this chapter, we investigate the consequences of the spatial distributions of the enzymes for the amplification properties of push-pull networks. Our calculations reveal that enzyme localization by itself can have a dramatic effect on the gain. The gain is maximized when the two enzymes are either uniformly distributed or colocalized in one region in the cell. Depending on the diffusion constants, however, the sharpness of the response can be strongly reduced when the enzymes are spatially separated. We discuss how our predictions could be tested experimentally.

2.1 Introduction

Living cells are information processing machines. In order to process information reliably, signals often need to be amplified. To this end, cells can employ a variety of amplification mechanisms. Signals can be amplified via positive feedback, cooperative binding of signaling molecules to receptors, or interactions between receptor molecules [23]. Another principal mechanism for signal amplification is zero-order ultrasensitivity [34, 50]. This mechanism operates in so-called push-pull networks, which are omnipresent in both prokaryotes and eukaryotes. In a push-pull network, two enzymes covalently modify a component in an antagonistic manner (see Fig. 2.1). One well-known example is a network in which a kinase phosphorylates a component, and a phosphatase dephosphorylates the same component. If both enzymes operate near saturation, then the modification reactions become zero order, which means that the reaction rates become insensitive to the substrate concentrations. Under these conditions, a small change in the concentration of one of the two enzymes (the input signal), will lead to a large change in the concentration of the modified protein (the output signal) [34, 50]. The amplification properties of push-pull networks have been analyzed in detail [34, 50, 51, 52, 53, 54, 55]. In these studies, however, it is assumed that the antagonistic enzymes are uniformly distributed in space. Yet, it is increasingly recognized that in many systems one or both of the two antagonistic enzymes are localized in space, for instance at the cell pole. Here,

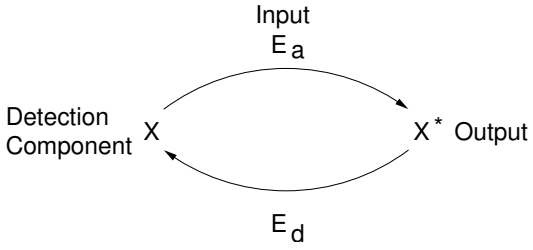

FIGURE 2.1 A push-pull network. Two enzymes, E_a and E_d, covalently (de)modify the components X and X*, respectively. The activating enzyme E_a provides the input signal, the unmodified component X is the detection component and the modified component X* provides the output signal.

we address the question how the spatial distribution of the antagonistic enzymes affects the amplification properties of push-pull networks.

If the two antagonistic enzymes are separated in space, then gradients of the messenger protein can form [56, 35, 57, 58, 59]. Recently, a number of protein gradients have been observed experimentally in both prokaryotic and eukaryotic cells. For example, in *Escherichia coli* cells, the kinase CheA and the phosphatase CheZ control the phosphorylation level of the messenger CheY, which transmits the chemotactic signal from the receptor cluster to the flagellar motors. In wild-type cells, the kinase and the phosphatase are both localized at the receptor cluster [60], and, as a result, the steady-state concentration profile of CheY is uniform [35]. However, in *E. coli* mutants, where the phosphatase is distributed in the cytoplasm, gradients of CheY have recently been observed [35]. Other examples of protein gradients include *Caulobacter*, in which MipZ gradients guide chromosome segregation and division site selection [61]. In eukaryotic cells, gradients of Ran, Stathmin, and HURP proteins aid in the formation of the mitotic spindle by providing directional cues for microtubule growth [62, 63, 64, 65]. Moreover, in eukaryotic cells, the kinases in the mitogen-activated protein kinase (MAPK) cascade often bind to scaffold proteins, while the phosphatases are distributed in the cytoplasm [66]. This will lead to concentration gradients of the activated kinases, which can become particularly important if the scaffolds are located near the membrane.

In this study, we compare the amplification properties of a canonical push-pull network, where all components are uniformly distributed in space, with those of a network in which the enzyme that provides the input signal is localized at one end of the cell, while all the other components can freely diffuse through the cell. In the latter case, the concentration profile of the messenger—the output signal—is non-uniform. Previous studies have focused on the time-dependent concentration profiles of the messenger [56, 58, 59] and on the 'control' of diffusion over protein fluxes [67] in similar systems. Here, we examine the effect of the spatial distribution of the enzymes on the amplification properties of push-pull networks. To this end, we compute for both systems the steady-state input-output relations. Our analysis reveals that the spatial distribution of the enzymes can have a dramatic effect on the capacity of push-pull networks to amplify input signals: the maximum gain of the network in which one enzyme is localized at one end of the cell, while the other is not, can be much lower than that of the network in which the components are uniformly distributed in space. Importantly, this effect occurs over

a range of diffusion constants, protein concentrations, and enzymatic activities that is typical for living cells.

In the next section, we first present the input-output relations for both networks. We show that the gain can be much reduced when the enzymes are spatially separated, and demonstrate that the magnitude of this effect depends upon the diffusion constants of the diffusing components. To elucidate the dose-response curves, we discuss in the subsequent sections the spatial concentration profiles in both the low and high activation limits. This analysis reveals that the maximum gain in the non-uniform system is reduced, because the response of the network depends on the position in the cell. Interestingly, the calculations also show that separating the enzymes in space does not only attenuate strong signals by limiting the maximum response, but can also enhance the propagation of weak signals.

2.2 Results

2.2.1 The input-output relation

Goldbeter and Koshland showed that if the antagonistic enzymes in a push-pull network operate near saturation (see Fig. 2.1), a small change in the concentration of the activating enzyme E_a can lead to a large change in the output, the modified messenger X^* [34]. The enzymes become more saturated with substrate when either the Michaelis-Menten constants $K_{M,a}$ and $K_{M,d}$ decrease, or the total substrate concentration $[S]_T = [X] + [E_aX]/L + [E_dX^*] + [X^*]$ increases. Fig. 2.2a shows the steady-state input-output relation for a push-pull network in which all the components are uniformly distributed in space, for different substrate concentrations. It is seen that as the substrate concentration is increased, the sharpness of the response is drastically enhanced. This is the hallmark of the mechanism of zero-order ultrasensitivity.

In many systems, such as the bacterial chemotaxis network of *E. coli* [35], the two antagonistic enzymes are colocalized at the same pole, while the detection component X and the messenger X^* can diffuse through the cytoplasm. While the time-dependent response curves of such a network will differ from those of the two networks considered here, the steady-state dose-response curves will be identical to those of a network in which all the components are homogeneously distributed in the cytoplasm. The response curves shown in Fig. 2.2a thus also pertain to push-pull networks in which the two enzymes are colocalized at one end of the cell, while their substrates freely diffuse in the cytoplasm. Indeed, also in these networks the mechanism of zero-order ultrasensitivity can strongly amplify input signals.

Spatially separating the enzymes reduces the gain. Fig 2.2b shows the dose-response curves for a push-pull network in which the activating enzyme E_a is localized at one pole of the cell, while the other components diffuse in the cytoplasm. Three points are worthy of note. The first is that the maximum output signal, the concentration of the messenger X^*, is much lower than that of the corresponding network in which all components are uniformly distributed in space (see Fig. 2.2). In fact, while in the spatially uniform network, the fraction of modified substrate, $[X^*]_T/[S]_T$, always approaches unity if $[E_a]_T/[E_d]_T$ becomes large, in the non-uniform network the fraction of modified substrate saturates to a lower level: even when the concentration of activating enzyme

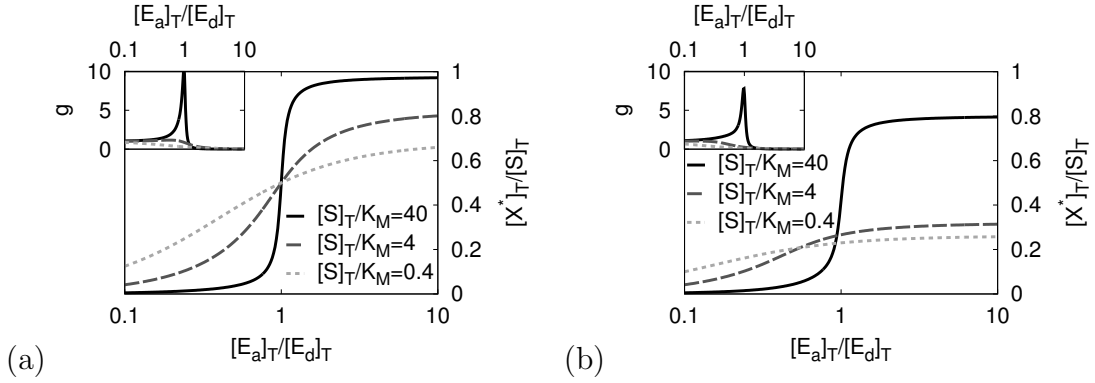

FIGURE 2.2 The input-output relation of the push-pull network shown in Fig. 2.1 as a function of the total substrate concentration $[\mathrm{S}]_\mathrm{T}$, for the case in which all components are uniformly distributed in space (a) and for the case in which the activating enzyme is located at one end of the cell, while the other components can diffuse freely through the cell (b). Here, $[\mathrm{X}^*]_\mathrm{T}/[\mathrm{S}]_\mathrm{T} = \int_0^L dx[\mathrm{X}^*]_\mathrm{T}(x)/\int_0^L dx[\mathrm{S}]_\mathrm{T}(x)$. In (a) and (b), $[\mathrm{E_d}]_\mathrm{T} = 0.5\,\mu\mathrm{M}$, $K_{\mathrm{M,a}} = K_{\mathrm{M,d}} = 0.5\ \mu\mathrm{M}$, and $k_3 = k_6 = 25\mathrm{s}^{-1}$. In (b), the diffusion constant is $D = 10\ \mu\mathrm{m}^2\mathrm{s}^{-1}$. The inset shows the logarithmic gain $g \equiv \partial \ln [\mathrm{X}^*]_\mathrm{T}/\partial \ln [\mathrm{E_a}]_\mathrm{T}$. It is seen that the sharpness of the response increases markedly with increasing substrate concentration when all the components are uniformly distributed in space (a), but much less so when the activating enzyme $\mathrm{E_a}$ is located at one pole of the cell, while the deactivating enzyme $\mathrm{E_d}$ is distributed in the cytoplasm. When both enzymes $\mathrm{E_a}$ and $\mathrm{E_d}$ are located at one pole, the steady-state dose-response curve is identical to that in (a).

is much higher than that of the deactivating enzyme, not all substrate X is converted into X^*. The second point to note is that as the total substrate concentration decreases, the inflection point of the dose-response curve shifts to lower values of $[\mathrm{E_a}]_\mathrm{T}/[\mathrm{E_d}]_\mathrm{T}$. The last, and perhaps most important, point to note is that the *sharpness* of the response of the network is much weaker than that of the network in which the enzymes are either colocalized or uniformly distributed in space. The insets of Fig. 2.2 shows the logarithmic gain, $g \equiv \partial \ln [\mathrm{X}^*]_\mathrm{T}/\partial \ln [\mathrm{E_a}]_\mathrm{T}$, as a function of $[\mathrm{E_a}]_\mathrm{T}/[\mathrm{E_d}]_\mathrm{T}$ for both networks ($[\mathrm{E_d}]_\mathrm{T}$ is kept constant). It is seen that for both low $[\mathrm{E_a}]_\mathrm{T}/[\mathrm{E_d}]_\mathrm{T}$ and high $[\mathrm{E_a}]_\mathrm{T}/[\mathrm{E_d}]_\mathrm{T}$ the gain is small and fairly similar for both networks, while for the symmetric networks considered here, at $[\mathrm{E_a}]_\mathrm{T} \approx [\mathrm{E_d}]_\mathrm{T}$ the gain is maximal, but smaller for the network in which the enzymes are spatially separated. Hence, spatially separating the two antagonistic enzymes reduces the maximum gain of a push-pull network.

The dose-response curves strongly depend on the diffusion constants. The extent to which the spatial separation of the opposing enzymes can change the response of the network depends on the magnitude of the diffusion constant of the components. This is illustrated in Fig. 2.3. This figure shows the input-output relation of a push-pull network where the activating enzyme is located at one end of the cell, while the other components diffuse freely in the cytoplasm, for different values of the diffusion constant. This network is in the zero-order regime: the total substrate concentration is large compared to the

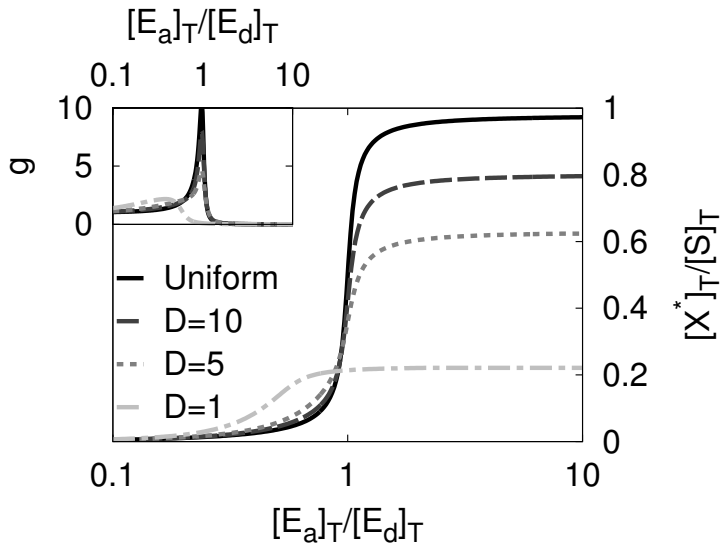

FIGURE 2.3 The input-output relation of a network in which the activating enzyme is located at one pole, while the other components can freely diffuse in the cytoplasm, for different values of the diffusion constant D (in $\mu\mathrm{m}^2\mathrm{s}^{-1}$) of the cytoplasmic components. The inset shows the logarithmic gain $g \equiv \partial \ln [\mathrm{X}^*]_\mathrm{T} / \partial \ln [\mathrm{E_a}]_\mathrm{T}$. It is seen that the gain of the push-pull network strongly increases with increasing diffusion constant. If $D \to \infty$, the dose-response curve approaches that of the push-pull network in which the components are uniformly distributed in space (and that of the network in which the enzymes are colocalized). The total substrate concentration is $[\mathrm{S}]_\mathrm{T} = 20\ \mu\mathrm{M}$, the total concentration of the deactivating enzyme is $[\mathrm{E_d}]_\mathrm{T} = 0.5\ \mu\mathrm{M}$, the Michaelis-Menten constants are $K_{\mathrm{M,a}} = K_{\mathrm{M,d}} = 0.5\ \mu\mathrm{M}$, and the catalytic rate constants are $k_3 = k_6 = 25\mathrm{s}^{-1}$.

concentrations of the enzymes and the Michaelis-Menten constants. Yet, for low values of the diffusion constants, the response is rather weak. As the diffusion constant increases, however, the sharpness of the response markedly increases. For $D \to \infty$, the input-output relation approaches that of a push-pull network in which all components are either uniformly distributed in space, or colocalized in one region of the cell.

Spatially separating the enzymes attenuates the propagation of strong signals, but can enhance the transmission of weak signals. Fig. 2.3 shows that in a zero-order network in which only the activating enzyme is localized at one pole of the cell, the concentration of X^* decreases with decreasing diffusion constant when $[\mathrm{E_a}]_\mathrm{T} > [\mathrm{E_d}]_\mathrm{T}$, but *increases* with decreasing diffusion constant when $[\mathrm{E_a}]_\mathrm{T} < [\mathrm{E_d}]_\mathrm{T}$. This means that when the input signal is strong (high kinase activity), the response of a network in which the enzymes are spatially separated is weaker than that of a network in which the enzymes are either uniformly distributed or colocalized in space; conversely, when the input signal is weak (low kinase activity), the spatially non-uniform network can respond more strongly than a uniform network. Spatially separating the antagonistic enzymes will thus attenuate strong input signals, but can also amplify weak input signals.

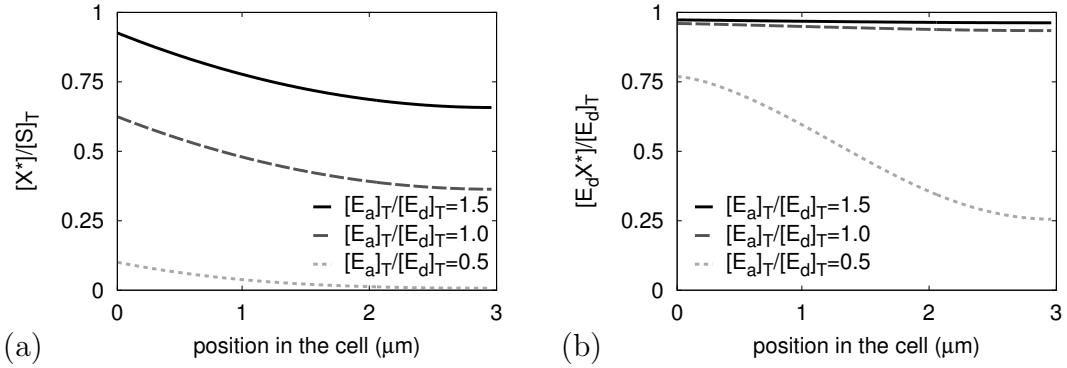

FIGURE 2.4 The concentration profiles for X^* (a) and E_dX^* (b) in a push-pull network in which the activating enzyme is located at one pole of the cell, while the other components are distributed in the cytoplasm, for three different concentrations of the activating enzyme. For all curves, $[S]_T = 20\ \mu M$, $[E_d]_T = 0.5\ \mu M$, $K_{M,a} = K_{M,d} = 0.5\ \mu M$, $k_3 = k_6 = 25 s^{-1}$, and $D = 10\ \mu m^2 s^{-1}$.

Mechanism: concentration gradients

To explain the effect of enzyme localization on the amplification properties of push-pull networks, it is instructive to consider the effect of diffusion on the input-output relation: in the limit that $D \to \infty$, the response of the network in which the activating enzyme is located at the pole, while the other is distributed in the cytoplasm, approaches that of a network in which the enzymes are either uniformly distributed in space or colocalized at the pole. The effect of diffusion on the response curves can be understood by considering the effects of diffusion on the spatial concentration profiles.

In a push-pull network where the antagonistic enzymes are either uniformly distributed or colocalized in space, the steady-state spatial concentration profiles of the freely diffusing components are uniform across the cell. In a push-pull network where the two antagonistic enzymes are spatially separated, concentration gradients of the freely diffusing components can form. Fig. 2.4 shows for a zero-order network in which the activating enzyme is located at one pole of the cell, while the other is not, the concentration profiles of X^* and E_dX^*, for three different (total) concentrations of the activating enzyme E_a, $[E_a]_T$. The concentrations of X^* and E_dX^* are highest near the pole where X is activated, and decay in the cytoplasm where X^* is deactivated. Moreover, the concentration profiles increase as $[E_a]_T$ increases. These gradients impose fundamental limits on the maximum gain of the system.

To clarify the effect of diffusion on the concentration profiles and the input-output relations, it is instructive to recall that, in general, the spatio-temporal evolution of $[X^*]$ is given by the interplay of activation, deactivation and diffusion of X^*:

$$\frac{\partial [X^*]}{\partial t} = D\frac{\partial^2 [X^*]}{\partial x^2} + J\delta(x) - \gamma(x). \tag{2.1}$$

Here, J denotes the influx of X^* into the system, while γ denotes the deactivation rate of X^* at position x. If the formation of the enzyme-substrate complexes is fast, then J

and γ are given by

$$J = k_3[\mathrm{E_a}]_\mathrm{T} L \frac{[\mathrm{X}](0)}{K_{\mathrm{M,a}} + [\mathrm{X}](0)} \tag{2.2}$$

$$\gamma(x) = k_6[\mathrm{E_d}]_\mathrm{T} \frac{[\mathrm{X^*}](x)}{K_{\mathrm{M,d}} + [\mathrm{X^*}](x)}. \tag{2.3}$$

Here, $[\mathrm{E_a}]_\mathrm{T} \equiv [\mathrm{E_a}]+[\mathrm{E_aX}]$ and $[\mathrm{E_d}]_\mathrm{T} \equiv [\mathrm{E_d}]+[\mathrm{E_dX^*}]$ are the total concentrations of $\mathrm{E_a}$ and $\mathrm{E_d}$, respectively. Combining Eq. 2.20 with Eq. 2.21 reveals that the total concentration profile of $\mathrm{E_d}$, $[\mathrm{E_d}]_\mathrm{T}(x)$, is constant in space if, as assumed here, the diffusion constants of the enzyme $\mathrm{E_d}$, and that of the enzyme bound to its substrate, $\mathrm{E_dX^*}$, are the same. The synthesis rate of $\mathrm{X^*}$ depends upon the concentration of X at contact and hence upon the concentration of $\mathrm{X^*}$ at contact; similarly, the deactivation rate of $\mathrm{X^*}$ at position x depends upon the concentration of $\mathrm{X^*}$ at x. This is important to note, because, as we discuss below, the dose-response curves are determined by the sensitivities of the influx J and the deactivation rate γ to changes in the substrate concentration. We will now first discuss the input-output relations of zero-order push-pull networks, and then briefly the response curves of push-pull networks that are in the linear regime.

2.2.2 Push-pull networks in the zero-order regime

Figs. 2.4-2.6 show the concentration profiles and dose-response curves of push-pull networks that are in the zero-order regime. We now discuss the limits of weak and strong activation separately.

2.2.3 Weak activation

We first consider the regime in which the concentration of the activating enzyme is lower than that of the deactivating enzyme, corresponding to Figs. 2.5a-c. In the limit that $[\mathrm{E_a}]_\mathrm{T} \ll [\mathrm{E_d}]_\mathrm{T}$, [X] will be large and $[\mathrm{X^*}]$ will be small. As a consequence, $\mathrm{E_a}$ is saturated with its substrate X, while $\mathrm{E_d}$ is not saturated with its substrate $\mathrm{X^*}$. Because $\mathrm{E_a}$ is saturated, the influx of $\mathrm{X^*}$ into the system is constant (i.e. independent of [X] and $[\mathrm{X^*}]$) and given by $J = k_3[\mathrm{E_a}]_\mathrm{T} L$ (see Eq. 2.2). Because $\mathrm{E_d}$ is unsaturated, the deactivation rate γ is proportional to $[\mathrm{X^*}]$: $\gamma(x) = \mu[\mathrm{X^*}](x)$, with $\mu = k_6/K_{\mathrm{M,d}}[\mathrm{E_d}]_\mathrm{T}$ (see Eq. 2.3). This means that in this regime the deactivation rate per particle is constant.

With the influx J being constant and the deactivation rate γ being proportional to $[\mathrm{X^*}]$, Eq. 2.1 can be solved analytically. Defining the characteristic decay length of $\mathrm{X^*}$ to be $\lambda = \sqrt{D/\mu}$, then, if $L \gg \lambda$, the solution is

$$[\mathrm{X^*}](x) = \frac{J\lambda}{D} \exp(-x/\lambda). \tag{2.4}$$

Eq. 2.4 reveals that when D increases, the profile decays more slowly, and the concentration of $\mathrm{X^*}$ at contact decreases. When D increases, the $\mathrm{X^*}$ molecules diffuse away from the pole more rapidly. Because in the regime considered here, namely $[\mathrm{E_a}]_\mathrm{T} \ll [\mathrm{E_d}]_\mathrm{T}$, the influx of $\mathrm{X^*}$ is constant and independent of D, the concentration of $\mathrm{X^*}$ close to the pole will decrease when the molecules diffuse away more rapidly, while the concentration further away will increase. In fact, in this limit the total concentration of $\mathrm{X^*}$, $[\mathrm{X^*}]^\mathrm{cell}$, is independent of the diffusion constant; this can be verified by integrating Eq. 2.4 over the whole cell, which yields $[\mathrm{X^*}]^\mathrm{cell} = J/\mu$. The fact that the total concentration of $[\mathrm{X^*}]$

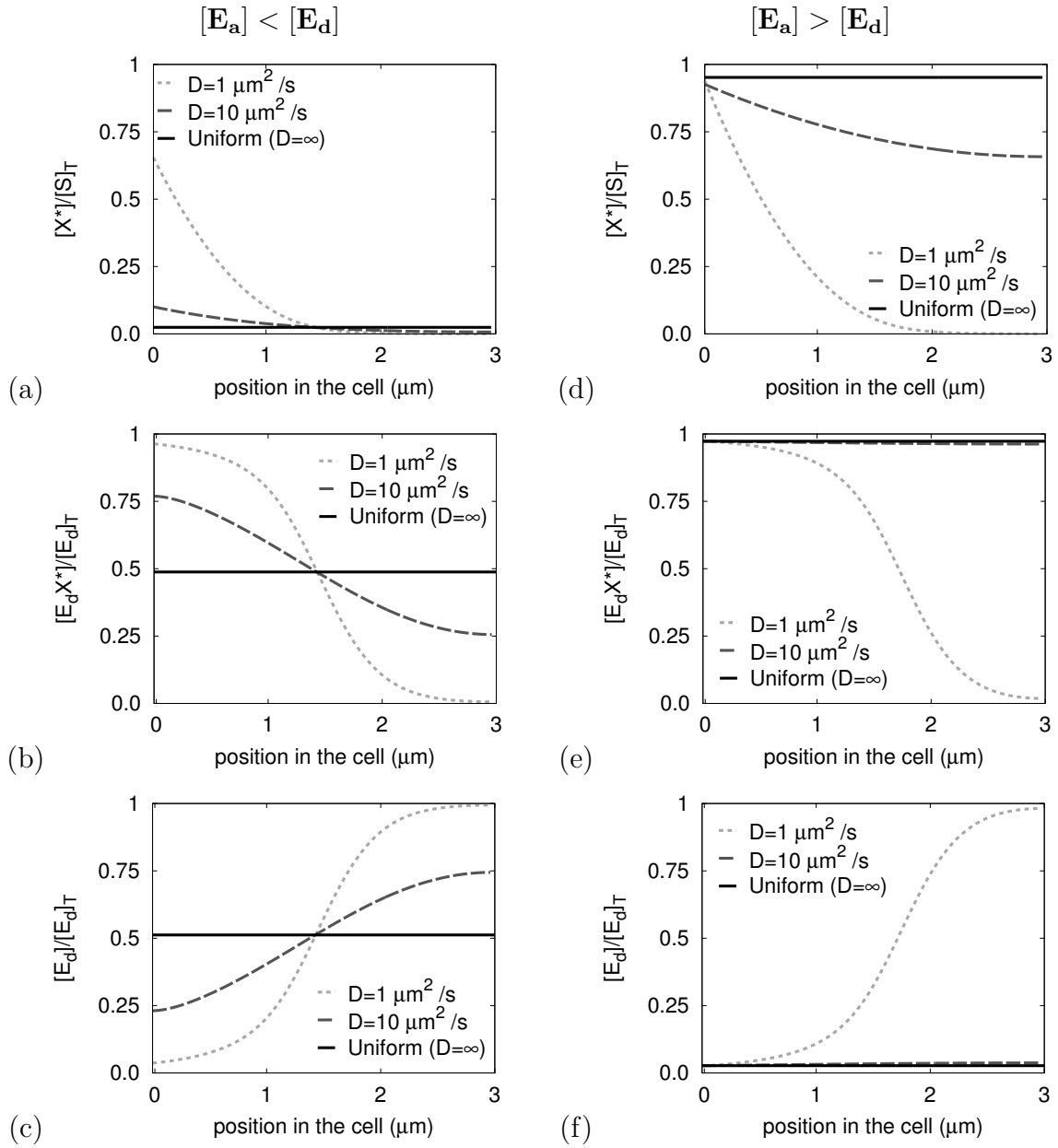

FIGURE 2.5 Profiles of [X*] (a and d), [E_dX*] (b and e) and [E_d] (c and f). a - c: Low concentration of activating enzyme, $[E_a]_T = 0.5[E_d]_T$; d-f: High activating enzyme concentration, $[E_a]_T = 1.5[E_d]_T$. For the other parameter values, see Fig. 2.4.

is independent of the diffusion constant, means that the response of the network does not depend upon the spatial distribution of the enzymes.

When $[E_a]_T$ increases, [X*] increases and [X] decreases. As a result, E_a becomes less saturated, while E_d becomes saturated. Hence, the influx J will at some point become sensitive to X, while the deactivation rate γ will no longer be proportional to [X*]. However, in the zero-order regime considered here, the total substrate concentration $[S]_T$ is large as compared to the enzyme concentrations and the Michaelis-Menten constants.

This means that as $[E_a]_T$ is raised, such that $[X](0)$ decreases and $[X^*](0)$ increases, initially E_a will remain fully saturated, while E_d will become saturated. This implies that there is a range of E_a concentrations, where the influx J is still constant, but the deactivation rate γ is no longer proportional to $[X^*]$. In this regime, the concentration of X^* increases with decreasing diffusion constant. Indeed, in this range, where $[E_a]_T < [E_d]_T$, the spatially non-uniform network will respond stronger than the spatially uniform network (see Figs. 2.3 and 2.5a-c).

Here we give a more intuitive explanation for the observation that a network in which the enzymes are spatially separated can respond stronger than a network in which the enzymes are similarly distributed in space. Ultimately, it is a consequence of the non-linear enzyme-substrate binding curve and the resulting hyperbolic dependence of the deactivation rate γ on $[X^*]$ (see Eq. 2.3). More specifically, this effect can arise when the diffusion constant is low and/or the deactivating enzyme operates close to, but not at, saturation in the uniform system; in this uniform system, X^* is distributed evenly through the cell and all particles X^* experience the same deactivation rate μ. In the spatially non-uniform system, $[X^*]$ is higher near the pole. If all the deactivating enzyme molecules would operate in the linear regime, i.e. if all deactivating enzyme molecules would not be saturated, then all particles X^* would still experience the same degradation rate μ; in this scenario, the increase in the number of X^* particles close to the pole would precisely balance the decrease in the number of X^* particles further away from the pole, as compared to the uniform network. However, if the concentration of the deactivating enzyme with respect to that of its substrate is lower, i.e. if the enzyme operates close to saturation, then the scenario can arise that the deactivating enzyme molecules near the pole become saturated (Fig. 2.5 b), while in the corresponding uniform network they are not. In this scenario, the X^* particles that are located close to the pole in the non-uniform network experience a lower effective deactivation rate than the X^* particles in the spatially uniform network. This will enhance the response of the non-uniform system as compared to that of the uniform system.

2.2.4 Strong activation

We now discuss the effect of the diffusion speed on the concentration profiles of X^* when $[E_a]_T > [E_d]_T$ (see Figs. 2.5d-f). In this regime, $[X]$ is low and $[X^*]$ is high. This reverses the saturation behavior of the antagonistic enzymes: while in the weak-activation limit E_a is saturated and E_d is unsaturated, now E_a is unsaturated and E_d is fully saturated. This also reverses the sensitivities of the influx J and the deactivation rate γ to changes in the substrate concentration. Indeed, in the strong-activation regime not the influx J is constant, but rather the deactivation rate: $\gamma = k_6[E_d]_T$ (see Eq. 2.3).

In the limit that the deactivation rate γ is constant, Eq. 2.1 can be solved in steady state. The solution is

$$[X^*](x) = c_0 + c_1 x + \frac{1}{2} c_2 x^2, \tag{2.5}$$

where $c_2 = k_6[E_d]_T/D$, $c_1 = -k_6[E_d]_T L/D$, and $c_0 = [X^*](0) = [S]_T - [E_d]_T(1 + k_6/k_3(1 + K_{M,a}/[E_a]_T))$. It is seen that in the high-activation regime, the concentration profile decays algebraically, rather than exponentially, as in the limit of weak activation. This

is precisely because in the high-activation regime the total deactivation rate γ is constant in space, while in the weak-activation limit γ is proportional to the concentration of X^*, which varies in space. In fact, in the weak-activation limit the deactivation rate *per particle* is constant in space and equal to μ. In contrast, in the strong-activation regime, the deactivation rate per particle is not only lower than μ on average, but also varies in space: the higher $[X^*]$ as compared to $[E_d]_T$ (which is constant in space and sets the total deactivation rate), the lower the deactivation rate per particle; activated particles close to the pole thus experience a lower deactivation rate and hence travel further on average before they are deactivated.

The expression for $c_0 = [X^*](0)$ reveals that as $[E_a]_T$ increases, the concentration of X^* close to the pole where E_a is located, increases. In the limit that $[E_a] \to \infty$, $[X^*](0) \to [S]_T - 2[E_d]_T \approx [S]_T$, which means that *close* to the pole of the cell where the activating enzyme is located, all the substrate X is converted into X^* and E_dX^* (see Fig. 2.5d). Importantly, Fig. 2.5d also shows that as the distance from the pole increases, the fraction $[X^*]_T(x)/[S]_T(x)$ decreases, *even in the limit that* $[E_a]_T \gg [E_d]_T$. When $[E_a]_T \gg [E_d]_T$, all the substrate molecules at the pole will indeed be modified. However, these molecules will then diffuse away from the pole into the cytoplasm, where they can be demodified by the deactivating enzyme molecules, but not remodified. Hence, when the activating enzyme is spatially separated from the deactivating enzyme, it will never be possible to convert all the substrate molecules in the system (see Fig. 2.2). This is in marked contrast with the situation in which the activating and deactivating enzymes are not spatially separated. In this case, all substrate molecules can be converted into X^* when $[E_a]_T \gg [E_d]_T$ (see Fig. 2.2).

The expression for $c_0 = [X^*](0)$ also reveals that in the limit that $[E_a]_T \gg [E_d]_T$, the concentration of X^* at $x = 0$ is independent of the diffusion constant. However, while $[X^*](0)$ does not depend on the diffusion constant, the rate at which $[X^*](x)$ decays with the distance from the pole, does depend on it. Eq. 2.5, with $c_1 = -k_6[E_d]_T L/D$, shows that the concentration profile of X^* decays more slowly when the diffusion constant increases (see also Fig. 2.5d). These two observations, when taken together, imply that the total concentration of X^* in the whole system increases with increasing diffusion constant. This can be verified by integrating Eq. 2.5 over the length of the cell, which gives $[X^*]^{\text{cell}} \sim a - b/D$, where a and b are positive constants.

These results can be understood by comparing the influx of X^* with the efflux of X^*. When $[E_a]_T > [E_d]_T$, the deactivation rate is constant and hence independent of the diffusion constant. Since the total deactivation rate of X^* is independent of the diffusion constant, the total influx of X^*, which in steady state must balance the total efflux by deactivation, is also independent of the diffusion constant. The influx of X^* depends on $[E_aX]$ and thus on the concentration of X^* at $x = 0$, as discussed above. Hence, the concentration of X^* at $x = 0$ must be independent of the diffusion constant. A more intuitive explanation is as follows: As the diffusion constant increases, the X^* molecules will diffuse away from the pole more rapidly. This would tend to lower the concentration of X^* at $x = 0$. However, this process is accompanied by an increase in the flux of X towards the pole ($[S]_T(x)$ is constant); because in the strong activation limit E_a is unsaturated, this would tend to increase $[E_aX]$ and thereby the influx of X^*, which would raise the concentration of X^*. In steady state, these processes balance each other such that the concentration of X^* at contact does not depend on the diffusion constant.

However, while $[X^*](0)$ does not change with the diffusion constant, the X^* molecules do diffuse away from the pole more rapidly when the diffusion constant increases. This means that the total concentration profile of X^* must increase with increasing diffusion constant (see Fig. 2.3). Indeed, only in the limit that $D \to \infty$ and $[E_a]_T \gg [E_d]_T$, can all the substrate molecules be converted into X^* (see Fig. 2.3 and Fig. 2.5d). In the strong-activation limit, spatially separating the antagonistic enzymes thus always weakens the response, in contrast to the behavior in the weak-activation limit.

It should also be noted that the decay length of the concentration profile of X^*, given by $c_1 = -k_6[E_a]_T L/D$, does not only depend upon the diffusion constant, but also upon the activity of the deactivating enzyme. In the spatially non-uniform system, the maximum response (i.e. the response when $[E_a]_T \gg [E_d]_T$) decreases as the catalytic activity of the deactivating enzyme, k_6, increases. The reason is that the X^* molecules will travel a shorter distance before they are deactivated, when the deactivation rate is higher. The extent to which spatially separating the enzymes weakens the maximum response thus depends upon both the diffusion constant and the deactivation rate of the X^* molecules.

2.2.5 Space-dependent amplification

Fig. 2.6 shows that if the activating enzyme is localized at one pole of the cell, while the deactivating enzyme can freely diffuse through the cytoplasm, the response of the network will depend upon the position in the cell. As can be deduced from Figs. 2.4 and 2.5, $[E_dX^*]$ depends significantly on the position in the cell when $[E_a]_T < [E_d]_T$. When $[E_a]_T > [E_d]_T$, however, $[E_dX^*]$ becomes virtually independent of the position x, because then all the deactivating enzyme molecules are saturated. The opposite trend is observed for $[X^*]$: when $[E_a]_T < [E_d]_T$, $[X^*]$ is low everywhere in the cell, while if $[E_a]_T > [E_d]_T$, $[X^*]$ strongly depends upon the position in the cell. The reason is, as discussed in the previous section, that even when $[E_a]_T \gg [E_d]_T$, not all X can be converted into X^* if the two antagonistic enzymes are spatially separated.

Interestingly, the average response of $[E_dX^*]$ in the spatially non-uniform system is very similar to that in the system in which the two enzymes are not spatially separated. Yet, the response of $[X^*]$ does differ markedly between the two systems. This is a result of the strong non-linearity in the amplification mechanism of zero-order ultrasensitivity: because the activation and deactivation reactions are zero-order in the substrate concentrations [X] and $[X^*]$, respectively, even when $k_3[E_aX]$ is only marginally larger than $k_6[E_dX^*]$, predominantly all X molecules will be converted into X^* [51].

Lastly, Fig. 2.6a shows that the inflection point of the dose-response curve depends on the position x in the cell. The inflection point shifts to higher $[E_a]_T/[E_d]_T$ as the distance from the anterior pole increases; this effect becomes more pronounced as D decreases (data not shown). The fact that the inflection point depends on the position x is one of the principal reasons why the response in the spatially non-uniform system is weaker than that of the uniform system.

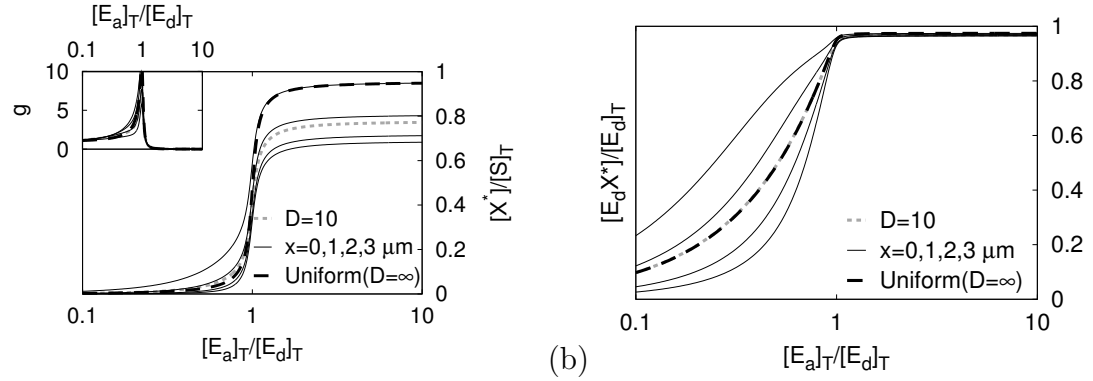

FIGURE 2.6 Dose-response curves of the push-pull network in which the activating enzyme is localized at one pole of the cell, while the other components diffuse in the cytoplasm, for different positions in the cell ($x = 0$ corresponds to the solid left most curve, while $x = 3$ μm corresponds to the solid right most curve); a) profiles of [X*] and b) profiles of [E_dX*]; note that the response becomes sharper further away from the pole. The dottes curves correspond to the average or integrated response of the non-uniform system, while the dashed curves correspond to the uniform system. The inset shows the logarithmic gain $g \equiv \partial \ln [\mathrm{X}^*]/\partial \ln [\mathrm{E_a}]_\mathrm{T}$ at the respective positions in the cell ($x = 0, 1, 2, 3, \mu$m). For the parameter values, see Fig. 2.4.

2.2.6 Push-pull networks in the linear regime

Push-pull networks in living cells are not always in the zero-order regime [51, 45]. In the linear regime, push-pull networks do not amplify signals, but can enhance the reliability of cell signaling by making it robust against fluctuations in the concentrations of the components due to noise in gene expression [68]. It is therefore meaningful to study how the input-output relation of a push-pull network in the linear regime depends upon the spatial distribution of the antagonistic enzymes. A push-pull network in the linear regime is given by:

$$\mathrm{E_a} + \mathrm{X} \xrightarrow{k_1} \mathrm{E_a} + \mathrm{X}^* \tag{2.6}$$

$$\mathrm{E_d} + \mathrm{X}^* \xrightarrow{k_2} \mathrm{E_d} + \mathrm{X} \tag{2.7}$$

The steady-state concentration profiles for these linear push-pull networks can be derived analytically.

The principal result is that for push-pull networks that are in the linear regime, spatially separating the antagonistic enzymes *always weakens the response*. This can be seen by comparing the response curve for $[\mathrm{S}]_\mathrm{T} = 0.4K_\mathrm{M}$ in Fig. 2.2a with that in Fig. 2.2b. The reason why for linear networks spatially separating the enzymes reduces the response in the strong-activation limit is the same as that for zero-order networks. The reason that, in contrast to zero-order networks, also in the weak-activation limit the response is weakened, is more subtle. In zero-order networks that are in the weak-activation limit, $\mathrm{E_a}$ is saturated and, consequently, the influx J is independent of the concentration of X at the pole. In linear networks, $\mathrm{E_a}$ is unsaturated and the influx J

is proportional to [X](0). As D decreases, [X*](0) tends to increase and [X](0) tends to decrease ($[\mathrm{S}]_\mathrm{T}(x)$ is constant in space). Because in the linear regime J is proportional to [X](0), this would lower the influx of X*, which, in turn, would lower the concentration of X*. Spatially separating the antagonistic enzymes thus amplifies weak signals if the push-pull network operates in the zero-order regime, but not in the linear regime.

2.3 Discussion

In a push-pull network that operates deeply in the zero-order regime, the activation rate is given by $k_3[\mathrm{E_a}]_\mathrm{T}$, while the deactivation rate is given by $k_6[\mathrm{E_d}]_\mathrm{T}$; both rates are thus independent of the substrate concentration. If both enzymes are uniformly distributed, or colocalized, then essentially all substrate molecules will be activated when $k_3[\mathrm{E_a}]_\mathrm{T} > k_6[\mathrm{E_d}]_\mathrm{T}$, while they will be predominantly deactivated when $k_3[\mathrm{E_a}]_\mathrm{T} < k_6[\mathrm{E_d}]_\mathrm{T}$. To drive the modification reactions to completion, it is indeed essential that the antagonistic enzymes are not spatially separated. If the antagonistic enzymes are separated, then the enzyme with the lower global activity, can locally still have a higher activity than the other enzyme. More in general, spatially separating the enzymes means that the balance between activation and deactivation depends upon the position in the cell, and this "smearing" of the response always tends to reduce the sharpness of the global response curve.

If information about changes in the environment has to be transmitted, then the gain—the change in the output divided by the change in the input—is a critical quantity. In fact, the *maximum* gain is then usually the most relevant quantity, because signaling networks are often tuned to this point of maximum gain: the input-output function of a module and the concentration of its input signal are often optimized with respect to each other. The intracellular chemotaxis network of *E. coli* provides a clear example: the steady-state intracellular concentration of the messenger CheYp is around 3 μM, which is precisely the concentration at which the flagellar motors respond most strongly. Our analysis shows that from the perspective of signal amplification, the best strategy is to either colocalize the antagonistic enzymes or to uniformly distribute them in space: spatially separating the enzymes always weakens the maximum response.

Nevertheless, as mentioned in the introduction, spatial gradients of messenger proteins are often observed. Indeed, maximizing the gain is not the only design principle in cell signaling. Firstly, while in some cases, such as *E. coli* chemotaxis, the signal has to be transmitted to a large number of places throughout the cell's cytoplasm or membrane [58], in other cases the signal has to be transmitted to distinct regions, such as the nucleus, or be confined to a small region near the membrane, as in the yeast pheromone response where the shmoo tip has to be formed locally; in this scenario, spatial gradients might be important, since they allow the cell to confine signaling to a narrow domain below the cell membrane [56, 59]. Secondly, a sharp response may not always be desirable. In order to respond strongly to changes in the input signal over a broad range of input signal strengths, the cell does not only need a sharp response curve, but it also needs to develop elaborate adaptation mechanisms that can reset the network to the point of maximum gain. In *E. coli*, for instance, the methylation and demethylation enzymes

CheR and CheB continually adjust the activity of the receptor cluster, such that the steady-state intracellular CheYp concentration is at 3 μM. A weaker response curve, however, would allow the cell to have a reasonable working range without adaptation mechanisms. In this scenario not only the maximum gain would be important, but, in fact, the full response curve. Thirdly, it might not always be possible to maximize signal amplification by optimizing the input-output function of a module with respect to its incoming signal, because, for instance, the downstream module also has to respond to other incoming signals, while the signal also has to act on other downstream modules; the yeast MAPK pathways, which exhibit cross talk, provide a prominent example of such a scenario. It seems likely that in this case the full response curve, with the absolute concentrations of the components, is important. In this context it is interesting to note that spatially separating the antagonistic enzymes weakens strong signals by reducing the maximum output signal (Figs. 2.3 and 2.5a), while it can enhance weak signals if the network operates in the zero-order regime (Figs. 2.3 and 2.5d). This dependence of the input-output relation on the spatial distribution of the antagonistic enzymes could be exploited by cells to relay different environmental signals specifically.

The analysis performed here is essentially a mean-field analysis. It is assumed that the concentrations are large and that fluctuations can be neglected. However, in the living cell, the concentrations are often low, which means that fluctuations can be important. This is particularly relevant for push-pull networks. Their high gain not only amplifies the mean of the input signal, but will also amplify the noise in the input signal [69, 70, 55]. Moreover, when the modification reactions become more zero order, the intrinsic fluctuations of the push-pull network, i.e. noise resulting from the modification reactions themselves, will also increase [52]. In fact, it has been shown that when push-pull networks operate deeply in the zero-order regime, fluctuations can lead to a bimodal response [54]. All these analyses of the effect of noise on the amplification mechanism of zero-order ultrasensitivity have been performed under the assumption that the enzymes are uniformly distributed in the cytoplasm. It would clearly be of interest to study the effect of enzyme (co)-localization on the noise characteristics of push-pull networks.

Finally, could our predictions be tested experimentally? To test our predictions, one would ideally like to perform an experiment on a system with a canonical push-pull network in which all the parameters—concentrations of components, rate constants, diffusion constants—are kept constant, except for the spatial location of one of the enzymes. This clearly seems a very difficult experiment to perform, and to our knowledge, no such experiment has been performed yet, with the possible exception of the experiment by Vaknin and Berg [35]. Vaknin and Berg studied the effect of phosphatase localization on the response of the intracellular chemotaxis network of *E. coli* cells. This network has a topology that is very similar to that of the canonical push-pull networks considered here, and it is believed that in the wild-type cells both the kinase and the phosphatase are localized at the cell pole. Vaknin and Berg compared the response of wild-type cells to that of mutant cells, in which the phosphatase was mutated such that it freely diffuses in the cytoplasm. They found that the spatial distribution of the phosphatase can have a marked effect on the the sharpness of the response, which seems to support the principal conclusion of our analysis. We would like to emphasize, however, that to assess the importance of the spatial distribution of the antagonistic enzymes in a push-pull network, a careful, quantitative analysis of the network is required. First of all,

our analysis shows that both the quantitative and qualitative consequences of enzyme localization, depend upon the regime in which the network operates. For instance, our calculations reveal that if the activation rate is independent of the messenger concentration, and if the deactivation rate is linear in the messenger concentration, then the localization of the phosphatase should have no effect at all on the response curve. Secondly, it is quite possible that in the mutant cells not only the spatial distribution of the enzymes is different, but also their expression level, or even other parameters such as rate constants. In fact, experiments by Wang and Matsumura suggest that the activity of the phosphatase in the *E. coli* chemotaxis network is enhanced at the receptor cluster [36]. Clearly, different rate constants would also tend to change the response curve of the mutant cells with respect to that of the wild-type cells. To elucidate the effect of enzyme localization on the dose-response curve of a network, thus requires quantitative experiments and quantitative modeling. In a future publication, we will present a detailed analysis on the importance of phosphatase localization in the chemotaxis network of *E. coli*.

2.4 Methods: The push-pull network

A push-pull network consists of two Michaelis-Menten reactions (see also Fig. 2.1):

$$\mathrm{E_a} + \mathrm{X} \underset{k_2}{\overset{k_1}{\rightleftharpoons}} \mathrm{E_aX} \overset{k_3}{\rightarrow} \mathrm{E_a} + \mathrm{X^*} \tag{2.8}$$

$$\mathrm{E_d} + \mathrm{X^*} \underset{k_5}{\overset{k_4}{\rightleftharpoons}} \mathrm{E_dX^*} \overset{k_6}{\rightarrow} \mathrm{E_d} + \mathrm{X} \tag{2.9}$$

Here, $\mathrm{E_a}$ is the activating enzyme that provides the input signal, and $\mathrm{E_d}$ is the deactivating enzyme. The substrate X is the unmodified messenger that serves as the detection component and $\mathrm{X^*}$ is the modified messenger that provides the output signal; $\mathrm{E_aX}$ denotes the activating enzyme bound to its substrate X and $\mathrm{E_dX^*}$ is the deactivating enzyme bound to its substrate $\mathrm{X^*}$.

If all the components are uniformly distributed in space, then the chemical rate equations that correspond to this network are:

$$\frac{\partial[\mathrm{X^*}]}{\partial t} = k_3[\mathrm{E_aX}] - k_4[\mathrm{E_d}][\mathrm{X^*}] + k_5[\mathrm{EdX^*}] \tag{2.10}$$

$$\frac{\partial[\mathrm{X}]}{\partial t} = k_6[\mathrm{E_dX^*}] - k_1[\mathrm{E_a}][\mathrm{X}] + k_2[\mathrm{EaX}] \tag{2.11}$$

$$\frac{\partial[\mathrm{E_a}]}{\partial t} = (k_2 + k_3)[\mathrm{E_aX}] - k_1[\mathrm{E_a}][\mathrm{X}] \tag{2.12}$$

$$\frac{\partial[\mathrm{E_aX}]}{\partial t} = k_1[\mathrm{E_a}][\mathrm{X}] - (k_2 + k_3)[\mathrm{E_aX}] \tag{2.13}$$

$$\frac{\partial[\mathrm{E_d}]}{\partial t} = (k_5 + k_6)[\mathrm{E_dX^*}] - k_4[\mathrm{E_d}][\mathrm{X^*}] \tag{2.14}$$

$$\frac{\partial[\mathrm{E_dX^*}]}{\partial t} = k_4[\mathrm{E_d}][\mathrm{X^*}] - (k_5 + k_6)[\mathrm{E_dX^*}] \tag{2.15}$$

Here, [...] denotes the concentrations of the species. The steady-state input-output curve of this network can be obtained analytically [34].

We compare the behavior of this network to that of a network in which the activating enzyme E_a is located at one pole of the cell, while the other components can freely diffuse in the cytoplasm. The cell is assumed to be cylindrically symmetric. Since we are interested in the mean concentration profiles, it is meaningful to integrate out the lateral dimensions y and z. We thus consider a simplified 1D model, with concentrations as a function of x only. This leads to the following reaction-diffusion equations:

$$\frac{\partial[X^*]}{\partial t} = D\frac{\partial^2[X^*]}{\partial x^2} + k_3[E_aX]\delta(x) - k_4[E_d][X^*] + k_5[EdX^*] \tag{2.16}$$

$$\frac{\partial[X]}{\partial t} = D\frac{\partial^2[X]}{\partial x^2} + k_6[E_dX^*] - k_1[E_a][X]\delta(x) + k_2[EaX]\delta(x) \tag{2.17}$$

$$\frac{\partial[E_a]}{\partial t} = (k_2 + k_3)[E_aX] - k_1[E_a][X](0) \tag{2.18}$$

$$\frac{\partial[E_aX]}{\partial t} = k_1[E_a][X](0) - (k_2 + k_3)[E_aX] \tag{2.19}$$

$$\frac{\partial[E_d]}{\partial t} = D\frac{\partial^2[E_d]}{\partial x^2} + (k_5 + k_6)[E_dX^*] - k_4[E_d][X^*] \tag{2.20}$$

$$\frac{\partial[E_dX^*]}{\partial t} = D\frac{\partial^2[E_dX^*]}{\partial x^2} + k_4[E_d][X^*] - (k_5 + k_6)[E_dX^*] \tag{2.21}$$

The components E_a and E_aX are localized in the membrane at one end of the cell; the unit of their concentrations is number of molecules per area. The other components diffuse in the cell. Their concentrations, which are in units of number of molecules per volume, depend on the position x in the cell, where x measures the distance from the pole at which E_a and E_aX are localized; only in Eqs. 2.18 and 2.19 is the x dependence explicitly indicated to emphasize that the E_a-X association rate depends on the concentration of X at contact. Zero-flux boundary conditions are imposed at both cell ends. The steady-state input-output relations of the network described by Eqs. 2.16-2.21 were obtained numerically by discretizing the system on a (1D) grid and propagating Eqs. 2.16-2.21 in space and time until steady-state was reached.

We consider a cell with the typical dimensions of an *E. coli* cell: the length of the cell, L, is thus on the order of 3 μm [35]. We assume the same diffusion constants for all the components that can diffuse in the cytoplasm. This is for reasons of simplicity; it is not essential for the main conclusions of our work. To focus on the effect of enzyme localization on the input-output relation, we assume for both networks that $k_1 = k_4$, $k_2 = k_5$, $k_3 = k_6$; the Michaelis-Menten constants for the modification and demodification reactions are thus the same: $K_{M,a} \equiv (k_2 + k_3)/k_1 = K_{M,d} \equiv (k_5 + k_6)/k_4$. To compare the two networks on equal footing, the total concentration of activating enzyme, $[E_a]_T \equiv [E_a] + [E_aX]$, was chosen such that $[E_a]_T^{nu} = L[E_a]_T^u$, where $[E_a]_T^{nu}$ is the concentration (per unit area) in the non-uniform system and $[E_a]_T^u$ is the concentration (per unit volume) in the spatially uniform network. This choice ensures that the total number of activating enzyme molecules in the whole cell is the same for both systems. We therefore report $[E_a]_T \equiv [E_a]_T^u$.

In the calculations, we vary the concentration of the activating enzyme, E_a, which is the input signal. The total concentration of the deactivating enzyme, E_d, is kept constant at $[E_d]_T = 0.5$ μM; the rate constants are fixed at $k_1 = k_4 = 10^8\,M^{-1}s^{-1}$, $k_2 = k_5 = 25\,s^{-1}$, $k_3 = k_6 = 25\,s^{-1}$, corresponding to Michaelis-Menten constants of

$K_{\mathrm{M}} = K_{\mathrm{M,a}} = K_{\mathrm{M,d}} = 0.5\ \mu$M. We have studied extensively the effect of changing the diffusion constant D and the total substrate concentration $[\mathrm{S}]_{\mathrm{T}} \equiv [\mathrm{X}]_{\mathrm{T}} + [\mathrm{X}^*]_{\mathrm{T}}$, where $[\mathrm{X}]_{\mathrm{T}} \equiv [\mathrm{X}] + [\mathrm{E_aX}]/L$ is the total concentration of X and $[\mathrm{X}^*]_{\mathrm{T}} \equiv [\mathrm{X}^*] + [\mathrm{E_dX}^*]$ is the total concentration of X^*. Their base-line parameters, however, were: $D = 10\ \mu\mathrm{m}^2\mathrm{s}^{-1}$ and $[\mathrm{S}]_{\mathrm{T}} = 20\ \mu$M. The magnitude of the diffusion constant [71], as well as the values of the Michaelis-Menten constants, enzyme concentrations, and substrate concentrations, are typical for prokaryotic [45] and eukaryotic cells [51].

3 The canonical model of E. coli chemotaxis

Push-pull networks, in which two antagonistic enzymes control the activity of a messenger protein, are ubiquitous in signal transduction pathways. A classical example is the chemotaxis system of the bacterium Escherichia coli*, in which the kinase CheA and the phosphatase CheZ regulate the phosphorylation level of the messenger protein CheY. Recent experiments suggest that both the kinase and the phosphatase are localized at the receptor cluster, and Vaknin and Berg recently demonstrated that the spatial distribution of the phosphatase can markedly affect the dose-response curves [Proc. Natl. Acad. Sci. USA* **101***, 17072-17077 (2004)]. We argue, using mathematical modelling, that the commonly accepted model of the chemotaxis network cannot explain the experimental observations of Vaknin and Berg. It should be noted that the experiments* can *be explained if one allows for the possibility that the mutant cells operate extremely far outside their sensitive range, which seems to contradict the observation that these mutants are able to chemotax.*

3.1 Introduction

The protein network that controls chemotaxis of *Escherichia coli* is arguably the most-studied and best-characterized signal transduction pathway. Its relative simplicity makes it an ideal model system for studying signal amplification, integration, transduction, and adaptation. The network consists of three parts: i) a cluster of receptors at the cell membrane, which detects the extracellular ligand; ii) the intracellular signaling pathway, which transmits the signal from the receptor cluster to the flagellar motors; iii) the network that controls the response of the flagellar motors. The intracellular signaling pathway is a push-pull network that consists of a kinase, CheA, that phosphorylates the messenger protein CheY and a phosphatase, CheZ, that dephosphorylates the phosphorylated messenger protein $\mathrm{CheY_p}$. In wild-type cells, CheA is localized exclusively at the receptor cluster, and also CheZ is predominantly localized at the receptor cluster [60]. Recently, however, Vaknin and Berg studied mutants in which CheZ can no longer bind the receptor cluster, as a result of which it is uniformly distributed in the cytoplasm [35]. They observed that the response of these mutant cells differs strongly from that of wild-type cells. Inspired by this observation, we showed in the previous chapter that the spatial distribution of the antagonistic enzymes by itself can have a dramatic effect on the response [72]. We have also seen, however, that the effect depends upon the regime in which the network operates. Here, we address by detailed mathematical analysis of the commonly accepted model of the *E. coli* chemotaxis network whether the difference

in response between wild-type and CheZ mutant cells can be explained by the different spatial distribution of CheZ in these cells. We find that this is not the case. Also realistic changes in parameters such as rate constants and protein concentrations do not seem sufficient to explain the difference in response. In the next chapter, we propose a new model that can explain the experiments proposed by Vaknin and Berg [35].

The commonly accepted model of the intracellular chemotaxis network of *E. coli* is described by the following set of chemical reactions:

$$\mathrm{A} \overset{\beta k_0}{\rightarrow} \mathrm{A_p} \tag{3.1}$$

$$\mathrm{A_p} + \mathrm{Y} \underset{k_2}{\overset{k_1}{\rightleftharpoons}} \mathrm{A_pY} \overset{k_3}{\rightarrow} \mathrm{A} + \mathrm{Y_p} \tag{3.2}$$

$$\mathrm{Y_p} + \mathrm{Z} \underset{k_5}{\overset{k_4}{\rightleftharpoons}} \mathrm{Y_pZ} \overset{k_6}{\rightarrow} \mathrm{Y} + \mathrm{Z} \tag{3.3}$$

In this network, the phosphorylated form of the messenger, $\mathrm{CheY_p}$ (Yp), transmits the signal from the receptor cluster to the flagellar motors. The phosphorylation level of CheY is regulated by a kinase CheA (A) and a phosphatase CheZ (Z). The input to the signal transduction pathway is βk_0, where β is a parameter between zero and one that reflects the activity of the receptor cluster and k_0 denotes the maximum rate of autophosphorylation of CheA. The value of β depends on the ligand concentration [L]: $\beta \equiv \beta([\mathrm{L}])$; β shifts to lower (higher) values upon the addition of attractant (repellent). In order for *E. coli* to adapt to a changing ligand concentration, the activity of the receptor cluster, β, is also modulated by the methylation and demethylation enzymes CheR and CheB, respectively.

In wild-type *E. coli* cells, not only CheA, but also CheZ is localized at the receptor cluster [60]. In these cells, CheZ is anchored to the receptor cluster by a variant of CheA, $\mathrm{CheA_s}$, which lacks enzymatic activity. In a recent experiment, Vaknin and Berg compared the response of wild-type cells to that of CheZ mutant cells, in which CheZ does not bind to $\mathrm{CheA_s}$, but diffuses in the cytoplasm [35]. They studied the response of the chemotaxis network by measuring the interaction between CheZ and $\mathrm{CheY_p}$ using FRET imaging. While the input of the network was thus the concentration of ligand, the measured output was proportional to the total, integrated concentration of $\mathrm{CheY_p}$ bound to CheZ, $[\mathrm{Y_pZ}]$ (see also Eq. 3.3).

Vaknin and Berg found that the colocalization of the antagonistic enzymes has a marked effect on the dose-response curve [35]. In wild-type cells, in which CheA and CheZ are colocalized at the receptor cluster, the response of $[\mathrm{Y_pZ}]$ to changes in the concentration of the attractant serine is more sensitive than in mutant cells, in which CheZ is distributed in the cytoplasm. Moreover, in *CheRcheB* cells, which lack the methylation and demethylation enzymes, the response to the addition of serine is also sharper when CheA and CheZ are colocalized at the receptor cluster [35].

In the next section, we show that the experiments of Vaknin and Berg [35] impose strong constraints on any model that aims to describe the intracellular chemotaxis network. In the subsequent section, we argue that the commonly accepted model does not meet these constraints: neither changes in the spatial distribution of CheZ, nor realistic changes in the rate constants and protein concentrations seem sufficient to explain the differences in the response curves of the mutant and wild-type cells. Indeed, we argue

that the experiments of Vaknin and Berg demonstrate that the the commonly accepted model needs to be augmented.

3.2 Decomposing the response

Analysis of the dose-response curves of Vaknin and Berg [35] is complicated by the fact that it is determined by both the response of the receptor cluster to the binding of ligand and by the response of the intra-cellular signaling pathway to changes in the activity of the receptor cluster. However, these two networks can be viewed as two independent modules connected in series, which can be analyzed separately, as we will argue now.

The first module is the receptor cluster. Its activity, β, depends upon the concentration of ligand, $[L]$, and upon the methylation states of the receptors, which is controlled by the methylation and demethylation enzymes CheR and CheB, respectively. However, the dynamics of receptor methylation and demethylation by CheR and CheB is much slower than that of receptor-ligand (un)binding and phosphorylation and dephosphorylation of CheY; in fact, this separation of time scales allows *E. coli* to both respond and adapt to a changing ligand concentration. This separation of time scales also makes it possible to model the response to ligand at short time scales without explicitly taking into account the (de)methylation dynamics; different ambient conditions, or the absence of CheR and CheB in *CheRCheB* cells, will lead to different methylation states of the receptors, yet can be modeled implicitly by taking different functional forms for $\beta k_0([\mathrm{L}])$.

The second module of the chemotaxis network, the intracellular signal transduction pathway, is described by the set of reactions in Equations 3.1-3.3. The input of this network is βk_0, while the output is the concentration of $\mathrm{CheY_p}$, $[\mathrm{Y_p}]$, or, as in the experiments of Vaknin and Berg, the total concentration of $\mathrm{CheY_p}$ bound to CheZ, $[\mathrm{Y_pZ}]$ [35]. The response curve of this network, $[\mathrm{Y_pZ}](\beta k_0)$, depends upon the spatial organisation of the network, and will thus be different for wild-type cells and CheZ mutant cells. Importantly, $[\mathrm{Y_pZ}](\beta k_0)$ is independent of the methylation states of the receptors. We assume that $[\mathrm{Y_pZ}](\beta k_0)$ also does not depend upon the presence of CheB, although phosphorylated CheA can phosphorylate not only CheY but also CheB, leading to another form of adaptation on a time scale longer than that of the response; we will come back to this in the next chapter. Thus, we assume that $[\mathrm{Y_pZ}](\beta k_0)$ of *CheRCheB* cells is the same as that of wild-type cells; the presence of CheR and CheB only affects $\beta k_0([\mathrm{L}])$.

If the receptor cluster and the intracellular chemotaxis pathway are two independent modules connected in series, the response function $[\mathrm{Y_pZ}]([\mathrm{L}])$ is given by the composite function $[\mathrm{Y_pZ}]\left(\beta k_0([\mathrm{L}])\right)$. This is illustrated graphically in Figure 3.1. Panel A shows the response of $[\mathrm{Y_pZ}]$ to the addition of serine, as obtained from the experimental data of Vaknin and Berg, who measured with FRET the response of $[\mathrm{Y_pZ}]$ to changes in [serine] [35]. Panels B and C show functions $[\mathrm{Y_pZ}](\beta k_0)$ and $\beta k_0([\mathrm{L}])$, respectively, that together reproduce the data in panel A. This decomposition is not unique, but, as we will discuss in more detail below, the combination of experimental results on wild-type cells, *CheRCheB* cells, and CheZ mutant cells, imposes strong constraints on the decomposition.

The experiments of Vaknin and Berg [35] allow us to verify whether the receptor cluster and the intracellular signaling pathway are indeed two independent modules

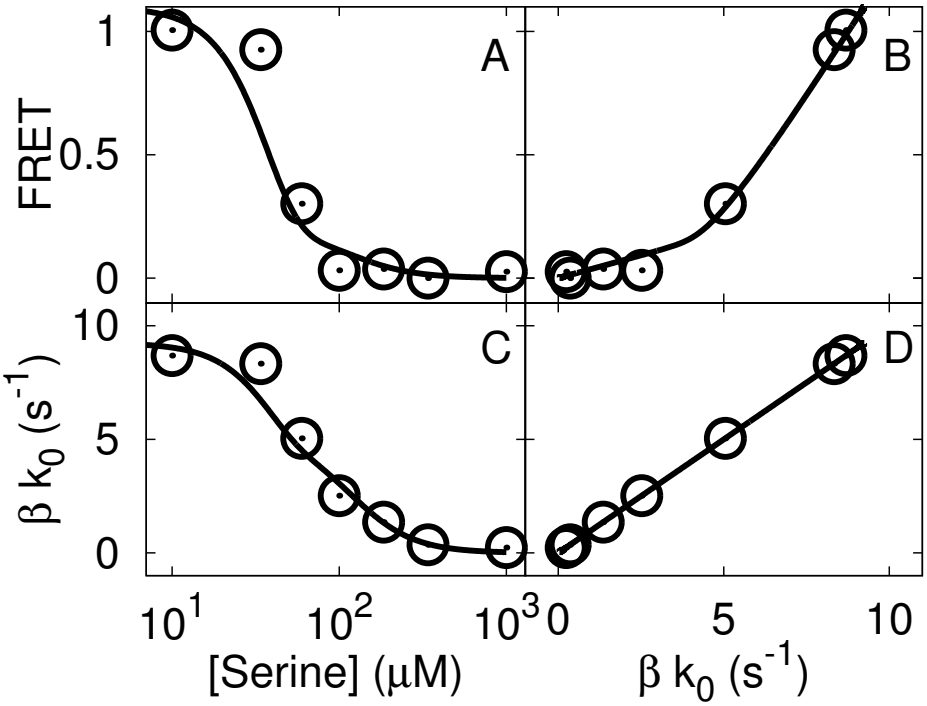

FIGURE 3.1 Decomposition of a dose-response curve. A. A dose-response curve taken from [35]. The concentration of CheY bound to CheZ [Y_pZ] was measured with FRET as a function of the concentration of the attractant Serine. As explained in the main text, this response can be decomposed into the response of [Y_pZ] to the activity of the receptor cluster βk_0 (panel B) and the response of the activity of the receptor cluster to the concentration of Serine (panel C). Panel D is an augmentary line that helps to visualize the conversion between panels B and C.

connected in series. Vaknin and Berg performed experiments on four bacterial strains: wild type $CheR^+CheB^+CheZ$ cells, $CheR^-CheB^-CheZ$ cells lacking CheR and CheB, $CheR^+CheB^+CheZ^*$ cells with mutant CheZ proteins that cannot bind the receptor cluster, and $CheR^-CheB^-CheZ^*$ cells lacking CheR and CheB and with $CheZ^*$ (CheZ mutated). As discussed above, we assume that $\beta k_0[L]$ is the same for wild type and CheZ mutant cells, but not for wild type and $CheR^-CheB^-$ cells; in contrast, $[Y_pZ](\beta k_0)$ is the same for wild type and $CheR^-CheB^-$ cells, but not for wild type and $CheZ^*$ cells. If the receptor cluster and the chemotaxis network are two independent modules connected in series, then it should be possible to describe the response curve $[Y_pZ]([L])$ of each of the four strains using two of the following response curves: $[Y_pZ]^{Z^{wt}}(\beta k_0)$ or $[Y_pZ]^{Z^*}(\beta k_0)$, and $\beta k_0^{R^+B^+}([L])$ or $\beta k_0^{R^-B^-}([L])$. In other words, all the four response curves measured in [35] should be of the composite form $[Y_pZ]^{\{Z^*,Z^{wt}\}}\left(\beta k_0^{RB\pm}([L])\right)$.

To demonstrate that this is the case, we show in Figure 3.2 $[Y_pZ]$ in cells containing wild-type CheZ as a function of $[Y_pZ]$ in cells containing mutant CheZ, both for $CheR^-CheB^-$ and $CheR^+CheB^+$ cells. These figures are obtained from Figures 5A and 5C of Ref. [35], which show the renormalized FRET signal (FRET([L])/FRET([L]=0))

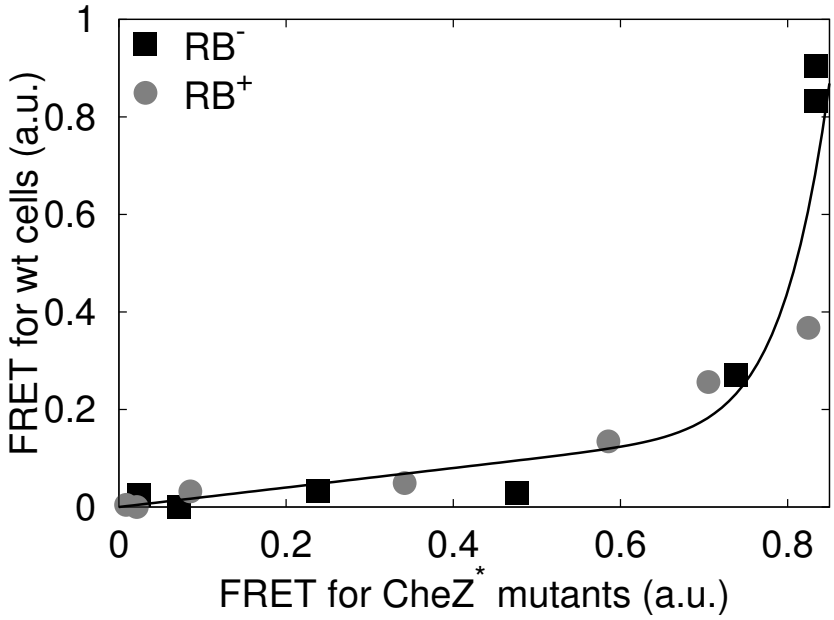

FIGURE 3.2 The relation between the four FRET signals of Figs. 5a and 5c in [35]. FRET signals of bacterial strains that differ only in the type of phosphatase—wild-type CheZ versus a non-localizing mutant–are plotted as a function of each other. This was done both for strains lacking the adaptation proteins CheR and CheB (squares) and for strains with CheR and CheB (circles). The FRET signals on the vertical and horizontal axes are linked via equal concentrations of attractant in the response curves. Because of the decoupling of the response of the intracellular signal transduction pathway from the response of the receptor cluster (see Figure 3.1), equal concentrations of attractant correspond to equal activities of the receptor cluster if the CheRCheB states are the same, and equal concentrations of $[Y_pZ]$ correspond to equal activities of the receptor cluster if the same type of phosphatase is present. As a consequence, the two curves should overlap (see main text). This could be achieved by rescaling only the FRET signal for the wild-type bacterium by a factor 0.5.

as a function of serine concentration for $CheR^-CheB^-$ and $CheR^+CheB^+$ cells, respectively. Since these figures show the *renormalized* FRET response, no absolute concentrations of $[Y_pZ]$ can be obtained. The concentrations in Figure 3.2 are therefore given in arbitrary units. This also means that the curves for $CheRCheB^+$ and $CheR^-CheB^-$ cells in Figure 3.2 can be scaled with respect to each other. Now, if $\beta k_0[L]$ only depends upon the presence of CheR and CheB while $[Y_pZ]$ only depends upon the nature of CheZ, it should be possible to scale these curves such that they coincide. Figure 3.2, which is obtained by scaling the FRET signal for the wild-type $CheR^+CheB^+CheZ$ cells by a factor 0.5, shows that this is indeed possible. This supports the idea that the receptor cluster and the intracellular pathway are two independent modules connected in series.

Figure 3.2 allows us to rescale the data of Figures 5A and 5C of Ref. [35] to obtain $[Y_pZ]$ as a function of [L]. The result is shown in Figure 3.3a, where the maximum $[Y_pZ]$,

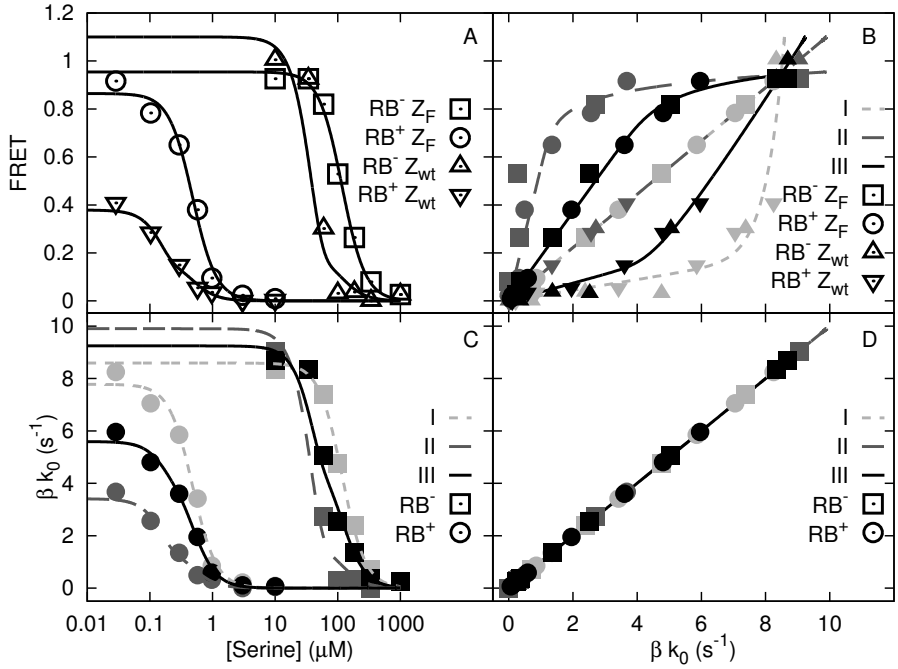

FIGURE 3.3 Three models that reproduce the response curves of [35]. A. The four response curves of Figure 5a in [35], rescaled according to Figure 3.2 and assuming a total concentration $[Z]_T = 1.1\mu M$. Model I (light grey data) is based on a linear dependence $[Y_pZ](\beta k_0)$ for cells containing the non-localizing phosphatase mutant CheZ (see panel B). As a consequence, the activity of the receptor cluster in panel C is proportional to the concentration of $CheY_pCheZ$ for CheZ mutant cells in panel A. The response $[Y_pZ](\beta k_0)$ for cells containing wild-type CheZ is extremely sharp for model I (see panel B). Model II (dark grey data) is based on a linear function of $[Y_pZ](\beta k_0)$ for cells with wild-type CheZ. As a consequence, $\beta k_0([L])$ is proportional to the dose-responses curve for cells with wild-type CheZ (compare panels A and C). In this case, the response curve $[Y_pZ](\beta k_0)$ for CheZ mutant cells is very concave. Model III was constructed by assuming that $\beta k_0([L])$ is a linear combination of the response functions of models I and II. The resulting response functions $[Y_pZ](\beta k_0)$ in panel B are less extreme than those of models I and II.

obtained for $CheR^-CheB^-CheZ$ cells at [L] = 0, was set to the total CheZ concentration as reported in [45]. These response curves impose strong constraints on any model that hopes to explain the response of $CheY_pCheZ$ to the addition of serine. It should be noted that there are two free scaling parameters left, since both the x-axis and the y-axis of Fig. 3.2 are in arbitrary units. The FRET signals for the two CheZ wt strains may be scaled *simultaneously*, as well as the FRET signals for the two CheZ mutant strains. In the modeling, we still allowed for this simultaneous scaling of the FRET signals.

While Figure 3.2 supports the idea that the network that controls the response of $CheY_pCheZ$ to changes in ligand concentration can be decomposed into two independent modules, it does not uniquely prescribe how this decomposition should be made. This is illustrated in Figures 3.3B-D, which show the response curves of three different models, indicated by different colors, that all can explain the dose-response curves of Figure 3.3A. Each model consists of two functions $[Y_pZ]^{Z^{wt}}(\beta k_0)$ and $[Y_pZ]^{Z^*}(\beta k_0)$ (Figure 3.3B) and two functions $\beta k_0^{RB^+}([L])$ and $\beta k_0^{RB^-}([L])$ (Figure 3.3C). For each model, the four composite functions $[Y_pZ]^{\{Z^*,Z^{wt}\}}\left(\beta k_0^{RB\pm}([L])\right)$ exactly reproduce the four dose-response curves of Figure 3.3A. Model I (light dotted lines and points) relies on the assumption that $[Y_pZ]^{Z^*}(\beta k_0)$ is a straight line over the concentration range of interest (see Figure 3.3B). This means that $\beta k_0^{RB^+}([L])$ and $\beta k_0^{RB^-}([L])$ are proportional to $[Y_pZ]([L])$ of $CheR^+CheB^+CheZ^*$ and $CheR^-CheB^-CheZ^*$ cells, respectively; this can be verified by comparing Figure 3.3A to Figure 3.3C. The remaining function $[Y_pZ]^{Z^{wt}}(\beta k_0)$ is now fully determined and can be constructed from $\beta k_0^{RB^+}([L])$ and $[Y_pZ]([L])$ of the $CheR^+CheB^+CheZ^{wt}$ cells, and $\beta k_0^{RB^-}([L])$ and $[Y_pZ]([L])$ of the $CheR^-CheB^-CheZ^{wt}$ cells (see Figure 3.3B); this function has a strongly convex shape. Model II (dark grey lines and points) relies on the assumption that $[Y_pZ]^{Z^{wt}}(\beta k_0)$ is a linear function (see Figure 3.3B). In this case $\beta k_0^{RB^+}([L])$ and $\beta k_0^{RB^-}([L])$ are proportional to $[Y_pZ]([L])$ of $CheR^+CheB^+CheZ^{wt}$ and $CheR^-CheB^-CheZ^{wt}$ cells, respectively (see Figure 3.3A and Figure 3.3C). The functional form $[Y_pZ]^{Z^*}(\beta k_0)$ now has a concave shape (see Figure 3.3B). These two models are two extreme scenarios that both can explain the data shown in Figure 3.3A.

In the following sections we will also consider models that have less extreme functional forms for $[Y_pZ](\beta k_0)$; these models lie in between model I and model II. We construct such models, starting from models I and II, by defining functions $\beta k_0([L])$ as linear combinations $\alpha\ \beta k_0^{II}([L]) + (1-\alpha)\ \beta k_0^{I}([L])$, where α is a parameter between zero and one; for $\alpha = 0$ the model reduces to model I, while for $\alpha = 1$ the model reduces to model II. Model III (black lines and points) was constructed by putting α equal to 0.5. For this model, $[Y_pZ]^{Z^*}(\beta k_0)$ is slightly concave, whereas $[Y_pZ]^{Z^{wt}}(\beta k_0)$ is slightly convex.

The model that can describe the response of $[Y_pZ]$ to changes in ligand concentration should not only be able to reproduce the dose-response curves of Figure 3.3, it should also satisfy other important conditions. Most importantly, wild-type cells can chemotax, which means that in their adapted state they can respond to the addition as well as to the removal of attractant. Bacteria lacking $CheA_s$ are able to chemotax towards attractants as well, although less efficiently than wild-type bacteria [73]. These mutants are similar to CheZ mutants in that the binding of CheZ to the receptor cluster is hampered in both strains. The requirement that both strains can chemotax means that the concentration of $CheY_p$ in the adapted state should be within the working range of the motor, i.e. between 1 and 5 μM [44, 45]. This constraint turns out to be particularly hard to meet.

3.3 Original model: the canonical push-pull network

We now address the question whether the commonly used model for the chemotaxis pathway of *E. coli*, as given by Equations 3.1-3.3, can describe the experimental results of Vaknin and Berg [35]. We first study the effect of the spatial distribution of CheZ,

thus leaving the other parameters unchanged. As we will show, the spatial distribution of CheZ alone is not sufficient to explain their experimental results. We will then also vary rate constants and concentrations to see whether the commonly accepted model can describe these results.

To elucidate the effect of CheZ localization, we have computed the input-output relations for a network in which CheA and CheZ are colocalized at the receptor cluster (corresponding to wild-type cells) and for a network in which CheA is localized at the receptor cluster, while CheZ is distributed in the cytoplasm (corresponding to CheZ mutant cells); for both networks, the chemical reactions are given by Equations 3.1-3.3. The steady-state input-output relations of these networks were obtained numerically by discretizing the system on a 1D grid and propagating the chemical rate equations, which are given in the *Methods* section, in space and time until steady state was reached.

As pointed out in the previous section, the input of the intracellular network is not directly the ligand concentration [L], but rather βk_0 (see Eq. 3.1), which implicitly depends upon [L]. Importantly, we first assume that the functional dependence of β on the ligand concentration [L], as well as the rate constants of all the reactions, is the same for wild-type and CheZ mutant cells: this allows us to elucidate the effect of colocalization of the antagonistic enzymes on the input-output relations. The model and the values of its parameters were taken from Sourjik and Berg [45].

The principal results of our calculations are shown in Figure 3.4. This figure shows for wild-type and CheZ mutant cells, the concentration of $\mathrm{CheY_pCheZ}$ and $\mathrm{CheY_p}$ as a function of βk_0 (see Equation 3.1); the bullets correspond to the state of the network after adaptation [45]. Figure 3.4 shows that the model predicts that the spatial distribution of CheZ affects the response to the addition of repellent or the removal of attractant, which corresponds to an increase in β. More importantly, the model predicts that the CheZ distribution should not affect the response to the addition of attractant: When βk_0 is lowered from its value $\beta^{\mathrm{adapted}} k_0$ in the adapted state, both the change in $[\mathrm{Y_p}]$ and $[\mathrm{Y_pZ}]$ do not depend much on the spatial distribution of CheZ. This result is thus in contrast with the drastic effect of enzyme localization on the response found by Vaknin and Berg [35].

The network given by Equations 3.1-3.3 is very similar to a canonical push-pull network, in which two enzymes covalently modify a substrate in an antagonistic manner [34] (see Methods for how these networks can be mapped onto each other). In chapter 2, we have studied in detail the effect of enzyme localization on the response of a push-pull network [72]. Our principal finding is that enzyme localization *can* have a marked effect on the gain and sensitivity of push-pull networks, seemingly consistent with the experiments of Vaknin and Berg [35], but contradicting the numerical results shown in Figure 3.4. The resolution of this paradox is that both the quantitative and qualitative consequences of enzyme localization depend upon the regime in which the push-pull network operates. In particular, if the activation rate is independent of the substrate concentration and if the deactivation rate is linear in the messenger concentration, then phosphatase localization has no effect on the response curve [72]. This is precisely the case for the chemotaxis network studied here. For $\beta k_0 < \beta^{\mathrm{adapted}} k_0$, CheZ is unsaturated [45] and the dephosphorylation rate of $\mathrm{CheY_p}$ is thus proportional to $[\mathrm{Y_p}]$. The influx J of $\mathrm{CheY_p}$ is constant, *i.e.* independent of [Y]. This is not because the phosphorylation reaction is in the zero-order regime; this reaction is, in fact, in the linear

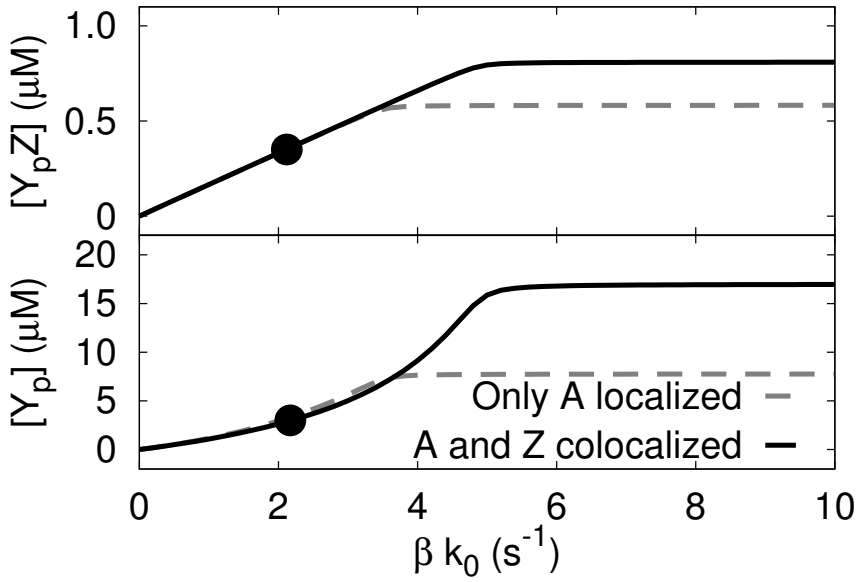

FIGURE 3.4 Total, integrated concentration of $\mathrm{CheY_pCheZ}$, $\int_0^L dx[\mathrm{YpZ}](x)$, and $\mathrm{CheY_p}$, $\int_0^L dx[\mathrm{Y_p}](x)dx$, as a function of βk_0 for the canonical model of the chemotaxis network of *E. coli*, shown in Equations 3.1-3.3. The solid curves correspond to wild-type cells in which CheA and CheZ are colocalized at the receptor cluster, while the dashed curves correspond to the mutant cells in which CheA is localized at the pole, while CheZ freely diffuses in the cytoplasm. The bullets correspond to the adapted state of the system. The diffusion constant of the diffusing components is $D = 5\mu\mathrm{m}^2\mathrm{s}^{-1}$ [71]. For other parameter values, see [45].

regime [45]. The influx J of $\mathrm{CheY_p}$ at the cell pole is constant because a) in steady state $J = k_3[\mathrm{A_pY}] = \beta k_0[\mathrm{A}]$ and b) in the weak activation regime CheA is predominantly unphosphorylated ($[\mathrm{A}] \approx [\mathrm{A}]_\mathrm{T}$), which means that [A] is fairly insensitive to the spatial distribution of CheZ. Hence, according to the model of Equations 3.1-3.3, in this regime the concentration of $\mathrm{CheY_p}$ does not depend upon the spatial distribution of CheZ, which is indeed what Figure 3.4 shows.

However, while the model of Equations 3.1-3.3 predicts that in wild-type cells the response of $[\mathrm{Y_pZ}]$ to the addition of attractant does not depend on the location of CheZ, the experiments by Vaknin and Berg clearly demonstrate that it does [35]. What could be the origin of the discrepancy between the model predictions and the experimental results of Vaknin and Berg? As mentioned above, the response of $[\mathrm{Y_pZ}]$ to the ligand concentration [L] depends upon the response of $[\mathrm{Y_p}]$ to the activity of the receptor cluster, βk_0, and upon the response of βk_0 to the ligand concentration [L]. If we keep with the assumption that the functional dependence of βk_0 on [L], $\beta k_0([\mathrm{L}])$, is the same for both wild type and CheZ mutant cells, the discrepancy between the predictions of the commonly adopted model and the experimental observations of Vaknin and Berg must lie in the dependence of $[\mathrm{Y_pZ}]$ on βk_0. It is quite likely that the rate constants and/or concentrations that are used in the calculations differ from those *in vivo*. It

is also possible that the topology of the commonly accepted model of the intracellular chemotactic pathway, Eqs. 3.1-3.3, is incorrect. In order to discriminate between these two scenarios, we will, in the rest of this section, first address the question whether it is possible to explain the experimental observations with the commonly accepted model by allowing for different values of parameters such as rate constants and protein concentrations. We will then argue that simply allowing for different parameter values is probably not sufficient to explain the experiments of Vaknin and Berg, and that thus the canonical model should be reconsidered.

Independently of the model parameters, it is always true that the rate of phosphorylation equals the rate of dephosphorylation if the system is in steady state. For the commonly accepted model, i.e. Equations 3.1-3.3, this means that for both the spatially uniform network in which CheA and CheZ are colocalized, and the spatially non-uniform network in which CheZ is distributed in the cytoplasm, the following relation holds in steady state:

$$\beta k_0[\mathrm{A}] = k_6[\mathrm{YpZ}] \propto k_6 \mathrm{FRET}. \tag{3.4}$$

Here, "FRET" denotes the FRET signal, which is proportional to the total, integrated, concentration of $\mathrm{CheY_p}$ bound to CheZ, [YpZ]. For the regime of interest, $\beta k_0 < \beta^{\mathrm{adapted}} k_0$, the concentration of unphosphorylated CheA, [A], is essentially constant for the conventional model, because only a small fraction of the total amount of CheA is phosphorylated; below we discuss scenarios in which this relation might not hold. Equation 3.4 thus shows that if $[\mathrm{A}] \approx [\mathrm{A}]_\mathrm{T}$, the FRET signal only depends upon the activity of the receptor cluster, βk_0, and upon the phosphatase activity, k_6, but not upon other rate constants in the network, nor upon the expression levels of, for instance, CheY and CheZ. Moreover, if $[\mathrm{A}] \approx [\mathrm{A}]_\mathrm{T}$, the FRET signal, in this model, is *linear* in the activity of the receptor cluster: $\mathrm{FRET} = c\beta([L])$, where $c = k_0[\mathrm{A}]/k_6$ is the proportionality constant. Incidentally, this explains the linear dependence of $[\mathrm{Y_pZ}]$ on βk_0 for $\beta k_0 < \beta k_0^{\mathrm{adapted}}$ in Figure 3.4B.

The linear relation between [YpZ] and βk_0 as predicted by the commonly accepted model would mean that the dose-response curves, i.e. FRET([L]), solely reflect the response of the receptor cluster to the addition of ligand, $\beta k_0([\mathrm{L}])$. Vaknin and Berg report the *renormalized* FRET response: they normalize the FRET signal at ligand concentration [L] to the FRET signal at zero ligand concentration, [L] = 0 [35]. If the response of $[\mathrm{Y_pZ}]$ to βk_0 would indeed be linear, then the renormalized FRET signal would be given by $\mathrm{FRET}([\mathrm{L}])/\mathrm{FRET}([\mathrm{L}] = 0) = \beta([\mathrm{L}])/\beta([\mathrm{L}] = 0)$. Hence, the proportionality factor c would drop out. The renormalized FRET signal would thus be given by the dependence of the activity of the receptor cluster on the ligand concentration, $\beta k_0([L])$. While plotting the renormalized FRET signal may mask potentially useful information, this observation does allow us to draw an important conclusion: *If* $\beta k_0([\mathrm{L}])$ *is the same for wild type and CheZ mutant cells, and as long as* $[\mathrm{Y_pZ}](\beta k_0)$ *is linear, the commonly accepted model cannot describe the experiments of Vaknin and Berg, even if we allow for different parameter values for the rate constants or protein concentrations.*

The experiments of Wang and Matsumura illustrate the importance of this conclusion [36]. Their experiments suggest that the phosphatase activity is enhanced by its interaction with $\mathrm{CheA_s}$, which localizes CheZ to the receptor cluster [36]. This would predict that in the CheZ mutant cells (in which CheZ is distributed in the cytoplasm),

the phosphatase activity, and hence k_6, is lower. This would change the dependence of $[Y_pZ]$ on βk_0 (see Equation 3.4); in particular, decreasing k_6 would increase the slope. However, as long as the dependence of $[Y_pZ]$ on βk_0 is still linear, the renormalized FRET response would still be given by $\beta k_0([L])$: merely changing the slope of $[Y_pZ]$ as a function βk_0 does not change the renormalized FRET response. More in general, only allowing for different rate constants or protein concentrations between the wild-type cells and mutant cells is not sufficient to explain the data, if indeed $\beta k_0([L])$ is the same for both cells and $[Y_pZ](\beta k_0)$ is linear.

3.4 Changing parameters in the canonical model

In vivo parameter values are typically not known with high precision: protein concentrations are often known only approximately and rate constants are typically measured *in vitro* rather than *in vivo*. We now address the question whether the experiments by Vaknin and Berg [35] could be explained if we allow for different parameter values in the commonly accepted model of the chemotaxis network of *E. coli*.

The critical ingredient in the above analysis is that $[Y_pZ]$ varies linearly with βk_0, both for the wild-type and the CheZ mutant cells. We now first address the question whether deviations from this linear relation could explain the data, and then how these deviations might arise. The simplicity of the commonly accepted model, Equations 3.1-3.3, does not allow for a convex dependence of $[Y_pZ]$ on βk_0. Figure 3.3B then immediately shows that any model that aims to describe the dose-response curves of both the the wild-type cells and the CheZ mutant cells, should exhibit a linear relationship $[Y_pZ](\beta k_0)$ for wild-type cells and a concave function $[Y_pZ](\beta k_0)$ for CheZ mutant cells (dark grey data set). For this reason, we now try to simultaneously fit the dose-response curves of FRET vs [serine] for both wild-type and mutant cells, by varying the parameters for the mutant bacterium, while keeping the parameters for the wild-type cells fixed.

Figures 3.5-3.8 show the effect of individually varying the rate constants k_1, k_3, k_4 and k_6 of the commonly accepted model of the intracellular chemotaxis network (Equations 3.1-3.3). For every parameter set we show the response of: A) $[Y_p]$ as a function of the receptor-cluster activity βk_0; B) $[Y_pZ]$ as a function of βk_0; C) [A] as a function of βk_0; D) the FRET signal as a function of added ligand (serine). Every plot shows the result for the wild-type cell with colocalized CheA and CheZ and with the baseline parameter set (thin solid black line), together with the response curves of mutant cells with diffusive CheZ, where each curve corresponds to a different value of the rate constant that is varied. The calculations were repeated for different concentrations $[A]_T$ and $[Y]_T$ with similar results (data not shown).

Figures 3.5C-3.8C show [A] as a function of βk_0. It is seen that for low values of βk_0, [A] is essentially constant, and given by $[A] \approx [A]_T$. This is an important observation. In steady state, $\beta k_0[A] = k_6[Y_pZ]$ for the commonly accepted model of the intracellular chemotaxis network. Hence, when [A] is constant, $[Y_pZ]$ varies linearly with βk_0. Since the FRET signal is proportional to $[Y_pZ]$, also the FRET signal varies linearly with βk_0, when [A] is constant. If the FRET signal is proportional to βk_0, then the *renormalized* FRET response is fully determined by the activity of the receptor cluster: $\text{FRET}([L])/\text{FRET}([L] = 0) = \beta k_0([L])/\beta k_0([L] = 0)$; it no longer depends upon

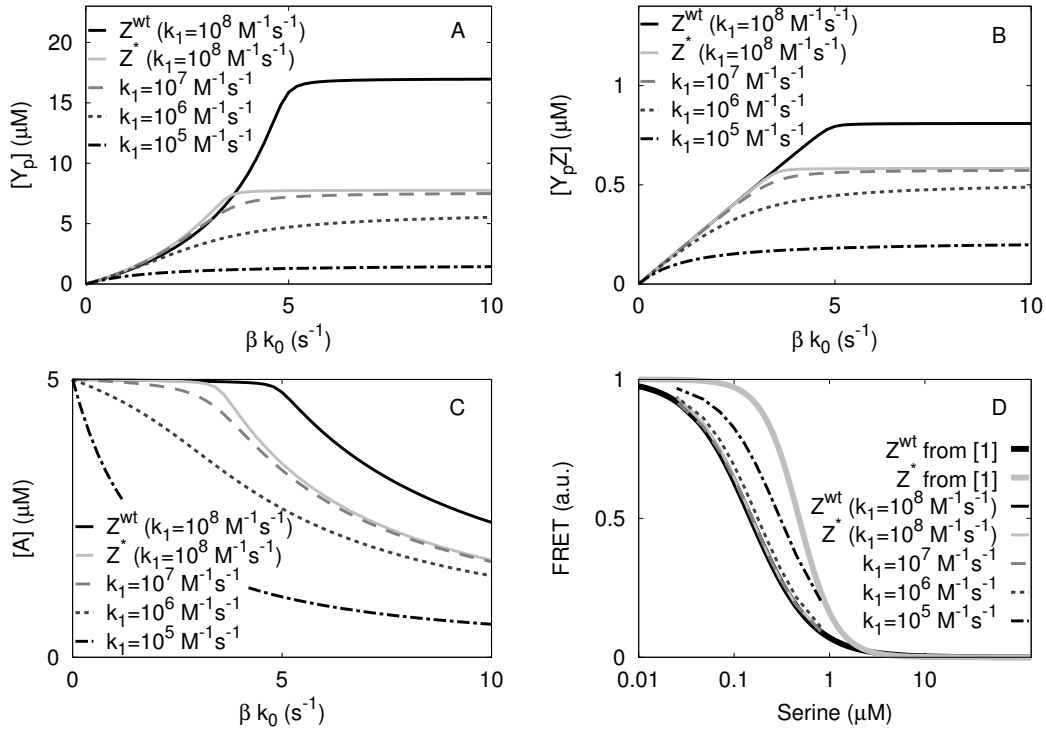

FIGURE 3.5 Effect of varying k_1 on the response of the commonly-adopted chemotaxis model (Equations 3.1-3.3). The thin black line corresponds to the predicted response of wild-type cells, the parameters of which are kept constant (except βk_0); the other thin lines correspond to predicted response curves of CheZ mutant cells, where each line corresponds to a different value of k_1. Shown are the response of $[\mathrm{Y_p}]$ (A), $[\mathrm{Y_pZ}]$ (B), [A] (C) to changes in the activity of the receptor cluster βk_0 and the FRET signal as a function of serine concentration (D). By construction (see text), the predicted FRET response of the wild-type cells (thin black line) coincides with the measured response [35] (thick black line). Please also note that for lower CheA-$\mathrm{CheY_p}$ association rates ($k_1 = 10^5 \mathrm{M^{-1}s^{-1}}$, dash-dotted line) in CheZ mutant cells, the predicted FRET response shifts in the direction of the one measured for CheZ mutant cells (grey thick line) [35]. The baseline parameters are $k_1 = 10^8$ $\mathrm{M^{-1}s^{-1}}$, $k_3 = 750$ $\mathrm{s^{-1}}$, $k_4 = 5 \cdot 10^6$ $\mathrm{M^{-1}s^{-1}}$, $k_5 = 0.5$ $\mathrm{s^{-1}}$, $k_6 = 30$ $\mathrm{s^{-1}}$, $[\mathrm{Z}]_\mathrm{T} = 1.1\mu\mathrm{M}$, $[\mathrm{A}]_\mathrm{T} = 5\mu\mathrm{M}$ and $[\mathrm{Y}]_\mathrm{T} = 17.9\mu\mathrm{M}$ ([45]) and $D = 5$ $\mu\mathrm{m^2s^{-1}}$.

parameters of the intracellular network. The observation of $[\mathrm{A}] \approx [\mathrm{A}]_\mathrm{T}$ is thus important, because a) it would justify the commonly made assumption that the renormalized FRET response reflects the activity of the receptor cluster; b) it would mean that the commonly accepted model cannot explain the difference in FRET response between wild-type cells and CheZ mutant cells, since the spatial distribution of CheZ is assumed to only affect the response of the intracellular network and not that of the receptor cluster.

Figure 3.5C shows that over the concentration range of interest (corresponding to $\beta k_0 < \beta k_0^{\mathrm{adapted}} \approx 3\mathrm{s^{-1}}$), $[\mathrm{A}] \approx [\mathrm{A}]_\mathrm{T}$ is fairly constant in wild-type cells and CheZ

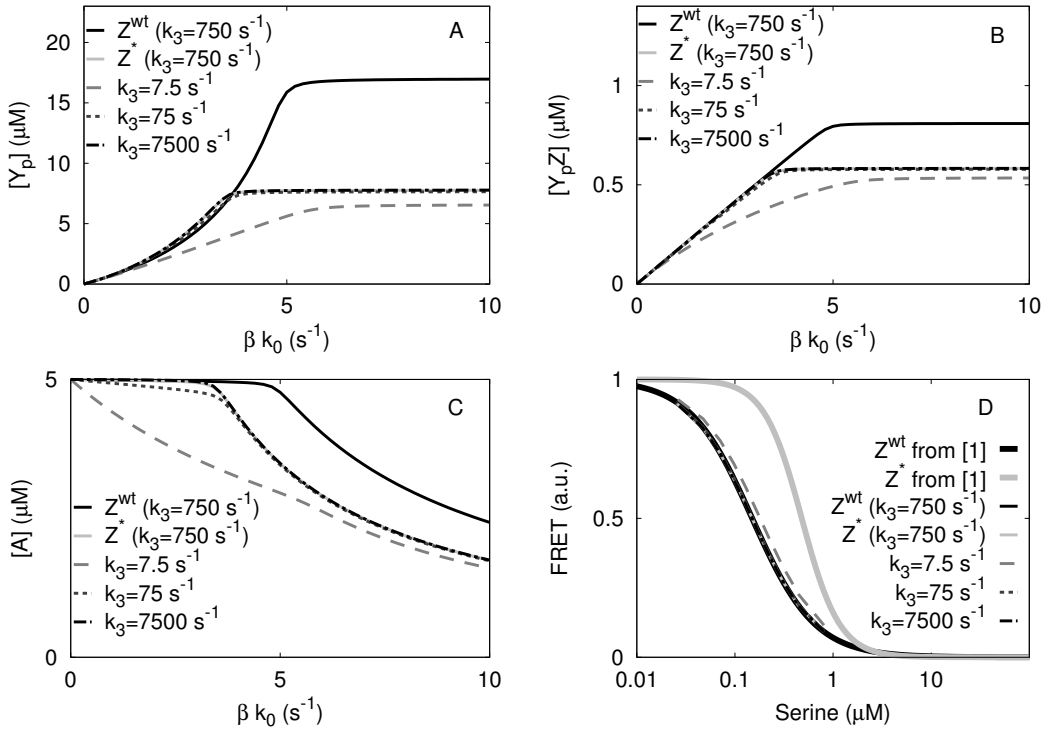

FIGURE 3.6 Effect of k_3 on the response of the commonly adopted chemotaxis model (Equations 3.1-3.3). Shown are the response of $[Y_p]$ (A), $[Y_pZ]$ (B), [A] (C) to changes in the activity of the receptor cluster βk_0 and the FRET signal as a function of serine concentration (D). The baseline parameters are given in Fig. 3.5.

mutant cells with the baseline parameter set. This would justify the assumption that the renormalized FRET response is a useful measure for the activity of the receptor cluster. However, by the same token, it also means that the commonly accepted model cannot explain the experiments by Vaknin and Berg [35].

Figures 3.5A–3.8A and 3.5B–3.8B show the response of $[Y_p]$ and $[Y_pZ]$ as a function of βk_0. There exists a simple relation between the curves $[Y_pZ](\beta k_0)$ and $[Y_p](\beta k_0)$. In steady state, $[Y_p][Z] = K_{MZ}[Y_pZ]$, where $K_{MZ} = (k_5 + k_6)/k_4$. Since, $[Z] = [Z]_T - [Y_pZ]$, $[Y_p]$ can be expressed in terms of [YpZ] as $[Y_p] = K_{MZ}[Y_pZ]/([Z]_T - [Y_pZ])$. This relation immediately gives the functional form of $[Y_p](\beta k_0)$ when $[Y_pZ]$ depends linearly on βk_0.

We now address the question *why* [A] as a function of βk_0 is initially constant, and then suddenly decreases. To this end, we will exploit the mapping between the *E. coli* chemotaxis network and the canonical push-pull network, as discussed in the appendix. This mapping is particularly useful for understanding the response of $[Y_p]$ and $[Y_pZ]$ and hence the FRET signal to changes in the activity of the receptor cluster βk_0. This is illustrated in Figures 3.9 and 3.10 for a spatially uniform push-pull network in the zero-order and linear regime, respectively; as discussed in [72], this also corresponds to a push-pull network in which the enzymes are colocalized at one end of the cell. In steady state, the chemotaxis network obeys the following relation:

$$\beta k_0[A] = k_1[A_p][Y], \tag{3.5}$$

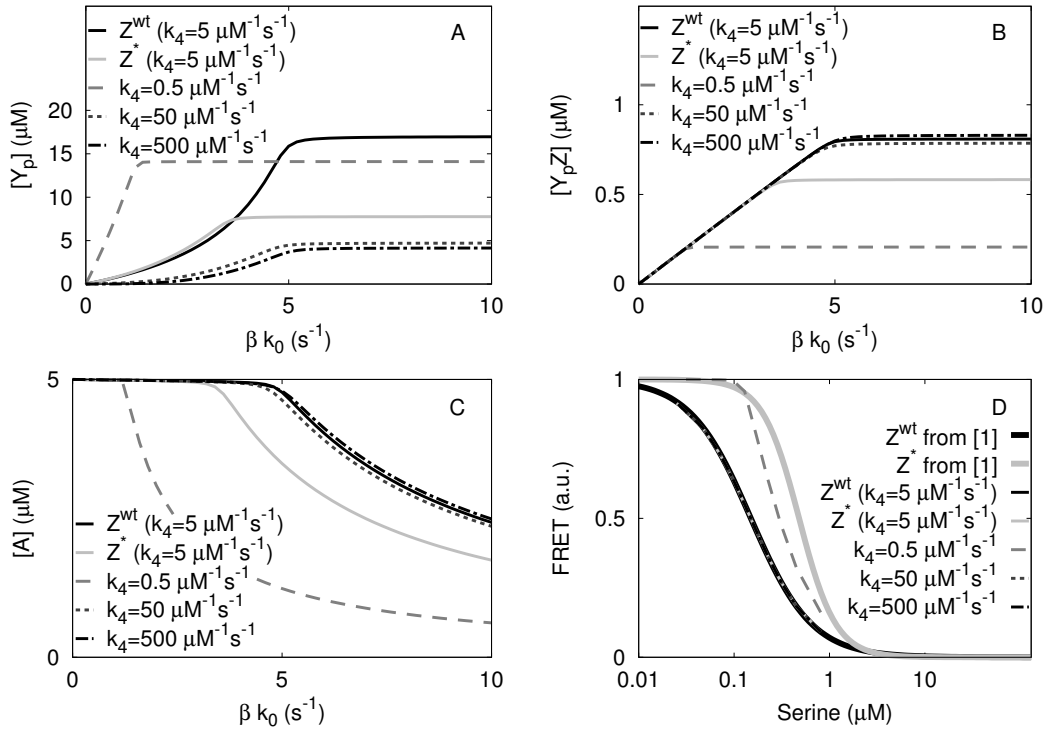

FIGURE 3.7 Effect of k_4 on the response of the commonly-adopted chemotaxis model (Equations 3.1-3.3). Shown are $[Y_p]$ (A), $[Y_pZ]$ (B), $[A]$ (C) as a function of βk_0, and the FRET signal as a function of serine concentration (D). Please note that for a lower CheZ-CheY$_p$ association rate ($k_4 = 10^5 \mathrm{M}^{-1}\mathrm{s}^{-1}$, dashed line) in CheZ mutant cells, the predicted FRET response of CheZ mutant cells agrees fairly well with the experimentally measured one (thick grey line) [35]. The baseline parameters are given in Fig. 3.5.

where we have assumed that $k_2 = 0$. The idea is now that $[A_p]$ and $[Y]$ are fully determined by the total concentration of phosphorylated CheA, $[A_p]_T \equiv [A_p] + [A_pY]$, as in a canonical push-pull network: $[A_p] \equiv [A_p]([A_p]_T)$ and $[Y] \equiv [Y]([A_p]_T)$. The functions $[A_p]([A_p]_T)$ and $[Y]([A_p]_T)$ can be obtained analytically [34], and they are shown in Figs. 3.9-3.10A and 3.9-3.10B, respectively. The concentration of $[A_p]_T$, in turn, is controlled by the value of βk_0. To obtain $[A_p]_T$ as a function of βk_0, we rewrite the above equation as

$$\beta k_0 \left([A]_T - [A_p]_T\right) = k_1 [A_p]([A_p]_T)[Y]([A_p]_T), \tag{3.6}$$

where $[A]_T \equiv [A] + [A_p]_T$ is the total concentration of CheA. This equation can now be solved for $[A_p]_T$ as a function of βk_0. The behavior of the solution can be understood by plotting the left-hand side and the right-hand side of the above equation separately, as is illustrated in Figures 3.9C and 3.10C for networks in the zero-order and linear regime, respectively; the intersection yields the value of $[A_p]_T$. The panels D in these figures show $[A] = [A]_T - [A_p]_T$ as a function of βk_0. Since all the other concentrations $[Y]$, $[Y_p]$, $[A_pY]$, and $[Y_pZ]$ are determined by $[A_p]_T$, the state of the system is now fully specified.

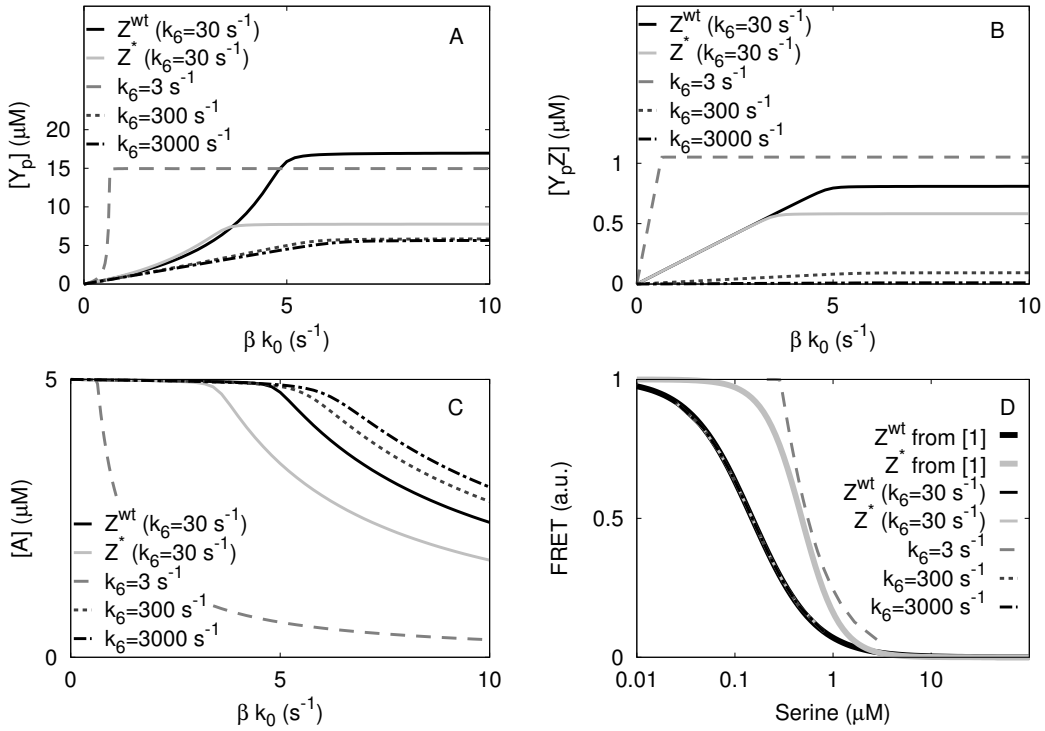

FIGURE 3.8 Effect of changing k_6 on the response of the commonly-adopted chemotaxis model (Equations 3.1-3.3). Shown are: $[\mathrm{Y_p}](\beta k_0)$ (A), $[\mathrm{Y_pZ}](\beta k_0)$ (B), $[\mathrm{A}](\beta k_0)$ (C), FRET([serine]) (D). Please note that for a lower phosphatase activity in CheZ mutant cells ($k_6 = 3\mathrm{s}^{-1}$, dashed line), the predicted FRET response agrees quite well with that measured experimentally (thick grey line) [35]. The baseline parameters are given in Fig. 3.5.

Figs. 3.9 and 3.10 show the results for a symmetric push-pull network in the zero-order and first-order regime, respectively. For the zero-order network, it is seen that $[\mathrm{A}](\beta k_0)$ has two distinct regimes. The first corresponds to the regime in which the phosphatase activity is larger than the kinase activity, and [Y] is large (Fig. 3.9A); note that since the network is zero-order, also the concentration of [A] is low (Fig. 3.9B). Because [Y] is high in this regime, the initial slope of $k_1[\mathrm{A_p}][\mathrm{Y}]$ as a function of $[\mathrm{A_p}]_\mathrm{T}$ is large (Fig. 3.9C). The second regime corresponds to the one in which the kinase activity exceeds the phosphatase activity; $[\mathrm{Y_p}]$ is large and [Y] is low; because [Y] is now very low, the slope is essentially reduced to zero (Fig. 3.9C). The situation differs markedly for a push-pull network in the linear regime. In this regime, the concentration of [Y] changes gradually as a function of $[\mathrm{A_p}]_\mathrm{T}$ (Fig. 3.10A) and this leads to a gradual change in the slope of $k_1[\mathrm{A_p}][\mathrm{Y}]$ as a function of $[\mathrm{A_p}]_\mathrm{T}$ (Fig. 3.10C). This gradual change in the slope manifests itself as a gradual change in $[\mathrm{A}](\beta k_0)$ (Fig. 3.10D).

Fig. 3.11C shows for the *E. coli* network the rate of $\mathrm{CheA_p}$ production and $\mathrm{CheA_p}$ deactivation, corresponding to the left-hand side (lhs) and right-hand side (rhs) of Equation 3.6, respectively, as a function of $[\mathrm{A_p}]_\mathrm{T}$. The rate of $\mathrm{CheA_p}$ deactivation (rhs) is given by $k_1[\mathrm{A_p}]([\mathrm{A_p}]_\mathrm{T})[\mathrm{Y}]([\mathrm{A_p}]_\mathrm{T})$. As shown in Fig. 3.11B, for the *E. coli* network

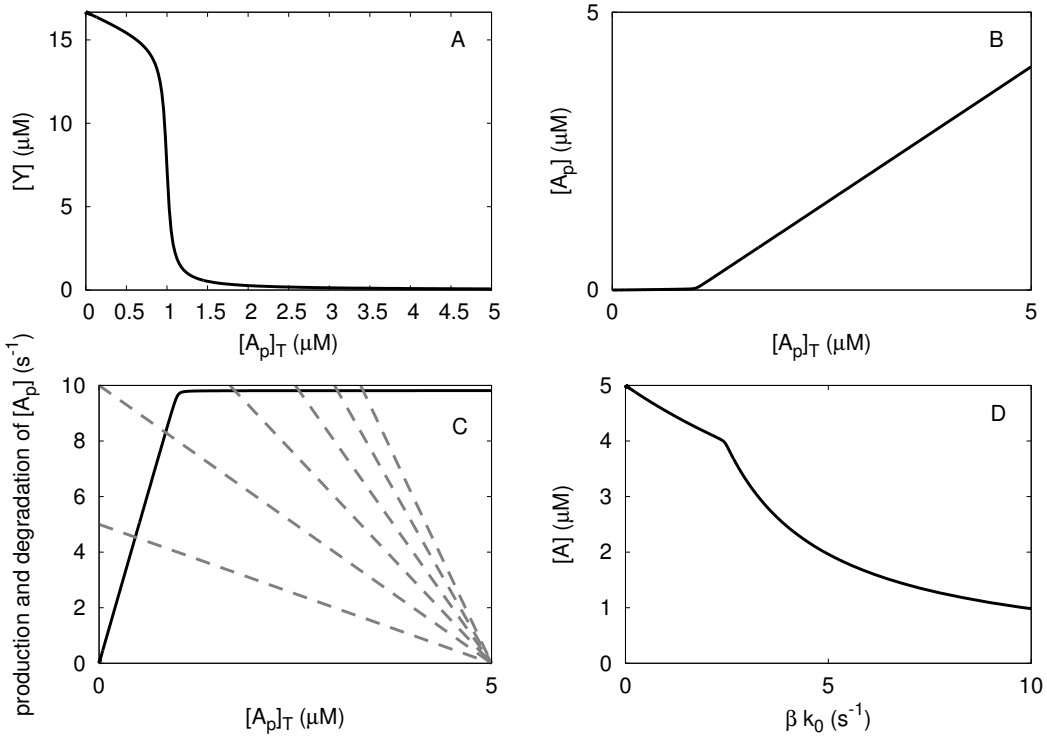

FIGURE 3.9 Mapping of a *symmetric* network with a topology of that of the canonical *E. coli* chemotaxis network (Equations 3.1–3.3) onto a symmetric canonical push-pull network (Equations 3.21-3.22), for networks that are in the *zero-order* regime. $k_1 = k_4 = 36\ \mu\mathrm{M}^{-1}\mathrm{s}^{-1}$; $k_3 = k_6 = 10\ \mathrm{s}^{-1}$ ($K_\mathrm{M} = 0.28\ \mu$M); $S_\mathrm{T} = [\mathrm{Y}]_\mathrm{T} = 16.7\ \mu$M; $[\mathrm{E_d}]_\mathrm{T} = [\mathrm{Z}]_\mathrm{T} = 1\ \mu$M; $[\mathrm{A}]_\mathrm{T} = 5\mu$M. In panel C: the black line is given by the right-hand side of Eq. 3.6, i.e. $k_1[\mathrm{A}]([\mathrm{A_p}]_\mathrm{T})[\mathrm{Y}]([\mathrm{A_p}]_\mathrm{T})$; the dashed lines are given by the left-hand side of Eq. 3.6, i.e. $\beta k_0([\mathrm{A}]_\mathrm{T} - [\mathrm{A_p}]_\mathrm{T})$; the different dashed lines correspond to different values of βk_0 : $\beta k_0 = 1, 2, 3, 4, 5, 6\,\mathrm{s}^{-1}$. The intersection of the solid and dashed curves yields $[\mathrm{A_p}]_\mathrm{T}$ as a function of βk_0. When $[\mathrm{A_p}]_\mathrm{T}$ is determined, the state of the system is fully determined.

$[\mathrm{A_p}] \approx [\mathrm{A_p}]_\mathrm{T}$. Hence, the slope of the rhs of Equation 3.6 is given by $k_1[\mathrm{Y}]([\mathrm{A_p}]_\mathrm{T})$. Fig. 3.11A shows $[\mathrm{Y}]([\mathrm{A_p}]_\mathrm{T})$. It is seen that [Y] is high for low values of $[\mathrm{A_p}]_\mathrm{T}$; this explains the large initial slope of $k_1[\mathrm{A_p}][\mathrm{Y}]$ as a function of $[\mathrm{A_p}]_\mathrm{T}$ in Fig. 3.11C. Fig. 3.11A also shows that as $[\mathrm{A_p}]_\mathrm{T}$ is increased, [Y] decreases strongly. This explains the strong drop in the slope of $k_1[\mathrm{A_p}][\mathrm{Y}]$ (rhs) as $[\mathrm{A_p}]_\mathrm{T}$ is increased. Because $k_1[\mathrm{A_p}][\mathrm{Y}]$ (rhs Eq. 3.6) initially rises rapidly with $[\mathrm{A_p}]_\mathrm{T}$ and then levels off abruptly, the intersection with the curve $\beta k_0[\mathrm{A}]$ (lhs Eq. 3.5), which determines the steady state, initially occurs for very low values of $[\mathrm{A_p}]_\mathrm{T}$ as βk_0 is increased from zero. Only when the activity of the receptor cluster, βk_0, is such that the total $\mathrm{CheA_p}$ concentration becomes large enough to decrease [Y], does $[\mathrm{A_p}]$ increase and [A] decrease, as shown in Fig. 3.11D. Put differently, initially the $\mathrm{CheA_p}$ molecules that are produced, immediately react with CheY molecules to yield CheA molecules again. This keeps the concentration of $\mathrm{CheA_p}$ low. However, in this process, the concentration of CheY does decrease, and this reduces the

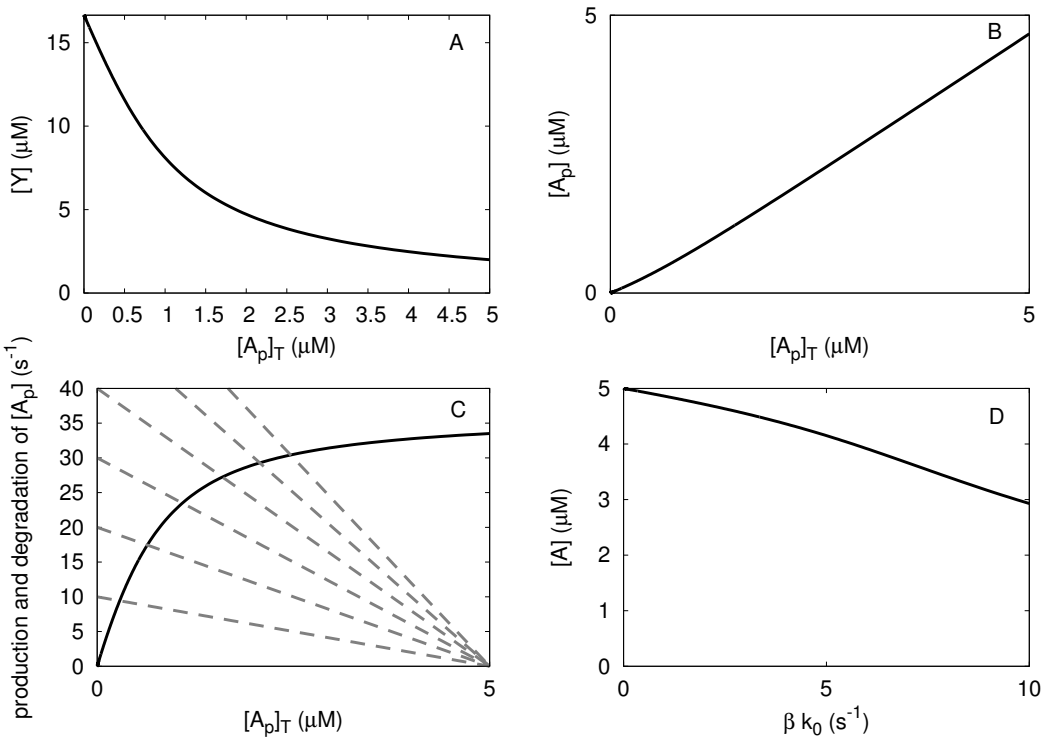

FIGURE 3.10 Mapping of a *symmetric* network with a topology of that of the canonical *E. coli* chemotaxis network (Equations 3.1–3.3) onto a symmetric canonical push-pull network (Equations 3.21-3.22), for networks that are in the *linear* regime. The different dashed lines correspond to different values of $\beta k_0 : \beta k_0 = 2, 4, 6, 8, 10, 12\,\mathrm{s}^{-1}$. $k_1 = k_4 = 3.6\ \mu\mathrm{M}^{-1}\mathrm{s}^{-1}$; $k_3 = k_6 = 100\ \mathrm{s}^{-1}$ ($K_\mathrm{M} = 28\ \mu$M); $S_\mathrm{T} = [\mathrm{Y}]_\mathrm{T} = 16.7\ \mu$M; $[\mathrm{E_d}]_\mathrm{T} = [\mathrm{Z}]_\mathrm{T} = 1\ \mu$M; $[\mathrm{A}]_\mathrm{T} = 5\mu$M.

rate at which $\mathrm{CheA_p}$ molecules are dephosphorylated. At some point, [Y], and hence the rate of $\mathrm{CheA_p}$ dephosphorylation, has decreased so much, that the concentration of $\mathrm{CheA_p}$ will rapidly rise.

We are now in a position to understand how the response curves change as the rate constants are varied. As k_1 is decreased, the push-pull network becomes more linear, as a result of which the concentration of $[\mathrm{Y_p}]$ decreases more gradually as $[\mathrm{A_p}]_\mathrm{T}$ increases. Moreover, as k_1 is decreased, the rate at which $\mathrm{CheA_p}$ molecules are dephosphorylated decreases. These two effects combine to yield a more gradual change in the rate of $\mathrm{CheA_p}$ deactivation (the rhs of Eq. 3.6) as a function of $[\mathrm{A_p}]_\mathrm{T}$; as seen for the symmetric push-pull network in the linear regime (Fig. 3.10C), such a gradual change in $k_1[\mathrm{A_p}][\mathrm{Y}]$ as a function of $[\mathrm{A_p}]_\mathrm{T}$, means that [A] starts to decrease at lower values of βk_0 and then does so more gradually (see Fig. 3.5). When k_3 is decreased, the network enters the zero-order regime more deeply, and the response becomes similar to that of the symmetric push-pull network in the zero-order regime (compare Figs. 3.9 and 3.6). When k_4 is decreased, [Y] decreases at lower values of $[\mathrm{A_p}]_\mathrm{T}$ and does so more gradually, since the network becomes more linear; consequently, [A] starts to decrease at lower values of βk_0 (Fig. 3.7C). Lastly, when k_6 is decreased, [Y] decreases more sharply for lower values of

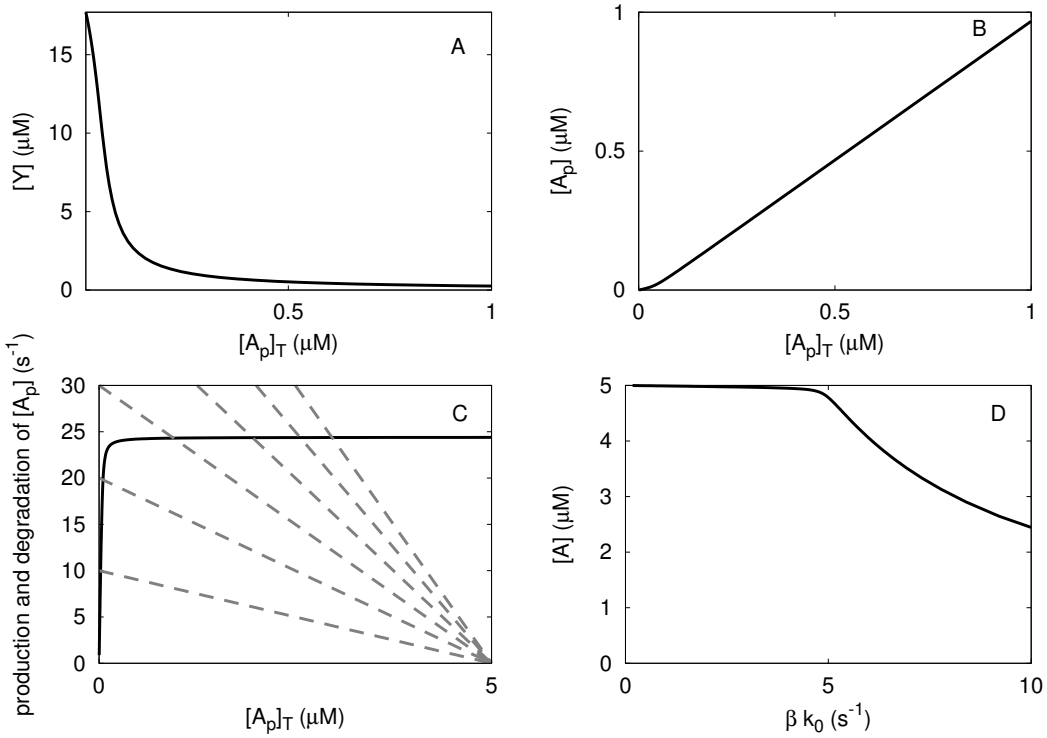

FIGURE 3.11 Mapping of the canonical *E. coli* chemotaxis network (Equations 3.1–3.3) onto a push-pull network (Equations 3.21-3.22). The solid line corresponds to the rate of $\mathrm{CheA_p}$ production as given by the right-hand side of Eq. 3.6, while the dashed lines correspond to the "decay" rate of $\mathrm{CheA_p}$ as given by the left-hand side of Eq. 3.6; each dashed line corresponds to a different value of βk_0: from left to right, $\beta k_0 = 2, 4, 6, 8, 10, 12\,\mathrm{s}^{-1}$. The intersection of the solid and dashed lines yield $[\mathrm{A_p}]_\mathrm{T}$ in steady state. Please note that since the rate of $\mathrm{CheA_p}$ deactivation (solid line) initially increases rapidly with $[\mathrm{A_p}]_\mathrm{T}$, [A] as a function of βk_0 is essentially constant and given by $[\mathrm{A}] \approx [\mathrm{A}]_\mathrm{T}$ for low values of βk_0, as shown in panel D. If $[\mathrm{A}] \approx [\mathrm{A}]_\mathrm{T}$, $[\mathrm{Y_pZ}]$ increases linearly with the activity of the receptor cluster, βk_0, since in steady state $\beta k_0[\mathrm{A}] = k_6[\mathrm{Y_pZ}]$ (see, e.g., Fig. 3.5). $k_1 = 100\mu\mathrm{M}^{-1}\mathrm{s}^{-1}$; $k_3 = 750\ \mathrm{s}^{-1}$; $k_4 = 5\ \mu\mathrm{M}^{-1}\mathrm{s}^{-1}$; $k_6 = 30\ \mathrm{s}^{-1}$; $[\mathrm{S}]_\mathrm{T} = [\mathrm{Y}]_\mathrm{T} = 17.9\ \mu M$; $[\mathrm{E_d}]_\mathrm{T} = [\mathrm{Z}]_\mathrm{T} = 1.1\ \mu\mathrm{M}$; $[\mathrm{A}]_\mathrm{T} = 5\mu\mathrm{M}$.

$[\mathrm{A_p}]_\mathrm{T}$. As a result, $[\mathrm{A}](\beta k_0)$ starts to decrease at lower values of βk_0 and then does so more strongly (Fig. 3.8C). Please note that in all cases, when [A] is no longer constant and equal to $[\mathrm{A}]_\mathrm{T}$, $[\mathrm{Y_pZ}](\beta k_0)$ is no longer a straight line, but becomes a concave function (Figs. 3.5B–3.8B). As discussed in Section 3.2, such a concave function for CheZ mutant cells over the concentration range of interest, could make it possible to simultaneously fit the measured dose-response curves for wild-type and CheZ mutant cells [35].

To show the degree of agreement with experiment that can be obtained, we present in Figures 3.5D–3.8D the predictions of the canonical model for the FRET signal as a function of ligand concentration for both wild-type and CheZ mutant cells. These curves are obtained as follows. First, we note that $[\mathrm{Y_pZ}]([\mathrm{L}])$ is given by $[\mathrm{Y_pZ}](\beta k_0([\mathrm{L}]))$. For

wild-type cells, $[Y_pZ]$ is linear in βk_0, which means that apart from a proportionality factor, $\beta k_0([L])$ is given by $[Y_pZ]([L])$. The latter is obtained up to a scaling factor by the FRET data in Fig 5c of [35], which can be fitted to a Hill function. Hence, $\beta k_0([L])$ can be described by a Hill function $\beta k_0([L]) = \frac{C_1}{1+([L]/K_D)^{n_H}}$, where K_D and n_H can directly be obtained from the fit to the FRET data. The constant C_1 is given by the value of βk_0 at zero ligand concentration, i.e. in the adapted state: $C_1 = \beta k_0^{\text{adapted}}$; we chose the constant such that $[Y_p](\beta k_0^{\text{adapted}}) \approx 3\mu$M, which is in the middle of the working range of the motor. Note that, by construction, the FRET response of wild-type cells, as predicted by the canonical model, agrees with that observed experimentally. The FRET curves for the CheZ mutant cells can now be obtained by combining the computed $[Y_pZ](\beta k_0)$ for these cells with $\beta k_0([L])$, which is assumed to be the same for both wild-type cells and CheZ mutant cells; thus, not only K_D and n_H are the same, but also $\beta k_0^{\text{adapted}}$ and hence C_1; as discussed before, this relies on the assumption that there is no feedback from CheY to the activity of the receptor cluster, which could affect the value of βk_0 in the adapted state.

The results of this procedure are shown in Figs. 3.5D-3.8D. For the wild-type cell, the predicted dose-response curve indeed coincides with the experimental curve as measured in [35], while for the mutant cells the predicted response curves typically deviate from those measured experimentally. A good simultaneous fit to the dose-response curves of the wild-type and CheZ mutant cells can be obtained by assuming a lower value of the catalytic rate k_6 for the CheZ mutant cells (see Fig. 3.8D). Both the lower sensitivity for the mutant cells as well as the increased sharpness of the dose response curve are reproduced if the catalytic activity of CheZ, k_6, is approximately ten times lower for the mutant cells than for the wild-type cells. The idea that this could explain the data of Vaknin and Berg [35] is supported by the experimental observation that the binding of CheZ to $CheA_s$ at the receptor cluster seems to increase the catalytic activity of CheZ [36].

Although the fit to the dose response curves is good, it can also be seen from Figs. 3.8A and 3.8B that the concentration of $CheY_p$ and the concentration of $CheY_pCheZ$ are at their maximum values for the mutant cells when they are in their adapted state, i.e. when $\beta k_0 \approx \beta k_0^{\text{adapted}}$. If the level of $[Y_p]$ is at its maximum level, it is impossible for the mutant cells to respond to repellents. Furthermore, since $[Y_p]$ is constant as a function of βk_0 around the adapted state, βk_0 must be lowered by a large amount upon the addition of attractant before the mutant cells can respond. Chemotaxis thus seems impossible for the mutant cells. However, it is known that bacteria with a non-localizing phosphatase are able to chemotax towards attractants, although less efficiently than wild-type bacteria [73]. Hence, while a lower catalytic activity of diffusive CheZ with respect to localized CheZ can explain the experimentally observed change in the dose-response curve [35], it seems inconsistent with the observation that the mutants are still able to chemotax.

A similar behaviour is seen in Fig. 3.7 for a ten times lower value of the association rate k_4 of $CheY_p$ to CheZ: although the dose response curves for wild-type and mutant bacteria can be simultaneously fitted, the mutant cells would adapt to the maximum values of both $CheY_p$ and $CheY_pCheZ$. Furthermore, $[Y_pZ]$ is much lower for the mutant cell than for the wild-type cell as can be seen from Fig. 3.7B, in contrast with the observations in [35]. We therefore argue that the commonly accepted model of the

intracellular chemotaxis network needs to be refined. In the next chapter, we present such a model.

3.5 Summary

The experiments by Vaknin and Berg on the effect of CheZ localization on the dose-response curves of *E. coli* [35] impose strong constraints on the design of a model of the intracellular chemotaxis network. These experiments unambiguously demonstrate that the second derivative of $[Y_pZ](\beta k_0)$ of CheZ wild-type cells is larger than that of CheZ mutant cells (see Figure 3.3). The topology of the intracellular chemotaxis network of the canonical model (Equations 3.1–3.3) is such that the second derivative of $[Y_pZ](\beta k_0)$ must be equal to or smaller than zero: according to the canonical model the response curve cannot be convex. One way to fit the data is to assume that the response curve $[Y_pZ](\beta k_0)$ of CheZ wild-type cells is a straight line over the concentration range of interest, while $[Y_pZ](\beta k_0)$ of CheZ mutant cells is concave. The canonical model can yield such response curves. However, this scenario requires that in the CheZ mutant cells, some of the rate constants, such as the phosphatase activity, differ strongly from those in wild-type cells. This seems unlikely, but cannot be ruled out. Moreover, it is unclear whether according to this model, CheZ mutant cells will be able to chemotax, since the concentration of $CheY_p$in the adapted state is outside the working range of the motor.

3.6 Methods

The canonical model of the intracellular chemotaxis network of *E. coli* is given by the chemical reactions shown in Equations 3.1–3.3. When CheA and CheZ are colocalized at the receptor cluster, the concentration profiles of CheY and $CheY_p$ are uniform in space, and the concentrations can be obtained by solving the following chemical rate equations:

$$\frac{\partial[Y_p]}{\partial t} = k_3[A_pY] - k_4[Z][Y_p] + k_5[Y_pZ] \tag{3.7}$$

$$\frac{\partial[Y]}{\partial t} = k_6[Y_pZ] - k_1[A_p][Y] + k_2[A_pY] \tag{3.8}$$

$$\frac{\partial[A]}{\partial t} = k_3[A_pY] - \beta k_0[A] \tag{3.9}$$

$$\frac{\partial[A_p]}{\partial t} = \beta k_0[A] + k_2[A_pY] - k_1[A_p][Y] \tag{3.10}$$

$$\frac{\partial[A_pY]}{\partial t} = k_1[A_p][Y] - (k_2 + k_3)[A_pY] \tag{3.11}$$

$$\frac{\partial[Z]}{\partial t} = (k_5 + k_6)[Y_pZ] - k_4[Z][Y_p] \tag{3.12}$$

$$\frac{\partial[Y_pZ]}{\partial t} = k_4[Z][Y_p] - (k_5 + k_6)[Y_pZ] \tag{3.13}$$

Here, [X] denotes the concentration of species X.

When CheZ cannot bind the receptor cluster and thus diffuses in the cytoplasm, concentration gradients of CheY and $\mathrm{CheY_p}$ will form. We will assume that the cell is cylindrically symmetric, and we will integrate out the lateral dimensions y and z. We thus consider a simplified 1-D model, with concentrations as a function of x. This leads to the following reaction-diffusion equations:

$$\frac{\partial[\mathrm{Y_p}]}{\partial t} = D\frac{\partial^2[\mathrm{Y_p}]}{\partial x^2} + k_3[\mathrm{A_pY}]\delta(x) - k_4[\mathrm{Z}][\mathrm{Y_p}] + k_5[\mathrm{Y_pZ}] \tag{3.14}$$

$$\frac{\partial[\mathrm{Y}]}{\partial t} = D\frac{\partial^2[\mathrm{Y}]}{\partial x^2} + k_6[\mathrm{Y_pZ}] - k_1[\mathrm{A_p}][\mathrm{Y}]\delta(x) + k_2[\mathrm{A_pY}]\delta(x) \tag{3.15}$$

$$\frac{\partial[\mathrm{A}]}{\partial t} = k_3[\mathrm{A_pY}] - \beta k_0[\mathrm{A}] \tag{3.16}$$

$$\frac{\partial[\mathrm{A_p}]}{\partial t} = \beta k_0[\mathrm{A}] + k_2[\mathrm{A_pY}] - k_1[\mathrm{A_p}][\mathrm{Y}](0) \tag{3.17}$$

$$\frac{\partial[\mathrm{A_pY}]}{\partial t} = k_1[\mathrm{A_p}][\mathrm{Y}](0) - (k_2 + k_3)[\mathrm{A_pY}] \tag{3.18}$$

$$\frac{\partial[\mathrm{Z}]}{\partial t} = D\frac{\partial^2[\mathrm{Z}]}{\partial x^2} + (k_5 + k_6)[\mathrm{Y_pZ}] - k_4[\mathrm{Z}][\mathrm{Y_p}] \tag{3.19}$$

$$\frac{\partial[\mathrm{Y_pZ}]}{\partial t} = D\frac{\partial^2[\mathrm{Y_pZ}]}{\partial x^2} + k_4[\mathrm{Z}][\mathrm{Y_p}] - (k_5 + k_6)[\mathrm{Y_pZ}] \tag{3.20}$$

The components CheA, $\mathrm{CheA_p}$ and $\mathrm{CheA_pCheY}$ are localized at one end of the cell; the unit of their concentrations is the number of molecules per area. The other components diffuse in the cell. Their concentrations, which are in units of number of molecules per volume, depend upon the position x in the cell, where x measures the distance from the pole at which CheA, $\mathrm{CheA_p}$ and $\mathrm{CheA_pCheY}$ are localized; only in Equations 3.17 and 3.18 is the x dependence explicitly indicated to emphasize that the $\mathrm{CheA_p}$-CheY association rate depends on the concentration of CheY at contact. Zero-flux boundary conditions are imposed at both cell ends. The steady-state input-output relations of the network described by Equations 3.14–3.20 were obtained numerically by discretizing the system on a (1-D) grid and propagating these equations in space and time until steady state was reached.

Appendix: Mapping between canonical push-pull network and chemotaxis network

The commonly accepted model for the cytosolic signal transduction pathway in the *E. coli* chemotaxis system is given by Eqns. 3.1-3.3. The system is very similar to the canonical push-pull network, given by the following chemical reactions:

$$\mathrm{E_a} + \mathrm{X} \underset{k_2}{\overset{k_1}{\rightleftharpoons}} \mathrm{E_aX} \xrightarrow{k_3} \mathrm{E_a} + \mathrm{X^*} \tag{3.21}$$

$$\mathrm{E_d} + \mathrm{X^*} \underset{k_5}{\overset{k_4}{\rightleftharpoons}} \mathrm{E_dX^*} \xrightarrow{k_6} \mathrm{E_d} + \mathrm{X} \tag{3.22}$$

In steady state, a direct mapping is possible between both networks. This can be seen by comparing the chemical rate equations and the total concentrations for the two systems:

$$\underline{\text{Chemotaxis network}} \text{vs.} \underline{\text{Canonical push} - \text{pull network}}$$

$$\frac{\mathrm{d[Y]}}{\mathrm{dt}} = \mathrm{k_2[A_pY] + k_6[Y_pZ] - k_1[A_p][Y]} \Leftrightarrow \frac{\mathrm{d[X]}}{\mathrm{dt}} = \mathrm{k_2[E_aX] + k_6[E_dX^*] - k_1[E_a][X]}$$

$$\frac{\mathrm{d[Y_p]}}{\mathrm{dt}} = \mathrm{k_5[Y_pZ] + k_3[A_pY] - k_4[Z][Y_p]} \Leftrightarrow \frac{\mathrm{d[X^*]}}{\mathrm{dt}} = \mathrm{k_5[E_dX^*] + k_3[E_aX] - k_4[E_d][X^*]}$$

$$\frac{\mathrm{d[Y_pZ]}}{\mathrm{dt}} = \mathrm{k_4[Z][Y_p] - (k_5 + k_6)[Y_pZ]} \Leftrightarrow \frac{\mathrm{d[E_dX^*]}}{\mathrm{dt}} = \mathrm{k_4[E_d][X^*] - (k_5 + k_6)[E_dX^*]}$$

$$\frac{\mathrm{d[Z]}}{\mathrm{dt}} = -\frac{\mathrm{d[Y_pZ]}}{\mathrm{dt}} \Leftrightarrow \frac{\mathrm{d[E_d]}}{\mathrm{dt}} = -\frac{\mathrm{d[E_dX^*]}}{\mathrm{dt}}$$

$$\frac{\mathrm{d[A_pY]}}{\mathrm{dt}} = \mathrm{k_1[A_p][Y] - (k_2 + k_3)[A_pY]} \Leftrightarrow \frac{\mathrm{d[E_aX]}}{\mathrm{dt}} = \mathrm{k_1[E_a][X] - (k_2 + k_3)[E_aX]}$$

$$\frac{\mathrm{d[A_p]}}{\mathrm{dt}} = -\frac{\mathrm{d[A_pY]}}{\mathrm{dt}} - \frac{\mathrm{d[A]}}{\mathrm{dt}} \Leftrightarrow \frac{\mathrm{d[E_a]}}{\mathrm{dt}} = -\frac{\mathrm{d[E_aX]}}{\mathrm{dt}} \tag{3.23}$$

$$\frac{\mathrm{d[A]}}{\mathrm{dt}} = \mathrm{k_3[A_pY] - \beta k_0[A]} \tag{3.24}$$

$$\mathrm{[Y]_T = [Y] + [Y_p] + [Y_pZ] + [A_pY]} \Leftrightarrow \mathrm{[X]_T = [X] + [X^*] + [E_aX] + [E_dX^*]}$$

$$\mathrm{[Z]_T = [Z] + [Y_pZ]} \Leftrightarrow \mathrm{[E_d]_T = [E_d] + [E_dX^*]}$$

$$\mathrm{[A_p]_T = [A_p] + [A_pY] = [A]_T - [A]} \Leftrightarrow \mathrm{[E_a]_T = [E_a] + [E_aX]} \tag{3.25}$$

As $\frac{\mathrm{dA}}{\mathrm{dt}}$ in Eqn. 3.23 equals zero in steady state, it follows that the steady state of the chemotaxis model with total concentrations $\mathrm{[Y]_T}$, $\mathrm{[Z]_T}$ and $\mathrm{[A_p]_T}$ is identical to the steady state of a push-pull network with total concentrations $\mathrm{[X]_T}$, $\mathrm{[E_d]_T}$ and $\mathrm{[E_a]_T}$, respectively. The remaining concentration of unphosphorylated A is then $\mathrm{[A] = [A]_T - [A_p]_T}$ (Eqn. 3.25) and $\beta \mathrm{k_0}$ equals $k_3[\mathrm{A_pY}][\mathrm{A}]^{-1}$ (Eqn. 3.24). This mapping also holds for non-uniform networks with any spatial arrangement of the enzymes, e.g., with the activating enzyme localized at one end of the cell and the deactivating enzyme freely diffusive.

The commonly accepted chemotaxis model is thus simply a push-pull network of which the concentration of activating enzyme $\mathrm{[E_a]_T}$ is tuned via the parameter βk_0 while the concentration of deactivating enzyme $\mathrm{[E_d]_T}$ is kept constant. The steady state of a push-pull network with given substrate and enzyme concentrations is fully determined by the ratio of the catalytic activities k_3/k_6 and the Michaelis-Menten constants $K_{M,a} \equiv (k_2 + k_3)/k_1$ and $K_{M,d} \equiv (k_5 + k_6)/k_4$, as can be verified from the above system of equations. Therefore, the steady state of the chemotaxis model is fully determined by the same combination of parameters, together with $\beta \mathrm{k_0}$. In particular, we can, without loss of generality, set k_2 and k_5 equal to zero—they only affect the response via their effect on the Michaelis-Menten constants.

4 Differential affinity and catalytic activity of CheZ

We present a model of the chemotaxis network of Escherichia coli, in which a small fraction of the phosphatase is localized at the receptor cluster, while the remainder freely diffuses in the cytoplasm; moreover, the phosphatase at the cluster has a higher binding affinity for the messenger protein and a higher catalytic activity than the phosphatase in the cytoplasm. This model is consistent with a large body of experimental data and can explain many of the experimental observations of Vaknin and Berg. More generally, the combination of differential affinity and catalytic activity provides a generic mechanism for amplifying signals that could be exploited in other two-component signaling systems. We also argue that, as the linear relation between the measured FRET signal and the activity of the receptor cluster would break down in this scenario, recent modeling studies, which aim to explain the chemotactic gain in terms of the activity of the receptor cluster, should be reconsidered.

4.1 Introduction

In biology, it has long been believed that the intra- and extracellular information is encoded in the chemical and physical states of the components of the signal transduction pathway. However, it is now clear that the information can also be encoded in the concentration levels of the signalling components. The concentration levels of messenger proteins are typically controlled by the action of enzymes. In a wide class of systems, the activity of an activating enzyme is modulated via its interaction with receptor molecules, which respond to the extracellular signal. In these systems, the activity of the deactivating enzymes is often assumed to be constant. The canonical model of the chemotaxis network of *Escherichia coli*, as discussed in the previous chapter, is a prime example of such a system. Here, we present a model in which the activity of the deactivating enzyme is not constant, but depends upon the spatial position of the deactivating enzyme within the cell. We show that this spatial dependence of enzymatic activity can markedly enhance the sharpness of the response.

In the previous chapter, we argued that the commonly accepted model of the chemotaxis system of *E. coli* cannot explain the recent experimental observations of Vaknin and Berg [35]. This canonical model is based upon the observation that in wild-type cells CheZ is active at the receptor cluster. However, we argue that a close examination of the data of Vaknin and Berg reveals that a large fraction of CheZ is still present in the cytoplasm. Moreover, this and other data suggest that the activity of CheZ that is

distributed in the cytoplasm differs from that of CheZ that is localized at the receptor cluster.

In this chapter, we present a refined model of the intracellular chemotaxis network of *E. coli*. The key ingredients of this model are: 1) in wild-type cells, a small, yet significant, fraction of CheZ is bound to the receptor cluster, while the remainder freely diffuses in the cytoplasm [35]; 2) the fraction of CheZ at the cluster has a higher binding affinity for the substrate CheY than that of cytosolic CheZ; 3) also the catalytic activity of CheZ bound to the cluster is higher than that of CheZ in the cytoplasm [36]. This model bears similarities to that recently proposed by Lipkow [74], although our model neither requires oligomerization of CheZ at the receptor cluster nor shuttling of CheZ between the cytoplasm and the receptor cluster. In the section 4.2 we show using a simplified model how the combination of differential binding affinity and differential catalytic activity provides a novel mechanism for amplifying signals: As the activity of the receptor cluster and hence that of the kinase CheA is increased from zero and CheY becomes phosphorylated, $CheY_p$ first binds CheZ at the receptor cluster; only when CheZ at the receptor cluster is saturated, does $CheY_p$ bind CheZ in the cytoplasm; since CheZ at the cluster has a higher catalytic activity than CheZ in the cytoplasm, the response of $CheY_p$ is sigmoidal. In the section 4.3 we present a more detailed model, which also takes into account cooperative binding of $CheY_p$ to CheZ [75, 76]. We show that this model can explain the response of *E. coli* to changes in serine concentration, as measured by Vaknin and Berg [35].

4.2 Differential affinity and catalytic activity of CheZ

The analysis in the previous chapter suggests that the commonly accepted model of the intracellular signaling pathway is incomplete. Also other experimental observations, discussed below, suggest that this network is more intricate. Based on these observations, we present a refined model of the intracellular chemotaxis network of *E. coli*.

The Model The key ingredients of our model are:

1. *In wild-type cells, a small fraction of CheZ, of 10-20%, is bound to the receptor cluster, while the remainder diffuses freely through the cytoplasm.* Figure 2b of Vaknin and Berg [35] shows the cyan signal, coming from CFP fused to CheZ, *after the addition of attractant*. This signal represents the spatial distribution of CheZ. The figure suggests that about 10-20% of CheZ is bound to the receptor cluster, with the remainder more or less homogeneously distributed in the cytoplasm. This estimate is consistent with that based on the known chemistry of CheZ binding to the receptor cluster. CheZ can be localized to the receptor cluster via binding to CheA, which is part of the receptor cluster. CheA exists in two forms, $CheA_s$ and $CheA_L$, which can form the following dimers: $CheA_LCheA_L$, $CheA_LCheA_s$, and $CheA_sCheA_s$. The first two, $CheA_LCheA_L$and $CheA_LCheA_s$, have catalytic activity and can transfer phosphoryl groups to CheY [77, 78, 79, 80]; the third, the homodimer $CheA_sCheA_s$, does not have catalytic activity, but can bind CheZ. Experiments have shown that CheZ binds selectively to $CheA_s$ [81, 36, 82]; in fact, as Lipkow [74] argued, the experiments of [36] suggest that CheZ predominantly binds the $CheA_sCheA_s$ homodimer, and not the $CheA_LCheA_s$ heterodimer. Following Lipkow [74], we estimate that the number of $CheA_sCheA_s$ homodimers is

about 360, while the number of CheZ dimers is about 1600 [83]. If we assume that each of the $CheA_sCheA_s$ homodimers strongly binds one CheZ dimer, we arrive at the estimate that about 20% of the CheZ dimers is bound to the cluster, consistent with the estimate based on the FRET data of Vaknin and Berg [35].

2. *In wild-type cells, $CheY_p$ has a much higher affinity for CheZ bound to $CheA_s$ than for CheZ freely diffusing in the cytoplasm.* Figure 3a of Vaknin and Berg [35] shows that in wild-type cells in their adapted state, the total amount of $[Y_pZ]$ in the cytoplasm roughly equals that of $[Y_pZ]$ at the receptor cluster; yet, as mentioned above, Figure 2b of Ref. [35] shows that the total amount of CheZ at the cluster is about 10-20% of that in the cytoplasm; this strongly suggests that CheZ bound to $CheA_s$ at the receptor cluster has a higher affinity for $CheY_p$ than CheZ in the cytoplasm. We conjecture that the affinity between $CheY_p$ and CheZ at the cluster is higher, because of the close physical proximity between CheA, where CheY is phosphorylated, and cluster-bound CheZ: a CheY molecule that has just been phosphorylated by a $CheA_p$ dimer at the cluster, can very rapidly bind cluster-bound CheZ, leading to a higher association rate.
3. *In wild-type cells, CheZ bound to $CheA_s$ at the receptor cluster has a higher phosphatase activity than CheZ in the cytoplasm.* The experiments of Wang and Matsumura [36] suggest that the interaction of CheZ with $CheA_s$ enhances its dephosphorylating activity.
4. *In CheZ mutant cells, CheZ cannot bind to $CheA_s$ at the cluster. CheZ in these cells has the same phosphatase activity and the same binding affinity for $CheY_p$ as CheZ in wild-type cells that is not bound to $CheA_s$ at the cluster.* As crystallographic data [84] and mutagenesis data [81, 74] suggest, we assume that in the CheZ mutant proteins only the domain that allows CheZ to interact with $CheA_s$ is affected; the part that allows CheZ to interact with $CheY_p$ is thus assumed to be unaffected in these mutants.

The canonical model, described in the previous chapter, is given by the reactions:

$$A \xrightarrow{\beta k_0} A_p \tag{4.1}$$

$$A_p + Y \underset{k_2}{\overset{k_1}{\rightleftharpoons}} A_pY \xrightarrow{k_3} A + Y_p \tag{4.2}$$

$$Y_p + Z \underset{k_5}{\overset{k_4}{\rightleftharpoons}} Y_pZ \xrightarrow{k_6} Y + Z \tag{4.3}$$

The model proposed here is described by this set of reactions, but includes the additional reactions:

$$Y_p + Z_b \underset{k_8}{\overset{k_7}{\rightleftharpoons}} Y_pZ_b \xrightarrow{k_9} Y + Z_b \tag{4.4}$$

Here, the total concentration of localized CheZ, $[Z_b]_T = [Z_b] + [Y_pZ_b]$, is low as compared to the total concentration of CheZ, $[Z]_T$. Furthermore, the association rate k_7 and the catalytic activity k_9 of localized CheZ, are high as compared to the corresponding rates k_4 and k_6 for diffusive CheZ. As we will show below, the critical parameters of this model are the fraction of CheZ bound to $CheA_s$ at the receptor cluster, the ratio of the association rates $k_7 : k_4$ and the ratio of the catalytic activities $k_9 : k_6$.

The model presented here is similar to that of Lipkow [74] in that both assume that part of CheZ can bind the cluster. However, the models also differ in two important aspects: 1) in the model of Lipkow [74], the binding of CheZ to $CheA_s$ is conditional on the binding of CheZ to $CheY_p$; consequently, while in our model the bound fraction of CheZ is fairly constant in time, in the model of Lipkow [74] the amount of CheZ bound to the cluster depends upon the current stimulus level: for instance, in her model, after the removal of attractant, CheZ moves from the cytoplasm to the cluster upon binding of $CheY_p$; 2) in the model of Lipkow [74], the binding of one $CheY_pCheZ$ molecule to a $CheA_s$ homodimer, can nucleate the formation of oligomers of $CheY_pCheZ$ at the cluster. The chemotaxis pathway of *E. coli* might exhibit CheZ oligomerisation and shuttling of CheZ between the cytoplasm and the cluster. However, our calculations reveal that this is not necessary; the conditions listed above, are both necessary and sufficient to explain the FRET data of Vaknin and Berg [35]. Moreover, the relative simplicity of our model makes it possible to elucidate the mechanism by which differential enzyme-substrate binding affinity and differential catalytic activity can sharpen the response curve.

Figures 4.1–4.3 show how the total amount of $CheY_pCheZ$ and $CheY_p$ is affected by varying the critical parameters in this model: the fraction of CheZ bound to the cluster (Figure 4.1), the rate k_7 at which $CheY_p$ associates with CheZ at the cluster (Figure 4.2), and the catalytic rate k_9 of CheZ at the cluster (Figure 4.3); the baseline parameters are given in Fig. 4.1. In all figures, the solid black line corresponds to CheZ mutant cells; the solid grey line corresponds to CheZ wild-type cells with the baseline parameter set; the dashed and dotted lines correspond to the results of the CheZ wild-type cells, where the parameter of interest is either increased or decreased (see caption for parameter values). The black and grey symbols correspond to the experimental results of Vaknin and Berg [35], as described in section 3.2 (*Decomposing the response*); the value of α was, somewhat arbitrarily, taken to be $\alpha = 0.65$, which means that $[Y_pZ](\beta k_0)$ is sigmoidal for CheZ wild-type cells and hyperbolic for CheZ mutant cells. The origin of the hyperbolic curve of the CheZ mutant cells is similar to that which underlies the response curves of the commonly accepted model: $[Y_pZ] \propto \beta k_0[A]$, where initially, as βk_0 increases from zero, $[A] \approx [A]_T$ is constant but then decreases as $[A_p]$ increases significantly (see section 3.3 (*Original Model*)). We will now discuss the origin of the sigmoidal curves of $[Y_pZ](\beta k_0)$ of the wild-type cells.

Figures 4.1–4.3 show that the response curves of $[Y_pZ](\beta k_0)$ of CheZ cells effectively consist of two parts, corresponding to the binding of $CheY_p$ to cluster-bound CheZ and freely diffusive CheZ, respectively. When βk_0 is low, a CheY molecule that has just been phosphorylated by a CheA dimer at the cluster, will most likely bind a CheZ dimer that is bound to the cluster because of the close physical proximity between CheA and cluster-bound CheZ; this is modeled by imposing a higher association rate between $CheY_p$ and cluster-bound CheZ, as compared to that between $CheY_p$ and freely diffusive CheZ: $k_7 > k_4$. Since cluster bound CheZ has a high phosphatase activity, the concentration of $CheY_p$ and hence $CheY_pCheZ$ will initially increase only slowly with βk_0. Nevertheless, at some point CheZ at the cluster will become saturated with $CheY_p$. When βk_0 is then increased further, a phosphorylated CheY molecule can no longer bind a cluster-bound CheZ dimer. It will then diffuse into the cytoplasm, where it can bind freely diffusive CheZ. Since the catalytic activity of CheZ in the cytoplasm is lower than that of CheZ bound to $CheA_s$ at the cluster, $[Y_pZ]$ and $[Y_p]$ will now quickly rise. This combination of

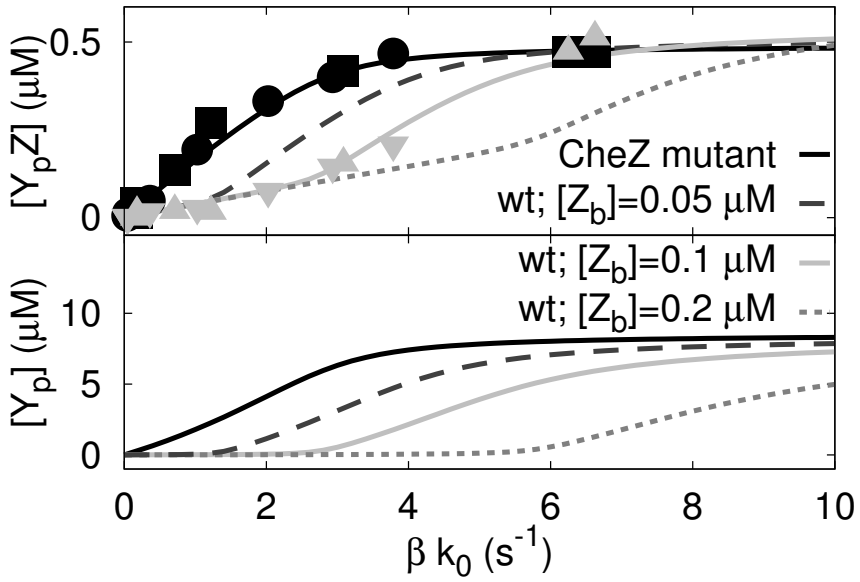

FIGURE 4.1 The effect of the total amount of CheZ that is bound to the cluster, as given by $[Z_b]_T$, on the response of $[Y_pZ]$ (FRET) and $[Y_p]$ in the differential affinity-and-catalytic-activity model (Equations 4.1-4.3 and Equation 4.4). The solid black line corresponds to the prediction of our model for CheZ mutant cells, while the solid grey line corresponds to the model prediction for wild-type cells, in which $[Z_b]_T = 0.1\mu$M. The dashed and dotted lines correspond to the model prediction for wild-type cells with $[Z_b]_T = 0.05\mu$M and 0.2μM, respectively. The symbols correspond to the experimental data of Vaknin and Berg [35]. The circles correspond to CheZ mutant cells with CheR and CheB, the squares correspond to CheZ mutant cells without CheR and CheB, the triangles correspond to wild-type cells and the inverted triangles correspond to wild-type cells without CheR and CheB. Since the affinity of $CheY_p$ for CheZ that is bound to the cluster, $CheZ_b$, is much higher than that for CheZ that freely diffuses in the cytoplasm, $CheY_p$ first binds CheZ that is bound to the receptor cluster, $CheZ_b$; only when $CheZ_b$ is essentially saturated, does $CheY_p$ bind freely diffusive CheZ. As $[Z_b]_T$ is increased, the inflection point separating the first from the second regime shifts to higher values of βk_0 and to higher values of $[Y_pZ]$—to a good approximation, at this point $[Y_pZ] \approx [Z_b]_T$. The baseline parameters are: $k_1 = 3 \cdot 10^6$ $M^{-1}s^{-1}$, $k_3 = 750$ s^{-1}, $k_4 = 3 \cdot 10^6$ $M^{-1}s^{-1}$, $k_6 = 30$ s^{-1}, $k_7 = 3 \cdot 10^9$ $M^{-1}s^{-1}$, $k_9 = 130$ s^{-1}, $[Y]_T = 17.9$ μM, $[Z]_T = 1$ μM, $[Z_b] = 0.1$ μM and $[A]_T = 5$ μM (for parameter values, see [85, 45]). The diffusion coefficient of all cytosolic components is 5 $\mu m^2 s^{-1}$; all enzyme-substrate dissociation rates were set to zero.

differential affinity and differential catalytic activity thus provides a generic mechanism for enhancing the sharpness of the response.

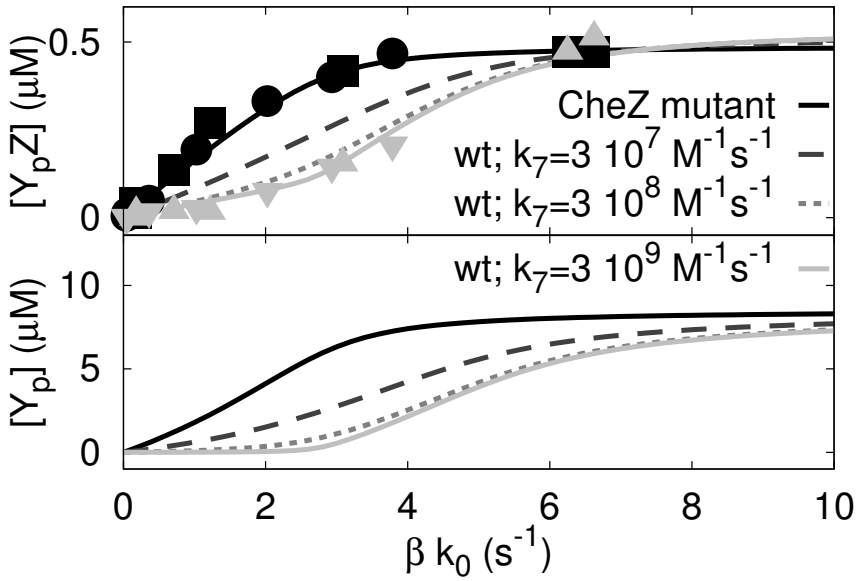

FIGURE 4.2 The effect of the rate of association between $CheY_p$ and CheZ bound to the receptor cluster, k_7, on the response of $[Y_pZ]$ and $[Y_pZ]$ in the differential-affinity-and-catalytic-activity model (Equations 4.1-4.3 and Equation 4.4). The solid black line and black symbols corresponds to the CheZ mutant cells (see also Figure 4.1), while the solid grey line and grey symbols correspond to wild-type cells, in which $k_7 = 3 \cdot 10^9 \mathrm{M}^{-1}\mathrm{s}^{-1}$; the dashed and dotted lines correspond to wild-type cells with $k_7 = 3 \cdot 10^7$ and $k_7 = 3 \cdot 10^8 \mathrm{M}^{-1}\mathrm{s}^{-1}$, respectively. Please note that as k_7 is lowered, the distinction between the two regimes becomes less sharp, because more $CheY_p$ molecules diffuse into the cytoplasm before they will bind CheZ molecules. For parameter values, see the caption of Figure 4.2.

We can now understand the effect of varying the critical parameters in this model. As the fraction of CheZ that is bound to the cluster increases (from dashed to solid grey to dotted in Figure 4.1), the amount of $CheY_p$ needed to saturate cluster-bound CheZ increases, leading to a shift of the inflection point in $[Y_pZ](\beta k_0)$ to higher values of βk_0. However, while increasing the fraction of cluster-bound CheZ shifts the inflection point to higher values of βk_0, it does not significantly change the initial slope of $[Y_pZ](\beta k_0)$, nor does it change the slope $[Y_pZ](\beta k_0)$ after the inflection point: these slopes are determined by the catalytic activities of cluster-bound CheZ and freely diffusive CheZ, k_9 and k_6, respectively. This can be seen in Figure 4.3: as the catalytic activity of k_9 is increased (from dotted to solid grey to dashed), the initial slope of $[Y_pZ](\beta k_0)$ decreases. Please also note that since the slope of $[Y_pZ](\beta k_0)$ after the inflection point is determined by parameters of freely diffusive CheZ, it is similar to the initial slope of $[Y_pZ](\beta k_0)$ of the CheZ mutant cells, which indeed only contain freely diffusive CheZ. Figure 4.2 illustrates the importance of the association rate. As the rate of association between $CheY_p$ and cluster-bound CheZ decreases (from solid grey to dotted to dashed), the response curve $[Y_pZ](\beta k_0)$ of CheZ cells moves towards that of the CheZ mutant cells. The reason is

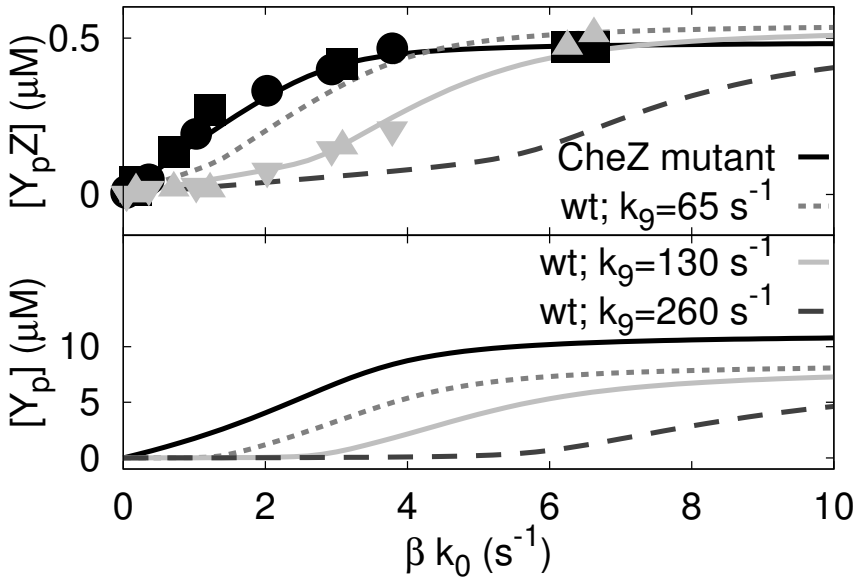

FIGURE 4.3 The effect of the catalytic rate of CheZ bound to the receptor cluster, k_9, on the response of $[Y_pZ]$ and $[Y_p]$ in the differential-affinity-and-catalytic-activity model (Equations 4.1-4.3 and Equation 4.4). The solid black line and black symbols corresponds to the CheZ mutant cells (see also Figure 4.1), while the solid grey line and grey symbols correspond to wild-type cells, in which $k_9 = 130\text{s}^{-1}$; the dotted and dashed lines correspond to wild-type cells with $k_9 = 65$ and $k_9 = 260$ s^{-1}, respectively. Please note that as k_9 is increased, the initial slope of $[Y_pZ](\beta k_0)$ of wild-type cells, which is inversely proportional to k_9, is decreased; the slope of the second regime is, to a good approximation, inversely proportional to the catalytic activity of freely diffusive CheZ, k_6, and thus fairly constant. Please also note that since the height of the inflection point is given by $[Y_pZ] \approx [Z_b]_T$ and thus independent of k_9, the inflection point shifts to higher values of βk_0 with increasing k_9.

that as the rate of association between $CheY_p$ and cluster-bound CheZ is lowered, it becomes more likely that a phosphorylated CheY molecule diffuses into the cytoplasm, where it will be dephosphorylated by freely diffusive CheZ with a lower catalytic activity.

The refined model is able to explain the measured difference between the response curves for the CheZ mutant cells and the CheZ wild-type cells. However, while the response curves of Vaknin and Berg [35] can be reproduced by the model, this is not the only constraint. As discussed above, both wild-type and CheZ mutant cells should be able to chemotax [73]. This means that the model should give $CheY_p$ concentrations between 1 and 5 μM for both strains in the adapted state [45]. As can be seen from the fit used in Figures 4.1-4.3, in the CheZ mutant, the $CheY_p$ concentration is 8 μM in the adapted state, which is well outside this range.

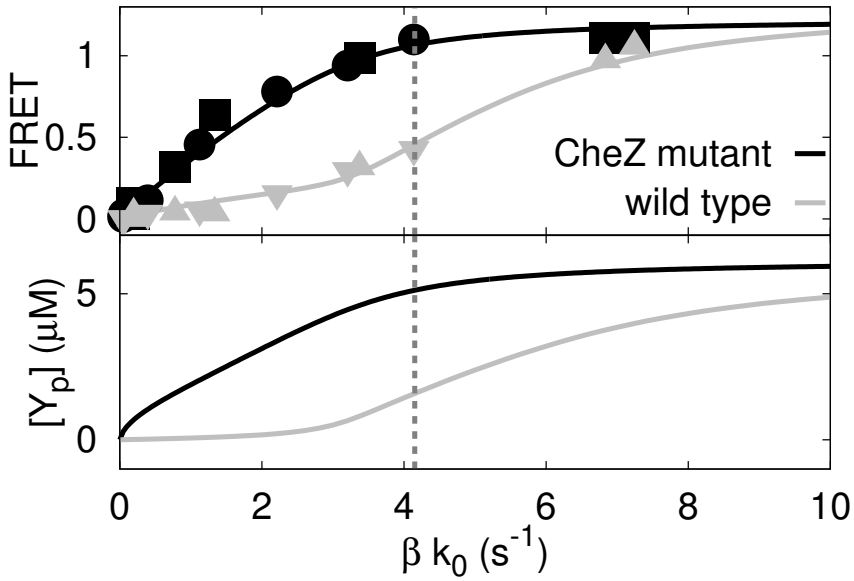

FIGURE 4.4 FRET vs. βk_0 and $[Y_p]$ vs. βk_0 for the best fit of the full differential-affinity-and-catalytic activity model, which includes cooperativity in CheZ (Equations 4.1-4.3, and Equations 4.4, 4.5 and 4.8). The FRET signal is assumed to be proportional to $[Y_pZ]+2\,[(Y_p)_2Z]+[Y_pZ_b]+2[(Y_p)_2Z_b]$; the value of $\alpha = 0.75$ (see Fig. 3.3). The dotted vertical line denotes the value of βk_0 in the adapted state. The parameter values are $k_1 = 3 \cdot 10^6\ \mathrm{M^{-1}s^{-1}}$, $k_3 = 750\ \mathrm{s^{-1}}$, $k_4 = 3.6 \cdot 10^5\ \mathrm{M^{-1}s^{-1}}$, $k_6 = 7.5\ \mathrm{s^{-1}}$, $k_7 = 6 \cdot 10^8\ \mathrm{M^{-1}s^{-1}}$, $k_9 = 40\ \mathrm{s^{-1}}$, $k_{10} = 3 \cdot 10^7\ \mathrm{M^{-1}s^{-1}}$, $k_{12} = 30\ \mathrm{s^{-1}}$, $k_{13} = 9 \cdot 10^8\ \mathrm{M^{-1}s^{-1}}$, $k_{15} = 160\ \mathrm{s^{-1}}$; $[Y]_T = 17.9\ \mu$M, $[Z]_T = 1\ \mu$M, $[Z_b]_T = 0.1\ \mu$M and $[A]_T = 5\ \mu$M (for parameter values, see [76, 85, 45]). The diffusion coefficient of all cytosolic components is set to $5\ \mu\mathrm{m^2s^{-1}}$; all enzyme-substrate dissociation rates are zero.

4.3 The effect of cooperativity

In the models presented so far, the phosphatase reactions were described by simple Michaelis-Menten reaction kinetics. Experiments by Eisenbach and coworkers, however, show that the activity of CheZ depends in a cooperative manner on the $CheY_p$ and CheZ concentration [75, 76]. As the activity of the receptor cluster, βk_0, is changed, the concentration of $[Y_p]$ changes, but not the total concentration of CheZ, $[Z]_T$. It is thus important to understand how the response curve $[Y_pZ](\beta k_0)$ is affected by the cooperative dependence of phosphatase activity on $CheY_p$ concentration. In this section, we present a simple model for the cooperative dependence of the phosphatase activity on $CheY_p$ concentration, which can be solved analytically.

The model is based upon the following assumptions: 1) a single CheZ dimer can bind up to two $CheY_p$ molecules; 2) CheZ can dephosphorylate $CheY_p$ in both $CheY_p$-bound states, thus dephosphorylation can occur when only a single $CheY_p$ molecule is bound or when two $CheY_p$ molecules are bound. This model can be described by two

coupled Michaelis-Menten reactions. For CheZ in the cytoplasm, the dephosphorylation reactions are given by Equation 4.3 in combination with the reactions

$$\mathrm{Y_pZ} + \mathrm{Y_p} \underset{k_{11}}{\overset{k_{10}}{\rightleftharpoons}} (\mathrm{Y_p})_2\mathrm{Z} \overset{k_{12}}{\rightarrow} \mathrm{Y} + \mathrm{Y_pZ} \tag{4.5}$$

Cooperativity arises when 3) the binding of the first substrate molecule facilitates the binding of the second one; 4) the catalytic activity is higher when two substrate molecules are bound than when one is bound. This can be shown mathematically. In steady state, the phosphatase activity is given by

$$\frac{d[\mathrm{Y}]}{dt} = \frac{[\mathrm{Z}]_\mathrm{T}[\mathrm{Y_p}](k_6 + k_{12}[\mathrm{Y_p}]/K_{\mathrm{M},2})}{K_{\mathrm{M},1} + [\mathrm{Y_p}] + [\mathrm{Y_p}]^2/K_{\mathrm{M},2}}, \tag{4.6}$$

where $[\mathrm{Z}]_\mathrm{T}$ is the total concentration of CheZ and $K_{\mathrm{M},1} = (k_5 + k_6)/k_4$ and $K_{\mathrm{M},2} = (k_{11} + k_{12})/k_{10}$ are the Michaelis-Menten constants of Equation 4.3 and Equation 4.5, respectively (see *Appendix A* for a derivation). It can be seen that if $k_{12} \gg k_6$ and if $K_{\mathrm{M},1} \gg K_{\mathrm{M},2}$, the desphosphorylation rate is given by

$$\frac{d[\mathrm{Y}]}{dt} = \frac{k_{12}[\mathrm{Z}]_\mathrm{T}[\mathrm{Y_p}]^2}{K_{\mathrm{M},1}K_{M,2} + [\mathrm{Y_p}]^2}. \tag{4.7}$$

This is a Hill function with a Hill coefficient of 2 and a concentration at which the rate is half maximal (the inflection point) given by $K_\mathrm{M}^\mathrm{eff} = \sqrt{K_{\mathrm{M},1}K_{\mathrm{M},2}}$. In *Appendix A* we give an extended analysis of this model, which shows that it can fit the *in vitro* data of Blat and Eisenbach [76] not only qualitatively, but also quantitatively. We nevertheless would like to emphasize that the rate constants derived from this fit to the *in vitro* data should be interpreted with care, since they might differ from the *in vivo* values. In particular, diffusion-limited rates will often be lower in living cells due to a lower diffusion constant, and a detailed analysis of this model (see *Appendix A*) suggests that in this system this might be the case.

The reaction scheme described by Equations 4.1-4.3 and 4.5 describes the activity of cytosolic CheZ. The corresponding rate equations for localized CheZ are given by

$$\mathrm{Y_pZ_b} + \mathrm{Y_p} \underset{k_{14}}{\overset{k_{13}}{\rightleftharpoons}} (\mathrm{Y_p})_2\mathrm{Z_b} \overset{k_{15}}{\rightarrow} \mathrm{Y} + \mathrm{Y_pZ_b} \tag{4.8}$$

in combination with Equation 4.4. Like in the differential affinity model of the previous section, we assume that both the affinity to $\mathrm{CheY_p}$ and the phosphatase activity of CheZ are enhanced when CheZ is localized to $\mathrm{CheA_s}$ at the receptor cluster. This means that the association rates k_7 and k_{13} are much larger than the corresponding association rates for cytosolic CheZ, and that the catalytic activity k_{15} is larger than the catalytic activity k_{12} for cytosolic CheZ.

Figure 4.4 shows $[\mathrm{Y_pZ}](\beta k_0)$ and $[\mathrm{Y_p}](\beta k_0)$ for CheZ wild-type cells and CheZ mutant cells [35]. In combination with a response curve for βk_0 vs. [Serine] with $\alpha = 0.75$, the four dose-response curves in Figs. 5a and 5c of [35] are reproduced. Comparing Figure 4.4 with Figs. 4.1–4.3 of the simplified differential-affinity-and-activity model shows that the cooperative dependence of the phosphatase activity on $\mathrm{CheY_p}$ concentration does not dramatically affect the dose-response curves, a conclusion that was also reached by Sourjik and Berg [45]. As before, $[\mathrm{Y_pZ}](\beta)$ is in agreement with experiment, both for CheZ wild-type and CheZ mutant cells. Moreover, the $[\mathrm{Y_p}](\beta k_0)$ response curve of

the CheZ wild-type cells agrees with experiment in the sense that the concentration of $CheY_p$ equals 2μ M in the adapted state, which is within the working range of the motor. The concentration of $CheY_p$ in the CheZ mutant cells in their adapted state is around 5μM, which is lower than that in the simplified differential-affinitiy-and-activity model, but still at the high end of the working range of the motor.

4.4 Discussion

We have presented a new model that can explain the experimental results of Vaknin and Berg [35]. In this model, $[Y_pZ](\beta k_0)$ of CheZ wild-type cells is sigmoidal, while $[Y_pZ](\beta k_0)$ of CheZ mutant cells is hyperbolic. The model relies on the assumption that a small fraction of CheZ is localized at the receptor cluster, while the remainder freely diffuses in the cytoplasm; moreover, it assumes that CheZ localized at the receptor cluster has both a higher binding affinity for $CheY_p$ and a higher catalytic activity than CheZ in the cytoplasm. All these assumptions seem to be supported by experiment [35, 36, 74].

In essence, the model that we propose consists of a push-pull network with one activating enzyme, CheA, and two deactivating enzymes, CheZ bound to the cluster and CheZ that freely diffuses in the cytoplasm. Our analysis shows that the competition between these two deactivating enzymes for binding and deactivating the substrate can yield an ultrasensitive response even when the push-pull network does not operate in the zero-order regime. In fact, this mechanism of differential-affinity-and-catalytic-activity is evocative of the "branch point effect", in which the interdependence of the activities of two branch-point enzymes that compete for a common substrate can yield an abrupt change in the flux through one of the enzymes [86]. In essence, in the model proposed here the two fractions of CheZ give rise to two different types of deactivating enzymes. Indeed, the spatial dependence of the activity of CheZ only acts to create two types of deactivating enzymes; the proposed could also work in a well-stirred model if one assumes that there exist two types of deactivating enzymes.

If the response function $[Y_pZ](\beta k_0)$ of wild-type cells is sigmoidal, and not a straight line as the canonical model of the intracellular chemotaxis network predicts, then the large number of recent studies on signal amplification by the receptor cluster has to be reconsidered [23, 1, 26, 24, 87, 30, 31, 88, 89]. If the relation between $[Y_pZ]$ and βk_0 would be linear as the commonly accepted model predicts, then the renormalized FRET response would be given by the dependence of the activity of the receptor cluster, βk_0, on the ligand concentration [L]. This would justify the studies that describe the 'front end' amplification of the chemotaxis network, namely the response of [YpZ] to changes in [L], in terms of the signal amplification properties of the receptor cluster [23, 1, 26, 24, 87, 30, 31, 88, 89]. However, if the dependence of $[Y_pZ]$ on the activity of the receptor cluster, βk_0, would not be linear, then the front end amplification would not be fully determined by the response of the receptor cluster to changes in the ligand concentration. Indeed, to explain the front-end gain, the extent to which the signal is amplified as it is transmitted from the receptor cluster to YpZ would then also have to be taken into account.

While the model presented here can describe the dose-response curves as reported by Vaknin and Berg [35], a number of issues remain. The first is that in the full differential-affinity-and-catalytic-activity model, which takes into account CheZ cooperativity, the *total* concentration of $[Y_p]$ in adapted CheZ mutant cells is on the border of the working range of the motor, while experiments on mutant cells lacking $CheA_s$, which localizes CheZ to the receptor cluster [73], suggest that CheZ mutant cells can chemotax. This raises an interesting question, which to our knowledge has not been studied yet: How strongly does the efficiency of chemotaxis depend upon the concentration of $CheY_p$ in the adapted state? In particular, how well must that be inside the working range of the motor? It is conceivable that cells with $[Y_p]$ at the high end of the motor's working range can chemotax, albeit less efficiently. Another possibility is that CheZ mutant cells can chemotax, because $[Y_p]$ forms spatial gradients inside CheZ mutant cells [35]: while $[Y_p]$ at some motors will be outside the motor's working range, $[Y_p]$ at other motors might be inside the working range of the motor.

But perhaps the most likely explanation is that $CheY_p$ provides a negative feedback loop on the activity of the receptor cluster via CheB and $CheA_p$. The concentration of $CheY_p$ in the adapted state is determined by the activity of the receptor cluster in the adapted state, which is controlled by the activity of the methylation and demethylation enzymes CheR and CheB, respectively. We have assumed that there is no feedback from the concentration of $CheY_p$ onto the activity of these enzymes and hence no feedback on the activity of the receptor cluster, βk_0. Accordingly, in our model, βk_0 in the adapted state, $\beta k_0^{\text{adapted}}$, is the same for CheZ wild-type cells and CheZ mutant cells. However, $CheA_p$ cannot only phosphorylate CheY, but also CheB: CheY and CheB thus compete with one another for phosphorylation by $CheA_p$ [68]. Moreover, phosphorylated CheB has a higher demethylation activity than unphosphorylated CheB. Hence, as $[Y_p]$ increases and [Y] decreases, $[CheB_p]$ increases. This decreases the activity of the receptor cluster, βk_0, which in turn tends to decrease $[Y_p]$. As a result of this negative feedback loop, it is conceivable that $[Y_p]$ in the CheZ mutant cells is lower than that predicted by our model assumptions, and hence within the motor's range.

Vaknin and Berg measured not only the response to the addition to serine, but also the response of $CheY_pCheZ$ to changes in aspartate concentration [35]. They found differences in the response between CheZ wild-type cells and CheZ mutant cells when α-methylaspartate was used as an attractant with $CheR^-CheB^-$ cells expressing *only* the aspartate receptor, Tar. However, no differences were detected when these experiments were repeated with either aspartate or α-methylaspartate in wild-type cells. In our model, the overall response of $[Y_pZ]$ to changes in ligand concentration [L] is determined by two independent modules connected in series: $[Y_pZ](\beta k_0([L]))$. A different attractant only leads to a different response of the receptor cluster, $\beta k_0([L])$: the response of $[Y_pZ](\beta k_0)$ to changes in the activity of the receptor cluster βk_0 is assumed to be independent of the type of attractant—while $[Y_pZ](\beta k_0)$ depends upon the nature of CheZ, it is the same for serine and aspartate. Our model would therefore predict that the response to aspartate also differs between CheZ wild-type cells and CheZ mutant cells, in contradiction with the experimental results of Vaknin and Berg [35]. It is conceivable that to explain these observations, the spatial organisation of the receptor

cluster, in particular the spatial position of CheZ with respect to the aspartate and serine receptors, has to be taken into account, and that a full particle-based model [90, 91] is required to explain the response to both aspartate and serine.

Lastly, could our predictions be tested experimentally? Our model yields a clear prediction for the relation between the concentration of $\mathrm{CheY_p}$ and that of $\mathrm{CheY_p}$ bound to CheZ; in our model $[\mathrm{Y_p}]$ as a function of $[\mathrm{Y_pZ}]$ deviates strongly from the functional dependence as given by simple Michaelis-Menten kinetics. By simultaneously measuring the interaction between $[\mathrm{Y_p}]$ and CheZ using one FRET pair, and the interaction between $[\mathrm{Y_p}]$ and the FliM proteins of the rotary motors using another FRET pair, it might be possible to extract the relation between the concentration of $\mathrm{CheY_p}$ and $\mathrm{CheY_pCheZ}$.

4.5 Methods

The reaction-diffusion equations for the models described here are solved in the manner analogous to that described in the previous chapter.

Appendix A Cooperativity in the phosphatase reaction

Cooperativity in the dephosphorylation of $\mathrm{CheY_p}$ by CheZ was first shown by Blat et al. [75]. A quantitative study of the cooperativity in $\mathrm{CheY_p}$ dephosphorylation was presented in [76]. In this section we discuss a model of CheZ activity that can describe the experimental data of Blat et al. [76]. We will show that this model can accurately reproduce the experimental data of Eisenbach *et al.*, although, as we will discuss, it seems likely that some of the rate constants obtained might differ from those *in vivo*. We also note here for clarity that since the experiments were performed *in vitro* and no CheAs was present, the results apply to dephosphorylation of $\mathrm{CheY_p}$ by diffusive CheZ and not to CheZ localized at the receptor cluster.

The model for the phosphatase activity is given by Equations 4.2–4.3. Together with the phosphorylation reaction of CheY, this yields the following model for the experimental setup of Ref. [76]:

$$\mathrm{Y} \overset{\mathrm{AcP}}{\rightarrow} \mathrm{Y_p} \tag{4.9}$$

$$\mathrm{Y_p} + \mathrm{Z} \underset{k_5}{\overset{k_4}{\rightleftharpoons}} \mathrm{Y_pZ} \overset{k_6}{\rightarrow} \mathrm{Y} + \mathrm{Z} \tag{4.10}$$

$$\mathrm{Y_pZ} + \mathrm{Y_p} \underset{k_{11}}{\overset{k_{10}}{\rightleftharpoons}} (\mathrm{Y_p})_2\mathrm{Z} \overset{k_{12}}{\rightarrow} \mathrm{Y} + \mathrm{Y_pZ} \tag{4.11}$$

Here, the first reaction describes the phosphorylation reaction in the *in vitro* experimental setup of Eisenbach *et al.* [76], in which CheY is continuously phosphorylated by acetyl phosphate AcP. Please note that Z corresponds to one CheZ *dimer*.

Figure 1c in [76] shows the results on the kinetics of CheY dephosphorylation by CheZ. $\mathrm{CheY_p}$, in the presence of acetyl phosphate, was instantaneously mixed with a small amount of CheZ. The total concentration $[\mathrm{CheY}]_\mathrm{T}$ was 5 μM and the concentration of CheZ dimers was 0.1 μM–much lower than in a living cell. The rate of phosphorylation of CheY by AcP was also low, 0.207 s^{-1} [76]. Four relevant quantities can be extracted from the phosphorylation kinetics in Fig. 1c of [76], i) the time duration of the delay, ii)

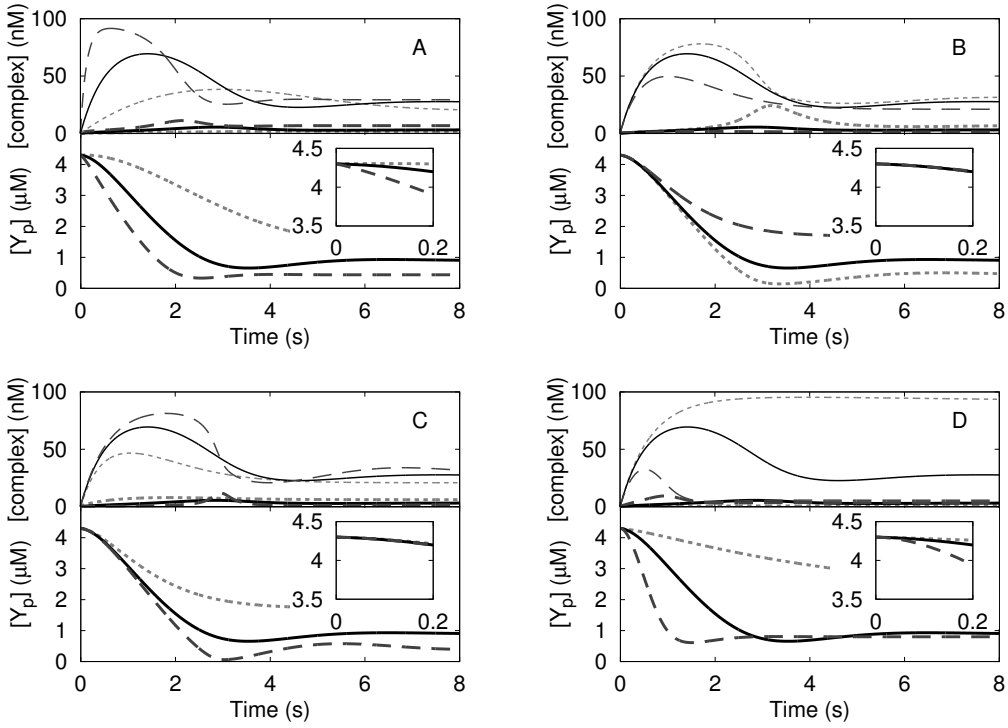

FIGURE 4.5 Effect of varying the parameters of the cooperative model (Equations 4.10–4.11) on the phosphatase kinetics. The upper panels show the concentrations of $[(Y_p)_2Z]$ (upper three curves) and of $[Y_pZ]$ (lower three curves) as functions of time. The lower panels show the evolution of the concentration of $CheY_p$ upon addition of CheZ. The concentration of $CheY_p$ does not go to zero because CheY is continuously phosphorylated by AcP, as in the experimental setup [76]. The insets show a magnification of the initial delay. A. Effect of k_4. B. Effect of k_6. C. Effect of k_{10}. D. Effect of k_{12}. The parameter values are 0.2 (dotted), 1 (solid) and 5 (dashed) times the baseline parameters of Fig. 4.7.

the value of $d[Y_p]/dt$ after the transient, iii) the size (and presence) of the undershoot before the steady state is reached and iv) the steady state concentration of $CheY_p$.

Figure 4.5 shows the effect of individually varying the parameters on the phosphatase kinetics. We assume that the two backward rates k_5 and k_{11} are zero, since the dissociation rates are smaller than the catalytic rates [92]. The initial delay is determined by the time it takes for $[(Y_p)_2Z]$ to reach its maximum level. In the limit that the binding of $CheY_p$ to $CheY_pCheZ$ is much faster than the association of $CheY_p$ to CheZ, i.e. if $k_{10} \gg k_4$, the delay is dominated by k_4 (see Fig. 4.5A). The association rate k_4 is, however, sufficiently fast, such that after this transient, a steady state can be reached in which CheZ is predominantly in the state $(Y_p)_2Z$. In this regime, the overall phosphatase activity per CheZ dimer is to a good approximation given by k_{12}, and the slope of $[Y_p](t)$ is given by $k_{12}[Z]_T$.

The undershoot of $[Y_p](t)$ in Fig. 4.5 arises from the subtle interplay between a number of factors. After a short transient of about 0.1 s, essentially all CheZ dimers

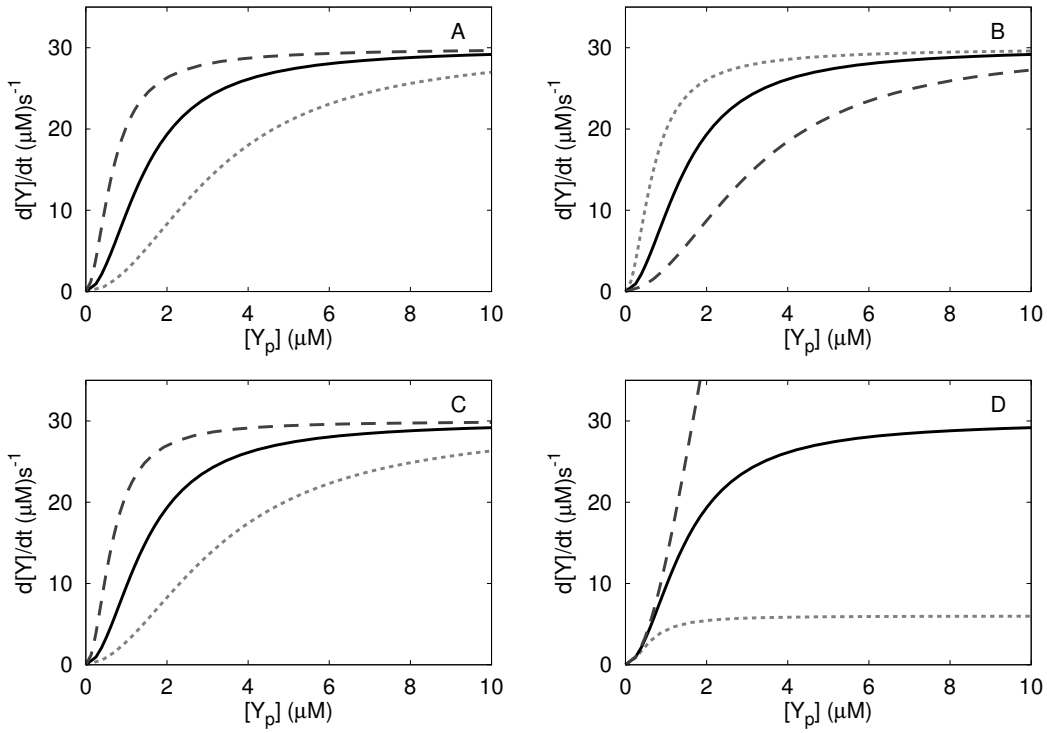

FIGURE 4.6 Effect of varying the parameters of the cooperative model (Equations 4.10–4.11) on the specific phosphatase activity. A. Effect of k_4. B. Effect of k_6. C. Effect of k_{10}. D. Effect of k_{12}. The parameter values were 0.2 (dotted), 1 (solid) and 5 (dashed) times the baseline parameters of Fig. 4.7.

are in the $(Y_p)_2Z$ state. In this state, the phosphatase activity of the CheZ dimers is high, and the concentration of $CheY_p$ drops rapidly. Importantly, when a $CheY_p$ molecule in a $(Y_p)_2Z$ complex is dephosphorylated, a Y_pZ complex is produced. When the concentration of $CheY_p$ is high, this complex can immediately rebind another $CheY_p$ molecule, from which another catalysis reaction can take place. However, after about $1-2\,s$, the concentration of $CheY_p$ has dropped so much that the rate of association between $CheY_p$ and $CheY_pCheZ$ decreases significantly. The concentration of $(Y_p)_2Z$ now decreases, while the concentration of Y_pZ *increases*. Since the phosphatase activity of Y_pZ is lower than that of $(Y_p)_2Z$, the concentration of $CheY_p$ will now increase again, until a new steady state is finally reached.

One would expect that the steady state concentration of $CheY_p$ can only decrease if any of the four association constants or catalytic activities is raised. Interestingly, this does not hold for k_6 (see Fig. 4.5B). While the total steady state catalytic activity of Y_pZ, as given by $k_6[Y_pZ]$, increases for larger values of k_6, the total catalytic activity of $(Y_p)_2Z$, $k_{12}[(Y_p)_2Z]$, decreases by a larger amount; the reason is that as k_6 increases, the concentration of $(Y_p)_2Z$ decreases. Consequently, the total steady state catalytic activity of Y_pZ and $(Y_p)_2Z$ together decreases as k_6 is raised. This increases the concentration of $CheY_p$.

Figure 2a in [76] shows the specific phosphatase activity of CheZ as a function of the concentration of $CheY_p$. The relevant quantities in Fig. 2a in [76] are the degree of cooperativity and the limiting value of the specific phosphatase activity. The effect of individually varying the parameters k_4, k_6, k_{10} and k_{12} on the specific phosphatase activity can be seen in Fig. 4.6. To analyse the dependence on these variables, we will first derive an expression for the phosphatase activity in steady state in the cooperative model given by Eqs. 4.10 and 4.11. First, $d[Z]/dt = 0$ gives $[Y_p][Z] = (k_5 + k_6)/k_4[Y_pZ] \equiv K_{M,1}[Y_pZ]$. Next, $d[(Y_p)_2Z]/dt = 0$ leads to $[Y_p][Y_pZ] = (k_{11} + k_{12})/k_{10}\ [(Y_p)_2Z] \equiv\ K_{M,2}[(Y_p)_2Z]$. The total concentration of CheZ equals $[Z]_T = [Z] + [Y_pZ] + [(Y_p)_2Z]$. Via elimination of $[(Y_p)_2Z]$ and $[Z]$, $[Y_pZ]$ can be expressed as

$$[Y_pZ] = \frac{[Z]_T[Y_p]}{K_{M,1} + [Y_p] + [Y_p]^2/K_{M,2}}. \tag{4.12}$$

The concentration of the doubly-bound state is given by

$$[(Y_p)_2Z] = [Y_pZ][Y_p]/K_{M,2}, \tag{4.13}$$

Since the production rate of CheY is equal to $k_3[Y_pZ] + k_6[(Y_p)_2Z]$, it follows that

$$\frac{d[Y]}{dt} = \frac{[Z]_T[Y_p](k_6 + k_{12}[Y_p]/K_{M,2})}{K_{M,1} + [Y_p] + [Y_p]^2/K_{M,2}}. \tag{4.14}$$

The network behaves cooperatively if the numerator is quadratic in $[Y_p]$ and the denominator only marginally depends on $[Y_p]$ when $[Y_p]$ is small. This is achieved if k_{12} is much larger than k_6 and if $K_{M,1}$ is larger than $K_{M,2}$: in the limit that $k_6 \ll k_{12}$ and $K_{M,1} \gg K_{M,2}$, the dephosphorylation rate is given by

$$\frac{d[Y]}{dt} = \frac{k_{12}[Z]_T[Y_p]^2}{K_{M,1}K_{M,2} + [Y_p]^2}. \tag{4.15}$$

This is a Hill function with a Hill coefficient of 2 and a concentration at which the rate is half maximal (the inflection point) given by $K_M^{\text{eff}} = \sqrt{K_{M,1}K_{M,2}}$. This can be verified from Fig. 4.6. An increase in either the association constant k_4 or k_{10} by a factor C, or a decrease by the same factor of either the catalytic activity k_6 or k_{12} leads to an increase in one of the Michaelis-Menten constants by the same factor and therefore to an increase by a factor $\sqrt{C}$ of K_M^{eff}. A change in k_{12} by a factor C additionally leads to a C times higher limiting phosphatase activity. The value of k_{12} can therefore be determined from the maximum phosphatase activity in Figure 2a in [76].

The best simultaneous fit to Figs. 1c and 2a of [76] is shown in Fig. 4.7. The used rate constants are $k_4 = 0.36(2.0) \cdot 10^6\ \text{M}^{-1}\text{s}^{-1}$, $k_6 = 7.5(5.0)\ \text{s}^{-1}$, $k_{10} = 3(3) \cdot 10^8\ \text{M}^{-1}\text{s}^{-1}$ and $k_{12} = 30(10)\ \text{s}^{-1}$. These values were also used as the baseline parameters in Fig. 4.6. While the best fits of the cooperative model show good agreement with the experimental data, it should be stressed that these experiments were performed *in vitro* rather than in a living bacterium. Therefore, it is well possible that the actual rate parameters in a living cell differ from those determined here. For example, it is well known that the diffusion coefficient *in vitro* can be ten times higher than that in a living cell. This means that especially diffusion-limited association reactions can slow down *in vivo*. We assume that the value of k_{10} is ten times lower *in vivo* than *in vitro*: *in vivo*, $k_{10}^{\text{cell}} = 3 \cdot 10^7\ \text{M}^{-1}\text{s}^{-1}$; we assume that k_4 is unchanged, since that rate is not diffusion limited.

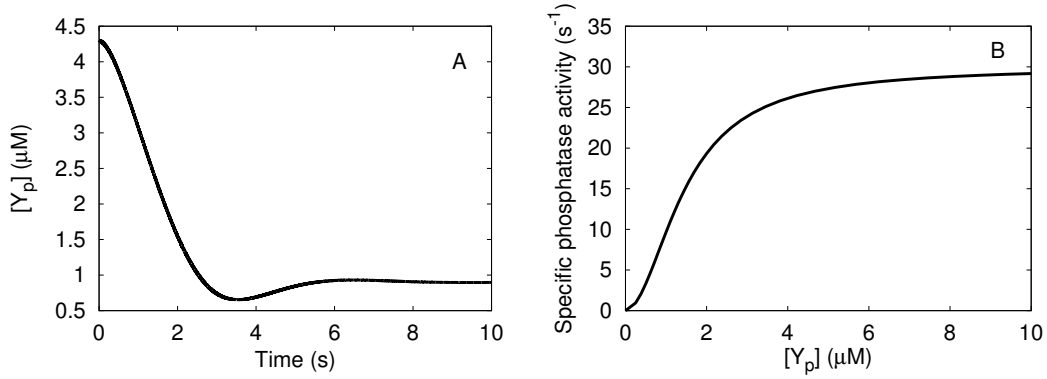

FIGURE 4.7 Best fit of the cooperative model to Figs. 1c and 2a of [76]. The parameter values are: $k_4 = 0.36(2.0) \cdot 10^6\ \mathrm{M^{-1}s^{-1}}$, $k_6 = 7.5(5.0)\ \mathrm{s^{-1}}$, $k_{10} = 3(3) \cdot 10^8\ \mathrm{M^{-1}s^{-1}}$, $k_{12} = 30(10)\ \mathrm{s^{-1}}$.

Appendix B The full model

The full model for the intracellular chemotaxis network of *E. coli* is given by the following chemical reactions (see the main text):

$$\mathrm{A} \overset{\beta k_0}{\rightarrow} \mathrm{A_p} \tag{4.16}$$

$$\mathrm{A_p} + \mathrm{Y} \underset{k_2}{\overset{k_1}{\rightleftharpoons}} \mathrm{A_pY} \overset{k_3}{\rightarrow} \mathrm{A} + \mathrm{Y_p} \tag{4.17}$$

$$\mathrm{Y_p} + \mathrm{Z} \underset{k_5}{\overset{k_4}{\rightleftharpoons}} \mathrm{Y_pZ} \overset{k_6}{\rightarrow} \mathrm{Y} + \mathrm{Z} \tag{4.18}$$

$$\mathrm{Y_p} + \mathrm{Z_b} \underset{k_8}{\overset{k_7}{\rightleftharpoons}} \mathrm{Y_pZ_b} \overset{k_9}{\rightarrow} \mathrm{Y} + \mathrm{Z_b} \tag{4.19}$$

$$\mathrm{Y_pZ} + \mathrm{Y_p} \underset{k_{11}}{\overset{k_{10}}{\rightleftharpoons}} (\mathrm{Y_p})_2\mathrm{Z} \overset{k_{12}}{\rightarrow} \mathrm{Y} + \mathrm{Y_pZ} \tag{4.20}$$

$$\mathrm{Y_pZ_b} + \mathrm{Y_p} \underset{k_{14}}{\overset{k_{13}}{\rightleftharpoons}} (\mathrm{Y_p})_2\mathrm{Z_b} \overset{k_{15}}{\rightarrow} \mathrm{Y} + \mathrm{Y_pZ_b} \tag{4.21}$$

In this model, in wild-type cells CheZ is present both bound to the receptor cluster, indicated by $\mathrm{Z_b}$, and freely diffusive. The majority of CheZ is assumed to be diffusive, but the affinity for $\mathrm{CheY_p}$ as well as the catalytic activity is much larger for the localized fraction of CheZ (for parameter values, see the caption of Fig. 4.8).

Fig. 4.8 shows the response of the concentration of $\mathrm{CheY_p}$ and the FRET signal to changes in the activity of the receptor cluster, βk_0. We assume that the FRET signal is given by: $\mathrm{FRET} \propto [\mathrm{Y_pZ}] + 2[(\mathrm{Y_p})_2\mathrm{Z}] + [\mathrm{Y_pZ_b}] + 2[(\mathrm{Y_p})_2\mathrm{Z_b}]$. It is seen that the functions $\mathrm{FRET}(\beta k_0)$ and $[\mathrm{Y_p}](\beta k_0)$ consist of two parts. In the first regime, corresponding to low concentrations of $\mathrm{CheY_p}$, the fraction of CheZ that is localized to the receptor cluster is not yet saturated. In this regime, $\mathrm{CheY_p}$ that is produced by $\mathrm{CheA_p}$ at the cluster will rapidly bind to CheZ at the cluster. While the FRET signal increases in this regime due to binding of $\mathrm{CheY_p}$ to $\mathrm{CheZ_b}$, the concentration of $\mathrm{CheY_p}$ hardly increases due to the large phosphatase activity of $\mathrm{CheZ_b}$. The second part of the response curves corresponds to the regime in which $\mathrm{CheZ_b}$ is fully saturated. In this regime, a $\mathrm{CheY_p}$ molecule that is produced at the receptor cluster, can no longer bind a CheZ dimer that is bound to

the receptor cluster; it will therefore diffuse into the cytoplasm, where it will bind a diffusive CheZ dimer. This CheZ has a lower phosphatase activity than $\mathrm{CheZ_b}$ and, as a result, the concentration of $\mathrm{CheY_p}$, as well as the FRET signal, will rise rapidly.

As discussed in the main text, if the activity $\beta k_0^{\mathrm{adapted}}$ of the receptor cluster is the same for wild-type and CheZ mutant cells, it is difficult to have $[\mathrm{Y_p}]^{\mathrm{adapted}}$ in the working range of the motor for both types of cells. As we discuss now, a cooperative (super-linear) dependence of the phosphatase activity on $[\mathrm{Y_p}]$ makes it easier to satisfy this constraint. First, we note that the constraint that $[\mathrm{Y_p}]$ should be within the working range of the motor for both wild-type and CheZ mutant cells is satisfied more easily if $[\mathrm{Y_p}]$ for diffusive CheZ is a concave (hyperbolic) function of βk_0. Such a concave functional form can be obtained when the phosphatase activity depends super-linearly on $[\mathrm{Y_p}]$: In steady state, the kinase activity $d[\mathrm{Y_p}]/dt$ is given by $\beta k_0[\mathrm{A}] = k_1[\mathrm{A_p}][\mathrm{Y}]$ and equal to the phosphatase activity $d[\mathrm{Y}]/dt$. If $[\mathrm{A}] \approx [\mathrm{A}]_\mathrm{T}$, the kinase activity is proportional to βk_0, which means that in steady state the specific phosphatase activity $d[\mathrm{Y}]/dt$ is proportional to βk_0. If the specific phosphatase activity (and hence βk_0) increases super-linearly (up to quadratically) with $[\mathrm{Y_p}]$ for low $[\mathrm{Y_p}]$ as in the cooperative CheZ model, $[\mathrm{Y_p}]$ as a function of βk_0 has a concave form, as can also be seen in Fig. 4.6.

We now briefly discuss the effect of varying the rate constants and the diffusion constant on the response curves $[\mathrm{Y_p}](\beta k_0)$ and $\mathrm{FRET}(\beta k_0)$, as shown in Fig. 4.8. The effect of changing the parameters related to the kinase reactions, k_1 and k_3, is similar to that of changing these rate constants in the canonical model, as discussed above. In particular, as long as $[\mathrm{A}] \approx [\mathrm{A}]_\mathrm{T}$, the total phosphorylation rate is independent of k_1 and k_3, and $[\mathrm{Y_p}]$ and FRET are fairly insensitive to changes in these rate constants.

The parameters k_4, k_6, k_{10} and k_{12} correspond to dephosphorylation reactions by CheZ in the cytoplasm. Clearly, changing these rate constants only affects the second regime of the response curves $[\mathrm{Y_p}](\beta k_0)$ and $\mathrm{FRET}(\beta k_0)$, in which CheZ bound to the cluster is saturated (see Fig. 4.8). The influence of varying these parameters on $[\mathrm{Y_p}](\beta k_0)$ can be deduced from the corresponding panels in Fig. 4.6, which shows the phosphatase activity for diffusive CheZ. Since the kinase activity $\beta k_0[\mathrm{A}]$ equals in steady state the phosphatase activity $d[\mathrm{Y}]/dt$, $[\mathrm{Y_p}](\beta k_0)$ is also given by $[\mathrm{Y_p}](d[\mathrm{Y}]/dt[\mathrm{A}]_\mathrm{T})$. Thus, by inverting the axes of Fig. 4.6, one can deduce the change in $[\mathrm{Y_p}](\beta k_0)$ upon varying k_4, k_6, k_{10} and k_{12}. As expected, changing the catalytic rate k_{12} has the largest effect on the response curve.

The parameters k_7, k_9, k_{13}, and k_{15} are rate constants associated with reactions of CheZ that is bound to the cluster; these rate constants correspond to, respectively, k_4, k_6, k_{10} and k_{12} of reactions of CheZ in the cytoplasm. As such, the effect of varying the parameters k_7, k_9, k_{13} and k_{15} on the response curve can be deduced from the effect of changing the parameters k_4, k_6, k_{10} and k_{12}, discussed above. However, since CheZ bound to the cluster is present in low concentrations, and has a much higher affinity for $\mathrm{CheY_p}$ and a higher catalytic activity, the magnitude of the effect is markedly different. In particular, changing k_7, k_9 and k_{13} hardly has any effect. This is because CheZ at the cluster is strongly driven to the $(\mathrm{Y_p})_2\mathrm{CheZ}$ state. For precisely the same reason, the largest effect is observed for changes in the catalytic rate k_{15}.

The last graph in Fig. 4.8 shows the effect of varying the diffusion coefficient D. The diffusion coefficient is assumed to be equal for all diffusive components. A decrease in D

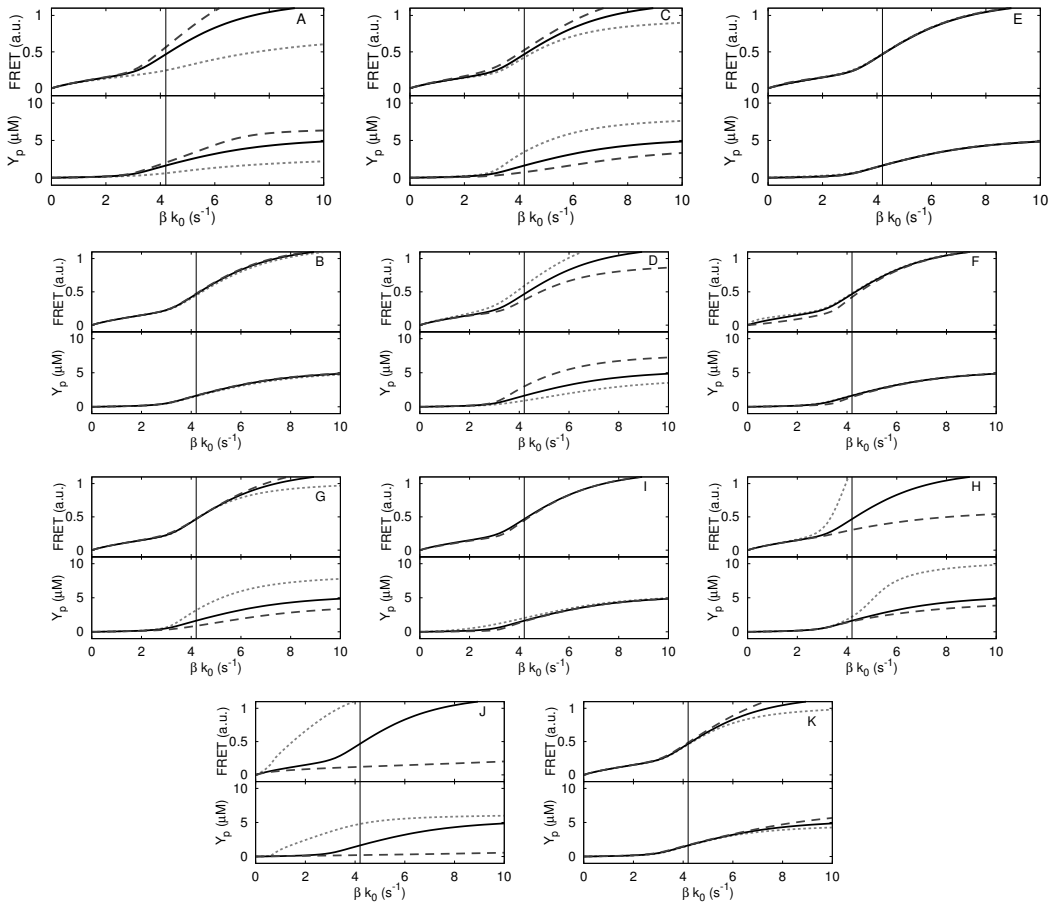

FIGURE 4.8 The effect of varying the different parameters of the full model of the intracellular chemotaxis network (Equations 3.1–4.8) on the response curves $[Y_p](\beta k_0)$ and FRET(βk_0); here FRET $\propto [Y_pZ] + 2[(Y_p)_2Z] + [Y_pZ_b] + 2[(Y_p)_2Z_b]$. A: k_1; B: k_3; C: k_4; D: k_6; E: k_7; F: k_9; G: k_{10}; H: k_{12}; I: k_{13}; J: k_{15}; K: D. The baseline parameters are $k_1 = 3\ 10^6\ \mathrm{M^{-1}s^{-1}}$, $k_3 = 750\ \mathrm{s^{-1}}$, $k_4 = 3.6\ 10^5\ \mathrm{M^{-1}s^{-1}}$, $k_6 = 7.5\ \mathrm{s^{-1}}$, $k_7 = 6\ 10^8\ \mathrm{M^{-1}s^{-1}}$, $k_9 = 40\ \mathrm{s^{-1}}$, $k_{10} = 3\ 10^7\ \mathrm{M^{-1}s^{-1}}$, $k_{12} = 30\ \mathrm{s^{-1}}$, $k_{13} = 9\ 10^8\ \mathrm{M^{-1}s^{-1}}$, $k_{15} = 160\ \mathrm{s^{-1}}$, $D = 5\ \mu\mathrm{m^2s^{-1}}$, $[Y]_T = 17.9\ \mu\mathrm{M}$, $[Z]_T = 1\ \mu\mathrm{M}$, $[Z_b]_T = 0.1\ \mu\mathrm{M}$ and $[A]_T = 5\ \mu\mathrm{M}$. The parameter values are 0.2 (dotted), 1 (solid) and 5 (dashed) times the baseline parameters. Exceptions are $k_{13} : k_{13} = 1.8\ 10^8$(*dotted*), $6\ 10^9$ (solid) and $3\ 10^{10}\ \mathrm{M^{-1}s^{-1}}$ (dashed) and the diffusion coefficient: $D = 3$ (dotted), 5 (solid) and 10 $\mu\mathrm{m^2s^{-1}}$ (dashed). The vertical lines indicate the adapted state for the baseline parameter set.

has the effect that larger gradients of $CheY_p$ arise. As a consequence, the concentration of $CheY_p$ integrated over the whole cell decreases. Since also larger gradients of Y_pZ and $(Y_p)_2Z$ occur, the total concentrations of Y_pZ and $(Y_p)_2Z$ decrease as well for lower values of the diffusion constant; this explains the decrease in FRET signal with decreasing diffusion constant.

5 Particle-based simulations on the effects of colocalization of antagonistic enzymes

The activity of messenger proteins is commonly controlled by two antagonistic enzymes. Recent experiments on the chemotaxis system of Escherichia coli *have revealed that such enzymes can be colocalized at the plasma membrane. We perform particle-based Monte Carlo simulations to study how the response characteristics of a push-pull network are influenced by colocalizing the antagonistic enzymes in a membrane. To this end, we compare the response dynamics and the steady-state input-output curve of a system in which the enzymes are distributed in the cytoplasm to those of a system in which the enzymes are both localized at the membrane. We find that colocalization leads to a wide distribution of enzyme-substrate association times, which implies that colocalization can have a strong influence on the response dynamics; in particular, it allows for both rapid and slow signalling. However, colocalization by itself does not change the* average *enzyme-substrate association time. Consequently, colocalization does not affect the steady-state input-output relation. We also develop simple mean-field theories, which give a good description of the steady-state response curves. These results support the use of chemical rate equations for predicting the steady-state response curves, but also highlight that spatially resolved, stochastic models are required if one is interested in the distribution of response times.*

5.1 Introduction

In the modelling of biochemical networks, the dominant paradigm has been to consider the living cell to be a spatially uniform system, analogous to a well-stirred reactor. However, in recent years it is increasingly recognized that biochemical networks not only operate in time, but also in space [93]. One key role of biochemical networks is to provide spatial information. Arguably the best example is embryonic development, where spatial gradients in the concentrations of morphogens encode the positional information for differentiating cells [94]. Also within single cells, biochemical networks often have to provide positional information, for instance during cell division. An elegant example is provided by the bacterium *Escherichia coli*, where three proteins locate the cell center via an oscillating reaction-diffusion pattern [95]. The importance of spatio-temporal dynamics of biochemical networks is, however, not limited to providing spatial information. Spatial fluctuations due to the diffusive motion of messenger proteins can provide a major source of noise in gene expression [96], which could be exploited for generating phenotypic diversity in a population of genetically identical cells. In preventing cross-talk between signal transduction pathways, spatial separation of shared components is

believed to be an important mechanism [97]. Localizing signalling components onto scaffold proteins provides a mechanism for modulating the amplitude and duration of transmitted signals [98]. Furthermore, recent studies suggest that spatial localization of (co)receptors in the immune response plays a critical role in amplifying incoming signals, allowing the immune system to discriminate between foreign cells and those of the host [83]. In this paper, we address the question whether colocalizing the two antagonistic enzymes of a push-pull network to a membrane, can enhance the sharpness of the input-output relation.

A well-known example of colocalization is given by the chemotaxis system of *E. coli*, in which the kinase CheA and the phosphatase CheZ together control the activity (phosphorylation level) of the messenger protein CheY. Recent experiments have shown that both enzymes are colocalized at the receptor cluster near the cell pole [35]. It has been argued that colocalizing the antagonistic enzymes CheA and CheZ is advantageous, because it leads to a uniform concentration profile of the messenger protein CheY [57], which in turn facilitates a concerted response of the flagellar motors. In chapter 2, we showed using a mean-field analysis based on macroscopic reaction-diffusion equations that the spatial distribution of the two antagonistic enzymes can have a dramatic effect on the input-output relation of the network. We compared the response of a system in which the enzymes are either uniformly distributed in space or colocalized at the cell pole, to the response of a network in which the enzymes are spatially separated, with one enzyme localized at the cell pole and the other freely diffusing in the cytoplasm. Our mean-field analysis revealed that spatially separating the two antagonistic enzymes reduces both the gain and the maximum response of a push-pull network; interestingly, it also showed that spatially separating the enzymes can also enhance the transmission of weak signals [72].

Recently, it has been conjectured that colocalization of the two antagonistic enzymes in a push-pull network could enhance the association rate between the antagonistic enzymes and their substrate [99]. For the chemotaxis system of *E. coli*, Silversmith argued that the *"Generation of* $\mathrm{CheY_p}$ *by the proximal CheA kinase would result in high local concentrations of both* $\mathrm{CheY_p}$ *and the CheZ C-helix, which would further increase the probability of their collision and subsequent association"* [99]. If the two antagonistic enzymes are colocalized, the position at which the messenger protein is activated by the activating enzyme, is close to the point at which it is deactivated by the deactivating enzyme. This close physical proximity, Silversmith argued, could enhance the association rate between the enzyme and its substrate. A higher enzyme-substrate association rate, in turn, may be beneficial, since it brings the push-pull network deeper into the zero-order regime, which enhances the sharpness of the response [34].

In this paper, we investigate whether colocalization of two antagonistic enzymes at a cell membrane can indeed enhance the enzyme-substrate association rate and thereby increase the sharpness of the response of a push-pull network. To address this question, a mean-field approach based on macroscopic reaction-diffusion equations cannot be used, since it cannot describe the behavior of a system at a distribution of length scales. We hypothesized that the following distinct length scales are important: 1) the distance between the antagonistic enzymes on the membrane; 2) the distance between the enzymes on the membrane and the substrates in the cytoplasm. These two length scales together determine the probability that a substrate molecule that has just been

activated by an activating enzyme at the membrane, can rapidly bind to a deactivating enzyme at the membrane, and vice versa.

To go beyond a mean-field analysis, we performed particle-based simulations of a push-pull network. To this end, we have developed a simulation scheme in which the particles are propagated on a lattice. This scheme, which is discussed in more detail in section 5.5.2, is fast and allows for a detailed study on the effect of enzyme colocalization. In the results section, we then compare the response of a network in which all components are uniformly distributed in the cytoplasm, with the response of a network in which the antagonistic enzymes form a checkerboard pattern at one end of the cell (see Fig. 5.1). In such a configuration, the turnover rate of the substrate can be enormous, as the substrate can rapidly diffuse from one enzyme to the next. A central question will be whether this rapid turnover rate of the substrate can give rise to an enhanced response sharpness or sensitivity. As we will show, colocalization *per se* is not sufficient to enhance the sharpness of the response. The reason is that even though activated substrate molecules will often have a much shorter lifetime, this is balanced by the fact that they also often have a much longer lifetime: when a substrate molecule diffuses away from the membrane and into the cytoplasm, it takes much longer to find the antagonistic enzyme, as compared to the case in which the enzymes are both distributed in the cytoplasm. While this phenomenon changes the response *dynamics*, it does not change the *average* enzyme-substrate association time; the steady-state input-output relation is therefore not significantly influenced.

5.2 The system

In the following, we will consider a generic push-pull network, as given by the following reaction scheme:

$$\mathrm{E_a} + \mathrm{X} \underset{k_2}{\overset{k_1}{\rightleftharpoons}} \mathrm{E_aX} \overset{k_3}{\rightarrow} \mathrm{E_a} + \mathrm{X^*} \tag{5.1}$$

$$\mathrm{E_d} + \mathrm{X^*} \underset{k_5}{\overset{k_4}{\rightleftharpoons}} \mathrm{E_dX^*} \overset{k_6}{\rightarrow} \mathrm{E_d} + \mathrm{X} \tag{5.2}$$

Here, $\mathrm{E_a}$ and $\mathrm{E_d}$ denote the activating and deactivating enzyme molecules, respectively, and $\mathrm{X^*}$ and X denote the active and inactive substrate molecules, respectively. Without loss of generality, we will set the backward rates $\mathrm{k_2}$ and $\mathrm{k_5}$ to zero.

The main focus of this section is to compare the response characteristics of a push-pull network in which the antagonistic enzymes are colocalized to a membrane at one pole of the cell to those of a push-pull network in which the enzymes are distributed in the cytoplasm. Colocalization of the enzymes at the cell pole is modelled by putting the antagonistic enzymes in a 2D checkerboard pattern in the first plane of the simulation box, as shown in Fig. 5.1. The active and inactive substrate molecules, $\mathrm{X^*}$ and X, respectively, diffuse through the three-dimensional half-space bounded by the enzyme lattice. Please note that in between one $\mathrm{E_a}$ and one $\mathrm{E_d}$ molecule one substrate molecule can bind to the membrane. This allows for a rapid turnover of the substrate molecules: for example, an X molecule that has just been turned into an active $\mathrm{X^*}$ molecule by an $\mathrm{E_a}$ particle will be placed adjacent to an $\mathrm{E_d}$ molecule with a probability 4/6; in the next time step this molecule can then immediately bind to an $\mathrm{E_d}$ molecule leading to its deactivation.

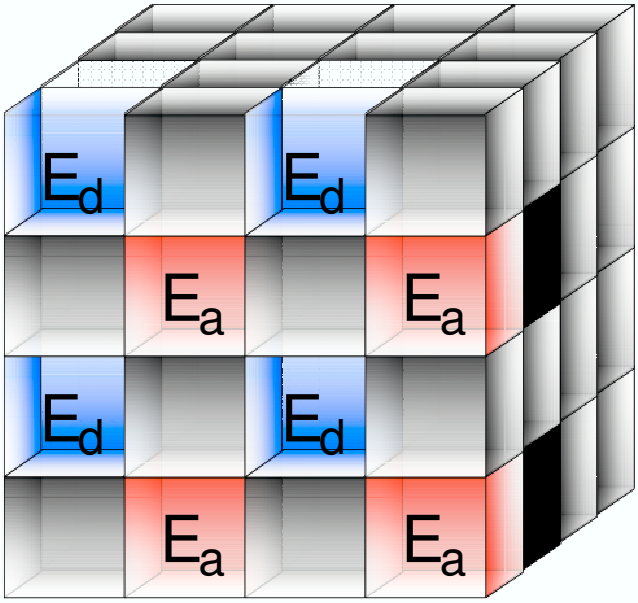

FIGURE 5.1 Colocalization of the antagonistic enzymes of a push-pull network to a membrane at one end of the cell. The enzymes are immobile and are arranged in a checkerboard configuration. The substrate molecules can freely diffuse in the cytoplasm, but can also occupy the space in between the enzyme molecules at the membrane. The density of X^* is indicated by different grey scales. The density of X^* is largest near E_a, where X^* is produced, and lowest near E_d, where X^* is deactivated. In the lattice columns that do not contain an enzyme molecule, the concentration of X^* (and X) is constant.

Concerning the case in which the enzymes are distributed in the cytoplasm, we will consider a scenario in which both the substrate and the enzyme molecules freely diffuse in the cytoplasm. However, to elucidate the underlying dynamics, we will also consider a scenario in which the substrate molecules diffuse freely, but the enzymes are fixed in space, either in a random configuration or in a regular "crystalline" array.

In all LRD simulations, the simulation box consists of 2240 lattice sites with a lattice constant of 30 nm: $4\times4\times140$ sites for the checkerboard configurations and $10\times14\times16$ for

the other configurations. Periodic boundary conditions were employed in all directions. The parameter values are given in the figure captions. The simulations were all run for 3×10^4 s after an equal equilibration time.

We will study this system by solving, in zero-dimensions, the chemical rate equations corresponding to Eqs. 5.1 and 5.2 and by performing LRD simulations, as described in the previous section. We will also develop for both scenarios a simple mean-field analysis that takes into account the effect of spatial concentration gradients (see below).

5.3 Results

5.3.1 Colocalization does not sharpen the response

The principal result of our analysis is shown in Fig. 5.2. Figure 5.2A shows the concentration of active substrate X^*, $[X^*]$, as a function of the catalytic activity of the activating enzyme, k_3, for a push-pull network in the linear regime, while Fig. 5.2B shows $[X^*]$ as a function of k_3 for a system in the zero-order regime. It is seen that in both regimes, the LRD results for the scenario in which the enzymes are colocalized at the cell pole are virtually indistinguishable from the results for the scenario in which the enzymes are distributed in the cytoplasm. Clearly, colocalization does not significantly change the steady-state input-output relation.

The reason that colocalizing the antagonistic enzyme does not significantly affect the response curve is that colocalization does not enhance the average enzyme-association rate as Silversmith conjectured [99]. This is illustrated in Fig. 5.3. This figure shows the distribution of lifetimes of an active substrate molecule, X^*, for the different configurations of the enzymes. It is seen that when the enzymes are distributed in the cytoplasm (random and 3D lattice configurations), the distribution of lifetimes is exponential, which is to be expected. When the antagonistic enzymes are colocalized at the receptor cluster, the distribution is markedly different. The probability that an active molecule has a short lifetime, is much higher when the enzymes are colocalized at the cell pole than when the enzymes are distributed in the cytoplasm (see *Inset*). This is due to a pathway in which a substrate molecule that has just been activated by an E_a molecule at the cell pole, rapidly binds to an E_d molecule at the cell pole. Colocalization indeed leads to a higher fraction of substrate molecules that have a very short lifetime, as Silversmith argued [99]. However, this is compensated by the fact that a large fraction of (in)active substrate molecules manages to escape from the cell pole before they are (de)activated, and diffuses into the cytoplasm. For these molecules, it takes much longer before they are (de)activated, as compared to the case in which both enzymes are distributed in the cytoplasm. Indeed, colocalization not only leads to a much larger fraction of substrate molecules with a very short lifetime, but also to a higher fraction of substrate molecules with a longer lifetime. In fact, these two effects precisely balance each other, such that the *average* lifetime of a substrate molecule is the same in both scenarios.

That the average lifetime is not affected by the spatial distribution of the enzymes is perhaps not a trivial result. It is instructive to make an analogy with a simple reversible reaction $A + B \leftrightarrow AB$, and consider a system in which the A molecules are immobile and the B molecules have to diffuse from one A molecule to another, in order for a

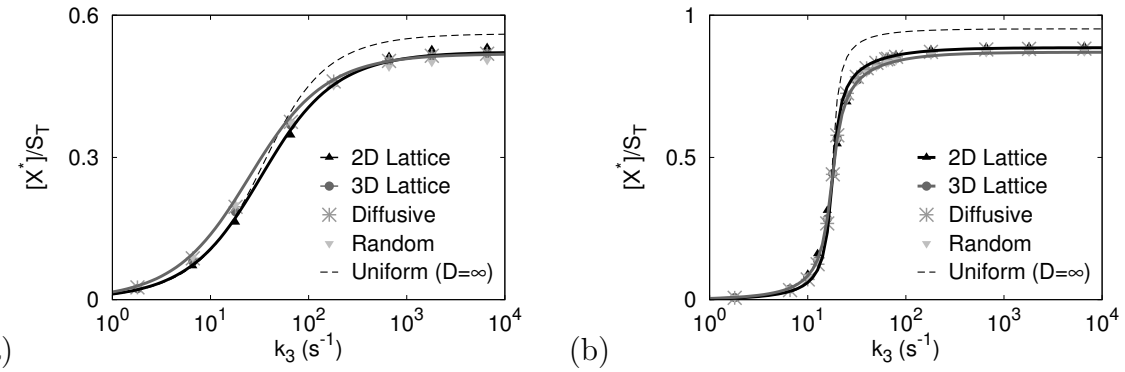

FIGURE 5.2 The response of the network, as measured by the concentration of X^*, as a function of the catalytic activity of the activating enzyme, k_3, for different spatial arrangements of the enzymes. Fig. A shows the response of the system in the linear regime ($[S]_T/K_{M,d} = 0.5$), while Fig. B shows the response of the system in the zero-order regime ($[S]_T/K_{M,d} = 20$). The dashed black line corresponds to the prediction of the chemical rate equation, in which it is assumed that the system is spatially uniform. The black triangles correspond to the LRD simulation results for a system in which the enzymes are colocalized to the membrane; the solid black lines correspond to the predictions of the mean-field analysis of Eqs. 5.9–5.15. The dark-grey circles correspond to the LRD simulation results for a system in which the enzymes are immobilized onto a 3D regular, simple cubic lattice; the dark-grey lines correspond to the mean-field predictions of Eqs. 5.22–5.26. The asterisks correspond to the LRD simulation results in which the enzymes (as well as the substrate molecules) can freely diffuse in the cytoplasm. The light-grey inverted triangles correspond to the case in which the enzymes are put in a quenched, random configuration. In Figs. A and B, $k_1 = k_4 = 1.08\,10^8$ $M^{-1}s^{-1}$, and $[E_a]_T = [E_d]_T = 0.22$ μM, corresponding to 8 molecules of each enzyme species; in Fig. A, $k_6 = 180\,s^{-1}$, $[S]_T \equiv [X] + [E_aX] + [X^*] + [E_dX^*] = 0.83\,\mu$M, corresponding to 30 molecules; in Fig. B, $k_6 = 18\,s^{-1}$, $[S]_T = 3.3\,\mu$M, corresponding to 120 molecules. In all cases, the diffusion constant of the diffusive species is $D = 1\,\mu m^2 s^{-1}$.

reaction to take place. We can then ask how the distribution of waiting times in between a dissociation and a subsequent association reaction, i.e. the lifetime of a B molecule, depends on the configuration of A molecules and how the equilibrium [A][B]/[AB], which is given by the ratio of the average dissociation time over the average association time, depends upon that configuration; in this comparison the overall densities of the molecules are considered to be the same. It is clear that the distribution of waiting times strongly depends upon the configuration of A molecules: if the A molecules are close together in space, then the distribution will have a large peak at short times, but also a long tail at long times, as compared to a scenario in which the A molecules are randomly distributed in space. However, we know that since this is an equilibrium system, detailed

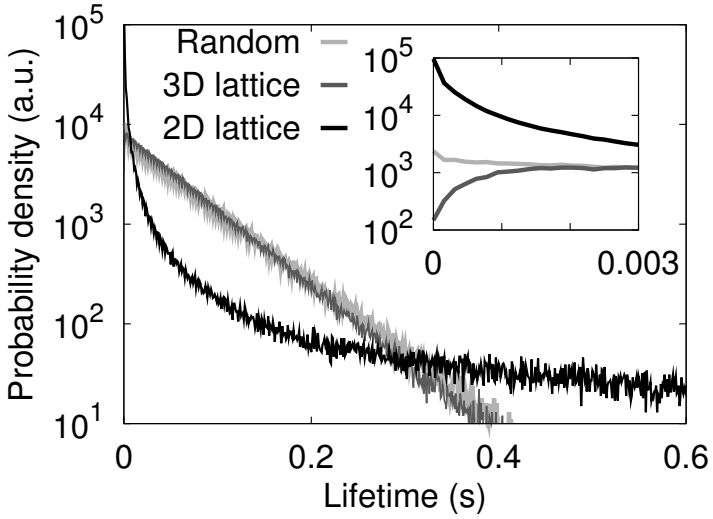

FIGURE 5.3 Distribution of lifetimes for X^*, for three different spatial arrangements of the antagonistic enzymes. The dark-grey line corresponds to the scenario in which the antagonistic enzymes form a regular, simple cubic lattice. The light-grey curve corresponds to the scenario in which the enzymes adopt a quenched random configuration. The black curve corresponds to the case in which the enzymes are colocalized to the membrane at one end of the cell, as shown in Fig. 5.1. The inset shows the same data zoomed in on early times. It is seen that when the enzymes are colocalized to the membrane, the distribution of X^* lifetimes is broad: many substrate molecules that have just been activated by E_a, will rapidly rebind to the membrane and be deactivated by E_d other activated substrate molecules will, however, escape from the membrane and diffuse into the cytoplasm. For these molecules it will take much longer before they are deactivated by E_d. However, while the distribution of lifetimes is much broader when the enzymes are colocalized, as compared to the case in which the enzymes are distributed in the cytoplasm, the average is, to a very good approximation, the same. This explains why the response curves, as shown in Fig. 5.2, are hardly affected by the spatial arrangement of the enzymes.

balance dictates that the concentration of bound molecules AB does not depend upon the spatial distribution of the A molecules. The resolution of the paradox is that the average association time does not depend upon the configuration of the A molecules: the short waiting times are precisely balanced by the long waiting times.

Now, the push-pull network is not an equilibrium system: a substrate molecule that has just been activated by an E_a molecule has to diffuse to an E_d molecule in order to become deactivated; the deactivated substrate molecule then has to diffuse to an E_a molecule again, to become reactivated. This process generates cycles in state space, which reflect the fact that a push-pull network is a non-equilibrium system that requires energy as an input. In fact, these cycles give rise to concentration gradients of substrate molecules around the enzyme molecules. As we discuss in more detail below,

these gradients do affect the response curve. However, the effect of these gradients is small, and to the extent that they can be neglected, the insensitivity of the location of the chemical equilibrium of a reversible reaction to the spatial distribution of the immobile species implies that the steady-state response curve of a push-pull network does not depend upon the spatial distribution of the enzymes: the response curve of a push-pull network depends on the occupancy of enzyme with substrate; the average occupancy of an enzyme molecule is determined by the ratio of the average enzyme-substrate association time and the average time it takes to catalyze the (de)modification reaction; in the equilibrium system, the average occupancy of an A molecule with a B molecule is given by the ratio of the average $A-B$ association time and the average $A-B$ dissociation time; while the enzyme-substrate association time is analogous to the $A-B$ association time, the catalysis reaction is analogous to the $A-B$ dissociation time. Since we know that the average $A-B$ association time and hence the average occupancy of an A with a B molecule does not depend upon the spatial distribution of the A species, it follows that also the average enzyme occupancy does not depend upon the spatial distribution of the enzymes. This explains why enzyme colocalization by itself is not sufficient to change the response curve.

5.3.2 Colocalization changes signal timing

While Fig. 5.2 shows that colocalization of the antagonistic enzymes to the cell pole does not significantly influence the steady-state input-output relation, Fig. 5.3 reveals that it does change the timing of activation. The broad distribution of lifetimes when the enzymes are colocalized implies that colocalization leads to a broad distribution of times over which the substrate molecules are activated. Indeed, colocalization allows for strong signalling at early times and for signalling at late times.

5.3.3 Gradients change the input-output relation

Figure 5.2 shows the prediction of the chemical rate equations in zero dimensions for the response curves (dashed *black* line). It is seen that the prediction agrees fairly well with the results from the LRD simulations, both when the system is in the linear regime (Fig. 5.2A) and when it is in the zero-order regime (Fig. 5.2B). Yet, deviations from the LRD simulation results can also be observed. These deviations could have various origins. While the LRD simulations take into account the discrete nature of the components, the stochastic character of their interactions, and resolves the stochastic motion and the non-uniform distribution of the particles in space, the chemical rate equations are based on a mean-field analysis that makes a number of assumptions. In particular, it assumes that: a) there are no spatial concentration gradients in steady state; b) there are no spatio-temporal correlations. For instance, the overall enzyme-substrate association rate is given by $k_1\langle N_{\mathrm{E_a}} N_{\mathrm{X}}(\sigma)\rangle/V^2$, where N_α is the copy number of species α, and $N_{\mathrm{X}}(\sigma)$ is the number of X molecules in contact with the $\mathrm{E_a}$ molecules; σ is the cross-section for the $\mathrm{E_a}$-X association reaction and V is the volume of the system. If the diffusion constant is high and/or the intrinsic association rate, which is the association rate given that the reaction partners are at contact, is low, the species are uniformly distributed at all times. In such a well-stirred system, the enzyme-substrate association rate can then be approximated as $k_1\langle N_{\mathrm{E_a}} N_{\mathrm{X}}\rangle/V^2$. The chemical rate equations make

the further assumption that: c) there are no temporal correlations. This means that the enzyme-substrate association rate can be approximated as $k_1\langle N_{\mathrm{E_a}}\rangle\langle N_{\mathrm{X}}\rangle/V^2 = k_1[\mathrm{E_a}][\mathrm{X}]$.

As we will show now, the difference between the LRD simulation results and the predictions of the chemical rate equations are predominantly due to concentration gradients. We will now present a simple mean-field analysis for the scenario in which the enzymes are colocalized and for the scenario in which they are distributed in the cytoplasm. These mean-field analyses take into account the concentration gradients, but neglect the temporal correlations. We will show that they give a remarkably good prediction for the input-output relation, both when the system is in the linear regime and in the zero-order regime.

Enzymes colocalized at the membrane: mean-field model

When the enzymes are colocalized to the plasma membrane, small gradients will arise around the activating and deactivating enzymes. This is illustrated in Fig. 5.1.

The activating and deactivating enzymes form a checkerboard pattern in the first plane of the lattice. The grey scale of the remaining lattice sites denotes the average concentration of active substrate molecules X^*. In the lattice columns that start with an activating enzyme molecule $\mathrm{E_a}$, the concentration of X^* is highest near $\mathrm{E_a}$ and then decreases with the distance from the cluster; in the columns starting with $\mathrm{E_d}$, the concentration of X^* is lowest near $\mathrm{E_d}$ and then increases with distance from the membrane. The total concentration $[\mathrm{S}]_{\mathrm{T}} = [\mathrm{X}] + [\mathrm{X}^*]$ is constant; the profiles of X are thus the mirror image of those of X^*. In the lattice columns that contain no enzyme molecules, the concentration profiles of X^* and X are uniform, as explained in the appendix.

The mean-field analysis is discussed in detail in the appendix. Here, we present the main results. The concentration profiles are given by

$$[\mathrm{X}]_{\mathrm{o}_i} = [\mathrm{X}]_\infty \forall i \tag{5.3}$$

$$[\mathrm{X}^*]_{\mathrm{o}_i} = [\mathrm{X}^*]_\infty \forall i \tag{5.4}$$

$$[\mathrm{X}]_{\mathrm{a}_i} = [\mathrm{X}]_\infty - [\mathrm{C}_0]\ \exp\{(1-i)\ K\} \forall i > 0 \tag{5.5}$$

$$[\mathrm{X}^*]_{\mathrm{a}_i} = [\mathrm{X}^*]_\infty + [\mathrm{C}_0]\ \exp\{(1-i)\ K\} \forall i > 0 \tag{5.6}$$

$$[\mathrm{X}]_{\mathrm{d}_i} = [\mathrm{X}]_\infty + [\mathrm{C}_0]\ \exp\{(1-i)\ K\} \forall i > 0 \tag{5.7}$$

$$[\mathrm{X}^*]_{\mathrm{d}_i} = [\mathrm{X}^*]_\infty - [\mathrm{C}_0]\ \exp\{(1-i)\ K\} \forall i > 0 \tag{5.8}$$

with $K = \mathrm{arccosh}(3)$ and $[\mathrm{C}_0] = \frac{k_3}{5-\exp(-K)} \frac{[\mathrm{E_aX}]}{[\mathrm{E_a}]_{\mathrm{T}}} \frac{1}{6lD}$. Here, $[\mathrm{Q}]_{\mathrm{a}_i}, [\mathrm{Q}]_{\mathrm{d_i}}, [\mathrm{Q}]_{\mathrm{o_i}}$ denote, respectively, the concentration of species Q in lattice site number i of a column starting with an activating enzyme, a deactivating enzyme, or in a column that contains neither an activating nor a deactivating enzyme. Furthermore, l is the lattice spacing and D the diffusion coefficient.

Once the concentration profiles are known, the rate equations can be derived straightforwardly. Below, they are compared to the uniform chemical rate equations:

$$\underline{\text{Mean}-\text{field equations for lattice model}}\text{vs.}\underline{\text{Chemical rate equations}}$$

$$[\mathrm{E_aX}] + [\mathrm{E_a}] = [\mathrm{E_a}]_\mathrm{T} \Leftrightarrow [\mathrm{E_aX}] + [\mathrm{E_a}] = [\mathrm{E_a}]_\mathrm{T} \tag{5.9}$$

$$[\mathrm{E_dX^*}] + [\mathrm{E_d}] = [\mathrm{E_d}]_\mathrm{T} \Leftrightarrow [\mathrm{E_dX^*}] + [\mathrm{E_d}] = [\mathrm{E_d}]_\mathrm{T} \tag{5.10}$$

$$[\mathrm{X}]_\infty + [\mathrm{X^*}]_\infty + [\mathrm{E_dX^*}] + [\mathrm{E_aX}] = [\mathrm{S}]_\mathrm{T} \Leftrightarrow \; [\mathrm{X}] + [\mathrm{X^*}] + [\mathrm{E_dX^*}] + [\mathrm{E_aX}] = [\mathrm{S}]_\mathrm{T}$$

$$k_6\ [\mathrm{E_dX^*}] = k_1\ [\mathrm{E_a}]\ \left(\frac{1}{3}[\mathrm{X}]_{\mathrm{a}_1} + \frac{2}{3}[\mathrm{X}]_\infty\right) \Leftrightarrow \; k_6\ [\mathrm{E_dX^*}] = k_1\ [\mathrm{E_a}]\ [\mathrm{X}] \tag{5.11}$$

$$k_3\ [\mathrm{E_aX}] = k_4\ [\mathrm{E_d}]\ \left(\frac{1}{3}[\mathrm{X^*}]_{\mathrm{d}_1} + \frac{2}{3}[\mathrm{X^*}]_\infty\right) \Leftrightarrow \; k_3\ [\mathrm{E_aX}] = k_4\ [\mathrm{E_d}]\ [\mathrm{X^*}] \tag{5.12}$$

$$k_3\ [\mathrm{E_aX}] = k_6\ [\mathrm{E_dX^*}] \Leftrightarrow k_3\ [\mathrm{E_aX}] = k_6[\mathrm{E_dX^*}] \tag{5.13}$$

$$[\mathrm{X}]_{\mathrm{a}_1} = [\mathrm{X}]_\infty - \frac{k_3}{C}\frac{[\mathrm{E_aX}]}{[\mathrm{E_a}]_\mathrm{T}}\frac{1}{6lD}\text{vs.}[\mathrm{X}] = [\mathrm{X}]_\infty \tag{5.14}$$

$$[\mathrm{X^*}]_{\mathrm{d}_1} = [\mathrm{X^*}]_\infty - \frac{k_6}{C}\frac{[\mathrm{E_dX^*}]}{[\mathrm{E_d}]_\mathrm{T}}\frac{1}{6lD}\text{vs.}[\mathrm{X^*}] = [\mathrm{X^*}]_\infty \tag{5.15}$$

Herein, $C = 5 - \exp\{-\operatorname{arccosh}(3)\}$. This system of eight equations can be numerically solved for the eight variables $[\mathrm{X}]_{\mathrm{a}_1}$, $[\mathrm{X^*}]_{\mathrm{d}_1}$, $[\mathrm{E_a}]$, $[\mathrm{E_d}]$, $[\mathrm{E_aX}]$, $[\mathrm{E_dX^*}]$, $[\mathrm{X}]_\infty$ and $[\mathrm{X^*}]_\infty$; once $[\mathrm{E_aX}]$ is known, $[\mathrm{C_0}]$ can be computed, and the concentration profiles can then be obtained from Equations 5.3–5.8.

The black data in Fig. 5.4 show the concentration profiles of $\mathrm{X^*}$ in the lattice columns starting with $\mathrm{E_d}$, as a function of the distance from the membrane; the black lines correspond to the mean-field prediction of Eqs. 5.9–5.15, while the black triangles correspond to the LRD simulation results. Fig. 5.4A shows the concentration profile for a system in the linear regime that is strongly activated ($k_3 = 6600\ \mathrm{s^{-1}}$, compare with Fig. 5.2A); Fig. 5.4B shows the concentration profile for a system in the zero-order regime that is strongly activated ($k_3 = 6600\ \mathrm{s^{-1}}$; compare with Fig. 5.2B). It is seen that the mean-field prediction of Eqs. 5.9–5.15 is highly accurate, both when the system is in the linear regime (Fig. 5.4A) and when the system is in the zero-order regime (Fig. 5.4B). Evidently, the effect of spatio-temporal correlations, which are not captured by the mean-field analysis, is negligible.

The solid black lines in Figs. 5.2A and 5.2B show the mean-field prediction for the steady-state response curves of a system in the linear and zero-order regime, respectively. As expected on the basis of the accurate description of the concentration profiles, the mean-field predictions for the response curves are in excellent agreement with the LRD simulation results.

Enzymes in the cytoplasm: mean-field model

When the enzymes are colocalized in a plane, an accurate mean-field analysis can be developed, as described above. When the enzymes are distributed in the cytoplasm, such an analysis is highly non-trivial, especially when the enzymes also diffuse. The antagonistic enzymes act as sinks and sources of substrate molecules, which gives rise to concentration gradients of X and $\mathrm{X^*}$ around the activating and deactivating enzymes.

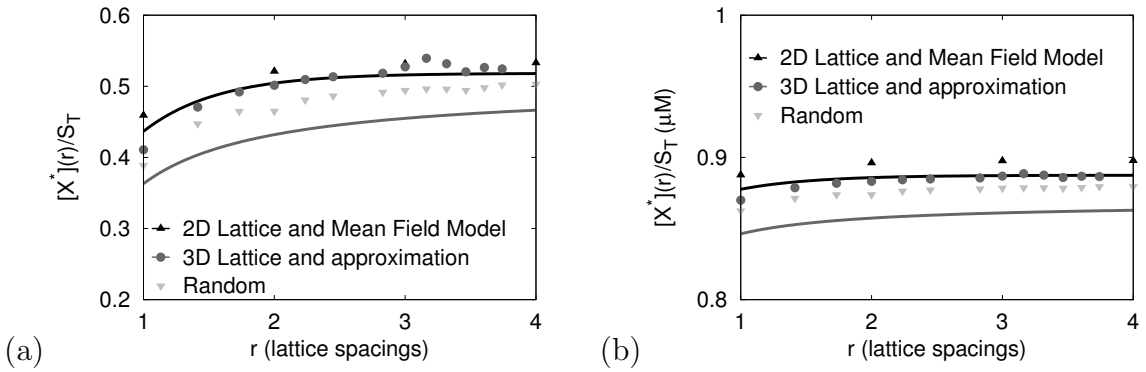

FIGURE 5.4 Concentration profiles of X^* for different spatial arrangement of the antagonistic enzymes. The profiles give the concentration of X^* as a function of the distance to the deactivating enzyme E_d. (A) Results for a network in the linear regime; (B) Results for a network in the zero-order regime. The black triangles show the LRD simulation results when the enzymes are colocalized to the membrane; the black lines show the mean-field predictions of Eqs. 5.9–5.15; shown are the concentration of X^* within *one* column containing a deactivating enzyme E_d, as a function of the distance to that enzyme. The grey circles are LRD simulation results when the enzymes are immobilized on a simple-cubic lattice; the grey lines correspond to the mean-field predictions of 5.22–5.26. The inverted light-grey triangles correspond the scenario in which the enzymes adopt a quenched, random configuration. Please note that the substrate concentration gradients are sharper when the system is in the linear regime (Fig. A). This is because in the linear regime the enzymes are predominantly unoccupied and thus act as strong sinks for the substrate molecules, while in the zero-order regime they are saturated, yielding a reflecting boundary condition for the substrate molecules.

When the enzymes are distributed in 3D space, these gradients interfere with one another, especially when the enzymes diffuse. We will show, however, that a simple analysis, which assumes that on length scales larger than the average spacing between the enzyme molecules the substrate concentration profiles are uniform, gives a reasonable description of the system.

Linear regime In the linear regime, the enzymes are predominantly unoccupied by substrate molecules. This allows for a simple, yet fairly accurate, description of the substrate concentration gradients around the enzyme molecules. Let's focus on one enzyme molecule, say an E_d molecule. The diffusion equation that describes the concentration profile of X^* around that enzyme molecule is

$$\partial_t[\mathrm{X}^*](x) = D\nabla^2[\mathrm{X}^*](x). \tag{5.16}$$

We can solve this diffusion equation in steady state, $\partial_t[\mathrm{X}^*](x) = 0$, with the following boundary conditions:

$$[\mathrm{X}^*](x \to \infty) = [\mathrm{X}^*]_\infty \tag{5.17}$$

$$4\pi\sigma^2 D \left.\frac{\partial[\mathrm{X}^*]}{\partial x}\right|_{x=\sigma} = k_4[\mathrm{X}^*](\sigma) \tag{5.18}$$

Concerning the first boundary condition, we assume that the concentration profiles of the substrate molecules are uniform, except in the vicinity of the enzyme molecules. This seems a strong assumption, since diffusion gives rise to gradients that decay as $1/r$. However, if the concentrations of the enzymes are sufficiently low, then the presence of the other enzyme molecules around an $\mathrm{E_d}$ molecule can be neglected. On a length scale given by the average distance between the enzyme molecules, the concentration of X^* is then, to a good approximation, given by $[\mathrm{X}^*]_\infty$.

The second boundary condition reflects the fact that an $\mathrm{E_d}$ molecule acts as a sink for the X^* molecules. Importantly, since the system is assumed to be in the linear regime, the enzyme is, by definition, unoccupied most of the time. This means that the flux due to diffusion at contact, which is written on the left-hand side of Eq. 5.18, is given by the concentration of X^* at contact, $[\mathrm{X}^*](\sigma)$ (where σ is the cross section or the reaction distance of the enzyme-substrate reaction), times the association rate k_4.

The diffusion equation, Equation 5.16, can now be solved with these two boundary conditions, yielding

$$[\mathrm{X}^*](r) = [\mathrm{X}^*]_\infty + ([\mathrm{X}^*]_{r=\sigma} - [\mathrm{X}^*]_\infty)\,\frac{\sigma}{r} \tag{5.19}$$

with the concentration of X^* at contact given by

$$[\mathrm{X}^*]_{r=\sigma} = \frac{k_4 4\pi\sigma D[\mathrm{X}^*]_\infty}{k_4 + 4\pi\sigma D} \tag{5.20}$$

$$\equiv k_4^{\mathrm{eff}}[\mathrm{X}^*]_\infty \tag{5.21}$$

where k_4^{eff} is the effective association rate, which takes into account that the overall reaction rate depends on both the rate at which substrate molecules diffuse to the enzyme molecules, given by $k_\mathrm{D} = 4\pi\sigma D$, and the reaction rate at contact, k_4: $1/k_4^{\mathrm{eff}} = 1/k_4 + 1/k_\mathrm{D}$ [100]. For the unmodified substrate molecules X a similar analysis can be applied.

This leads to the following set of rate equations:

$$\underline{\text{Mean}-\text{field analysis for 3D lattice}}\text{vs.}\underline{\text{Chemical rate equations}}$$

$$[\mathrm{E_aX}] + [\mathrm{E_a}] = [\mathrm{E_a}]_\mathrm{T} \Leftrightarrow [\mathrm{E_aX}] + [\mathrm{E_a}] = [\mathrm{E_a}]_\mathrm{T} \tag{5.22}$$

$$[\mathrm{E_dX^*}] + [\mathrm{E_d}] = [\mathrm{E_d}]_\mathrm{T} \Leftrightarrow [\mathrm{E_dX^*}] + [\mathrm{E_d}] = [\mathrm{E_d}]_\mathrm{T} \tag{5.23}$$

$$[\mathrm{X}]_\infty + [\mathrm{X}^*]_\infty + [\mathrm{E_dX^*}] + [\mathrm{E_aX}] = [\mathrm{S}]_\mathrm{T} \Leftrightarrow [\mathrm{X}] + [\mathrm{X}^*] + [\mathrm{E_dX^*}] + [\mathrm{E_aX}] = [\mathrm{S}]_\mathrm{T}$$

$$\mathrm{k_3}\ [\mathrm{E_aX}] = \mathrm{k_6}\ [\mathrm{E_dX^*}] \Leftrightarrow \mathrm{k_3}\ [\mathrm{E_aX}] = \mathrm{k_6}\ [\mathrm{E_dX^*}] \tag{5.24}$$

$$\mathrm{k_3}\ [\mathrm{E_aX}] = \mathrm{k_1^{eff}}\ [\mathrm{E_a}]\ [\mathrm{X}]_\infty \text{vs. } \mathrm{k_3}\ [\mathrm{E_aX}] = \mathrm{k_1}\ [\mathrm{E_a}]\ [\mathrm{X}] \tag{5.25}$$

$$\mathrm{k_6}\ [\mathrm{E_dX^*}] = \mathrm{k_4^{eff}}\ [\mathrm{E_d}]\ [\mathrm{X}^*]_\infty \text{vs. } \mathrm{k_6}\ [\mathrm{E_dX^*}] = \mathrm{k_4}\ [\mathrm{E_d}]\ [\mathrm{X}^*] \tag{5.26}$$

The last two equations reveal that the effect of the substrate concentration gradients can, in this simple model, be captured by replacing the intrinsic association rates, k_1 and k_4, respectively, by the effective association rates, k_1^{eff} and k_4^{eff}, respectively. The

last three equations show in combination with Equations 5.18 and 5.21, that in steady state, $J_{\rm in}^{\rm X} = J_{\rm D}^{\rm X} = J_{\rm out}^{\rm X} = J_{\rm in}^{\rm X^*} = J_{\rm D}^{\rm X^*} = J_{\rm out}^{\rm X^*}$, where $J_{\rm in}^{\alpha}$, $J_{\rm D}^{\alpha}$, $J_{\rm out}^{\alpha}$, are the influx, flux due to diffusion, and outflux of species α, respectively. For instance, the influx of species $\rm X^*$ is given by $J_{\rm in}^{\rm X^*} = k_3[\rm E_aX]$, while the outflux of species $\rm X^*$ is given by $k_4\langle N_{\rm E_d} N_{X^*}(\sigma)\rangle/V^2 \approx k_4^{\rm eff}[\rm E_d][X^*]_\infty$, where N_α is the copy number of species α. This illustrates that each substrate molecule undergoes the cycle $\rm X \rightarrow E_aX \rightarrow X^* \rightarrow E_dX^* \rightarrow X \ldots$, where in steady state the flux along the cycle is constant.

Figure 5.4A shows the concentration profiles as obtained from the LRD simulations (grey circles) and as obtained by numerically solving Eqns. 5.22-5.26 (grey line) for a system in the linear regime. Figure 5.2A compares the input-output curve as measured in the LRD simulations to the prediction of Eqns. 5.22-5.26 (grey line) for the same system. It is seen that the solution of the diffusion equation, Equation 5.19, underestimates the concentration profiles around the enzyme molecules (Fig. 5.4A). Yet, this simple analysis gives a remarkably accurate prediction for the dose-response curves (Fig. 5.2A).

The critical assumption in the above analysis is that the outflux of $\rm X^*$ is given by $J_{\rm out}^{X^*} = k_4\langle N_{\rm E_d} N_{X^*}(\sigma)\rangle/V^2 \approx k_4^{\rm eff}[\rm E_d][X^*]_\infty$, and similarly for X. This assumption seems reasonable when the system is in the linear regime: in this regime, the enzyme molecules are predominantly unoccupied; as a consequence, when a substrate molecule encounters an enzyme molecule, the two can react with an intrinsic association rate k_1 or k_4; this gives rises to concentration gradients given by Equation 5.19 and an outflux of $\rm X^*$ that is simply given by the total number of $\rm E_d$ molecules times $k_4[\rm X^*](\sigma)$, and an efflux of X that is given by the total number of $\rm E_a$ molecules times $k_1[\rm X](\sigma)$.

Zero-order regime In the zero-order regime, one or both of the enzyme species are highly saturated with substrate. For instance, if the input signal k_3 is high, $\rm E_d$ will be predominantly occupied by $\rm X^*$ molecules. As a result, most of the collisions of the $\rm X^*$ molecules with the $\rm E_d$ molecules will be non-reactive. This tends to lower the effective $\rm E_d$-$\rm X^*$ association rate and reduce the gradient of $\rm X^*$. Fig. 5.4B (grey lines) shows that Equation 5.19 indeed leads to a poor prediction for the substrate concentration profile when the system is in the zero-order regime. Nevertheless, even though the average concentration profile is close to a uniform profile, the average enzyme-substrate reaction time is, to a good approximation, given by $1/k_{\rm eff}$. We have therefore plotted the prediction of Eqns. 5.22-5.26 for the response curve of a system in the zero-order regime in Fig. 5.2B. It is seen that the agreement with the LRD simulation results is surprisingly good.

5.3.4 Gradients can both reduce and enhance the response

The results above demonstrate that substrate concentration gradients can reduce the strength of the response. However, substrate concentration gradients can also *enhance* the response of the network. This is illustrated in Fig. 5.5. This figure shows the response of a system with a lower association rate between the activating enzyme $\rm E_a$ and substrate X. By comparing the LRD simulation results (symbols) with the prediction of the chemical rate equations (dashed black line), which ignores spatial gradients, it is seen that concentration gradients can indeed enhance the response of a push-pull network.

In order to understand the effect of substrate concentration gradients on the response curve, it should be realized that when the diffusion constants of X and $\rm X^*$ are the same, *the concentration gradient of* X *near* $\rm E_a$ *is the same as that of* $\rm X^*$ *near* $\rm E_d$*, once the system*

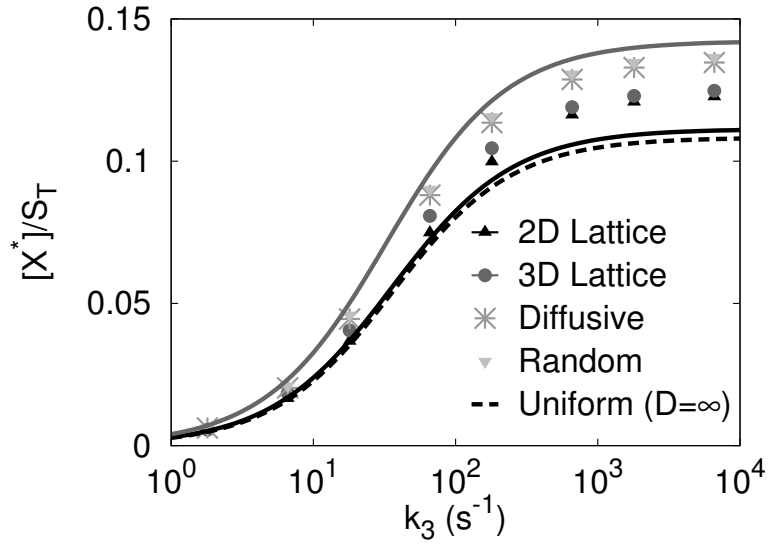

FIGURE 5.5 Response of X^* as a function of k_3 when the E_a-X association rate is such that it limits the response; compared to Fig. 5.2, the E_a-X association rate is reduced by a factor ten ($k_1 = 1.08\,10^7 M^{-1}s^{-1}$). For explanation of lines and symbols, see Fig. 5.2. By comparing the symbols, which are the LRD simulation results, with the dashed black line, which corresponds to the prediction of the chemical rate equation that ignores spatial concentration gradients, it is seen that gradients can not only reduce the response, as shown in Fig. 5.2, but also enhance the response. The reason is that the effect of the reduction of the enzyme-substrate association rate resulting from the substrate concentration gradients, is larger for the minority substrate species.

is in steady state. This statement reflects the fact that in steady state, the diffusive flux of X^* from E_a to E_d which is given by $D\nabla[X]$ must equal the diffusive flux of X from E_d to E_a which is given by $D\nabla[X^*]$. This means that if we write the concentration of X in contact with E_a as $[X](\sigma) = [X]_\infty - \epsilon$, where ϵ denotes the deviation from the uniform profile $[X]_\infty$ due to the gradient, then the concentration of X^* at contact with E_d is given by $[X^*](\sigma) = [X^*]_\infty - \epsilon$. Now, if [X] is high and $[X^*]$ is thus low, then the *relative* decrease in the E_a-X association rate, given by $([X] - \epsilon)/[X])$, will be small , while the relative decrease in the E_d-X^* association rate, $([X^*] - \epsilon)/[X^*])$ will be large. As a result, the production of X^*, which is given by $J^* = k_3[E_aX] = k_1[E_a][X](\sigma)$, will decrease more as a result of the gradient than the production of X, which is given by $J = k_6[E_dX^*] = k_4[E_d][X^*](\sigma)$. Thus, when the diffusion constants of X and X^* are equal, concentration gradients will decrease the concentration of X^* when $[X^*]$ is high, and increase $[X^*]$ when $[X^*]$ is low. This is precisely what is observed in Figs. 5.2 and 5.5: in Fig. 5.2, $[X^*]$ is large when k_3 is large; in this regime, gradients reduce the response; in Fig. 5.5, $[X^*]$ is small even when k_3 is large, because of the limiting E_a-X association rate; in this regime, gradients enhance the response.

5.4 Discussion and conclusions

It is becoming increasingly clear that enzymes are often colocalized to the plasma membrane. Here, we address the question how colocalization affects the response characteristics of a push-pull network using particle-based simulations. The principal result is that colocalization *per se* does not strongly affect the steady-state input-output relation (see Fig. 5.2). The reason is that to the extent that spatial concentration gradients can be neglected, the spatial distribution of the enzymes does not affect the degree to which they are saturated with substrate. The average enzyme occupancy is determined by the ratio of the catalytic rate and the effective association rate. Colocalization leads to a wide distribution of association times: as compared to the scenario in which the enzymes are distributed in the cytoplasm, enzyme colocalization leads not only to a higher probability of short association times, but also to a higher fraction of substrate molecules with long enzyme-association times (see Fig. 5.3). The net result is that the average association time, and hence the average enzyme occupancy, is unaffected by the spatial distribution of the enzymes.

The wide distribution of enzyme-substrate association times in the scenario in which the enzymes are colocalized, means that the dynamics of the response of the network to an external signal will be markedly different from the well-stirred case. Colocalization allows for signalling at both early and late times. Controlling the times over which the substrate molecules are activated may be exploited in directing a specific response in downstream signalling pathways. For instance, recent experiments have shown that in some MAPK pathways, *specificity* is encoded in the duration of MAPK activation [101]. Our prediction that colocalization affects the distribution of response times could be tested in experiments that monitor time courses of activated proteins, for instance using Förster Resonance Energy Transfer (FRET).

Comparing the LRD simulation results with the predictions of mean-field analyses, shows that the effect of spatio-temporal correlations is small, even though the copy numbers are relatively small: while the total number of substrate molecules varied between 30 and 120 molecules, the total number of molecules of each enzyme species was only 8. The main deviations from the predictions of the chemical rate equations are due to the presence of substrate concentration gradients, both in the scenario that the enzymes are colocalized and in the scenario in which the enzymes are distributed in the cytoplasm (Fig. 5.4). Simple mean-field models that take into account the spatial concentration gradients, give a remarkably good description of the steady-state input-output curves (Fig. 5.2). These results support the use of chemical rate equations for describing the steady-state response curves, even when the copy numbers are as low as 10. However, if one is interested in the distribution of response times, then stochastic, spatially-resolved simulation schemes are required—the wide distribution of time scales, as observed for the system in which the enzymes are colocalized, cannot be captured by mean-field reaction-diffusion equations.

We should discuss one limitation of our current model that could affect our conclusions. In our model, the maximum *intrinsic* association rate, k_1, is given by the diffusion-limited association rate: a reaction can occur only when a trial *diffusion* move leads to an overlap between reaction partners; this move is accepted with a probability $P = k_1 \Delta t / l^3$, with $\Delta t = l^2/(6D)$; consequently, the maximum association rate, obtained

by taking $P = 1$, is given by $k_1 = l^3/\Delta t = 6lD$, which is the diffusion-limited rate for a system on a lattice. With an alternative scheme, it would be possible to achieve higher intrinsic association rates: for instance, a scheme in which two reaction partners can react with a probability P_{react} when they are adjacent on the lattice, and particles diffuse by making hops with a probability $P_{\mathrm{hop}} < P_{\mathrm{react}}$, will yield intrinsic association rates that are higher than the diffusion-limited rate. This will generate larger concentration gradients of substrate molecules around the enzyme molecules. Indeed, it would be of interest to study whether a) also in this regime colocalization of the enzymes has only a small affect on the steady-state input-output relation; b) whether the mean-field analyses given here still give a good description of the response curve. Yet, it should be realized that the biological relevance of such a study strongly depends on the values of the intrinsic protein-protein association rates in nature. If we assume that the maximum intrinsic association rate is given by the time scale on which two proteins in close proximity diffuse over a molecular length scale λ into contact, then $k_{\mathrm{a}}^{\mathrm{max}}$ would be given by $k_{\mathrm{a}}^{\mathrm{max}} = 4\pi\sigma^2 D/\lambda$; the enhancement over the diffusion limited rate, $k_{\mathrm{D}} = 4\pi\sigma D$, would thus be $k_{\mathrm{a}}^{\mathrm{max}}/k_{\mathrm{D}} = \sigma/\lambda$. Clearly, if we assume that the molecular length scale λ is given by the diameter of the proteins, σ, then the maximum association rate is given by the diffusion-limited rate, which is, indeed, precisely the value we have taken here. In general, however, λ could be smaller than σ, leading to a higher intrinsic association rate. To our knowledge, intrinsic protein-protein association rates have not been measured systematically. This would require experiments in which not only the effective association rates are measured, $1/k_{\mathrm{eff}} = 1/k_{\mathrm{a}} + 1/(4\pi\sigma D)$, but also the diffusion constants of the proteins.

Lastly, we would like to mention that while the close physical proximity between the antagonistic enzymes that arises from colocalization might not by itself affect the response curve, the interplay between colocalization and other factors could change the steady-state input-output relation. For instance, if the substrate molecules have an affinity for the membrane, or for a receptor cluster at the membrane as in the chemotaxis system of *E. coli*, then this could enhance the substrate concentration at the membrane. If both enzymes are colocalized at the membrane, then this higher substrate concentration could increase the overall enzyme-substrate association rate and thereby enhance the sharpness of the response.

5.5 Methods

5.5.1 Overview of techniques to simulate biochemical networks

The conventional approach to simulate biochemical networks is to write down the differential equations corresponding to the chemical rate equations, and to propagate the equations in time. In this approach, the evolution of the network is deterministic: it is assumed that the concentrations are large and that fluctuations can be neglected. If the spatial distribution of the components is important, the macroscopic reaction-diffusion equations can be solved numerically. While this technique describes the network in time and space, it does assume that fluctuations are unimportant and that the evolution of the network is deterministic.

The most popular scheme to take into account fluctuations is the Gillespie algorithm [102]. The Gillespie algorithm is a kinetic Monte Carlo algorithm [103] that allows the efficient simulation of the zero-dimensional chemical master equation. This approach takes into account the stochastic character of chemical reactions and the discrete nature of the components. However, it does assume that the system is well-stirred. The scheme can therefore not be used when there are spatial concentration gradients. Moreover, even when there are no concentration gradients on average, the scheme may not be applicable. Even when the system is spatially uniform on average, the zero-dimensional master equation does make the assumption that the particles are uniformly distributed in space *at all times*; the approach thus relies on many non-reactive collisions in between the reactive collisions to stir the system. The validity of this assumption increases as the probability of reaction upon collision decreases, thus as the intrinsic reaction rate (the reaction rate when the reactants are at contact) decreases. The scheme also becomes more accurate as the diffusion constant increases—the higher the diffusion constant, the more the system is stirred in between the reactive collisions. The accuracy of this approach decreases as the concentrations of the components decrease. This is interesting, because the scheme is typically used at low concentrations, where the stochastic character of the reactions and the discrete nature of the components becomes important. But at sufficiently low concentrations, not only the stochastic character of the reactions becomes important, but also the spatial fluctuations due to the diffusive motion of the components [96].

If the spatial distribution of the components and the stochastic character of the interactions are important, several approaches can be taken. One class of techniques is based upon the reaction-diffusion master equation [104, 105, 106, 107]. In this approach, the system is divided into little cells; components can react within each cell and diffuse from one cell to the next. Importantly, it is assumed that within each cell, the system is well-stirred; the approach thus relies on a length scale on which the particles are uniformly distributed. Another class of techniques simulate biochemical networks at the particle level in time and space. While schemes based on the reaction-diffusion master equation are relatively fast at higher concentrations, particle-based schemes are more efficient at low concentrations of the components. Moreover, the assumption of the existence of a length scale on which the system is uniform, becomes less accurate as the concentrations of the components decrease.

In recent years, several particle-based techniques have been developed. One class of techniques is based upon Brownian Dynamics [108, 109, 110, 111]. In Brownian Dynamics, the particles are propagated according to the overdamped limit of the Langevin equation. When two reaction partners happen to meet each other, they can react with a probability that is consistent with the reaction rate. Brownian Dynamics is a truly particle-based simulation scheme, but has the disadvantage that small time steps are needed in order to properly resolve the collision events. We have recently developed a particle-based scheme, called Green's Function Reaction Dynamics (GFRD) [90, 91], that uses Green's functions to concatenate the propagation of the particles in space with the chemical reactions between them. The crux of GFRD is to exploit the Green's functions to set up an event-driven algorithm, in which the system jumps from one reaction event to the next. This event-driven nature makes it possible to make large jumps in time and space when the particles are far apart. However, in the system considered here,

all reactions take place at the membrane, where the reactants are close to each other. This makes GFRD relatively inefficient.

We have therefore developed a particle-based simulation scheme in which the particles are propagated on a lattice. The lattice-based nature makes the algorithm very fast, since one can rapidly check for overlap with potential reaction partners. In the next section, we describe our lattice-based reaction-diffusion algorithm, which, for convenience, we will refer to as Lattice Reaction Dynamics (LRD).

5.5.2 Lattice Reaction Dynamics (LRD)

In most lattice-based simulation schemes of reaction-diffusion systems, all the particles are first propagated in space, without checking for overlap; in the second step, particles that occupy the same lattice site can react with a probability as given by the reaction rate. These algorithms propagate the system according to the reaction-diffusion master equation; they are indeed very similar to the schemes of [104, 105, 106, 107]. However, these algorithms do not take into account excluded volume interactions.

LRD takes into account excluded volume interactions. The particles are propagated on a simple cubic lattice of $M_x \times M_y \times M_Z = M$ lattice sites. Each particle takes up exactly one lattice site and at most one particle can occupy a single lattice site—this reflects the excluded volume interactions. The lattice spacing, l, corresponds to the typical size of a protein. Each time step Δt, each diffusive particle can hop to a neighboring lattice site with a probability p_α if the neighboring site is unoccupied; if the chosen lattice site is occupied and no reaction between the two particles can occur, the trial displacement is rejected. At low densities, when excluded volume interactions can be neglected, the particles of type α will move with a diffusion coefficient $D_\alpha = l^2/(6p_\alpha\Delta t)$. In what follows, we assume that the diffusion coefficients of all the different species are the same, and that $p_\alpha = 1$.

Next, we will discuss how unimolecular and bimolecular reactions are taken into account. For this purpose, let us consider the reversible chemical reaction

$$A + B \underset{k_\mathrm{d}}{\overset{k_\mathrm{a}}{\rightleftharpoons}} C, \tag{5.27}$$

Herein, k_a is the intrinsic association rate, i.e. the association rate given that a pair of particles A and B is at contact; k_d is the intrinsic dissociation rate, which is the rate that a C particle dissociates into a particle A and a particle B that are at contact. In LRD, a pair of particles A and B can react when a move of either an A or a B particle leads to an overlap of these two particles. The probability $P_{\mathrm{acc,u\to b}}$ that such an overlap leads to a reaction is related to the intrinsic association rate k_a, as described below. Conversely, a C particle can dissociate into a pair of A and B particles with a probability $P_{\mathrm{acc,b\to u}}$ that is related to the intrinsic dissociation rate k_d. In LRD, the association and dissociation moves are constructed such that detailed balance is obeyed [112]. The detailed-balance condition for one given pair of particles A and B is

$$P_\mathrm{u}(\mathbf{r}_A, \mathbf{r}_B) P_{\mathrm{gen,u\to b}} P_{\mathrm{acc,u\to b}} = P_\mathrm{b}(\mathbf{r}_C) P_{\mathrm{gen,b\to u}} P_{\mathrm{acc,b\to u}} \tag{5.28}$$

Here, $P_\mathrm{u}(\mathbf{r}_A, \mathbf{r}_B)$ is the probability that the A and B particles are not bound and at position $\mathbf{r}_A$ and $\mathbf{r}_B$, respectively; $P_\mathrm{b}(\mathbf{r}_C)$ is the probability that the particles form the bound particle C at position $\mathbf{r}_C$; $P_{\mathrm{gen,u\to b}}$ and $P_{\mathrm{acc,u\to b}}$ are the probabilities of generating and accepting the association moves, respectively, while $P_{\mathrm{gen,b\to u}}$ and $P_{\mathrm{acc,b\to u}}$ are the

probabilities of generating the dissociation moves. The probabilities $P_{\rm u}(\mathbf{r}_A, \mathbf{r}_B)$ and $P_{\rm b}(\mathbf{r}_C)$ can be obtained by noting that the probability $P(\mathbf{r}_A^{N_A}, \mathbf{r}_B^{N_B}, \mathbf{r}_C^{N_C}; \{N_A, N_B, N_C\})$ that the system has (N_A, N_B, N_C) molecules *and* that these molecules are located at positions $\{\mathbf{r}_A^1, \cdots, \mathbf{r}_A^{N_A}\}$, $\{\mathbf{r}_B^1, \cdots, \mathbf{r}_B^{N_B}\}$, $\{\mathbf{r}_C^1, \cdots, \mathbf{r}_C^{N_C}\}$ is

$$P(\mathbf{r}_A^{N_A}, \mathbf{r}_B^{N_B}, \mathbf{r}_C^{N_C}; \{N_A, N_B, N_C\}) = \frac{q_{A,\rm cm}^{N_A} q_{B,\rm cm}^{N_B} q_{C,\rm cm}^{N_C}}{\mathcal{Q}}, \tag{5.29}$$

where $q_{X,\rm cm}$ is the partition function corresponding to the degrees of freedom of the center of mass of a particle X, and $\mathcal{Q}$ is the canonical partition function of the system. The ratio of probabilities of being in the bound vs unbound state is therefore given by

$$\frac{P_{\rm b}(\mathbf{r}_C)}{P_{\rm u}(\mathbf{r}_A, \mathbf{r}_B)} = \frac{q_{C,\rm cm}}{q_{A,\rm cm} q_{B,\rm cm}} \equiv K_{\rm eq} = \frac{k_{\rm a}}{k_{\rm d}}, \tag{5.30}$$

where $K_{\rm eq}$ is the equilibrium constant. The detailed-balance condition, Equation 5.28, then becomes

$$\frac{P_{\rm gen,u\to b} P_{\rm acc,u\to b}}{P_{\rm gen,b\to u} P_{\rm acc,b\to u}} = \frac{k_{\rm a}}{k_{\rm d}}. \tag{5.31}$$

In practice, we have adopted the following simulation scheme

1. Select a particle.
2. If the particle is
   (a) a C particle, then
      (i) Try to dissociate the particle with probability $P_{\rm acc,b\to u} = k_{\rm d}\Delta t$.
      (ii) If accepted: put either the A or the B particle at the site previously occupied by the C particle with a probability of a half; attempt to put the other particle onto one of the z neighbouring sites; if this neighbouring site is occupied, reject the whole move.
      If not accepted: attempt to move the C particle to one of the neighbouring sites. If the attempted site is occupied, reject the move.
   (b) an A or a B particle, then attempt to move the particle to one of the z neighbouring sites. If the neighbouring site
      (i) contains a reaction partner, then accept the move with a probability $P_{\rm acc,u\to b} = 1/2\ N/(N-1) k_a \Delta t$, where N is the total number of particles in the system. Put the C particle at either the site previously occupied by A or by B with a probability of a half. If not accepted, put the particle back at its original spot.
      (ii) contains an other particle, reject.
      (iii) is empty, then accept the move.

It can be verified that this scheme satisfies detailed balance:

$$\frac{P_{\rm b}(\mathbf{r}_C)}{P_{\rm u}(\mathbf{r}_A, \mathbf{r}_B)} = \frac{P_{\rm gen,u\to b} P_{\rm acc,u\to b}}{P_{\rm gen,b\to u} P_{\rm acc,b\to u}} \tag{5.32}$$

$$= \frac{[2/N\ 1/z\ 1/2]\ \ (1/2\, k_{\rm a}\Delta t N/(N-1))}{[1/(N-1)\ 1/z\ 1/2]\ \ (k_d \Delta t)} \tag{5.33}$$

$$= \frac{k_{\rm a}}{k_{\rm d}}. \tag{5.34}$$

Here, the factors between the square brackets [...] correspond to the generation moves, while the factors between normal brackets (...) correspond to the acceptance moves. Typically, N is large enough that the factor $N/(N-1)$ can be neglected. The association move is then accepted by $k_\mathrm{a}\Delta t/2$, where the factor 2 comes from the fact that there are two ways of generating an overlap (selecting A and moving it onto B, and vice versa). Typically, association rates are given in units of volume per second. In this case, the trial association move should be accepted with a probability $k_\mathrm{a}\Delta t/(2l^3)$.

Appendix: Mean-field model Colocalization

We will derive mean-field relations for the steady state concentrations of substrate and enzyme for a push-pull network in which the antagonistic enzymes are arranged in a two-dimensional checkerboard pattern, for the setup described in Fig. 5.1. The activating enzymes $\mathrm{E_a}$ and deactivating enzymes $\mathrm{E_d}$ form a checkerboard pattern in the first plane of the lattice. The greyscale of the remaining lattice sites denotes the average concentration of active substrate $\mathrm{X^*}$. We will consider a cell that is very long in the direction perpendicular to the plane formed by the enzymes, with periodic boundary conditions in all three dimensions.

We will refer to the lattice sites in the columns starting with $\mathrm{E_a}$ by $\mathrm{a}_0, \mathrm{a}_1, \mathrm{a}_2, ...$, to the lattice sites in the columns starting with $\mathrm{E_d}$ by $\mathrm{d}_0, \mathrm{d}_1, \mathrm{d}_2, ...$ and to the lattice sites in the columns without any enzymes by $\mathrm{o}_0, \mathrm{o}_1, \mathrm{o}_2, ...$ The enzymes themselves are located at positions a_0 and d_0.

If the system is in steady state, gradients of substrate will arise around the enzymes. Because the activating and deactivating enzymes act as sources and sinks for $\mathrm{X^*}$, respectively, the concentration of $\mathrm{X^*}$ is highest near $\mathrm{E_a}$ and lowest near $\mathrm{E_d}$, as indicated by the greyscales in Fig. 5.1.

In the following, we will make use of the symmetries of the system. First, it can be seen that all columns starting with an activating enzyme are equivalent. The same holds for all columns starting with a deactivating enzyme, and all columns not containing any enzymes. Next, since the system is in steady state, the rate at which X is converted to $\mathrm{X^*}$ by the activating enzyme $\mathrm{E_a}$ equals the rate at which $\mathrm{X^*}$ is converted back to X by the deactivating enzyme $\mathrm{E_d}$. As a consequence, the gradients of X and $\mathrm{X^*}$ around the activating enzymes are exactly opposite to the respective gradients around the deactivating enzymes. Interchanging all activating and deactivating enzymes therefore has the result that all gradients are inverted. However, the effect of interchanging all activating and deactivating enzymes can also be achieved by shifting the whole system by one lattice spacing over the diagonal of the checkerboard. For the set of columns in between the enzymes, which stays at the same position under both transformations, this means that inverting the gradients leaves the concentrations unaltered. Therefore, the concentrations of X and $\mathrm{X^*}$ must be constant in these columns: the values are the same as the concentrations far away from the enzymes, $\mathrm{X}_{\mathrm{o}_i} = \mathrm{X}_\infty$ and $\mathrm{X}^*_{\mathrm{o}_i} = \mathrm{X}^*_\infty$ $(i = 0 \ldots \infty)$. It also follows from the symmetry of the system that the concentration gradients of X are exactly opposite to the gradients of $\mathrm{X^*}$ at all lattice sites, such that the total substrate concentration $\mathrm{S_T}$ is constant over space.

For all lattice sites that are not directly neighbouring an enzyme, the steady state concentrations of X and X* are fully governed by the homogeneous diffusion equation, also called the Laplace equation. On a lattice, the solution to the Laplace equation satisfies the condition that all local concentrations equal the average over the six neighbouring lattice sites:

$$0 = \frac{\Delta[\mathrm{X}]_{\mathrm{a}_i}}{\Delta t} = \frac{D}{l^2}\Big(4\ [\mathrm{X}]_{\mathrm{o}_i} + [\mathrm{X}]_{\mathrm{a}_{i-1}} + [\mathrm{X}]_{\mathrm{a}_{i+1}} - 6\ [\mathrm{X}]_{\mathrm{a}_i}\Big)\forall i > 1 \tag{5.35}$$

$$0 = \frac{\Delta[\mathrm{X}]_{\mathrm{d}_i}}{\Delta t} = \frac{D}{l^2}\Big(4\ [\mathrm{X}]_{\mathrm{o}_i} + [\mathrm{X}]_{\mathrm{d}_{i-1}} + [\mathrm{X}]_{\mathrm{d}_{i+1}} - 6\ [\mathrm{X}]_{\mathrm{d}_i}\Big)\forall i > 1 \tag{5.36}$$

$$0 = \frac{\Delta[\mathrm{X}^*]_{\mathrm{a}_i}}{\Delta t} = \frac{D}{l^2}\Big(4\ [\mathrm{X}^*]_{\mathrm{o}_i} + [\mathrm{X}^*]_{\mathrm{a}_{i-1}} + [\mathrm{X}^*]_{\mathrm{a}_{i+1}} - 6\ [\mathrm{X}^*]_{\mathrm{a}_i}\Big)\forall i > 1 \tag{5.37}$$

$$0 = \frac{\Delta[\mathrm{X}^*]_{\mathrm{d}_i}}{\Delta t} = \frac{D}{l^2}\Big(4\ [\mathrm{X}^*]_{\mathrm{o}_i} + [\mathrm{X}^*]_{\mathrm{d}_{i-1}} + [\mathrm{X}^*]_{\mathrm{d}_{i+1}} - 6\ [\mathrm{X}^*]_{\mathrm{d}_i}\Big)\forall i > 1 \tag{5.38}$$

Herein, [...] denotes the local concentration of the different components, which is defined as the probability that a particle occupies a given lattice site divided by the volume l^3 of a lattice site. $\frac{\Delta[...]}{\Delta t}$ denotes the change in concentration in a finite time step $\Delta t \equiv \frac{l^2}{6D}$. The solution to the above equations with the aforementioned boundary conditions is of the form

$$[\mathrm{X}]_{\mathrm{o}_i} = [\mathrm{X}]_\infty \forall i \tag{5.39}$$

$$[\mathrm{X}^*]_{\mathrm{o}_i} = [\mathrm{X}^*]_\infty \forall i \tag{5.40}$$

$$[\mathrm{X}]_{\mathrm{a}_i} = [\mathrm{X}]_\infty - [\mathrm{C}_0]\ \exp\{(1-i)\ K\}\forall i > 0 \tag{5.41}$$

$$[\mathrm{X}^*]_{\mathrm{a}_i} = [\mathrm{X}^*]_\infty + [\mathrm{C}_0]\ \exp\{(1-i)\ K\}\forall i > 0 \tag{5.42}$$

$$[\mathrm{X}]_{\mathrm{d}_i} = [\mathrm{X}]_\infty + [\mathrm{C}_0]\ \exp\{(1-i)\ K\}\forall i > 0 \tag{5.43}$$

$$[\mathrm{X}^*]_{\mathrm{d}_i} = [\mathrm{X}^*]_\infty - [\mathrm{C}_0]\ \exp\{(1-i)\ K\}\forall i > 0 \tag{5.44}$$

with $K = \mathrm{arccosh}(3)$. This can be verified by substitution of Eqns. 5.39- 5.44 in Eqns. 5.35- 5.38.

The value of $[\mathrm{C}_0]$ can be determined from the boundary conditions, e.g.:

$$0 = \frac{\Delta[\mathrm{X}^*]_{\mathrm{a}_1}}{\Delta t} = \frac{D}{l^2}\Big(4\ [\mathrm{X}^*]_{\mathrm{o}_1} + [\mathrm{X}^*]_{\mathrm{a}_2} - 5\ [\mathrm{X}^*]_{\mathrm{a}_1}\Big) + k_3\ \frac{[\mathrm{E_aX}]}{[\mathrm{E_a}]_\mathrm{T}}\ \frac{1}{6l^3} \tag{5.45}$$

$$= \frac{D}{l^2}\Big([\mathrm{C}_0]\ \{\exp(-K) - 5\} + k_3\ \frac{[\mathrm{E_aX}]}{[\mathrm{E_a}]_\mathrm{T}}\ \frac{1}{6lD}\Big) \tag{5.46}$$

$$\Rightarrow [\mathrm{C}_0] = \frac{k_3}{5 - \exp(-K)}\frac{[\mathrm{E_aX}]}{[\mathrm{E_a}]_\mathrm{T}}\frac{1}{6lD} \tag{5.47}$$

Eq. 5.45 describes the change in the concentration of X* per time step Δt at position a_1, which is the position in the cytoplasm adjacent to an activating enzyme $\mathrm{E_a}$. The first three terms on the right-hand side describe the diffusive flux of X*, while the last term describes the influx of X* due to the production of X* at a_0. The influx equals the local concentration of $\mathrm{E_a}$ at position a_0, l^{-3}, times the probability that $\mathrm{E_a}$ is in the form $\mathrm{E_aX}$, $\frac{[\mathrm{E_aX}]}{[\mathrm{E_a}]_\mathrm{T}}$, multiplied by the catalytic activity k_3 and 1/6 since a molecule X* can be put in one of the 6 sites that are adjacent to $\mathrm{E_a}$. Now, the concentration profiles are known,

the rate equations can be derived straightforwardly. They are shown in Eqs. 5.9–5.15 of the main text.

6 Switching dynamics of the bacterial flagellar motor

Many swimming bacteria are propelled by flagellar motors that can rotate in two directions. Recent experiments by Cluzel and coworkers [Korobkova et al.*, Phys Rev. Lett* **96***, 058105 (2006)] showed that the switching dynamics of the rotary flagellar motor of* Escherichia coli *exhibits a peak in the power spectrum. We present a statistical-mechanical model for the switching dynamics of a bacterial flagellar motor. The model predicts that the peak in the power spectrum is caused by the interplay between the relaxation dynamics of the flagellum after a switching event and the exponential dependence of the switching propensity on the torque that is exerted on the motor. The model also predicts that at high viscous loads and low rotation speeds, the average switching frequency is fairly independent of the load, but that the switching frequency linearly decreases with speed for rotation speeds higher than about 25-50 Hz.*

6.1 Introduction

The bacterium *Escherichia coli* is able to swim towards attractants such as sugars, amino acids, oxygen and minerals, and away from repellents like salts, acids, bases and alcohols. It is propelled by several flagella. Each flagellum is under the action of a rotary motor, which can rotate either in a clockwise (CW) or a counterclockwise (CCW) direction. When all the motors run in the counterclockwise direction, the flagella form a helical bundle and the bacterium swims smoothly. When one motor runs in the clockwise direction, however, the connected flagellum adopts a semi-coiled or curled conformation and the bacterium performs a so-called tumble. These tumble events randomize the cell's trajectory, and it is the modulation of their occurrence that allows *E. coli* to chemotax. Here, we present a statistical-mechanical model of the switching dynamics of the rotary motor. The model predicts that the peak in its power spectrum, as recently observed by Cluzel *et al.* [49], arises from the interplay of the dependence of the switching frequency on the load and the dynamics of the flagellum.

A cartoon of the bacterial flagellar motor is shown in Fig. 6.1. It consists of a protein complex called the rotor, and a number of stator proteins that are fixed in the inner membrane and the peptidoglycan layer. Forces applied by the stator proteins on a ring of FliG proteins of the rotor protein complex drive the rotation of the rotor, and thereby the rotation of the flagellum, which is connected to the rotor. The rotation of the motor is powered by a flow of protons down an electrochemical gradient across the cytoplasmic membrane. The switching of the rotation direction is determined by the concentration of the phosophorylated form of the messenger protein CheY. The

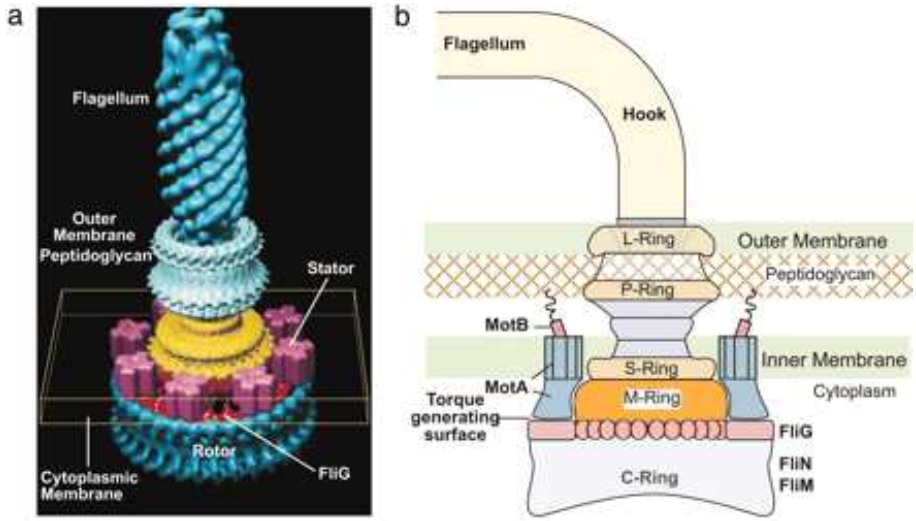

FIGURE 6.1 Cartoon of the flagellar motor of the bacterium *E. coli*. The figure is taken from Ref. [114]

concentration of phosphorylated CheY, $\mathrm{CheY_p}$, depends upon the phosphatase activity of CheZ and the kinase activity of CheA; the latter, in turn, depends upon the activity of the receptor cluster, which is determined by the degree of receptor methylation, necessary for adaptation, and ligand binding.

To elucidate the working principles of the bacterial flagellar motor, a number of motor characteristics have to be understood. One is the torque-speed relationship of the motor. At low speeds, the torque varies linearly with speed. Beyond a "knee" velocity of around 200 Hz, however, the torque rapidly drops to reach zero at around 300 Hz [113]. Recently, Oster *et al.* developed a mathematical model [114] that is based on the qualitative proposal of Blair and coworkers [115]. In this model, the binding and unbinding of protons to the stator proteins drive conformational transitions of the stator proteins, which, in turn, allow the stator proteins to exert a force on the FliG rotor proteins. This model can describe the torque-speed relationship, as well as the linear dependence of the motor rotation speed on the proton motive force at low and high rotation speeds.

Another characteristic of the motor is the power spectrum computed from binary time series of CW↔CCW switching. Recently, Cluzel and coworkers measured power spectra by monitoring the rotation of a 0.5 μm latex bead connected to a flagellum [48, 49]. Intriguingly, the measured power spectra are not consistent with a two-state Poisson process, in which the switching events are independent and the CW and CCW intervals are uncorrelated and exponentially distributed. The power spectrum of *wild-type* cells exhibits a power-law frequency dependence at low frequencies [48]. Experiments and simulations by the same group [48] and theory by Tu and Grinstein [116] revealed that the power-law dependence is due to the slow methylation dynamics of the receptor cluster, which lead to fluctuations in the concentration of $\mathrm{CheY_p}$, and hence to fluctuations in the CW↔CCW transition rates, on time scales *longer* than the intrinsic CW↔CCW switching time scale. Cluzel *et al.* also measured power spectra of *mutant cells* in which a mutant CheY protein, $\mathrm{CheY^*}$, was stably preexpressed [48, 49]. This protein mimics

the effect of $CheY_p$, but does not need to be phosphorylated to bind to the motor. The concentration of this mutant protein is thus not affected by the slow dynamics of the chemotaxis network, and, consequently, it does not exhibit fluctuations on time scales longer than the switching time. The power spectra of these mutant cells therefore reflect the intrinsic switching dynamics of the motor.

The power spectra of these $CheY^*$ mutant cells do not exhibit a power-law behavior at low frequencies, as the spectra of the wild-type cells do, but they exhibit a peak at around $1\,s^{-1}$ [49]. The peak means that there is a characteristic frequency at which the motor switches. This cannot be explained by a memoryless, two-state Poisson process. Cluzel *et al.* [49] suggest that an earlier model developed by Duke and Bray [47] might be able to explain the peak in the power spectrum. In this model, the ring of FliM proteins is modeled as a circular 1D Ising system, where each protein can exist in two distinct conformational states, corresponding to the up and down spins of the Ising system. The Ising system, however, is an over-damped, mesoscopic equilibrium system, and as we show in the appendix, such a system cannot exhibit a peak in the power spectrum. The peak means that the switching dynamics is coupled to a non-equilibrium process.

We argue that in order to explain the peak in the power spectrum, we have to integrate a description of the switching dynamics of the rotor proteins with a description of both the flagellum dynamics and the dynamics of the stator proteins that drive the rotation of the rotor. The rotor protein complex is modeled as an MWC model [29], in which the proteins of the complex continually and collectively switch between a clockwise and a counter-clockwise conformational state. In a given conformational state, the FliG rotor proteins interact with the stator proteins according to the model developed by Oster and coworkers [114]. This model allows us to compute the propensity to switch between the CW and CCW states as a function of the torque exerted on the rotor. Our calculations predict that the switching propensity increases exponentially with the external load. We argue that this property, in combination with the dynamics of the flagellum, is key to understanding the peak in the power spectrum. After a motor has switched direction, the flagellum first has to unwind. During this time, the switching propensity is low. After this transient, however, the flagellum winds up and the torque on the motor increases. Due to the exponential dependence of the switching propensity on the applied torque, the switching propensity now increases rapidly. This system can thus be characterized as a two-state system, in which the rate constants for switching between the two states are not constant, but increase in time. This, according to our model, is the explanation for the bump in the power spectrum.

In the next section, we first briefly present the model developed by Oster and coworkers [114], upon which our model is based. We then present a simple analytical framework, which can explain the torque-speed relation of the flagellar motor. This framework also shows that the non-equilibrium dynamics that arises from the proton concentration gradient cannot explain the bump in the power spectrum: the characteristic time scale on which the stator proteins change their conformation in response to proton binding, which ultimately drives the rotation of the rotor, is sufficiently slow for this process to occur close to equilibrium. In the subsequent section, we discuss how we model the rotor switching dynamics and show that the switching propensity exponentially increases with the external load. We also show that, according to our model, the switching of the rotor itself can be modeled as a two-state, memoryless Poisson process. However, Cluzel *et*

al. did not directly monitor the rotation of the motor [48, 49], but rather the rotation of a bead connected to the flagellum of a motor. In the next section, we therefore include the dynamics of the flagellum. We show that this model can describe the peak in the power spectrum. In the discussion section, we discuss possible extensions of our model, and how our predictions could be tested. One important test would be to measure the switching frequency as a function of the applied lead, which could be done by taking beads of varying sizes. But perhaps the most important test of our model would be to connect a small bead directly to the stub of a rotor that lacks the flagellum: this would reveal whether the switching dynamics of the motor itself is memoryless or not.

6.2 The stator-rotor interaction

The interaction between the stator proteins and the rotor proteins is modeled according to the model of Oster and coworkers [114], which is based upon the description of Blair *et al.* [115]. Here, we briefly describe the main ingredients of the model.

According to the proposal of Blair, the motor cycle of each stator protein consists of two "half strokes". Let us imagine that the motor has only one stator protein. During the first power stroke of the stator protein, two proteins bind the MotB D32 residues of the stator protein [115] (Fig. 6.2). This leads to a thermally activated conformational transition, which allows one MotA loop to exert a force on one FliG protein of the rotor protein complex (Fig. 6.2). During the second stroke, the recovery stroke, the two protons are released to the cytoplasm, which triggers another conformational transition of the stator protein; during this conformational transition another MotA loop exerts a force on the FliG protein. Thus, during the entire two-step cycle, the stator is almost continuously engaged with the rotor, allowing for a duty ratio that is close to 1. At the end of one two-step cycle, the stator has returned to its conformational state at the beginning of the cycle, and the rotor has advanced by one step, corresponding to an angle which is given by 2π divided by 26, the number of FliG proteins within the ring.

Fig. 6.3 shows the free-energy surfaces of this model, as proposed by Oster *et al.* [114]. The different surfaces correspond to the different conformational states of the stator protein. They consist of identical piecewise linear functions offset in the rotation direction by half a wavelength $2\pi/26$ and in height by a magnitude that is related to the proton motive force. The hopping from one surface to the next corresponds to a proton binding or unbinding event, followed by a conformational transition; the hopping rates thus depend on both the rates of proton (un)binding and the conformational-transition rates. After a hopping event, the new conformation allows the stator to exert a force on the rotor; this power stroke is, for simplicity, modeled as a constant force. The sharp peaks in the potentials prevent thermal fluctuations from taking the system down the backside of the potential. This ensures tight coupling between rotation and proton flux. Each motor cycle transports two protons from the periplasm to the cytoplasm, which decreases the free energy of the system by $2\ e \times$ pmf, where pmf is the proton-motive force.

In the experiments of Korobkova *et al.* the motion of the flagellum is visualized via a latex bead connected to the flagellum [48, 49]. The bead exerts a force on the rotor protein, which, effectively, tilts the energy surfaces shown in Fig. 6.3. When a) the connection between the load and the motor is soft, b) the dynamics of the motor

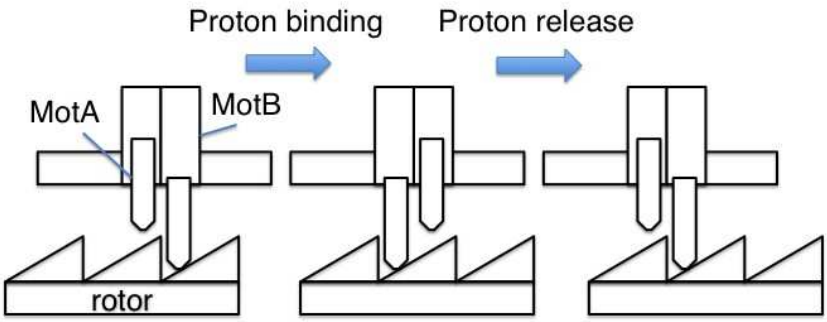

FIGURE 6.2 The rotor-stator interaction as proposed by Oster and Blair *et al.* [115]. At the end of the previous cycle, one MotA loop of the stator protein is in contact with the rotor. The binding of protons to the stator protein induces a conformational transition of the stator protein. In the new conformational state, the stator protein exerts a force on the rotor with its other MotA loop. At the end of the first half step, the protons are released, which induces a transition to the original conformational state. During the second half stroke, the first MotA loop exerts a force on the rotor.

is much faster than that of the load, and c) chemical transitions lead on average to a fixed translation distance of the rotor, as in the current model, then the torque-speed curves under conservative load and viscous load are identical [117, 118, 114]. However, as we will show below, the type of load does markedly affect the CW $\leftrightarrow$ CCW switching dynamics.

So far, we have assumed that the motor has only one stator protein. Resurrection experiments, however, suggest that *in vivo* the number of stator proteins is around 10 [119, 120]. At high load, the stator proteins act cooperatively, and the motor speed increases with the number of stator proteins, which can be varied experimentally by varying their expression level [119]; the model of Oster *et al.* can reproduce this observation [114]. The original model of Oster *et al.* also predicts that at *zero external load*, the speed will *decrease* as the number of stator proteins increases, because the stator proteins hinder each other [114]. However, very recent experiments by Yuan and Berg clearly show that near zero external load the speed is independent of the number of stator proteins [121]. They also found that the Oster model could reproduce this behavior if it was assumed that the stator proteins are connected to the rigid framework of the cell wall via very soft springs, instead of infinitely stiff springs, as in the original Oster model—soft springs essentially uncouple the stator proteins from each other. However, to generate a speed that is independent of the number of stator proteins, the springs had to be made so soft that they would stretch a distance of order 10 nm, which, as Yuan and Berg point out, seems unlikely. We therefore focus here on a motor that has only one stator protein. In future work, we will investigate the effect of the number of stator proteins on the switching dynamics.

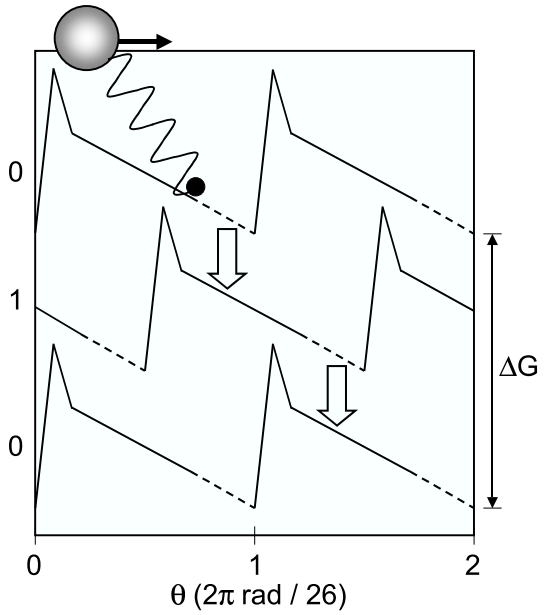

FIGURE 6.3 The potential energies for the rotor-stator interaction in the model as proposed by Oster and Blair *et al.* [115, 114]. At the end of the previous cycle, the binding of protons to the stator leads to a conformational transition. In the new conformational state, the potential energy for the rotor-stator interaction is shifted with respect to previous state. In the new state, the one of the MotA loops of the stator exerts a constant force on the rotor. As a consequence, the rotor will move over one half period, until it reaches the next proton hopping window. At this position, the protons are released to the cytoplasm, which induces a transition back to the original conformational state. During the second half stroke, the other MotA loop of the stator exerts a force on the rotor. The hopping windows are denoted by dashed lines. The thermodynamic driving force is $\Delta G = 2e \times \mathrm{pmf}$.

The dynamics of a single stator protein pulling a load is described by the following overdamped Langevin equation:

$$\gamma_{\mathrm{M}} \frac{d\theta}{dt} = -\frac{\partial U_s(\theta)}{\partial \theta} + F_{\mathrm{L}} + \eta_{\mathrm{M}}(t) \tag{6.1}$$

Here, γ_{M} is the friction coefficient of the rotor; $U_s(\theta)$ is the free-energy surface shown in Fig. 6.3, with θ being the rotation angle and s a binary variable denoting the state of the stator; F_{L} denotes the external load and $\eta_{\mathrm{M}}(t)$ is a Gaussian white noise term of magnitude $\sqrt{2k_{\mathrm{B}}T\gamma_{\mathrm{M}}}$.

The transition (or *hopping*) rate for a stator protein to go from one energy surface to another depends upon the free-energy barrier separating the two surfaces. We make the phenomenological assumption that the hopping rate depends exponentially on the free-energy difference, in a manner that obeys detailed balance. Furthermore, following Blair and Oster *et al.*, we assume that the access of the periplasmic protons to the stator-binding sites is triggered by a rotor-stator interaction [115, 114]. This yields the

Parameter	Value	Description
d	2π rad/26	Potential periodicity
pmf	76 mV	Proton-motive force
ΔG	5.88 $k_{\mathrm{B}}T$	$\Delta G = 2e \times$ pmf
k	3.5 10^4 s^{-1}	Hopping prefactor
d_1	0.05 d	Position potential maximum
d_2	0.1 d	Position start power stroke
d_3	0.9 d	Center of transition window
d_4	0.2 d	Width of transition window
h_1	25 $k_{\mathrm{B}}T$	Height potential maximum
h_2	10 $k_{\mathrm{B}}T$	Height start power stroke
$F_{\mathrm{M}} = -h_2/(d - d_2)$	46 $k_{\mathrm{B}}T$ rad^{-1}	Force motor during power stroke
γ_{M}	1.7 10^{-3} $k_{\mathrm{B}}T$ s rad^{-2}	Friction coefficient motor
$\tilde{k}_0$	0.3 s^{-1}	Switching prefactor
γ_{L}	0.51 $k_{\mathrm{B}}T$ s rad^{-2}	Friction coefficient load
κ	0.22 $k_{\mathrm{B}}T$ rad^{-2}	Spring coefficient flagellum

TABLE 6.1 Parameters as used in the simulations.

following expression for the hopping rates:

$$k_{s\to s'}(\theta) = k_0 w(\theta) \exp[\Delta U_{ss'}(\theta)/2], \quad s, s' = 0, 1 \tag{6.2}$$

Here, k_0 sets the basic time scale, and $\Delta U_{ss'}(\theta) = U_{s'}(\theta) - U_s(\theta)$. The function $w(\theta)$ describes the proton hopping windows (see Fig. 6.3), which reflect the idea that the ion channel through the stator is gated by the motion of the rotor.

Fig. 6.4 shows the torque-speed relation for this model as obtained from Langevin dynamics simulations (symbols). It is seen that at high torques and low speeds, the torque-speed relation is essentially linear, while at high speeds, the torque-speed curve sharply drops to zero. The maximum velocity, at zero external load, is around 300 Hz, as recently observed by Yuan and Berg for a motor with one stator protein [121]. The parameter values used in the simulations are given in Table 6.1. All values are similar to those used in [114].

To elucidate the torque-speed relation, it is instructive to consider the following simple model. First, we assume that, apart from an offset, the energy surfaces $U_0(\theta)$ and $U_1(\theta)$ are identical and given by $U(\theta)$. Secondly, we assume, for simplicity, that the dynamics of the proton hopping onto the stator at the beginning of the first half stroke is the same as that of the proton hopping off the stator at the beginning of the second half stroke. The hopping rates $k_{0\to1}(\theta)$ and $k_{1\to0}(\theta)$ are then given by the same function $k(\theta)$ (apart from an offset in θ). When the diffusive motion along the rotation angle θ is fast as compared to the time scale on which the stator hops from one energy surface to the next, then the motor speed ω is given by the effective hopping rate k_{hop} times the average distance over which the motor progresses during one half cycle, $2\pi/(2 * 26)$:

$$\omega = k_{\mathrm{hop}}\pi/26, \tag{6.3}$$

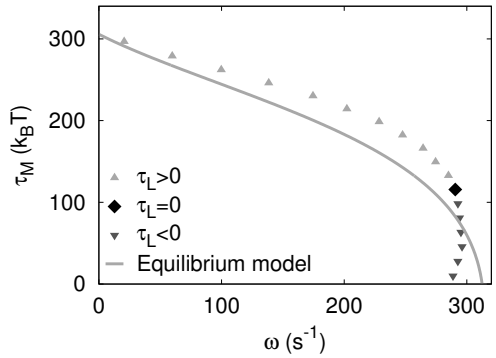

FIGURE 6.4 The torque-speed relation as predicted by the model used here, which is based on the model of Oster *et al.* [114] The symbols denote the results of the Langevin simulations, while the solid line denotes the analytical result of Equations 6.5 and 6.8. The light-grey triangles correspond to the regime in which the load pulls the motor in the backward direction; the dark-grey inverted triangles correspond to the regime in which the load pulls the motor in the *forward* direction, which is the scenario right after a switching event.

.

with the effective hopping rate given by

$$k_{\rm hop} = \int_0^{2\pi/26} d\theta P_{\rm S}(\theta) k(\theta). \tag{6.4}$$

Here, $P_{\rm S}(\theta)$ is the stationary distribution. When the diffusive dynamics is fast compared to the hopping dynamics, the stationary distribution $P_{\rm S}(\theta)$ is, to a good approximation, equal to the equilibrium distribution $P_{\rm eq}(\theta)$, which is proportional to $\exp[-\beta U_{\rm eff}(\theta)]$; $U_{\rm eff}(\theta)$ is the effective potential, which depends on the energy surface $U(\theta)$, shown in Fig. 6.3, and the the external load $\tau_{\rm L}$: $U_{\rm eff}(\theta) = U(\theta) + \tau_{\rm L}\theta$. The average speed is then

$$\omega = \frac{\pi}{26} \frac{\int_0^{2\pi/26} k(\theta) \exp[-\beta(U(\theta)+\tau\theta)]}{\int_0^{2\pi/26} \exp[-\beta(U(\theta)+\tau\theta)]}. \tag{6.5}$$

The motor torque is given by $\tau_{\rm M} \equiv -\int d\theta P_{\rm S}(\theta) \partial U(\theta)/\partial\theta$. In the limit of slow hopping dynamics, it is given by

$$\tau_{\rm M} = \frac{-\int_0^{2\pi/26} \partial U(\theta)/\partial\theta \exp[-\beta(U(\theta)+\tau\theta)]}{\int_0^{2\pi/26} \exp[-\beta(U(\theta)+\tau\theta)]}, \tag{6.6}$$

$$= -\tau_{\rm L} + \frac{-k_{\rm B}T \left[\exp[-\beta(U(\theta)+\tau)]\right]_0^{2\pi/26}}{\int_0^{2\pi/26} \exp[-\beta(U(\theta)+\tau\theta)]}, \tag{6.7}$$

$$\approx -\tau_{\rm L}, \tag{6.8}$$

where in going from Eq. 6.7 to Eq. 6.8 we used the fact that the probability for the stator to be at the boundaries of the periodic potential well is very small. The last line shows that when the hopping dynamics is slow and the stator properly samples the energy surfaces, the motor torque equals the external load. In this limit, the motor does

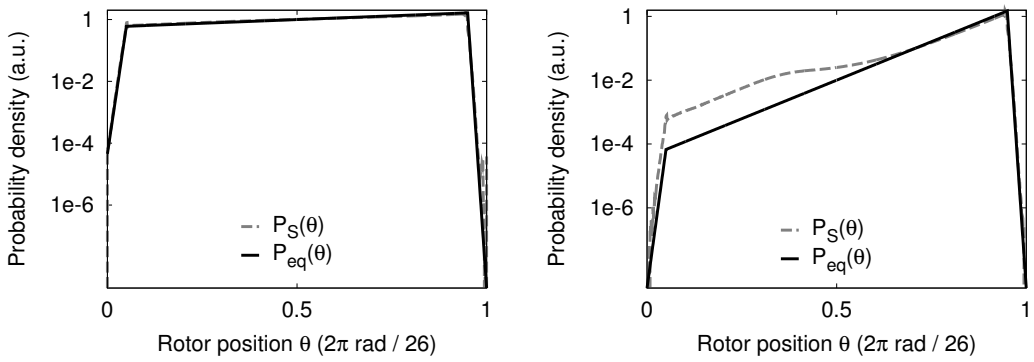

FIGURE 6.5 The stationary distribution $P_{\rm S}(\theta)$ (dashed line) and the equilibrium distribution $P_{\rm eq}(\theta)$ (solid line) of observing a rotation angle between θ and $\theta+d\theta$ for high load ($\tau_{\rm M} = 260\ k_BT$; panel A) and zero external load (panel B).

not work against its own friction associated with moving over the energy surfaces. This can be understood by noting that for an equilibrium system, the fluctuation-dissipation theorem implies that the random forces must balance the frictional forces. In this context, it is instructive to consider the opposite limit from the one considered here, namely that in which the hopping dynamics is much faster than the diffusion dynamics along the energy surfaces. In this limit, the motor torque is given by $\tau_{\rm M} = \tau_{\rm L} + \gamma_{\rm M}\omega$; for a viscous load, this reduces to $\tau_{\rm M} = (\gamma_{\rm L} + \gamma_{\rm M})\omega$.

As mentioned, the critical assumption in deriving Eqs. 6.5 and 6.8 is that the stationary distribution is given by the equilibrium distribution. Fig. 6.5 shows the stationary distribution $P_{\rm S}(\theta)$ and the equilibrium distribution $P_{\rm eq}(\theta)$, for two points on the torque-speed curve. It is seen that for low speeds and high torques, the assumption of equilibrium dynamics is an excellent one; for high speeds and low loads, however, deviations are noticeable. Fig. 6.4 shows the predictions of Eqs. 6.5 and 6.8, which can be evaluated analytically since the energy surfaces consist of piecewise linear potentials. It is seen that the agreement with the stochastic simulation results is quite good. As we will discuss below, this observation is important for understanding the switching dynamics.

We can now explain the shape of the torque-speed curve [114]. Increasing the load, which has the effect of tilting the energy surfaces (Fig. 6.3), shifts the distribution $P_{\rm S}(\theta)$ to lower values of θ. In the low speed regime, this decreases the probability of being in the hopping window, and thereby the effective hopping rate $k_{\rm hop}$ and hence the speed (see Eqs. 6.4 and 6.5). The sharp drop of the torque-speed curve at high speeds is a result of the fact that in this regime, the distribution $P_{\rm S}(\theta)$ is peaked *beyond* the center of the hopping window [114]. Decreasing the load moves the system against the flank of the next potential period, which leads to a sharp drop of the motor torque.

6.3 The rotor switching dynamics

In *E. coli*, the fraction of time the motor rotates in the clockwise direction, the so-called clockwise (CW) bias, is controlled by the concentration of the intracellular messenger

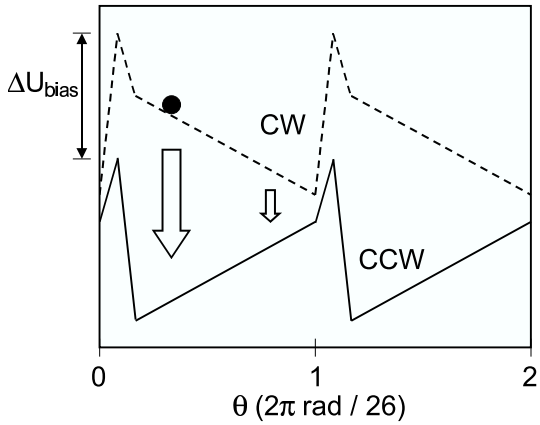

FIGURE 6.6 Two energy surfaces of the motor, corresponding to the CCW and CW states of the rotor, for a given conformational state of the stator protein. In total, each cycle of the motor is characterized by 4 surfaces, corresponding to the different conformational states of the stator and rotor proteins.

protein $\mathrm{CheY_p}$. This protein modulates the CW bias by binding to the ring of FliM proteins. This ring is connected to the ring of FliG proteins, which interact with the stator proteins (Fig. 6.1).

The molecular mechanism of the switch is unknown. However, it is widely believed that the binding of $\mathrm{CheY_p}$ molecules to individual FliM molecules causes a change in their conformation. Following earlier work, we assume that each FliM protein can exist in either a CW or CCW conformational state and that binding of $\mathrm{CheY_p}$ shifts the relative stability of these two conformational states [43, 122, 47]. Moreover, we assume that also each FliG protein can exist in either a CW or CCW conformational state. In principle, we could model the whole rotor complex as an Ising system, where each protein molecule is modeled as a spin that can exist in two states, corresponding to the CW and CCW conformational states; in this model, the interactions between the protein molecules would be modeled via spin-spin coupling constants J_{MM}, J_{MG} and J_{GG}, corresponding to FliM-FliM, FliM-FliG, FliG-FliG interactions, respectively. However, to limit the number of parameters, we will model the rotor complex as an MWC model [29]. In this model, the energetic cost of having two protein molecules in two different conformational states is prohibitively large. Consequently, at any given moment in time, all proteins of the rotor complex are in the same conformational state; when the proteins change their conformation, they do so in concert. In this limit, we can speak of the rotor being in either the CW or the CCW state.

When the rotor complex switches from one state to another, the interactions between the FliG proteins and the stator proteins change, due to the new conformational state of the FliG proteins. In our model, there are two energy surfaces, corresponding to the CW and CCW states of the rotor, for each of the two conformational states of a stator protein. Thus, one motor cycle is described by 4 energy surfaces, $U_{\mathrm{s}}^{\mathrm{r}}$, with the subscript $s = 0, 1$ denoting the state of the stator protein and the superscript $r = 0, 1$ the state of the rotor protein. We assume that the two rotor surfaces corresponding to a given state of the stator are simply each other's mirror image (the potentials are

flipped in the θ direction), but offset by an energy difference $\Delta U_{\rm bias}$ that is given by the CW bias $P_{\rm CW} = \exp(-\beta\Delta U_{\rm bias})/(1+\exp(-\beta\Delta U_{\rm bias})$ (see Fig. 6.6). As before, we make the natural phenomenological assumption that the instantaneous rotor switching rates depend exponentially on the free-energy difference:

$$k_s^{r\to r'} = \tilde{k}_0 \exp[\Delta U_s^{rr'}(\theta)/2],\ r, r' = 0, 1; s = 0, 1, \tag{6.9}$$

where $\Delta U_s^{rr'}(\theta) = U_s^{r'}(\theta) - U_s^r(\theta)$. Importantly, the instantaneous switching rate does not depend upon the applied load, although the average, effective switching rate does depend upon the applied load, as discussed below. The Langevin dynamics along the "reaction coordinate" θ is again given by Eq. 6.1, but with $U_s(\theta)$ replaced by $U_s^r(\theta)$.

Fig. 6.7 shows the rotor switching dynamics when the load is conservative. The conservative load is modeled as a constant force in a direction opposite to that of the direction of the rotor (see Eq. 6.1); after the rotor has switched direction, the conservative force *instantaneously* changes sign. Fig. 6.7A shows the average switching rate in the forward and backward switching direction as a function of the conservative load. As expected, the CCW $\to$ CW switching rate increases as the CW bias increases. More interestingly, the switching rate increases exponentially with the external load. This is one of the main results of this study. As we describe below, it is key to understanding the bump in the power spectrum.

The exponential dependence of the switching rate on the torque can be understood by noting that the overall switching rate is given by

$$k_{\rm switch}^{r\to r'} = \int d\theta P_{\rm S}(\theta) k^{r\to r'} \tag{6.10}$$

where, as before, $P_{\rm S}(\theta)$ is the stationary distribution and we have dropped the subscript s, because we assume that apart from an offset $U_0(\theta) = U_1(\theta)$. As the external load is increased, the stationary distribution $P(\theta)$ shifts to lower values of θ when the motor runs in the CW direction of increasing θ (Fig. 6.5). In this region, the driving force for switching, $\Delta U^{r\to r'}$, is larger (Fig. 6.6). Since the switching rate $k^{r\to r'}(\theta)$ depends exponentially on $\Delta U^{r\to r'}$ (See Eq. 6.9), the overall switching rate $k_{\rm switch}^{r\to r'}$ increases dramatically with external load.

Fig. 6.7B shows the power spectra of the switching dynamics. It is seen that the power spectrum is given by a Lorentzian, which shows that the switching dynamics can be modeled as a random telegraph process. Clearly, with a conservative force, there is no peak in the power spectrum. This is perhaps surprising, because, as described in the previous paragraph, the switching rate depends upon the position within one period of the potential; if the system would move at a constant speed along the successive energy surfaces, then the switching rate would periodically be higher, which would lead to peaks in the power spectrum [96]. However, as discussed in the previous section, on the time scale of a hopping event, the system properly samples one period of the potential. Moreover, on the time scale of a rotor switching event, which is on the order of $\tau_{\rm switch} = 0.1 - 1$ s, the stator undergoes many hopping events, i.e. on the order of $N_{\rm hop} = \tau_{\rm switch} \times \omega \times 26$, where 26 is the number of FliG proteins and ω is the motor rotation rate, which is on the order of $100 - 300$ Hz. Clearly, on the time scale of switching, the system effectively integrates over the rough features of the energy surfaces.

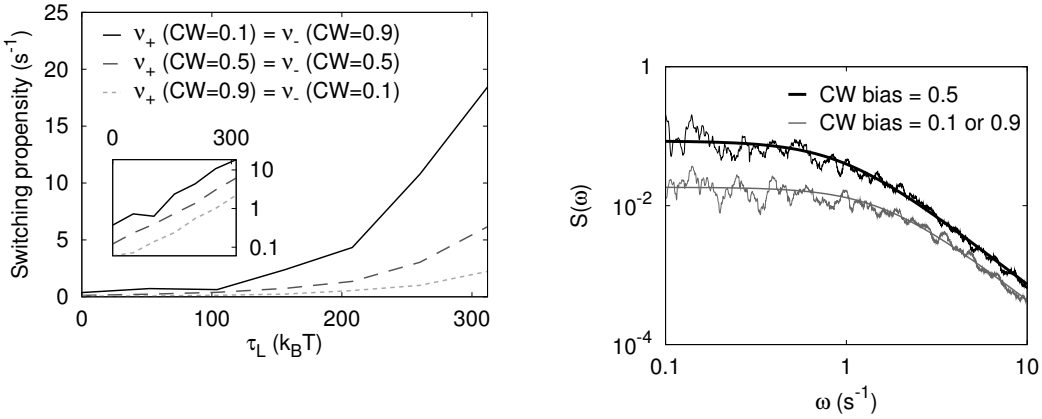

FIGURE 6.7 Switching dynamics with conservative load. A: The switching rate in the forward CW → CCW and backward (CCW → CW) direction for CW bias = 0.1, 0.5, and 0.9. Note that due to the symmetry of our model, the switching dynamics in the forward (backward) direction for CW bias = x, equals the switching dynamics in the backward (forward) direction for CW bias = $1 - x$. The inset shows the same data in a semi-logarithmic plot. B: Power spectra for CW bias = 0.1, 0.5 and 0.9

6.4 Flagellum dynamics

In the model discussed above, after a switching event, the torque exerted by the bead on the motor immediately changes sign and instantaneously reaches its steady-state value. However, in the experiments of Cluzel *et al.*, the switching of the motor was visualized via a large, 0.5 μm latex bead that was attached to the flagellum [48, 49]. We argue that the flagellum dynamics is critical for understanding the switching dynamics of the flagellar motor.

We model the flagellum as a harmonic spring with spring constant κ, although the precise form of the bead-rotor potential is not important. Denoting the position of the load (bead) with θ_{L}, we obtain the following equations of motion for, respectively, the load and the motor:

$$\gamma_{\mathrm{L}} \frac{d\theta_{\mathrm{L}}}{dt} = \kappa(\theta - \theta_{\mathrm{L}}) + \eta_{\mathrm{L}}(t) \tag{6.11}$$

$$\gamma_{\mathrm{M}} \frac{d\theta}{dt} = -\frac{\partial U_s^r(\theta)}{\partial \theta} - \kappa(\theta - \theta_{\mathrm{L}}) + \eta_{\mathrm{M}}(t) \tag{6.12}$$

Here, γ_{L} is the friction coefficient of the bead, and η_{L} is a Gaussian white noise term of magnitude $\sqrt{2k_{\mathrm{B}}T\gamma_{\mathrm{L}}}$. The 0.5 μm latex bead, as used by Cluzel *et al.* in their experiments [49], is large on microscopic length scales. We therefore take $\gamma_{\mathrm{L}} \gg \gamma_{\mathrm{M}}$, which means that the effect of the stochastic motion of the bead on the motor dynamics is negligible.

Fig. 6.8 shows the switching characteristics of this system. The parameter values used in the simulations are given in Table 6.1. The parameter values for the switching prefactor and for the spring coefficient of the flagellum were obtained by fitting to the results in [49]. All other values, corresponding to motor rotation, are similar to those

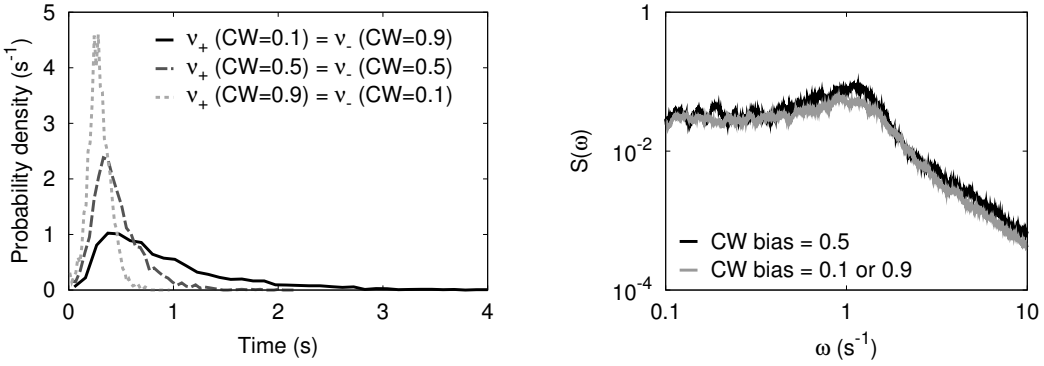

FIGURE 6.8 The switching dynamics of a motor with viscous load. Panel A: Distribution of waiting times for the forward CW → CCW transition and backward CCW → CW transition, for CW bias = 0.1, 0.5 and 0.9. Panel B: The power spectra for CW bias = 0.1, 0.5 and 0.9.

used in [114]. We show the dynamics of the bead instead of the motor, since that has been measured experimentally; however, the switching dynamics of the two are very similar. Fig. 6.8A shows the distribution of waiting times, for CW bias = 0.1, 0.5, and 0.9. These distributions agree remarkably well with those observed by Cluzel *et al.* [49]. Firstly, the distributions are not exponential, as would be expected for a random telegraph process. The distributions exhibit a clear peak, located between 0.1 and 1 s^{-1}, depending on the CW bias. Secondly, the waiting-time distribution for the forward (CW→CCW) transition shifts from a narrow distribution at CW bias = 0.1 to a broad distribution at CW bias = 0.9. Moreover, the position of the maximum of the distribution shifts to longer times. All these features are in near quantitative agreement with experiment. Lastly, our model is symmetric by construction—the CW energy surface is the mirror image of the CCW surface. This means that in our model the distribution for the forward (backward) transition for CW bias = x overlaps with that for the backward (forward) transition for CW bias = $1-x$. Intriguingly, the distributions as measured by Cluzel *et al.* also exhibit this property to a very good approximation [49]. This clearly supports the use of our symmetric model.

Fig. 6.8B shows the power spectra of our model, for CW bias = 0.5, and for CW bias = 0.1, 0.9 (they are identical because of the symmetry of our model). It is seen that the power spectra of our model exhibit a clear peak at $\omega \sim 1$ s^{-1}. Moreover, the peak is most pronounced when the CW bias = 0.5. These characteristics are observed experimentally [49].

Our model predicts that the peak in the power spectra arises from the interplay between the dynamics of the flagellum and the dependence of the switching propensity on the load (Fig. 6.7A). The idea is illustrated in Fig. 6.9. Figure 6.9A shows a typical time trace for the bead position, the rotor position, and the torque exerted by the rotor on the bead via the flagellum. It is seen that after a switching event of the motor, the bead initially keeps moving in its original direction. The flagellum, however, unwinds and the torque between the bead and the flagellum decreases until it becomes zero when the angular positions of the bead and the motor become equal. At this point the bead changes direction and the flagellum starts to wind up; consequently, the torque between

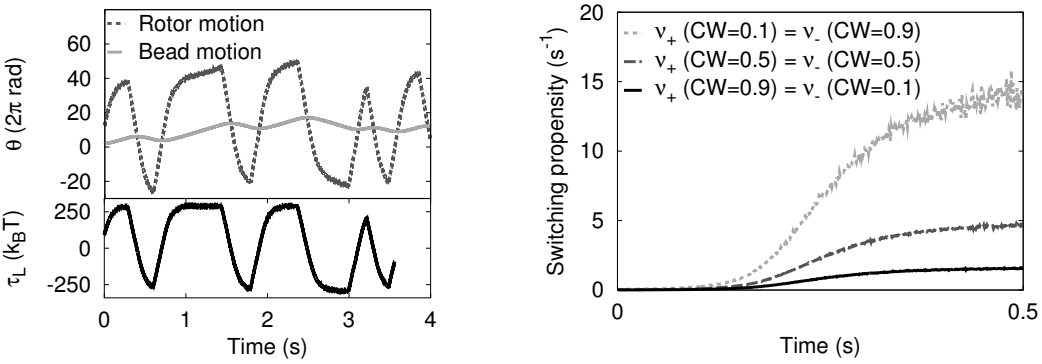

FIGURE 6.9 The mechanism of switching. A: Typical time traces for the motor and bead position (upper panel) and for the torque exerted by the rotor on the bead (lower panel), for CW bias = 0.5. B: The switching propensity as a function of time after a switching event, for CW bias = 0.1, 0.5, and 0.9. This figure is obtained by combining the switching propensity as a function of the conservative load, as shown in Fig. 6.7A, with the average torque as a function of time after a switching event, as shown in panel A.

the bead and the rotor starts to increase. The peak in the power spectra can now be understood by combining the time trace of the torque (Fig. 6.9A) with the dependence of the switching propensity on the load (Fig. 6.7A); these can be combined to obtain to a good approximation the switching propensity as a function of time, as shown in Fig. 6.7B. Right after a switching event, the spring pulls the motor *forward* in its new rotation direction; the probability to switch back is now very low (Fig. 6.7A). When the distance between the motor and the bead increases again, however, the bead pulls with increasing force on the motor in the backward direction. The switching propensity now increases rapidly, as the switching rate depends exponentially on the external load (Fig. 6.7B). The peak in the spectrum is precisely caused by the fact that the switching propensity function is not constant in time, as for a Markovian Poisson process, but increases with time.

Interestingly, Fig. 6.9B also shows that the switching propensity saturates after some time. This plateau corresponds to the regime in which the distance between the bead and the motor, and hence the torque, has reached a new steady-state value. If the motor would predominantly switch in this plateau regime, then switching would reduce to a Markovian Poisson process and there would be no peak in the spectrum. Indeed, to obtain a peak, the motor has to switch in the regime in which the propensity function increases with time. This means that the propensity function has to rise dramatically: the switching survival probability as a function of time must have dropped to a low value before the plateau regime is reached. In our model, this is the case, because the switching propensity function depends exponentially on the applied torque.

The switching propensity as a function of time can also explain the change in the waiting time distributions when the CW bias is varied (Fig. 6.8A). When the CW bias is large, the backward CCW $\rightarrow$ CW transition rate is large (Fig. 6.7A). This means that after a CW $\rightarrow$ CCW switching event, the propensity to flip back to the CW state

increases rapidly with time. Indeed, the rotor most likely switches back to the CW state before the CCW → CW switching propensity has reached its plateau value. This explains the very narrow distribution of CCW intervals when the CW bias is large, as observed in both the model (Fig. 6.8A) and experiment [49]. For the reverse transition, from CW to CCW, the situation is qualitatively different. When the CW bias is large, the forward CW → CCW is low, which means that after the rotor has switched to the CW state, the propensity to switch to the CCW state only slowly increases with time. The system can now enter the plateau regime in which the switching propensity becomes constant in time. This constant propensity leads to an exponential tail in the distribution of CW (CCW) intervals when the CW (CCW) bias is large, as observed in both the distributions of the model (Fig. 6.8A) and those measured experimentally [49].

6.5 Discussion

Our model predicts that the peak in the switching power spectrum relies on two characteristics of the rotary flagellar motor: 1) its propensity to switch depends upon the load; 2) after a switching event, it takes a finite amount of time for the load to build up, due to the slow relaxation dynamics of the flagellum. We expect that these features are general characteristics of flagellar rotary motors, even when the details of the model might be different.

Our calculations suggest that a useful coarse-grained model for understanding the flagellar switching dynamics would be one in which the system stochastically flips between two states with time-dependent propensity functions (Fig. 6.9B):

$$\mathrm{CCW} \underset{k_\mathrm{b}(t)}{\overset{k_\mathrm{f}(t)}{\rightleftharpoons}} \mathrm{CW}, \tag{6.13}$$

where the propensity functions are given by a "Hill function in time":

$$k_{\alpha(t)} = k_{\max} \frac{t^n}{t_{\mathrm{lag}}^n + t^n}. \tag{6.14}$$

The important parameters of this model are the lag time, t_{lag}, the maximum propensity, $k_\alpha(t \to \infty) = k_{\max}$, and to a lesser extent the sharpness of the transition, as determined by n; in the limit $n \to \infty$, the propensity function reduces to a step function in time. The maximum propensity, $k_{\max}$, does not depend upon the properties of the flagellum, but it does depend upon the CW bias, which determines how the propensity function depends upon the torque (Fig. 6.7A), and the maximum torque itself, which is determined by the drag coefficient of the load, γ_L, and the torque-speed relation of the motor; to a good approximation, the maximum torque is given by the intersection of $\gamma_\mathrm{L}\omega$ and the torque-speed curve. The lag time t_{lag} and the coefficient n depend not only on the torque-speed relation of the motor, but also on the dynamics of the flagellum. We have modeled the connection between the bead and the rotor as a harmonic spring, but is conceivable that more non-linear potentials would be more appropriate. In fact, it is known that a flagellum adopts a helical conformation upon winding it in the counterclockwise direction, while it adopts a semi-coiled or curled conformation upon winding it in the clockwise direction. In principle, this leads to an asymmetric potential, which could make t_{lag} and n different for the transitions in the two directions, even when the CW bias = 0.5. We believe, however, that these aspects are not critically important.

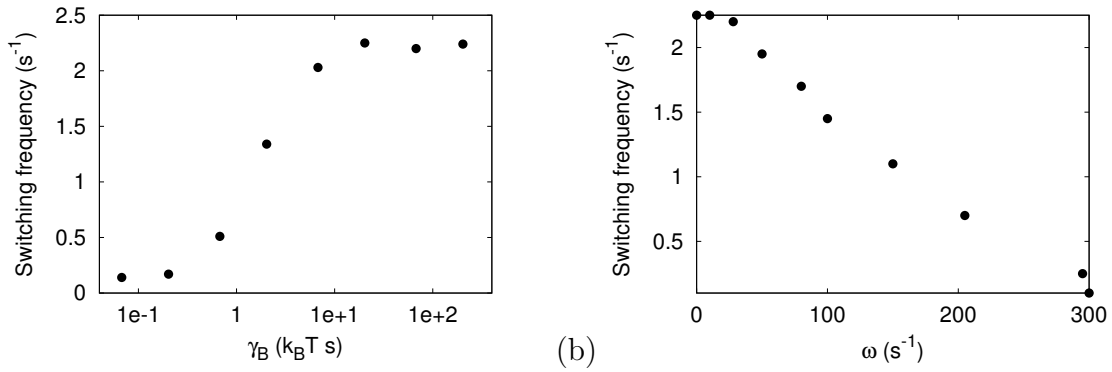

FIGURE 6.10 The switching frequency as a function of the viscous load. The average switching frequency as a function of the drag coefficient (A) and rotation speed (B).

What is important is that the time it takes to reach a critical torque and hence a critical switching frequency is finite: the dynamics of the flagellum should not be too fast. In this context, it is important to note that the flagellum has been observed to exhibit dynamics at time scales of 0.1 s [123].

Perhaps the most critical prediction of our model is shown in Fig. 6.10. This figure shows for CW bias = 0.5 the average switching frequency as a function of the drag coefficient of the load (A) and the average switching frequency as a function of the motor speed, if the motor were to run at constant speed in one direction (B). It is seen that in the low speed, high torque regime, the average switching frequency is nearly constant. For higher rotation speeds, the average switching frequency decreases almost linearly with the rotation speed. Moreover, our model predicts that at zero external load, switching is characterized by a two-state, memoryless Poisson process. These predictions could be tested experimentally by monitoring the switching dynamics of a small bead directly connected to the stub of a motor lacking a filament [121].

Appendix: Power Spectra of an equilibrium system

Let us consider a system with states indexed by i. Each state has a probability $p_i(t)$, which evolves according to the master equation

$$\frac{d\boldsymbol{p}}{dt} = \boldsymbol{M}\boldsymbol{p}(t) \tag{6.15}$$

where $\boldsymbol{M}$ is the "master matrix". Detailed balance is encoded in the matrix $\boldsymbol{M}$ and can be defined as the existence of a vector $\boldsymbol{p}^0$ such that

$$\boldsymbol{M}_{ij}p_j^0 = \boldsymbol{M}_{ji}p_i^0. \tag{6.16}$$

This vector satisfies the condition for a stationary probability

$$0 = \boldsymbol{M}\boldsymbol{p}^0 \tag{6.17}$$

The detailed-balance condition also implies that the matrix

$$\boldsymbol{M}'_{ij} = \sqrt{\frac{p_i^0}{p_j^0}}\boldsymbol{M}_{ij} \tag{6.18}$$

is symmetric. As a consequence, the eigenvectors and eigenvalues of $\boldsymbol{M}$ are real (and non-positive) due to the fact that $\boldsymbol{M}$ is a "master matrix". This means that one has $\boldsymbol{c}^i$, $\boldsymbol{p}^i$ and λ_i such that

$$\lambda_i \boldsymbol{c}^i = \boldsymbol{c}^i \boldsymbol{M}, \quad \lambda_i \boldsymbol{p}^i = \boldsymbol{M}\boldsymbol{p}^i \tag{6.19}$$

$$0 = \lambda_0 > \lambda_1 > \dots \quad c_j^i = \frac{p_j^i}{p_j^0} \quad \forall i \geq 0 \tag{6.20}$$

$$\boldsymbol{p}(t) = \sum_i \left(\mathrm{e}^{\lambda_i t} b^i \boldsymbol{p}^i\right), \quad b^i = \sum_j c_j^i p_j(t=0) \tag{6.21}$$

If one considers a quantity N that adopts the values N_i in the states i, then the correlation function can be expressed as

$$C_N(t) = \sum_i \left[\left(\sum_j c_j^0 N_j p_j^i\right) \mathrm{e}^{\lambda_i t} \left(\sum_j c_j^i N_j p_j^0\right)\right]. \tag{6.22}$$

Thus,

$$C_N(t) = \sum_i a_i \mathrm{e}^{\lambda_i t} \tag{6.23}$$

and the power spectrum of the fluctuations of N derived from C_N becomes a sum of Lorentzians

$$S_N(\omega) = \sum_i k_i \frac{\lambda_i}{\omega^2 + \lambda_i^2} \tag{6.24}$$

It is easy to show that this sum does not have a "bump", especially because $k_i\lambda_i > 0$ which makes each term positive. This last inequality can be derived using the relation

$$\left(\sum_j c_j^0 N_j p_j^i\right) = \left(\sum_j c_j^i N_j p_j^0\right) \tag{6.25}$$

. Therefore the detailed balance condition implies that there is "no bump" in the power spectrum. It is important to realize that the detailed balance equality is a reversibility relation based on the existence of an "energy" function $\log \boldsymbol{p}^0$.

The same ideas apply to overdamped Langevin dynamics of the type

$$\dot{x}_i = -f_i(\boldsymbol{x}) + \eta_i \tag{6.26}$$

as long as one has $\boldsymbol{f}(\boldsymbol{x})$ derived from a potential such that the Hessian is symmetric:

$$\frac{\partial f_i}{\partial x_j} = \frac{\partial f_j}{\partial x_i} \tag{6.27}$$

It is important to realize that standard Langevin dynamics with noise does not obey detailed balance. Indeed, the "forces" in

$$\dot{x} = v \tag{6.28}$$

$$\dot{v} = -\gamma v - \frac{\partial V(x)}{\partial x} + \eta \tag{6.29}$$

are not derived from an overall potential, allowing for "oscillations". One should therefore understand detailed balance as a property of mesoscopic models with no inertia.

Bibliography

[1] T. A. J. Duke and D. Bray, Proc. Natl. Acad. Sci. USA **96**, 10104 (1999).
[2] D.L. Milligan and D.E. Koshland Jr., J. Biol. Chem. **263**, 6268-6275 (1988).
[3] J.A. Gegner, D.R. Graham, A.F. Roth, and F.W. Dahlquist, Cell **70**, 975-982 (1992).
[4] S.C. Schuster, R.V. Swanson, L.A. Alex, R.B. Bourret, and M.I. Simon, NAT **365**, 343-347 (1993).
[5] K.K. Kim, H. Yokota, and S.-H. Kim, NAT **400**, 787-792 (1999).
[6] P. Ames, C.A. Studdert, R.H. Reiser, and J.S. Parkinson, PNAS **99**, 7060-7065 (2002).
[7] C.A. Studdert and J.S. Parkinson, PNAS **101**, 2117-2122 (2004).
[8] J. R. Maddock, and L. Shapiro, Science **259**, 1717 (1993).
[9] R.M. MacNab and D.E. Koshland, PNAS **69**, 2509-2512 (1972).
[10] M.S. Springer, M.F. Goy, and J. Adler, NAT **280**, 279-284 (1979).
[11] R. Mesibov, G.W. Ordal, and J. Adler, J. Gen. Physiol. **62**, 203-223 (1973).
[12] N. Barkai and S. Leibler, Nature **387**, 913 (1997).
[13] J.L. Spudich and D.E. Koshland, NAT **262**, 467-471 (1976).
[14] T.C. Terwilliger, J.Y. Wang, and D.E. Koshland, J. Biol. Chem. **261**, 10814-10820 (1986).
[15] M.J. Shapiro, D. Panomitros, and Jr. D.E. Koshland, J. Biol. Chem. **270**, 751-755 (1995).
[16] A. Borczuk, A. Staub, and J. Stock, Biochem. Biophys. Res. Commun. **141**, 918-923 (1986).
[17] D.A. Sanders and D.E. Koshland Jr., PNAS **85**, 8425-8429 (1988).
[18] U. Alon, M. G. Surette, N. Barkai and S. Leibler, Nature **397**, 168 (1999).
[19] T.-M. Yi, Y. Huang, M. I. Simon, and. J. Doyle, Proc. Natl. Acad. Sci. USA **97**, 4649 (2000).
[20] B.A. Mello and Y. Tu, Biophys. J. **84**, 2943-2956 (2003).
[21] R. Jasuja, Y.-L. Lin, D.R. Trentham, and S. Khan, PNAS **96**, 11346-11351 (1999).
[22] J. E. Segall, S. M. Block, and H. C. Berg, Proc. Natl. Acad. Sci. USA **83**, 8987 (1986).
[23] Dennis Bray, Matthew D. Levin, and Carl J. Morton-Firth, Nature **393**, 85-88 (1998).
[24] Tom S. Shimizu, S. V. Aksenov, and Dennis Bray, J. Mol. Biol. **329**, 291-309 (2003).
[25] V. Sourjik and H. C. Berg, Proc. Natl. Acad. Sci. USA **99**, 123 - 127 (2002).
[26] Bernardo A. Mello and Yuhai Tu, Proc. Natl. Acad. Sci. USA **100**, 8223-8228 (2003).
[27] L.L. Kiessling J.E. Gestwicki, NAT **415**, 81-84 (2002).
[28] V. Sourjik and H. C. Berg, NAT **428**, 437-441 (2004).
[29] Jacob Monod, J Wyman, and J-P Changeux, J. Mol. Biol. **12**, 88-118 (1965).
[30] Bernardo A. Mello and Yuhai Tu, Proc. Natl. Acad. Sci. USA **102**, 17354-17359 (2005).
[31] Juan E. Keymer, Robert G. Endres, Monica Skoge, Migal Yeir, and Ned S. Wingreen, Proc. Natl. Acad. Sci. USA **103**, 1786-1791 (2006).
[32] T.S. Shimizu, N. E. Le Novère, M.D. Levin, A.J. Beavil, B.J. Sutton, and D. Bray, Nat. Cell Biol. **2**, 792-296 (2000).
[33] M.D. Levin, T.S. Shimizu, and D. Bray, Biophys. J. **82**, 1809-1817 (2002).
[34] Albeter Goldbeter and Daniel E Koshland, Jr., Proc. Natl. Acad. Sci. USA **78**, 6840-6844 (1981).
[35] Ady Vaknin and Howard C. Berg, Proc. Natl. Acad. Sci. USA **101**, 17072–17077 (2004).
[36] Hui Wang and Philip Matsumura, Mol. Microbiol. **19**, 695-703 (1996).
[37] D. C. Fung and H.C. Berg, NAT **375**, 809-812 (1995).
[38] C.V. Gabel and H.C. Berg, PNAS **100**, 8748-8751 (2003).
[39] R. Berry and H.C. Berg, PNAS **94**, 14433-14437 (1997).
[40] X. Chen and H.C. Berg, Biophys. J. **78**, 1036-1041 (2000).
[41] Y. Sowa, H. Hotta, M. Homma, and A. Ishijima, JMB **327**, 1043-1051 (2003).
[42] J.H. Xing, F. Bai, R. Berry, and G. Oster, PNAS **103**, 1260-1265 (2006).
[43] B. E. Scharf, K. A. Fahrner, L. Turner, and H. C. Berg, Proc. Natl. Acad. Sci. USA **95**, 201 (1998).
[44] Philippe Cluzel, Michael Surette, and Stanislas Leibler, Science **287**, 1652-1655 (2000).
[45] V. Sourjik and H. C. Berg, Proc. Natl. Acad. Sci. USA **99**, 12669 - 12674 (2002).

[46] Y. Sagi, S. Khan, and M. Eisenbach, J. Bio. Chem. **278**, 25867-25871 (2003).
[47] T. A. J. Duke, N. E. Le Novère, and D. Bray, J. Mol. Biol. **308**, 541 (2001).
[48] E. Korobkova, T. Emonet, J. M. G. Vilar, T. S. Shimizu, and P. Cluzel, Nature **428**, 574-578 (2004).
[49] Ekaterina A Korobkova, Thierry Emonet, Heungwon Park, and Philippe Cluzel, Phys. Rev. Lett. **96**, 058105 (2006).
[50] Albeter Goldbeter and Daniel E Koshland, Jr., J. Biol. Chem. **259**, 14441-14447 (1984).
[51] James E Ferrell, Jr., Trends Biochem. Sci. **21**, 460-466 (1996).
[52] O. G. Berg, J. Paulsson, and M. Ehrenberg, Biophys. J. **79**, 1228-1236 (2000).
[53] P. B. Detwiler, S. Ramanathan, A. Sengupta, and B. I. Shraiman, Biophys. J. **79**, 2801 - 2817 (2000).
[54] M. Samoilov, S. Plyasunov, and A. P. Arkin, Proc. Natl. Acad. Sci. USA **102**, 2310-2315 (2005).
[55] S. Tănase-Nicola, P. B. Warren, and P. R. ten Wolde, Phys. Rev. Lett. **97**, 068102-1-4 (2006).
[56] Guy C. Brown and Boris N. Kholodenko, FEBS Lett. **457**, 452-454 (1999).
[57] Karin Lipkow, Steven S. Andrews, and Dennis Bray, J. Bacteriol. **187**, 45–53 (2005).
[58] Christopher V. Rao, John R. Kirby, and Adam P. Arkin, Physical Biology **2**, 148-158 (2005).
[59] Borin N. Kholodenko, Nat. Rev. Mol. Cell Biol. **7**, 165-176 (2006).
[60] V. Sourjik and H. C. Berg, Mol. Microbiol. **37**, 740-751 (2000).
[61] Martin Thanbichler and Lucy Shapiro, Cell **126**, 147-162 (2006).
[62] Petr Kalab, Kartsen Weis, and Rebecca Heald, Science **295**, 2452-2456 (2002).
[63] Philipp Niethammer, Philippe Bastiaens, and Eric Karsenti, Science **303**, 1862-1866 (2004).
[64] M Caudron, G Bunt, P Bastiaens, and E Karsenti, Science **309**, 1373-1376 (2005).
[65] Jim Wong and Guowei Fang, J. Cell Biol. **173**, 879-891 (2006).
[66] B. Alberts, D. Bray, J. Lewis, M. Raff, K Roberts, and J.D. Watson, *Molecular Biology of the Cell*, Gardland Publishing, New York (1994).
[67] Boris N. Kholodenko, Guy C. Brown, and Jan B. Hoek, Biochem. J. **350**, 901-907 (2000).
[68] Markus Kollmann, Linda Loevdok, Kilian Bartholomé, Jens Timmer, and Victor Sourjik, Nature **438**, 504-507 (2005).
[69] J. Paulsson, Nature **427**, 415 - 418 (2004).
[70] T. Shibata and K. Fujimoto, Proc. Natl. Acad. Sci. USA **102**, 331 - 336 (2005).
[71] M. B. Elowitz, M. G. Surette, P.-E. Wolf, J. B. Stock, and S. Leibler, J. Bacteriol. **181**, 197-203 (1999).
[72] Siebe B Van Albada and Pieter Rein Ten Wolde, PLoS Comp. Biol. **3**, e195 (2007).
[73] H Sanatinia, E C Kofoid, T B Morrison, and Parkinson J S, J. Bacteriol. **177**, 2713-2720 (1995).
[74] K. Lipkow, PLoS Comp. Biol. **2**, 301-310 (2006).
[75] Yuval Blat and Michael Eisenbach, J. Biol. Chem. **271**, 1226-1231 (1996).
[76] Yuval Blat, Blake Gillespie, Anat Bren, Frederick W. Dahlquist, and Michael Eisenbach, J. Mol. Biol. **284**, 1191-1199 (1998).
[77] A J Wolfe and R C Stewart, Proc. Natl. Acad. Sci. USA **90**, 1518-1522 (1993).
[78] R V Swanson, R B Bourret, and M I Simon, Mol. Microbiol. **8**, 435- 441 (1993).
[79] M Levit, Y Liu, M Surette, and J Stock, J. Biol. Chem. **271**, 32057-32063 (1996).
[80] D D Ellefson, U Weber, and A J Wolfe, J. Bacteriol. **179**, 825-830 (1997).
[81] Brian H Cantwell, Roger R Draheim, Richard B Weart, Cameran Nguyen, Richard C Stewart, and Michael D Manson, J. Bacteriol. **179**, 825-830 (1997).
[82] L Kott, E H Braswell, A L Shrout, and R M Weis, Biochim Biophys Acta **1696**, 131-140 (2004).
[83] Mingshan Li and Gerald L Hazelbauer, J. Bacteriol. **186**, 3687-3694 (2004).
[84] Rui Zhao, Edward J Collins, Robert B Bourret, and Ruth E Silversmith, Nat. Struct. Biol. **9**, 570=575 (2002).
[85] R C Stewart, K Jahreis, and Parkinson J S, Biochemistry **3**, 13157–13165 (2000).
[86] David C LaPorte, Kenneth Walsh, and Daniel E Koshland Jr, J. Biol. Chem. **259**, 14068-14075 (1984).
[87] Christopher V. Rao, M. Frenklach, and Adam P. Arkin, J. Mol. Biol. **343**, 291-303 (2004).
[88] Robert G. Endres and Ned S. Wingreen, Proc. Natl. Acad. Sci. USA **103**, 13040 - 13044 (2006).
[89] Bernardo A. Mello and Yuhai Tu, Biophys. J. **92**, 2329 - 2337 (2007).
[90] J. S. van Zon and P. R. ten Wolde, Phys. Rev. Lett. **94**, 128103 (2005).

[91] J. S. van Zon and P. R. ten Wolde, JCP **123**, 234910 (2005).
[92] R E Silversmith, J G Smith, G P Guanga, J T Les, and R B Bourret, J. Biol. Chem. **276**, 18478-18484 (2001).
[93] Pieter Rein Ten Wolde and Sorin Tănase-Nicola, Nat. Phys. **2**, 371-372 (2006).
[94] Lewis Wolpert, J. Theor. Biol. **25**, 1-47 (1969).
[95] Martin Howard, Andrew D Rutenberg, and Simon de Vet, Phys. Rev. Lett. **87**, 278102 (2001).
[96] Jeroen S van Zon, Marco Morelli, Tănase-Nicola, and Pieter Rein Ten Wolde, BPJ **91**, 4350-4367 (2006).
[97] Maosong Qi and Elaine A Elion, J Cell Sci **118**, 3569–3572 (2005).
[98] Jason W Locasale, Andrey S Shaw, and Arup K Chakraborty, Proc Natl Acad Sci U S A **104**, 13307–13312 (2007).
[99] Ruth E Silversmith, Biochemistry **44**, 7768-7776 (2005).
[100] Agmon, Noam and Szabo, Attila, J. Chem. Phys. **92**, 5270 - 5284 (1990).
[101] W Jr Sabbagh, L J Flatauer, A J Bardwell, and L Bardwell, Mol Cell **8**, 683–691 (2001).
[102] D. T. Gillespie, J. Phys. Chem. **81**, 2340 - 2361 (1977).
[103] A. B. Bortz, M. H. Kalos, and J. L. Lebowitz, J. Comp. Phys. **17**, 10 (1975).
[104] Johan Hattne, David Fange, and Johan Elf **21**, 2923-2924 (2005).
[105] M. Ander, P. Beltrao, B. Di Ventura, J. Ferkinghoff-Berg, M. Foglierini, A. Kaplan, C. Lemerle, I. Toma's-Oliveira, and L. Serrano, Syst. Biol. **1**, 129-138 (2004).
[106] C. Lemerle, B. Di Ventura, and L. Serrano, FEBS Letters **579**, 1789-1794 (2005).
[107] J Vidal Rodriguez, Jaap A. Kaandorp, Maciej Dobrzynski, and Joke G Blom **22**, 1895-1901 (2006).
[108] J. Schaff, C. C. Fink, B. Slepchenko, J. H. Carson, and L. M. Loew, Biophys. J. **73**, 1135-1146 (1997).
[109] S. S. Andrews and D. Bray, Physical Biology **1**, 137-151 (2004).
[110] J. R. Stiles, *Computational Neuroscience: Realistic Modeling for Experimentalists*, CRC Press, Boca Raton (2000).
[111] Marco Morelli, *Fluctuations in Genetic Networks: a Computational Study*, PhD Thesis, Amsterdam (2007).
[112] D. Frenkel and B. Smit, *Understanding Molecular Simulations: From Algorithms to Applications, 2nd ed.*, Academic, Boston (2002).
[113] Howard C Berg and L Turner, Biophys J **65**, 2201-2216 (1993).
[114] Jianhua Xing, Fan Bai, Richard Berry, and George Oster, Proc Natl Acad Sci U S A **103**, 1260–1265 (2006).
[115] Seiji Kojima and David F Blair, Biochemistry **40**, 13041-13050 (2001).
[116] Yuhai Tu and G Grinstein, Phys. Rev. Lett. **94**, 208101 (2005).
[117] Thimoty C Elston and Charles S Peskin, Siam J. Appl. Math. **60**, 842-867 (2000).
[118] Thimoty C Elston, Dwight You, and Charles S Peskin, Siam J. Appl. Math. **61**, 776-791 (2000).
[119] William S Ryu, Richard M Berry, and Howard C Berg, Nature **403**, 444-447 (2000).
[120] Stuart W Reid, Mark C Leake, Jennifer H Chandler, Chien-Yung Lo, Judith P Armitage, and Richard M Berry, Proc. Natl. Acad. Sci. USA **101**, 8066-8071 (2006).
[121] Junhua Yuan and Howard C Berg, Proc. Natl. Acad. Sci. USA **105**, 1182-1185 (2008).
[122] L. Turner, A. D. T. Samuel, A. S. Stern, and H. C. Berg, Biophys. J. **77**, 597-603 (1999).
[123] L Turner, Ryu W S, and Howard C Berg, J. Bacteriol. **182**, 2793-2801 (2000).

Samenvatting

Een Computationele Studie van E. coli Chemotaxis

Denken zonder brein

In dit proefschrift speelt de bacterie E. coli een centrale rol. Hij is langwerpig; 0.003 millimeter lang en 0.001 millimeter dik en beweegt zich voort door middel van een aantal lange zweepstaarten. Hij leeft in ons darmkanaal, waar hij onder andere helpt bij het verdrijven van schadelijke bacterien en schimmels. De bacterie E. coli bestaat uit slechts een enkele cel. Toch kan de bacterie een aantal belangrijke beslissingen nemen en taken uitvoeren. Een van de belangrijkste daarvan is het zoeken naar voedsel. E. coli zal zich altijd voortbewegen in de richting van hogere concentraties van voedsel. Dit verschijnsel, waarbij cellen zich bewegen als reactie op de aanwezigheid van voedsel of andere aantrekkende of afstotende stoffen, heet chemotaxis. E. coli is zo klein, dat hij onmogelijk richtingsgevoel kan hebben. De enige manier om voedsel te zoeken is, om op goed geluk vooruit te zwemmen. Als hij merkt dat de hoeveelheid voedsel toeneemt, zwemt hij verder door, maar wanneer de hoeveelheid voedsel afneemt, dan stopt hij even, draait een aantal rondjes (dit wordt een tuimeling genoemd), en zwemt vervolgens op goed geluk - in een willekeurige andere richting verder. Maar hoe neemt een eencellige als E. coli de beslissing om te zwemmen of te tuimelen? Hij heeft namelijk geen hersenen zoals wij. In plaats daarvan zijn in de bacterie eiwitmoleculen aanwezig, die samen een netwerk vormen dat in staat is om deze beslissingen te nemen. Veel eiwitten kunnen in twee (of meer) verschillende toestanden bestaan. Voor het gemak zullen we deze toestanden de aan- en de uittoestand noemen. De cel bevat verschillende soorten eiwitmoleculen, die elk hun eigen taak hebben. Een taak van een eiwit kan bijvoorbeeld zijn, om in de aan-toestand over te gaan wanneer het aan een voedselmolecuul bindt. Een ander eiwit kan als taak hebben om een aan- of uitsignaal door te geven van het ene naar het andere eiwit. Samen vormen de eiwitten een netwerk dat ingewikkelde taken kan uitvoeren, als een klein computertje. Zelfs de zweepharen van de bacterie bestaan uit eiwitten, en die worden aangedreven door een motor, die weer uit andere soorten eiwitten is opgebouwd.

Chemotaxis

Het eiwitnetwerk dat verantwoordelijk is voor het zwemmen van de bacterie in de richting van voedsel, wordt het chemotaxisnetwerk genoemd, het onderwerp van dit proefschrift. Kort gezegd bestaat het chemotaxisnetwerk uit drie componenten. De eerste component is de “neus”, waar zich zogenaamde receptor-eiwitten bevinden, gespecialiseerd in het

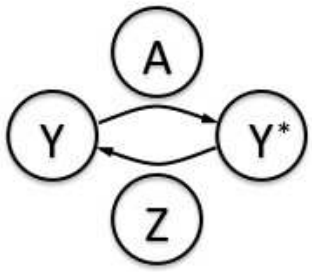

FIGURE 6.11 Een push-pull-netwerk. Het eiwit Y kan in twee toestanden bestaan: Y ("uit") en Y* ("aan"). Het enzym A stimuleert de omzetting van Y naar Y*, en het enzym Z stimuleert de tegengestelde omzetting van Y* naar Y.

herkennen van en binden aan voedseldeeltjes. Hier wordt ook de beslissing genomen om ofwel verder te zwemmen, ofwel te tuimelen. De motoren vormen de laatste schakel van het chemotaxisnetwerk. Zij kunnen in twee richtingen draaien. Draaien ze tegen de klok in, dan vormen de zweepharen een bundel, en zwemt de bacterie netjes rechtdoor. Als de motoren met de klok mee draaien, dan slaan de zweepharen uiteen, wat leidt tot een tuimeling. Tussen de "neus" en de motoren bevindt zich het signaaltransductie-netwerk, dat verantwoordelijk is voor het doorgeven van dit besluit aan de motoren. Een eiwit CheY, speelt hierin een belangrijke rol. CheY kan in twee toestanden voorkomen: "aan" en "uit". CheY staat "aan" als de bacterie moet tuimelen, en "uit" als hij moet zwemmen. In de hoofdstukken 2-5 van dit proefschrift richten wij ons op het middelste gedeelte van het chemotaxisnetwerk, het signaaltransductie-netwerk. Het laatste hoofdstuk gaat over de motoren.

Push-pull-netwerken

Laten we ons nu eerst richten op het tweede deel van het chemotaxisnetwerk, het signaaltransductie-netwerk. Centraal staat het bovengenoemde eiwit CheY, of kortweg Y, dat in twee toestanden voorkomt: Y ("uit"), en Y* ("aan"). Dit eiwitnetwerk bevat slechts twee andere eiwitten, die de omzetting tussen Y en Y* stimuleren (zie figuur 1). Zulke eiwitten worden enzymen genoemd. Het ene enzym, A, zet Y om in Y*, terwijl het andere enzym Z, juist Y* omzet in Y. Dus Z bevordert de "uit"-toestand, en A bevordert de "aan"-toestand. Aangezien A en Z in tegengestelde richting op Y werken, wordt dit netwerk een push-pull-netwerk genoemd. We zullen nu laten zien dat een push-pull-netwerk een heel goede signaalversterker is. We zullen dit uitleggen aan de hand van figuur 1. Stel dat enzym A harder werkt dan enzym Z, bijvoorbeeld doordat er een iets grotere hoeveelheid van enzym A aanwezig is dan van enzym Z. In dat geval wordt alle Y omgezet in Y*, totdat er nauwelijks nog Y over is. Andersom, wanneer enzym Z harder werkt dan enzym A, bijvoorbeeld, wanneer er iets meer van enzym Z in de cel is dan van enzym A, wordt alle Y* omgezet in Y, totdat er nauwelijks nog Y* is. Hoeveel Y* er uiteindelijk is, hangt dus heel sterk af van de verhouding tussen de aanwezige hoeveelheden van de enzymen A en Z. Dit kunnen we goed zien in Figuur 2.3 in hoofdstuk 2 van dit proefschrift. De zwarte lijngeeft de totale hoeveelheid Y*

aan, afhankelijk van de verhouding tussen de hoeveelheden van de enzymen A en Z. Een dergelijke grafiek wordt een responscurve genoemd. Het is duidelijk dat er maar weinig Y* in de cel aanwezig is wanneer er minder A is dan Z, en dat de hoeveelheid Y* plotseling omhoog schiet wanneer er meer A is dan Z. Wanneer we de hoeveelheid van het enzym A als ingangssignaal beschouwen, en de hoeveelheid Y* als uitgangssignaal, betekent dit dat het uitgangssignaal van een push-pull-netwerk enorm kan veranderen wanneer het ingangssignaal maar een heel klein beetje verandert. Zulke signaalversterking is van groot belang op vele plaatsen in de natuur. Overal waar zwakke signalen gemeten worden vindt signaalversterking plaats. Een typisch voorbeeld is het vermogen van onze ogen om te zien in het donker: we kunnen signalen waarnemen die slechts bestaan uit enkele lichtdeeltjes.

Verdeling van de eiwitten over de cel

In de bovenstaande analyse van het push-pull-netwerk hebben we impliciet aangenomen dat de drie eiwitten A, Z en Y gelijkmatig zijn verdeeld over de cel. In werkelijkheid zijn de verschillende componenten van een eiwitnetwerk vaak zeer ongelijkmatig over de cel verdeeld. Zo komt het vaak voor dat een aantal componenten samen complexen vormt. In dit proefschrift staat de vraag centraal hoe de ruimtelijke verdeling van de componenten van een eiwitnetwerk de eigenschappen van het netwerk beinvloedt. Daarbij spelen experimentele waarnemingen door Ady Vaknin en Howard Berg een belangrijke rol []. Vaknin en Berg maakten gebruik van een nieuwe techniek, waarmee de interacties tussen twee soorten moleculen binnen een enkele cel gevolgd kunnen worden. Hierbij wordt het ene te onderzoeken eiwit gekoppeld aan een fluorescent eiwit, en het andere te onderzoeken eiwit aan een ander fluorescent eiwit. Door met lasers op de bacterie te schijnen, kunnen zowel de posities van de twee soorten eiwitten in de cel zichtbaar worden gemaakt, alsook de posities waar de twee eiwitten aan elkaar binden. Met deze techniek onderzochten Vaknin en Berg de interacties tussen de eiwitten Y en Z uit het chemotaxisnetwerk van E. coli. Hoewel bekend was dat zowel de Y-moleculen als de Z-moleculen over de hele cel verspreid voorkwamen, bleken de interacties tussen Z en Y voornamelijk bij de “neus” van de cel plaats te vinden. De neus van de cel is dus de plaats in de cel waar Y* in Y wordt omgezet door Z. Interessant is, dat de omgekeerde reactie, waarbij Y in Y* wordt omgezet door A, ook bij de neus van de cel plaatsvindt. Zowel de push-, als de pull-reactie vinden dus plaats bij de neus van de cel. Vaknin en Berg voerden ook een experiment uit waarbij ze de structuur van het enzym Z zodanig veranderden dat het niet meer aan de neus van de cel kon binden. Zoals verwacht vonden de interacties tussen Y en Z nu verspreid door de hele cel plaats. Bovendien vonden Vaknin en Berg dat deze cellen minder gevoelig reageerden op de toevoeging van voedsel.

Resultaten in dit proefschrift

In **hoofdstuk 2** van dit proefschrift onderzoeken we wat de invloed is van de positie in de cel van de enzymen A en Z, op de respons van een push-pull-netwerk. We vinden dat de respons het scherpste is wanneer de twee enzymen zich op dezelfde plaats in de cel bevinden: beide gebonden aan de neus, ofwel beide vrij rondbewegend. We vinden ook dat er van de grote versterking nog maar weinig overblijft wanneer de enzymen A en Z

van elkaar gescheiden zijn.
In dat geval is het niet langer zo dat ofwel alle Y wordt omgezet in Y*, ofwel alle Y* in Y, zoals we hebben gezien in het generieke push-pull-netwerk. Wanneer de enzymen ruimtelijk van elkaar gescheiden zijn kan het zo zijn dat, terwijl aan de ene kant van de cel alle Y in Y* is omgezet door enzym A, aan de andere kant van de cel er juist relatief meer Y is dan Y* door de aanwezigheid van Z. Dit leidt altijd tot een verzwakking van de respons, zoals we in Figuur 2.3 in hoofdstuk 2 kunnen zien.
In **hoofdstuk 3** passen we onze bevindingen van hoofdstuk 2 toe op het chemotaxisnetwerk van E. coli. Zowel uit hoofdstuk 2, alsook uit de experimenten van Vaknin en Berg blijkt dat de respons van het netwerk sterk kan afhangen van de lokalisatie van de enzymen in de cel. Vaknin en Berg meten de respons van het chemotaxisnetwerk na toevoeging van voedsel. Deze respons is de gecombineerde respons van de eerste twee schakels van het chemotaxisnetwerk: zowel de respons van de "neus" als de respons van het signaaltransductienetwerk spelen een rol. Wij stellen een algemeen model op voor de respons van de "neus", en koppelen dit model aan de respons van het signaaltransductienetwerk uit hoofdstuk 2. Echter, we redeneren dat voor geen enkele mogelijke combinatie van de respons van de "neus" aan die van het push-pull-netwerk, de resultaten van Vaknin en Berg bevredigend verklaard kunnen worden. We concluderen daarom dat het signaaltransductienetwerk van E. coli's chemotaxissysteem niet beschreven kan worden als een push-pull-netwerk, en dat het model voor het signaaltransductienetwerk daarom verfijnd dient te worden.
In **hoofdstuk 4** presenteren we een alternatief model voor het signaaltransductienetwerk van E. coli's chemotaxissysteem. Dit model is consistent met een groot aantal experimentele waarnemingen. De belangrijkste ingredient van dit alternatieve model is dat het enzym Z zowel voorkomt gebonden aan de "neus", als in de rest van de cel. We postuleren dat de gebonden hoeveelheid Z weliswaar klein is ten opzichte van de resterende fractie, maar wel veel effectiever werkt: het bindt sterker aan Y* en zet het sneller om in Y. Met dit model zijn we in staat om de resultaten van Vaknin en Berg te verklaren.
In **hoofdstuk 5** onderzoeken we de gevolgen van de colokalisatie van de enzymen A en Z van een push-pull-netwerk aan de "neus" van de cel. In tegenstelling tot de eerdere hoofdstukken, waar we rekenden met de concentraties van de verschillende eiwitten, modelleren we het systeem ditmaal op het niveau van individuele moleculen. Zoals we hebben gezien, vinden in dit geval alle omzettingen van Y naar Y* door A, en van Y* naar Y door Z, aan de neus van de cel plaats. Wanneer we een enkel eiwit Y volgen dat zich aan de neus van de cel bevindt, zien we dat dit enorm snel van toestand verandert: zodra Y is omgezet in Y* door A, wordt het zo ontstane Y* weer omgezet in Y door Z, en dit gaat zo door. Men zou kunnen verwachten dat dit effect de respons van het push-pull-netwerk nog sterker maakt doordat de concentratie van Y dichtbij de neus verhoogd zou worden. Namelijk, een van de eigenschappen van een push-pull-netwerk is, dat de respons scherper wordt wanneer de concentratie van Y hoger wordt. Dit blijkt echter niet het geval te zijn: de gemiddelde respons is vrijwel gelijk aan die van het generieke push-pull-netwerk. Dat komt doordat de beschreven periodes van extreem snelle omzettingen worden afgewisseld met zeer lange excursies van Y, waarin Y ver wegbeweegt van de enzymen A en Z. Het gevolg is dat de gemiddelde concentraties van Y en Y* precies even hoog zijn als in het geval van het generieke push-pull-netwerk. Ook in deze studie vinden we dat de respons afhangt van ruimtelijke verdeling van de

componenten van een push-pull-netwerk: hoe verder de enzymen A en Z van elkaar verwijderd zijn, hoe minder scherp de respons is. Dit komt doordat er dan gebiedjes ontstaan waar A het "wint" van Z, en gebiedjes waar Z de overhand heeft, waardoor er ruimtelijke variaties ontstaan in de concentratie van Y*.
In **hoofdstuk 6** modelleren we de motoren van E. coli, die de zweepharen laten rond-draaien. In het bijzonder bestuderen we het "switchen" van de motor, waarbij de draairichting van de motor verandert. In recente experimenten is het switchgedrag van de motoren bestudeerd []. In deze experimenten werd een zeer klein bolletje aan de zweephaar bevestigd om de rotatie van de motor te kunnen waarnemen. Vervolgens werd gemeten hoe lang de motor gemiddeld in dezelfde richting bleef draaien. Verrassend werd gevonden dat de motoren een sterke voorkeur hadden om al van richting te veranderen na een korte periode van ongeveer 0,2 tot 0,3 seconden. Gebaseerd op een eerder model voor het draaien van de motor, stellen wij een model voor voor het switchen van de motor. Een belangrijke voorspelling van ons model is, dat de motor sneller van richting verandert wanneer er een grotere externe kracht op de motor wordt uitgeoefend. Daarnaast is ons model gebaseerd op de experimentele gegevens dat de zweephaar een spiraalvorm heeft, en dat deze spiraal in de andere richting wordt opgewikkeld wanneer de motor van richting verandert. We verklaren de voorkeur voor korte switchtijden nu als volgt: wanneer de motor net van richting is veranderd, begint de spiraal van de zweephaar zich aanvankelijk af te wikkelen, en vervolgens op te wikkelen in de andere richting. Naar gelang de spiraal verder wordt opgewikkeld, neemt de kracht op de motor toe. Na een wachttijd van ongeveer 0,2 tot 0,3 seconden is de kracht op de motor dusdanig hoog geworden, voornamelijk door de wrijvingskracht op het bolletje dat aan de zweephaar bevestigd is, dat de kans om te switchen aanzienlijk begint te worden. Met dit mechanisme zijn we inderdaad in staat om de experimentele switchtijd-verdelingen te verklaren.

Dankwoord

Toen ik mijn promotieonderzoek op Amolf begon, wist ik maar weinig van wat er zich binnen de levende cel afspeelt. Zo herinner ik me dat ik op mijn sollicitatie geheel onvoorbereid bij Sander werd langsgestuurd, en echt geen idee had waar hij het over had; ik herinner me alleen nog vaag het woord epistase. Gelukkig is daar langzaamaan verandering in gekomen. Pieter Rein is voor mij een leermeester geweest op alle gebieden. Hij vindt werkelijk alles interessant en kan over alles meepraten. Hoewel de naam van de groep slechts de termen "bio" en "chemie" bevat, zijn wiskunde, informatica en vooral natuurkunde zeker zo belangrijk. Niet alleen qua breedte, maar ook qua diepgang is Pieter Rein ongeëvenaard. De klassieke werkbesprekingen namen vrijwel de hele dag in beslag, mede dankzij Jeroens onverzadigbare interesse (jammer dat je maar eens per week langskwam!), en wat later ook door Sorins onuitputtelijke ideeën. (Sorin, thank you for the collaboration; you always come up with surprising new ideas (very inspiring indeed!))
Pieter Rein, van jou heb ik enorm veel geleerd. Bedankt ook voor je grote enthousiasme en betrokkenheid. Dank je wel!
Heleen, mijn excuses dat ik Pieter Rein zo vaak in beslag heb genomen, en dank je voor de heerlijke couscous op de boot!
Bela en Daan, fantastisch dat ik bij julie altijd met vragen terecht kon, waarop jullie bovendien altijd een antwoord hebben, namelijk het goede!
Beste Joost en Marcel, aan jullie heb ik mijn grote interesse voor statistische fysica te danken. Jullie enorme enthousiasme en kunde stimuleerden mij om op dit gebied verder te gaan. Dank voor de lange discussies, brainstorms en aanmoedigingen!
Harald, het was geweldig om je kamergenoot te zijn! Dank je voor je hulp, inspiratie en gezelschap. Met mijn nieuwe kamergenoten zet ik toch maar geen Schnittke of Stockhausen op...
Rutger, bij jou kon ik altijd terecht voor vragen over de meest uiteenlopende onderwerpen. Verder is het altijd gezellig en eindigt de conversatie altijd in een goede grap.
Rosalind, thank you for your great help and for always being in a good mood!
Christian, bedankt voor de bijzondere boottochten en de mooie foto's!
Marco, thanks for the tiramisu and the great holiday in Canada, and just for being a nice colleague!
Thank you for your good company, my (former) fellow group members, Bas, Daiane, Filipe, Josef, Pim, Thorsten and Wiet.
Rhoda and Suckjoon, thank you for an inspiring friendship!
Simon, enorm bedankt voor je hulp! Na een lange fotosessie bood je aan om even snel een omslag voor me in elkaar te zetten. Uiteindelijk heb je hier minstens tweemaal tot diep in de nacht aan gewerkt!
Dr. Frank en dr. Laura, dank voor jullie dagelijkse nachtelijke gezelschap! Heel veel succes samen in de VS! En geniet ervan; ik denk dat maar weinigen zó graag werken!
Beste Adriaan, het was erg leuk om je collega op Amolf te zijn; het was altijd goed om

je even te spreken. En de vogelavonturen vergeet ik nooit!
Sanne, ontzettend bedankt voor je hulp, enthousiasme en gezelligheid!
Niels, dank je voor het organiseren van alle spelletjesavonden en wandeltochten!
Liedewij en Sven, bedankt, onze trouwe concertbezoekers!
Daan, ik zal de voetbalpoule, de blubberrace en Donkey Kong missen!
Koos en Dorit, bedankt voor de gezelligheid in de Kerkstraat, en de heerlijke cocktails!
Ruud en Astrid, hopelijk kunnen we jullie overhalen om toch nog eens naar Noorwegen te komen!
Hinco, bedankt voor de gezelligheid en de bootfeesten!
Julien, thanks for your ridiculous humor and nice drawings all over the place:-)
Gerbrand, wellicht tot ziens in Noorwegen!
Lars en Jan, bedankt voor de goede computerondersteuning!
Beste OR-mannen, het was een plezier om met jullie samen te werken!
Beste teamgenoten van de Maaiveldcompetitie Eva, Maarten, Gerbrand, Rimco en Annemieke, bedankt voor de intense en inspirerende samenwerking.
Thank you all, my dear colleagues, for making Amolf the nice place it is:
Aileen, Ana, Andrea, Anne, Anne Mie, Astrid, Behnaz, Benjamin, Bianca, Chantal, Duncan, Eelco, Erny, Eva, Gertjan, Gijsje, Guillaume, Jan-Willem, Kim, Kostya, Iza, Live, Jerien, Manju, Marian, Marileen, Marina, Marjon, Marjo, Matt, Mel, Nefeli, Nicolas, Ndika, Nienke, Paige, Patrick, Philip, Philipp, Piet, Roland, Rutger, Sander, Sjoerd, Svenja, Tatiana, Thomas, Trees, Wenbing, Willemijn and Wouter.
Beste Huygens-leden en olo's, bedankt voor de gezellige vergaderingen, waar ik veel heb geleerd, en waar ik lezingen over mijn passies mocht houden, zoals de verdeling van taart en dronkemanswandelingen.
Marcelo, bedankt voor de inwijding in de tangomuziek, je enthousiasme en vertrouwen. Je arrangementen zijn super en jouw cd heeft dit proefschrift begeleid!
Beste Bas, Reinout, Michael en Ruth, jullie ben ik zeer dankbaar voor het jarenlange samenspel en de gezelligheid in strijkkwartet en -kwintet.
Beste Claire, Miriam, Pieter en Leonard, dank jullie voor de fantastische tijd in het ConCordeKwartet. Concerten, bruiloften, fotosessies, diners en lessen... altijd weer enorm gezellig!
Miriam en Pieter, superleuk dat jullie straks naast mij komen staan op de grote dag, als paranimfen!
Johan en Bart, beste makkers, helaas zien we elkaar veel te weinig. Maar, wanneer het Aumann-trio weer bijeen is, is het goed!
En Kasper, nu heb ik eindelijk tijd om weer eens een potje te schaken!
Beste Opa, het is altijd fijn om u te zien. Altijd scherp en op de hoogte van alle nieuws, en altijd met een enorme stapel dikke boeken, die u altijd al uit hebt...
Sas, mijn lieve zus, ik kijk ernaar uit om weer dichter bij je in de buurt te wonen. Het is altijd een feest als je belt, of de telefoon opneemt. Succes met je talloze bezigheden, en hopelijk tot heel snel!
Lieve pap en mam, dank jullie voor je enorme steun. Jullie zijn er altijd wanneer ik je nodig heb. En ik waardeer het erg dat jullie op de belangrijke momenten toch altijd kritisch blijven.
Kjære Clazien, Terje, Marius, Yrjan og farmor, tusen takk for at dere alltid husker på meg og tror på meg!

Tenslotte bedank ik jou, mijn lieve Siri. Jouw warmte en positieve instelling maken niet alleen mij gelukkig, maar iedereen om je heen. Dank je voor je oneindige liefde, vertrouwen en steun. Dat je hier de hele nacht bent gebleven om me te helpen is voor jou een vanzelfsprekendheid. Je bent een engel.

Ik ben zeker mensen vergeten, daarvoor bij voorbaat mijn excuses. Mocht je in dit dankwoord je naam niet terugvinden, en je vindt dat je best bedankt had mogen worden: hierbij mijn hartelijke dank!

Siebe van Albada
Amsterdam, Juli 2008